NASA Conference Publication 2097

Solar Cell High Efficiency and Radiation Damage - 1979

A conference held at
Lewis Research Center
Cleveland, Ohio
June 13-14, 1979

NASA

NASA Conference Publication 2097

Solar Cell High Efficiency and Radiation Damage - 1979

A conference held at
Lewis Research Center
Cleveland, Ohio
June 13-14, 1979

NASA
National Aeronautics and
Space Administration

Scientific and Technical
Information Office

1979

FOREWORD

Twenty-five years ago, in May 1954, Chapin, Fuller, and Pearson published a paper entitled "A New Silicon P-N Junction Photocell for Converting Solar Radiation into Electrical Power" in the Journal of Applied Physics. That paper announced the discovery of the modern solar cell. The silicon p-n junction solar cell has been found to be a remarkable device of important, lasting value. Its invention in 1954 was timely. It made possible the rapid progress in the space program. Conversely, the space program made possible the development of this invention into an efficient, reliable, and commercially available device. Not only has it been the workhorse source of power for satellites, but it is now also a leading candidate for generating solar-electric power for widespread use on the ground. Let this meeting then be a commemoration of the 25th anniversary of the invention of the modern solar cell and the beginning of this rewarding field of endeavor which still stimulates our scientific and engineering talents.

This meeting is the third in a series that started in 1974. The objective of these meetings is to assess where we stand in our efforts to increase the end-of-life efficiency of solar cells for space use. This assessment includes review of progress, problems, and future directions. These meetings were not intended to be miniature versions of professional society conferences, like the Photovoltaic Specialists Conference, whose primary purpose is to disseminate recently generated information. This meeting and those preceding it are intended to serve as forums in which the experts in photovoltaics can express their individual and collective judgments on suitable, attainable goals for space solar cells, the barriers remaining, and the most viable approaches past these barriers toward the goals. The emphasis is on the exchange and discussion of ideas and opinions rather than data.

In the November 1974 meeting the same questions were addressed and the following major conclusions were reached:

- The maximum practical efficiency of silicon solar cells is between 17 and 20 percent AMO and is still a reasonable goal.
- The long-range R&D approach toward this goal should continue to focus on low-resistivity (0.1 ohm-cm) silicon.
- Near-term R&D should continue to focus on higher resistivity silicon, back surface fields, thinner grid fingers, and surface texturing to produce efficiency improvements.
- More research should be undertaken on radiation damage to raise end-of-life efficiency.

- Development of a production cell involves trade-offs among fabricability, cost, and performance.

In April 1977 the second meeting was held. In response to the 1974 conclusions, more attention was given to radiation damage and to gallium arsenide cells. The conclusions from the 1977 meeting were as follows:

Silicon cell efficiency

- Nearly 20 percent AMO is possible if the open-circuit voltage is raised to 0.7 volt.
- Voltage-limiting mechanisms were listed.
- High-quality silicon is not needed.

Radiation damage

- Radiation damage must be addressed as well as beginning-of-life efficiency.
- Major gains are yet to be made.
- Much basic theoretical and experimental work remains to be done.

Gallium arsenide cells

- Eighteen percent AMO has been achieved.
- Twenty-two percent AMO is the estimated limit.
- Theoretical models are inadequate.
- Radiation tolerance is uncertain.
- Radiation damage mechanisms are not well understood.

At this meeting the same basic questions were asked, but the scope has been broadened again - now to include 30 percent devices in addition to silicon and gallium arsenide cell efficiency and radiation damage.

Short presentations of the latest and most significant developments were made to provide a basis for subsequent discussions. These short papers are assembled in this proceedings. Unfortunately it was not possible to record the fruitful and stimulating discussions.

Following the presentation of the papers and the discussion, four concurrent workshop sessions were conducted to address goals, barriers, and approaches in the following areas:

Silicon High Efficiency Solar Cells

Workshop Chairman, Henry W. Brandhorst, Jr., NASA Lewis Research Center

Silicon Solar Cell Radiation Damage

Workshop Chairman, Richard L. Statler, Naval Research Laboratory

GaAs Solar Cell Performance and Radiation Damage

Workshop Chairman, G. Sanjiv Kamath, Hughes Research Laboratories

30 Percent Devices

Workshop Chairman, Joseph J. Loferski, Brown University

An oral report of each workshop was presented and discussed in a plenary session. Written workshop reports prepared by the workshop chairmen are included in this proceedings.

The Meeting Coordinator, Cosmo R. Baraona and his Committee, Thomas M. Klucher, George Mazaris, and Clifford K. Swartz, are to be commended for their skillful and persistent efforts that resulted in a smoothly operating, informative meeting. The meeting participants' stimulating, insightful, candid, and thoughtful discussions helped make the meeting a total success.

Cochairmen:
Daniel T. Bernatowicz
Henry W. Brandhorst, Jr.
NASA Lewis Research Center

CONTENTS

Page

FOREWORD iii

OVERVIEW

The NASA Lewis Research Center Program in Space Solar Cell Research and Technology
Henry W. Brandhorst, Jr., NASA Lewis Research Center 1

Solar Photovoltaic Research and Development Program of the Air Force Aero Propulsion Laboratory
Joseph Wise, Air Force Aero Propulsion Laboratory. 5

The JPL Space Photovoltaic Program
John A. Scott-Monck, Jet Propulsion Laboratory 9

Langley Program of GaAs Solar Cells
E. J. Conway, NASA Langley Research Center 13

SILICON HIGH EFFICIENCY SOLAR CELLS

Updating the Limit Efficiency of Silicon Solar Cells
M. Wolf, University of Pennsylvania. 15

Limiting Process in Shallow Junction Solar Cells
A. Meulenberg and E. Rittner, COMSAT Laboratories. 35

Design of High Efficiency HLE Solar Cells for Space and Terrestrial Applications
A. Neugroschel and F. A. Lindholm, University of Florida 37

Application of Ion Implantation to High Performance, Radiation Tolerant Silicon Solar Cells
Allen R. Kirkpatrick, John A. Minnucci, and Keith W. Matthei, Spire Corporation. 51

Open-Circuit-Voltage Improvements in Low-Resistivity Solar Cells
Michael P. Godlewski, Thomas M. Klucher, George A. Mazaris, and Victor G. Wiezer, NASA Lewis Research Center 61

A New Method for Modeling Multilayer Solar Cell Structures
M. Wolf and Y. H. Wu, University of Pennsylvania 71

Modeling of Thin, Back-Wall Silicon Solar Cells
Cosmo A. Baraona, NASA Lewis Research Center 73

Design Considerations for the Tandem Junction Solar Cell
W. T. Matzen, B. G. Carbajal, and R. W. Hardy, Texas Instruments, Inc. 79

Thin Cells for Space
G. Storti, J. Wohlgemuth, and C. Wrigley, Solarex, Inc. 87

High Efficiency Cell Geometry
R. N. Hall, General Electric Company 97

Silicon Solar Cells for Space Use: Present Performance and Trends
P. A. Iles, F. F. Ho, and S. Khemthong, Photoelectronics Corporation of America 101

Laser Techniques in Photovoltaic Research
R. T. Young, R. F. Wood, R. D. Westbrook, J. Narayan, and C. W. White, Oak Ridge National Laboratory 105

Summary of Silicon High Efficiency Solar Cell Workshop
Henry W. Brandhorst, Jr., NASA Lewis Research Center 113

SILICON SOLAR CELL RADIATION DAMAGE

An Interim Report on the NTS-2 Solar Cell Experiment
Richard L. Statler and Delores H. Walker, Naval Research Laboratory. 117

Electron Irradiation of Tandem Junction Solar Cells
Bruce E. Anspaugh, Tetsuo F. Miyahira, and John A. Scott-Monck, Jet Propulsion Laboratory 131

Radiation Damage in High-Voltage Silicon Solar Cells
Irving Weinberg, Clifford K. Swartz, and Victor G. Weizer, NASA Lewis Research Center 137

CO_2 Laser Annealing of 50-μm-Thick Silicon Solar Cells
Frank E. Walker, Boeing Aerospace Company. 145

Reverse Annealing in Radiation-Damaged Silicon Solar Cells
Irving Weinberg and Clifford K. Swartz, NASA Lewis Research Center. 161

Effect of Dopants on Annealing Performance of Silicon Solar Cells
John A. Scott-Monck and Bruce E. Anspaugh, Jet Propulsion Laboratory. 173

High-Energy Electron-Induced Damage Production at Room Temperature in Aluminum-Doped Silicon
J. W. Corbett, L.-J. Cheng, A. Jaworowski, J. P. Karins, Y. H. Lee, L. Lindström, P. M. Mooney, G. Oehrlein, and K. L. Wang, State University of New York at Albany 185

Oxygen Microdistribution in Silicon and Its Effects on Electronic Properties
Harry C. Gatos, Massachusetts Institute of Technology. 197

Summary of Silicon Solar Cell Radiation Damage Workshop
Richard L. Statler, Naval Research Laboratory. 199

GaAs SOLAR CELL PERFORMANCE AND RADIATION DAMAGE

Radiation Damage in GaAs Solar Cells
E. J. Conway and G. H. Walker, NASA Langley Research Center. . . . 201

Fabrication of High Efficiency and Radiation Resistant GaAs Solar Cells
S. Kamath, R. C. Knechtli, and R. Loo, Hughes Research Laboratories 209

Temperature and Intensity Dependence of the Performance of an Electron-Irradiated (AlGa)As/GaAs Solar Cell
Clifford K. Swartz and Russell E. Hart, Jr., NASA Lewis Research Center 217

Shallow-Homojunction GaAs Solar Cells
John C. C. Fan, Massachusetts Institute of Technology 227

Radiation Effects in GaAs AMOS Solar Cells
B. K. Shin and R. J. Stirn, Jet Propulsion Laboratory 235

Capacitance Transients in p-Type GaAs MOS Structures and Application to Lifetime Mapping During Solar Cell Fabrication
G. Vitale, J. J. Loferski, and Y. Ercil, Brown University 245

Annealing in Electron-Irradiated AlGaAs Solar Cells
Bruce E. Anspaugh and John A. Scott-Monck, Jet Propulsion Laboratory 247

Summary of GaAs Solar Cell Performance and Radiation Damage Workshop
G. S. Kamath, Hughes Research Laboratories 253

30 PERCENT DEVICES

A Review of Air Force High Efficiency Cascaded Multiple Bandgap Solar Cell Research and Development
W. P. Rahilly, Air Force Aero Propulsion Laboratory 255

Efficiency of Tandem Solar Cell Systems as Function of Temperature and Solar Energy Concentration Ratio
N. A. Gokcen, U.S. Bureau of Mines, and J. J. Loferski, Brown University 263

Computer Modeling of a Two-Junction, Monolithic Cascade Solar Cell
M. F. Lamorte and D. Abbott, Research Triangle Institute 267

Intercell Ohmic Contacts for High Efficiency Multijunction Solar Converters
Stanley W. Zehr, D. L. Miller, J. S. Harris, Jr., Rockwell International Electronics Research Center 283

Summary of Workshop on 30 Percent Devices
J. J. Loferski, Brown University 293

APPENDIX - ATTENDEES 297

THE NASA LEWIS RESEARCH CENTER PROGRAM IN SPACE SOLAR CELL RESEARCH AND TECHNOLOGY

Henry W. Brandhorst, Jr.
National Aeronautics and Space Administration
Lewis Research Center

ABSTRACT

The NASA Lewis program in space solar cell research and technology has as its objectives to improve conversion efficiency, to reduce mass and cost, and to increase the operating life of solar cells and blankets. The major thrusts of the program are to produce an 18%-AMO-efficient silicon solar cell, to effect substantial reduction in the radiation damage suffered by silicon solar cells in space, to develop high efficiency wrap-around contact and thin (50 μm) coplanar back contact silicon solar cells, to substantially reduce the cost of silicon cells for space use, to develop cost-effective GaAs solar cells, to investigate the feasibility of 30% AMO solar energy conversion and to develop reliable encapsulants for space blankets. The major targets and milestones that guide this program are shown in figure 1. The major targets are shown within ellipses.

The major solar cell and blanket development activities are shown in figure 2. In the 18% cell development area, substantial progress has been made in understanding voltage limiting mechanisms. Silicon cells with voltages of about 645 mV have been fabricated by three techniques. Because of this progress, a contract to develop an 18% efficient cell is anticipated.

Significant increases in the understanding of radiation damage have also occurred. The three defects responsible for performance degradation have been identified and schemes to prevent their formation are under study. Alternative means for removing damage, such as annealing or use of healing additives, are under study. Additionally, cell designs that should show improved performance in a radiation environment are being persued.

Development of the 14% efficient, high efficiency wrap-around contact cell is proceeding. This cell is 200 μm and has dielectric edge insulation. Thin (50 μm) interdigitated back contact cells are being developed on contract, with the goal of achieving 13% efficient cells.

Low cost area cells with areas of at least 25 cm^2 are going to be developed under contract. Previous effort has established the feasibility of a number of low-cost, high-volume processing steps that should enable high performance, space quality cells to be produced for costs under $5/W.

A new program area is being initiated to develop cost-effective, radiation-resistant GaAs solar cells. One promising approach that is being supported is at MIT Lincoln Laboratory for the n/p CVD shallow junction cell.

The types of missions that GaAs cells would be suited for are also under study. Another area of new program development lies in the domain of 30% solar energy conversion. The feasibility of achieving this efficiency is presently being assessed.

The primary focus of blanket technology is the development of practical thin encapsulants for solar cell blankets. The feasibility of electrostatic bonding of 50-75 μm 7070 cover glasses has been demonstrated. Additionally, a variety of different types of encapsulants such as silicones and glass resins are being evaluated for their durability to space UV and particulate radiation.

In summary, the NASA Lewis Research Center program in space solar cell research and technology seeks to understand and eliminate barriers to achieving 18% silicon cell conversion efficiency, to develop and implement the technologies necessary to produce radiation resistant, high efficiency, and low cost solar cells and blankets. New programs of GaAs cell development and 30% conversion devices are beginning. Significant progress has been made in all areas of research.

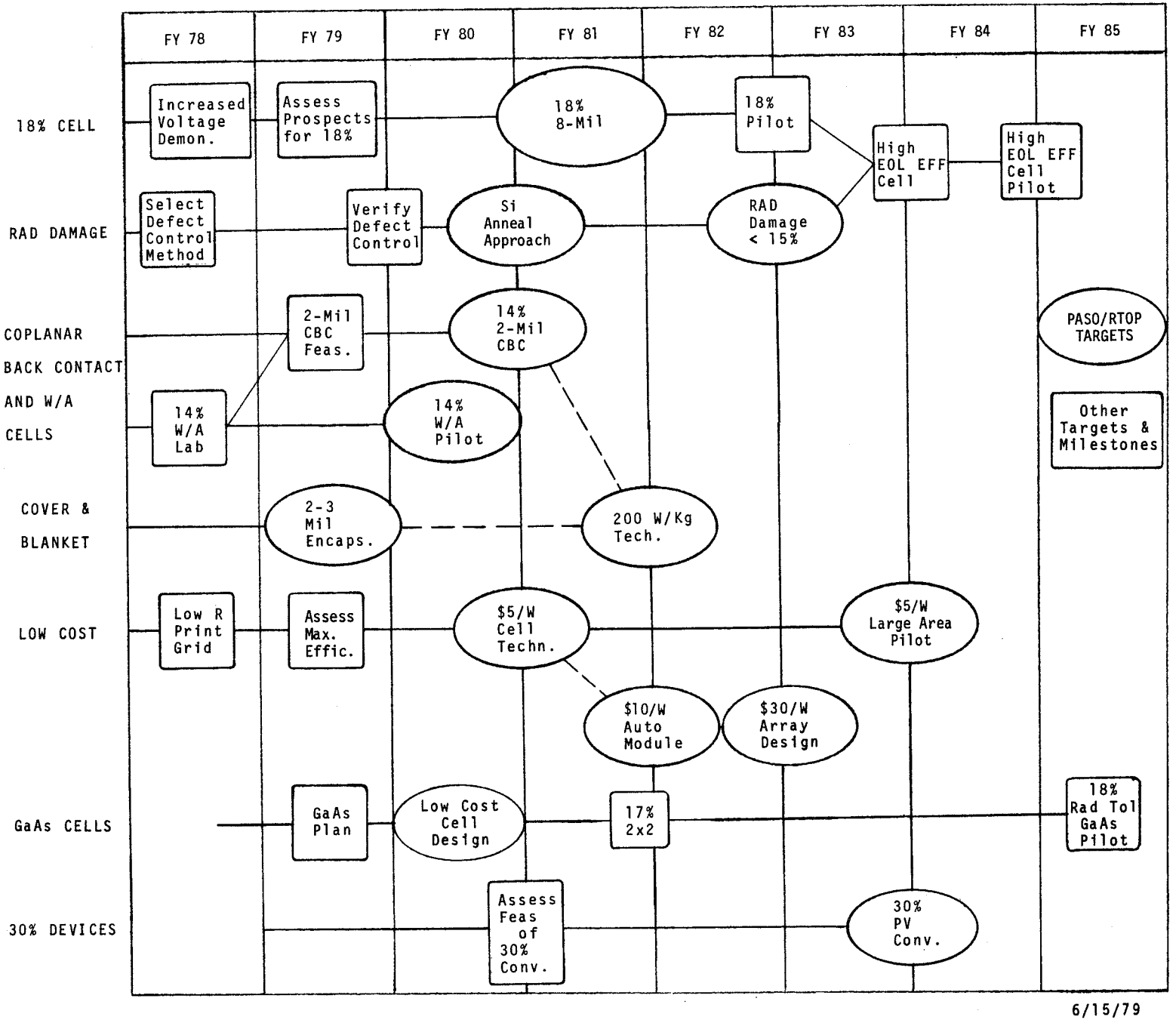

Figure 1.- Lewis solar cell and blanket research-and-development activities.

18% CELL

- STUDY OF RECOMBINATION CENTERS IN 0.1 Ω-CM Si, U. FLA.
- DEVELOPMENT OF 18% EFFICIENT Si SOLAR CELL (NEW CONTRACT).
- DIFFUSED TAILORED JUNCTION (I-H).

RADIATION DAMAGE

- FUNDAMENTALS OF RADIATION TOLERANCE IN Si SOLAR CELLS, SUNY-ALBANY.
- SOLAR CELL PROCESSING FOR IMPROVED RADIATION TOLERANCE, SPIRE CORP.
- MICRODISTRIBUTION OF RADIATION DAMAGE IN SOLAR CELLS, MIT.
- LASER ANNEALING OF RADIATION INDUCED DEFECTS (NEW).
- RADIATION RESISTANT THIN NIP CELL, COMSAT CORP.
- RADIATION DAMAGE EFFECTS (I-H).

COPLANAR BACK CONTACT

- THIN INTERDIGITATED CELL DEVELOPMENT, SOLAREX CORP.
- THIN INTERDIGITATED CELL DEVELOPMENT, (NEW).
- CBC PROTOTYPE DEVELOPMENT (I-H).
- HIGH EFFICIENCY W/A CONTACT SOLAR CELL DEVELOPMENT, SPECTROLAB, INC.

LOW COST CELL TECHNOLOGY

- LOW COST, LARGE-AREA Si CELLS (NEW).
- LARGE-AREA, LOW COST CELL DEVELOPMENT (I-H).

GaAs SOLAR CELLS

- GaAs CVD HOMOJUNCTION SOLAR CELL DEVELOPMENT, MIT LINCOLN LABORATORY, (BEING NEGOTIATED).
- GaAs CELL DEVELOPMENT (I-H).

30% DIRECT SOLAR CONVERSION

- 30% CONVERSION ANALYSIS (NEW).
- 30% CONVERSION ANALYSIS (I-H).

SOLAR CELL BLANKET TECHNOLOGY

- COVER EVALUATION (NEW).
- ESB MODULE DEVELOPMENT (NEW).
- EXPLORATORY DEVELOPMENT AND EVALUATION (I-H).

Figure 2.- Solar cell development activities.

SOLAR PHOTOVOLTAIC RESEARCH AND DEVELOPMENT PROGRAM OF THE AIR FORCE AERO PROPULSION LABORATORY

Joseph Wise
Air Force Aero Propulsion Laboratory
Wright-Patterson Air Force Base

The Air Force space program has continuing requirements for increased power system capability in terms of volume, area, weight, life, power level, and survivability. Figure 1 shows our goals in these various areas. Nuclear radiation survivability has generally been accomplished, but the degradation on exposure to the particulate species of nuclear weapon effects still requires improvement.

The laser weapon effects program again is primarily aimed at survivability for certain dose levels as well as determination of the thresholds for failure of the various solar cell array configurations. Much of this background has been acquired in continuous wave radiation, and approaches to minimize degradation are under development in the SMATH programs conducted under the AF Materials Lab contracts. The pulsed laser effects area is just beginning investigation, and the program initiated in FY79 is addressing several laser wavelengths and pulse durations. For the first time also we are attempting to handle advanced cell assemblies, i.e., high efficiency silicon, GaAs, and multiband gap if sufficient cells are fabricated in the next three years. The effort is irradiating both cw and pulsed laser species.

The silicon solar cell concepts investigated include textured, planar cells for ESB, various field combinations and non-reflecting vertical junction combinations. Funding from basic research exploratory development and advanced development are utilized. The basic research work deals with theoretical efforts as well as experimental investigation of effects of selected dopants such as gallium in high purity silicon. The HESP II silicon advanced development program contractor reported 16% efficiency in a textured cell configuration with 2 Ω-cm silicon. Because of high α the modeling of this cell in orbit results in a temperature of 10 to 15 C° higher, negating most of this gain. For this reason we have also supported development of planar silicon cells with multilayer antireflective coating, yielding 14.8% efficiency at 25° C. This cell is slightly better than the textured cell at operating temperature. Vertical junction solar cell work is directed toward 16 to 18% initial efficiency with 14% after 10^{15}, 1 MeV e^-/cm^2 equivalent radiation. Technology appears in hand for 15% initial efficiency without fields or use of optimum geometry. With back surface field to enhance voltage and geometry optimization, we hope to approach 16% efficiency. The high-purity, high-lifetime silicon from our basic research effort may also help out both initial and end-of-life efficiency.

The relationships of our near, intermediate, and long term solar cell development are shown in figure 2. The current GaAs cell program was initiated in 1976 and we have achieved better than 17% in the laboratory with radiation resistance superior to that of silicon up to $5X10^{15}$, 1 MeV e^-/cm^2. Companion programs to this GaAs cell development are the development of dendrite ribbon material and the development of solar array panel technology presently under negotiation for a FY79 start. This technology, when developed, should yield 50% greater end-of-life power at orbit temperature. The multiband-gap cell work is aimed at an initial efficiency of 25% and is considered relatively high risk because of the problems of lattice mismatch and band-gap matching required. (Dr. W.P. Rahilly discusses this in greater detail.) This technology will not come on line before the mid 80's and is very important to our weight, volume, and area goals for satellite power systems.

In addition to weapon effects and cell technology efforts, we are also initiating a high-voltage hardened, high-power system technology program. For the first time we are also addressing thermal energy management. The effort is directed toward future requirements in the 5 to 50 kW range and power densities of 6 to 12 W/lb. Weight reductions in all facets of power system technology, including batteries, are needed to achieve this capability. This effort also addresses Shuttle compatibility and modular power system component technology.

The present weight limit on satellites in synchronous orbit is about 3300 lb using a Titan III C and high-energy second stage. With the advent of the Shuttle and the use of the inertial upper stage (IUS) this weight capability increases to 5200 lb. Figure 3 shows the power system capability in this scenario. Present capability could insert 4.3 kW satellite BOL power. With the introduction of the two intermediate concepts of GaAs cells and NiH_2 battery, we can boost this power to 8 kW. Advanced technology can go to an 11 kW power level without an orbit assembly. Lower altitude orbits can, of course, accommodate higher weight vehicles and correspondingly higher power levels.

- SPACE: HIGH EFF. WEAPON HARD, LONG LIFE, LIGHT WEIGHT, LOW VOLUME, LOW COST
- NUCLEAR WEAPON HARDEN SI PRESENT - HASP
  APPLY TO ADVANCED CELLS SI, GaAs
- LASER HARDENING C.W. - UNDERSTAND - APPROACHES IN DEV.
  PULSED - PROBLEMS BEING DEFINED, INITIATE DEV.
- SOLAR CELL CONCEPTS
  - NEAR TERM: SILICON HESP II 16% 12% EOL
    NRVJ 14% EOL
    6.1 MATERIALS
  - INTERMEDIATE: GaAs HESP II 16% EFF. OPER.
    ULTIMATE 18-20% EFF. 1983
  - LONG TERM: MULTIJUNCTION 25% EFF. 1985
    30% 1990

Figure 1. - Solar power R&D objectives (AFAPL).

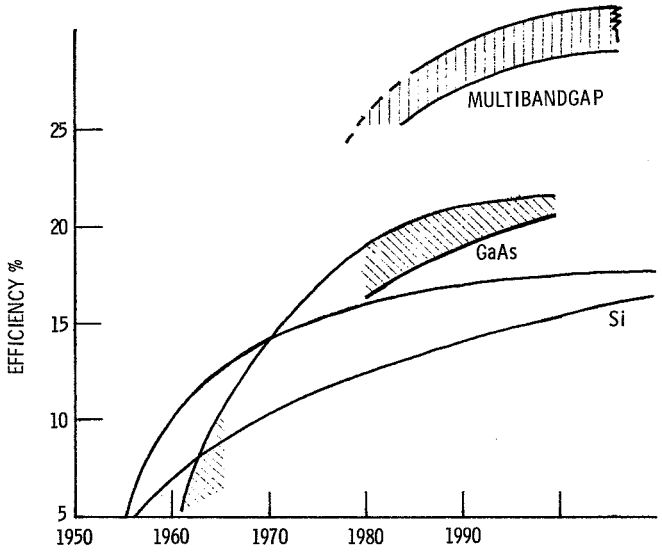

Figure 2. - Solar cell efficiency as function of time.

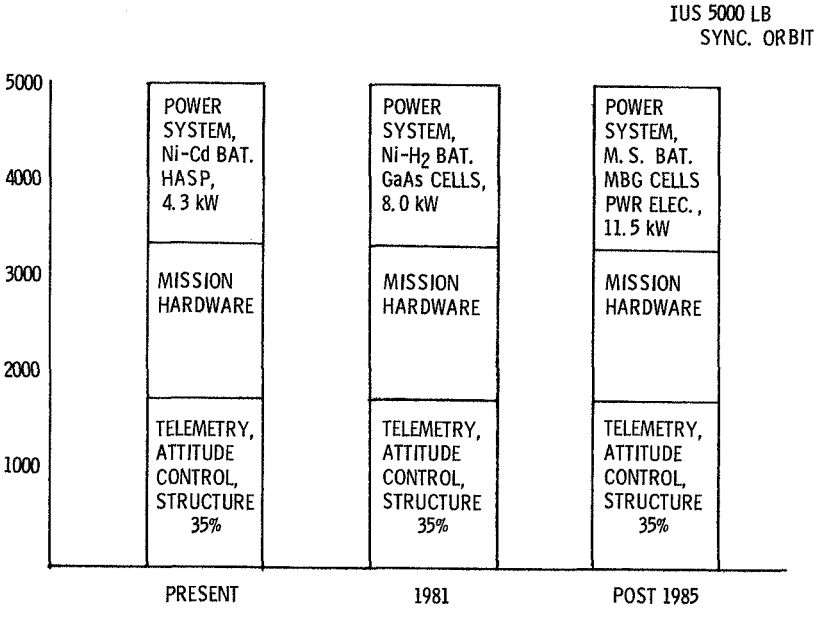

Figure 3. - Power-component payoff in synchronous-orbit satellites - high-voltage, high-power, hardened system.

THE JPL SPACE PHOTOVOLTAIC PROGRAM*

John A. Scott-Monck
Jet Propulsion Laboratory
California Institute of Technology

SUMMARY

A brief overview of the JPL activities in space photovoltaic research and development is presented. Work that is being performed at JPL, as well as external programs directed by JPL for the NASA Office of Aeronautics and Space Technology are described.

INTRODUCTION

JPL has as its primary charter, interplantary exploration. Many missions, due to environment or solar distance, have in the past precluded employment of photovoltaics. Those JPL missions that use solar cells for power often operate at other than 1 AU. Therefore, a significant amount of our effort is involved in evaluating solar cells under rather novel conditions of temperature, solar intensity and radiation.

The JPL activities in array design and development are oriented to high performance goals such as extremely high specific power or increased radiation resistance. The need for advanced cells to support these efforts has been the main stimulus for the work in pilot cell development of advanced silicon solar cells such as the OAST thin cell.

Future requirements will demand that solar cell panels deliver even more power per unit area without sacrificing mass. Radiation resistance, which has always been an important parameter in panel design, will become even more critical as NASA begins to develop a new generation of satellites for operation in geosynchronous orbit. For these reasons, JPL has had an active internal program in GaAs solar cells. This material has already demonstrated superiority to silicon with respect to power per unit area and radiation resistance.

CELL PILOT PRODUCTION

JPL is in the process of bringing the OAST thin cell to flight readiness by demonstrating that this advanced silicon solar cell can be produced in

*This paper presents the results of one phase of research carried out by the Jet Propulsion Laboratory, California Institute of Technology, under Contract NAS7-100 sponsored by the National Aeronautics and Space Administration.

quantity at a cost which is competitive with present state-of-the-art space solar cells. This activity is the culmination of a four year program that has resulted in a silicon solar cell which is only 50μm thick, yet can produce the equivalent power of silicon cells which are four to five times thicker.

It is anticipated that within a year the pilot production effort being carried out by the Solarex Corp. for JPL will demonstrate an average AM0 conversion efficiency of 13 percent at a production rate of ten thousand 2x2 cm cells per month. In addition, the pilot line will be capable of producing up to one thousand 5x5 cm OAST thin cells with an average efficiency of greater than 11 percent.

This pilot line effort serves two critical purposes, demonstration of production readiness and support of other JPL programs involved in incorporating these cells into high performance arrays. This should act as a stimulus to array designers to seriously consider implementing this advanced silicon solar cell for future space missions.

CELL EVALUATION

This work is divided into two general categories; parametric studies of the electrical performance of solar cells as a function of temperature and solar intensity, and investigation of the influence of radiation and subsequent thermal annealing on the electrical behavior of cells.

The first mentioned effort has been actively pursued by JPL for many years. A great variety of state-of-the-art production cells and mature laboratory devices have been evaluated at JPL. This data has been used by JPL and other organizations involved in flight projects to design suitable solar cell arrays for a great number of missions.

During the past year, evaluation of candidate wraparound contact solar cells for use on SEP type missions has been performed. OAST thin cells from the pilot line have been evaluated. A number of new, high efficiency production cells employing back surface fields, multiple anti-reflection coatings, back surface reflectors and textured surfaces are being examined. In addition there are plans to begin a preliminary characterization of GaAs solar cells, as they become available.

As the interest in such missions as Comet Rendezvous or new array technology such as concentrator enhancement grows, the need for this type of information becomes even more critical. In addition, JPL is beginning a preliminary screening of the new cells being produced for DOE in hopes that some aspects of this emerging technology will demonstrate applicability for space applications.

JPL has placed a strong emphasis on studying radiation damage effects in solar cells, since this is a critical parameter for array design. The JPL Dynamitron facility has been the main tool for this work, but

often other facilities are used to provide data on proton effects. During this year approximately fifty types of production, advanced development and research cells have been tested at the Dynamitron. Wraparound contact, tandem junction, vertical junction, dendritic web, cast silicon, and OAST thin solar cells are just a few examples of what has been done in silicon. Also a number of AlGaAs and GaAs solar cells have been tested.

This year has seen the JPL work extend into the field of annealing. The main stimulus for this activity is the concept of using on-panel annealing of solar cells as a means of either extending mission lifetime or enabling certain mission classes such as orbital transfer to use photovoltaics. However, annealing studies also can be used as a tool to understand those mechanisms which control the radiation damage properties of solar cells. JPL is investigating the annealing behavior of both silicon and AlGaAs solar cells using electron and proton irradiation. Although this is a recent activity, JPL has already begun to produce a significant body of data on the annealing characteristics of solar cells.

GaAs RESEARCH AND DEVELOPMENT

This area represents the commitment of JPL to high technology which will ultimately benefit the NASA space program. JPL has been involved in GaAs solar cell research for a number of years with the emphasis placed on thin film cell types such as the AMOS (Antireflecting Metal-Oxide-Semiconductor) cell. With the recent advances in liquid phase epitaxial grown AlGaAs devices and the chemical vapor deposited GaAs cells, JPL has reoriented its research approach to capitalize on this new technology.

Recognizing that such pragmatic considerations as cell cost and mass will ultimately determine whether GaAs is used for space applications, the JPL effort is focused on an approach that will minimize these factors. The basic thrust of the program is to use organo-metallic chemical vapor deposition methods to grow GaAs on relatively low cost and low mass substrates.

This approach uses silicon as a substrate, thus reducing the cost and mass when compared to other substrate candidates such as germanium or gallium arsenide. The key technology problem now being addressed is to develop a thin interface material layer that will allow a uniform transition between the differing lattice constants of silicon and the CVD grown GaAs. At this point it is not known whether p or n-type base homojunction GaAs cells are the more radiation resistant. Thus, techniques for controlling the resistivity of both types of GaAs over a wide range are being developed. Once these various pieces of technology are assembled, work will begin on developing reliable contacts and anti-reflection coatings.

It is anticipated that the GaAs solar cell developed by JPL will demonstrate marked improvement in output power and radiation resistance when compared to silicon and also be more than competitive with respect to specific power at the array level. These factors combined with the high temperature

properties of GaAs will offer a unique opportunity to demonstrate a solar cell array which under certain conditions will meet the specific power and stability goals of an SPS type mission.

LANGLEY PROGRAM OF GaAs SOLAR CELLS

E. J. Conway
National Aeronautics and Space Administration
Langley Research Center

The Langley Research Center program on GaAs solar cells began in the early 1970's. Its objectives were to develop the technology for (a) 18- to 20-percent AMO efficiency, (b) stability under radiation and elevated-temperature operation, and (c) high power-to-weight ratio. To achieve the efficiency objective, we focused most of our effort on the original heteroface cell. With the achievement of 18-percent cells, the program of grants, contracts, and in-house research was broadened to include (fig. 1) radiation stability, operation at elevated temperature, thin cells, and costs.

The radiation stability research program has three elements:

(1) Device and material damage studies: The effects of proton irradiation on GaAs cells is investigated at Hughes Research Laboratory (HRL). More fundamental measurements on the effects of proton irradiation on cell materials (i.e., n-GaAs, p-GaAs, etc.) are made at the University of Florida. Electron damage of cells is performed in-house. The cells are grown at Langley, irradiated at Lewis, and characterized at Langley.

(2) Annealing studies: Annealing of cells after degradation by 1-MeV-electron irradiation is studied in-house. General parameters studied so far include annealing temperature and time, total fluence, and junction depth. University of Florida studies involve the use of deep-level transient spectroscopy to follow proton damage annealing.

Operation of GaAs cells at elevated temperature is studied through closely coordinated research at the Old Dominion University and at Langley. A series of measurements and analyses of cell characteristics at temperatures to 350° C are in progress.

Thin cells offering high power-to-weight ratio are a very new program element. Some preliminary investigations will be performed at IBM by using CVD techniques. A novel approach, deposition of GaAs and GaAlAs from molten salts, is being investigated at the University of Southern California.

Cell cost and availability appear to be major problems for utilization of GaAs solar cells. A short-term study by A. D. Little, Inc., seeks to define the cost and availability problems and potential solutions for the early 1980's. The final report will be available late this summer.

In summary, Langley has a small, research-oriented program on GaAs solar cells. Our emphasis is on assessing the potential and stimulating the development of technology for these cells.

OVERVIEW OF LaRC PROGRAM
ON GaAs SOLAR CELLS

1. Radiation Stability

   a. Device and Material Damage Studies - LaRC, HRL, U of Fla.
   b. Annealing Studies - LaRC, U of Fla.
   c. Device Optimization by LPE and CVD - LaRC

2. High Temperature Operation

   a. Device Studies - ODU, LaRC

3. Thin Film Cells

   a. Thick and Thin Cells - IBM
   b. Electrodeposition - U. S. C.

4. Processing Technology

   a. Study - A. D. Little

Figure 1.

UPDATING THE LIMIT EFFICIENCY OF SILICON SOLAR CELLS*

M. Wolf
University of Pennsylvania

The last recognized evaluation of the "limit-efficiency" and of design goals for silicon solar cells, based on realistic appearing material parameters and on an idealized device structure, was performed in 1970 under the auspices of the National Academy of Sciences (ref. 1). Since that time, a number of phenomena not recognized then have become reasonably well understood, and some device structuring approaches have evolved which permit "remedial designs" to gain high performance in albeit somewhat more complicated solar cell structures than envisioned earlier. These new circumstances warrant re-evaluation of both the idealized "limit efficiency" and of the design goals, the latter being values that can be expected to be approached in real, produceable devices.

An evaluation of the limit efficiency is suitably based on the simplest, most basic mathematical method that is appropriate for the conditions imposed by the cell model. In this connection, it is important to recognize that the "limit efficiency" has traditionally been evaluated for the idealized "one sun" case, which means no optical concentration and a normal irradiance of 1 kW m^{-2}, which has been obtained by a low-moisture, low-turbidity, direct-beam, air-mass 1 spectral distribution without addition of indirect radiation. For continuity and simplicity, this practice has been extended to this work. An evaluation of the "appropriateness" of approach has shown that the recalculation of the "limit efficiency", as essentially an upper limit, will be carried out with maximum clarity and fully adequate accuracy by application of the existing basic analytical model of a solar cell (ref. 2) to a simple, idealized solar cell structure. From this limit efficiency, a first set of "design goals" can be derived by application of "experience factors", as done here. However, the design calculations can be improved by more sophisticated modeling, which will permit the close evaluation of the relative merits of various realizable structure design options. Following a stepped procedure, in moving from the idealized structure to one more closely resembling a real current or projected design and in applying more sophisticated analysis methods, will have dual benefits: It permits determining the influence on performance of each part of the real solar cell structure relative to the idealized structure; and it permits an evaluation of the relative accuracies obtainable by applying exact analytical methods to approximate structure or operating mechanism models in contrast to applying numerical methods to more closely representative models.

This publication deals only with the limit efficiency obtainable by application of the base analytical method to the simplest idealized solar cell

---

*This work was performed in connection with the activities of the Advisory Group on High Performance, Low-Cost Solar Cells to the DOE/JPL LSA Program, and was partially supported by the U.S. Department of Energy through the Jet Propulsion Laboratory under contract No. KM 68903.

structure. It contains a description of the methodology, of the solar cell structure, of the selection of the material parameters used in the evaluation, and a discussion of the results, including a new set of design goals derived from the limit efficiency. Further publications, in preparation, will extend, in a simple way, the one-dimensional analytical method which is accurately applicable at low level injection to any quasi-neutral region with constant parameters in the device, to general multilayer structures, and apply it to solar cells with at least 2 to 3 layers in each of the two main regions of the device, closely approximating currently realizable structures.

DIFFERENCES TO PRIOR EVALUATIONS OF SOLAR CELL LIMIT EFFICIENCY

A significant number of endeavors have previously been undertaken at determining a "limit efficiency" of solar cells in general, and in particular of silicon solar cells. These endeavours fall essentially into two groups: In the first, the researchers have tried to establish an "absolute theoretical efficiency" based on the application of basic physical principles only, without introduction of structure or material parameters. Some of these approaches were based primarily on the laws of thermodynamics (ref. 3). The larger number of endeavours fall into the second group, having been based on contemporary semiconductor device analysis methods, applied to a somewhat idealized device structure, and using, at the time, realistic appearing material properties. In this second group, the structures were idealized in so far as known, technology-limited effects were extrapolated to levels which appeared to be achieveable in the future, or to the 100% performance level, where the losses resulting from such effects were already rather small. Following the current penchant for abbreviations, this second group might suitably be classified as ReMPIDS modeling, with the abbreviation standing for "realistic material parameters/idealized device structure."

There are clearly three preceding generations of the ReMPIDS approach discernible, so that the current undertaking would represent the fourth generation. The preceding generations date to the 1953-55 period (ref. 4), the 1958-61 periof (ref. 5), and to 1970 (ref. 1). The 1970 model, developed for a committee commissioned by the National Academy of Sciences, was concerned primarily with illuminating the technologically feasible appearing methods for improving the efficiency of the silicon solar cells beyond that at which they had stagnated for a number of years.

The key results of this 1970 analysis included the potential collection efficiency increase from the contemporary level of 72% to about 88% by improving the short-wavelength response of the device through thickness reduction of the diffused region and a modest decrease of the "effective surface recombination velocity" at the front surface of the cell, and additionally through a moderate increase of the diffusion length in the base region, as well as a small reduction in the reflectance of the front surface. A larger efficiency improvement was expected from an increase in the open circuit voltage and the curve factor. Based on applying Shockley's diffusion theory for PN junction characteristics and the Shockley-Read theory of recombination, this improvement was predicted to be achieved primarily by reducing the resistivity of the base region with maintenance of a reasonable minority carrier saturation lifetime at these lower resistivities. The following assumptions had been

made in that analysis, which were characteristic of the understanding of that time: (a) the surface recombination velocity approaches infinity under the ohmic contacts, and is very high and only moderately influenceable on the open front surface; (b) the onset of Auger recombination and of band-gap narrowing at very high impurity levels was not recognized; (c) wide-base diode analysis was applied since it appeared valid on the basis of contemporary diffusion length to or beyond the base width had not been recognized which might have necessitated the application of appropriate correction factors for narrow base widths in these measurements.

The improvements in the collection efficiency predicted by the 1970 ReMPIDS modeling effort, were achieved rather quickly and amazingly close to the predicted value (ref. 6). However, the long wavelength collection improvement and the reflectance reduction were achieved essentially by a clever work-around, namely by texturing the front surface of the solar cell (ref. 7). In addition, considerable efforts have been spent to achieve the predicted voltage and curve factor improvements, but open circuit voltages exceeding approximately 0.62 Volt at 28°C could not be obtained. Consequently, numerous speculations for the potential causes of this apparent "open circuit voltage limitation" were advanced, which gradually narrowed down to the most likely effects of Auger recombination (ref. 8) and bandgap narrowing (ref. 9). (Table I)

In addition to the introduction of the "textured" solar cell surface, an optical internally reflecting back contact has also been introduced in recent years (ref. 10). While the former causes the photons to transit the solar cell bulk material, before absorption, under oblique angles rather than normal, in normally incident light, the latter provides a second chance for absorption, with charge carrier generation, for those photons which would otherwise have been absorbed, without carrier generation, at the back contact surface. Thus, both measures serve to create the effect, for the absorption of photons, of the existence of a thicker wafer than is actually used.

In parallel to these experimental efforts, the understanding of the cell operating mechanisms also advanced further. In 1972, it had already been shown that a drift field in a part of the base region can be used to considerably reduce the influence on the collection efficiency normally exerted by the high surface recombination velocity from the back contact (ref. 11). Simultaneously, it was recognized that with the contemporary tendency to increasing diffusion lengths and decreasing base region thicknesses, the transition to intermediate width and narrow width base regions was occurring. Consequently, the diode saturation current should be expressed as

$$j_o = j_{o,\infty} \cdot (GF)$$

where $j_{o,\infty}$ is the commonly used saturation current for the wide base diode, and (GF) is a dimensionless "geometry factor", which describes the influence of the physical configuration (ref. 12, 11) (Fig. 1). It thus was shown, that the dark diode saturation current in intermediate and narrow base diodes can be considerably larger or smaller than the corresponding saturation current in the wide base diode, depending on the magnitude of the surface recombination velocity (ref. 11). About the same time, interest started to steadily grow in the application of a drift field in a narrow part of the base region near the back contact surface which gradually led to the coining of the name "Back

Surface Field" (BSF) solar cell (ref. 13). A great deal of speculation has developed about the actual influence of such a drift field on the carrier transport in the base region which is still not fully resolved. Also, application of the narrow-base corrections in the measurements of diffusion length in solar cells has started, and amazingly long diffusion lengths were found (ref. 14). But despite the gradually growing acceptance of these new recognitions, they have not been applied to a reevaluation of the limit efficiency of the silicon solar cell.

The current application of the ReMPIDS model thus differs from the last prior one in the following details: (a) the availability of high minority carrier lifetime material, with consequently long diffusion lengths; (b) the applicability of intermediate width or narrow-base diode theory, partially in consequence of point a); (c) the surface recombination velocity has no longer to be reckoned with as a nature-given, essentially unalterable effect since both theoretical and experimental efforts have indicated that the influence of surface recombination velocity can be greatly reduced by applying drift field regions, inversion layers, or wide band-gap windows; (d) thinner base regions can be advantageously used by application of a textured cell front surface and an optical internally reflecting back contact; and (e) the application of very low resistivity material entails the introduction of Auger recombination, bandgap narrowing, and possibly other performance degrading effects.

As an outcome of point (a) above, "realistic material parameters" should now include the use of minority carrier lifetime values as obtained on the best recently available silicon. These values are approximately an order of magnitude higher than those used previously. Also, in consequence of point (c) above, the "idealized device structure" can appropriately include the use of zero surface recombination velocity on both the front and back surfaces of the solar cell.

THE ANALYTICAL MODEL

The analytical model used is a transport equation for minority carriers derived from the Shockley equations (ref. 15) which contain descriptions of the continuity of charge carrier flow, including generation and recombination, for both electrons and holes, and of the electrical current based on diffusion and on drift of charge carriers, again for holes and electrons. The generation term in this transport equation is based on charge carrier pair generation by photon absorption, with a wavelength dependent absorption coefficient according to the specific semiconductor used, and to the operating temperature. The photon incidence is assumed to be uniform over the light-exposed surface of the solar cell. Also, the geometry of the device is taken as plane and parallel to the front surface, and the two dimensions of these planes are assumed to be very large compared to the diffusion length of the minority carriers, so that surface effects at the edges of the device can be neglected. These two assumptions, together with a third one stipulating the uniformity of all relevant material parameters in the planes parallel to the front surface, permit the transport equation be written and solved in one-dimensional form. In addition to this condition of "planar uniformity", the condition of "low level injection" is imposed to obtain independence of the minority carrier lifetime from carrier concentration, and to avoid the requirement for coupled solution with a second

transport equation describing the majority carrier flow. The third key condition imposed is that of maintenance of "space charge neutrality" which eliminates the need for using the Poisson equation as a further coupled differential equation.

With these three conditions, and for the steady state case of interest here, the transport equation becomes an inhomogeneous one-dimensional, linear, second order differential equation, which can be analytically solved for certain cases. Imposing the low level injection condition is instrumental in providing linearity of the differential equation, and maintaining the linearity of the transport equation permits the superposition of the different solutions arising from various forcing functions. Such forcing functions describe, for instance, minority carrier injection across the pn junction due to forward bias, or the generation of minority carriers from photons within a given wavelength band of the spectral distribution of the light source. This latter feature provides the possibility of obtaining separate solutions, and thus individual light generated current contributions, for each individual spectral range, and the superposition of these solutions over the whole spectral distribution of the source, to obtain the total light generated current. Similarly, separate solutions of the transport equation, obtained for the two major regions of the solar cells, can be superimposed both for the light generated current and the diffusion current injected across the PN-junction under forward bias condition. The two major regions of the device are the front region, which is defined as the region between the light exposed front surface of the device and the boundary surface between the depletion region of the PN junction and this layer; and the base region, which is the region between the back surface of the cell and the boundary surface between the depletion region and this base layer. The third major region is the depletion region of the PN junction, which also contributes light generated current. For the idealized device structure, the assumption has been made that recombination does not take place in this depletion region, resulting in 100% collection efficiency for this region.

Through the additional assumption of constancy in the direction of minority carrier mobility and lifetime and, where present, the drift field, throughout a region of the semi-conductor device for which a solution of the differential equation is to be found, the transport equation becomes a differential equation with constant coefficients, for which an analytical solution can be readily found (ref. 16). In most cases where the conditions and assumptions outlined here are not fulfilled, only numerical methods can be applied to the solution of the transport equation or the coupled system of equations. For the idealized device structure treated here, the analytical solution is fully appropriate. However, for most real silicon solar cell structures, and under many of their applications, the analytical method also provides a very good approximation, as long as it is realized that it cannot yield information for certain effects which may be interesting for study.

The general solution of the transport equation is subjected to the appropriate boundary conditions which, in this particular application, include zero surface recombination velocity at both the front and the back surfaces. The PN junction itself is modeled according to Shockley's diffusion theory which means that the injection currents are based exclusively on recombination

within the bulk and at the surfaces of the neutral regions. It has been shown in carefully prepared solar cells that the recombination current from the depletion region can be made negligibly small in the part of the I-V characteristic near the maximum power point, which is the only part of interest for the establishment of the limit conversion efficiency. The diffusion or injection current is determined for both regions according to the impurity concentrations chosen for the individual cell structure. A single-sided injection model is not used. Also, the diffusion currents are obtained for the actual thicknesses of the two regions chosen for the cell structure, so that their determination is not limited by either wide base or narrow base assumptions. Although recombination in the depletion region is neglected, its width is not assumed to be zero, but is calculated from the linear graded junction model. The diffusion currents are then determined for the actual dimensions of the neutral regions.

The computations of the light generated currents have been based on the Airmass 1 sunlight spectrum. Its spectral distribution and irradiance have been derived from the Airmass 0 spectral distribution, with an irradiance of 135.3 mW cm^{-2}, according to the NASA/ASTM Standard (Ref. 17). This derivation has been based on the computation of the atmospheric absorption using the Bouguer relationship (Ref. 18), by assuming an ozone content of 2.5 mm, a precipitable water content of 10 mm, and a dust content of the atmosphere of 300 particles per cubic meter. A total direct Airmass 1 irradiance of 99.3 mW cm^{-2} is thus obtained, and no indirect radiation has been added.

The solutions of the transport equation under the appropriate boundary conditions are available in a computer program which steps, in 50 nm wavelength increments, through the whole Airmass 1 solar spectrum to determine the total light generated current contributions from each of the three regions of the solar cell, as well as the total for the cell. Similarly, applying the corresponding solution of the transport equation without the generation term provides the diffusion current from the front and the base regions for zero bias condition. Having obtained the total light generated current and the diffusion current, the entire current-voltage characteristic for the idealized-structure solar cell is determined. In an iteration procedure, the maximum power point of this current-voltage characteristic is then found, using a series resistance value entered as a parameter into the computation. For the current evaluations of an idealized model, this series resistance is assumed to be zero.

It may be noted that for the values of impurity concentration assumed for the front and the base regions, the condition of low level injection is maintained for the light generated current in any part of the cell up to light intensities which would correspond to moderate optical concentration ratios, i.e. ratios in the 10 to 100 range.

A violation of the low level injection condition can arise, however, from the diffusion current in certain device configurations (Ref. 19). This situation can occur, for instance, in regions adjacent to the depletion region, which are very narrow compared to a diffusion length, and out of which very little minority carrier flow occurs, as would be the case from layers with low surface recombination velocity. Also, large diffusion currents are needed primarily at or near the open circuit condition, at which the diffusion current has to be equal

and opposite to the light generated current. This phenomenon is illustrated in Fig. 2, simplified by considering all light generated current to be originating from the base region, and all diffusion current flowing into the base region. Figure 2 shows that the current equality requires

$$\left.\frac{dn_L}{dx}\right|_{x=x_{j,B}} = -\left.\frac{dn_d}{dx}\right|_{x=x_{j,B}}$$

assuming that both currents are principally based, near the depletion region, on carrier diffusion. The subscripts "L" and "d" indicate minority carriers resulting from light generation and injection across the depletion region, respectively. $x_{j,B}$ denotes the depletion region boundary on the base side. It is thus the minority carrier density gradients, and not the densities themselves, that have to be equal. In fact, the diffusion current equals the total recombination in the base region, postulating negligible minority carrier outflow. But the recombination rate U is proportional to the minority carrier density, in low level condition. Thus, if the minority carrier lifetime (τ_n) is large, a high minority carrier density is needed to achieve a given recombination rate. This is commonly expressed in the "charge control model"

$$q\int_{x_{j,B}}^{x_{B,1}} U\,dx = \frac{q}{\tau_n}\int_{x_{j,B}}^{x_{B,1}} (n_d - n_o)\,dx = \frac{Q_n}{\tau_n}$$

where τ_n is kept constant in accordance with the low level condition. Q_n is the total charge stored in the base region by minority carriers n_d injected across the depletion region, n_o being the equilibrium minority carrier concentration. Thus n_d can be much larger than n_L, and can begin to violate the "low level" condition, or even approach the "high level" condition, long before n_L leaves the low level situation.

Here, however, only the determination of the limit efficiency is of concern, which entails a performance evaluation at or near the maximum power point. At this point, the needed diffusion current density is approximately an order of magnitude smaller than that for the open circuit condition. Thus, the low level injection condition in this part of the I-V characteristic is still maintained in nearly all practical cases of concern here.

THE "REALISTIC MATERIAL PARAMETERS"

The evaluation of the limit solar cell performance has been performed for a

range of resistivities in the base and front regions of the cell, respectively. In most cases, the front region resistivity has been made at least one order of magnitude lower than the resistivity of the base region. However, to avoid complications encountered through the onset of bandgap narrowing, through a severe influence of Auger recombination, or other possible very low resistivity effects, the highest impurity concentration used in these calculations has been 2×10^{18} cm^{-3}.

The key material parameters needed for the calculations are the minority carrier mobility and the minority carrier lifetime. For the minority carrier mobility, relatively recent experimental data have been used (Ref. 20). For the minority carrier lifetime, a set of values at three different resistivities, was chosen which is representative of experimental values repeatedly found in the best available silicon of the respective resistivities. (See the 3 points shown in Fig. 3) These minority carrier lifetimes are therefore thought to be fully within the capability of today's silicon material technology and should, once appropriate attention is paid to this aspect, be produceable in quantity at acceptable prices for solar cell manufacture. These lifetime values are applicable in both n-type and p-type material. Lifetime values at resistivities other than the three given points were obtained by interpolation and extrapolation using Shockley-Read recombination theory and Auger recombination. (Ref. 21) (Fig. 3) The data of Fischer and Pschunder (Ref. 8) show the availability of 1 ms lifetimes already at a 1 Ω resistivity, and indicate a very high saturation lifetime based on a small concentration of deep levels, so that no influence of doping concentration occurs, outside of Auger recombination.

THE IDEALIZED SOLAR CELL STRUCTURE

As was outlined in the section on the "analytical model", the basic solar cell structure is assumed to be plane parallel, and extending, in the lateral dimensions, far in comparison to the minority carrier diffusion length. The basic cell structure is assumed to consist of three regions: the front region, the transition region, and the base region, arranged in this order counting from the front surface of the cell. As was mentioned, the width of the transition region is computed using the linear graded junction model. While recombination in this region is assumed to be zero, the collection efficiency of this region is assumed to be 100%. The front and the base regions of the cell have been assumed to have constant material parameters throughout, and to be free of any electrostatic field.

As an extrapolation from current technology capabilities, the surface recombination velocities at the front and the back surfaces of the cell have been assumed to be zero. This assumption can be interpreted in a different way: There could be an idealized layer, in front of the front region, of such properties that it transmits 100% of the incoming photons into the solar cell, but transforms the electronic properties of the open surface so that, at the interface of this additional front layer with the active front layer of the cell, a boundary exists into which no minority carrier current flows. Simultaneously, the interface and the layer itself shall have no resistance to majority carrier current flow. Such a layer might be a "window layer" of a wide band gap ma-

terial, similar to the usage in the $Ga_xAl_{1-x}As$/GaAs solar cells, or a layer incorporating a "high low junction", or an inversion layer. A similar idealized layer could be assumed to be interspersed between the real back surface of the cell and the base region. This layer would have the same electronic properties as the "idealized window layer", but it needs not to be transparent to photons. This layer would, however, have to effect a suitable transformation from the electronic properties of an ohmic contact which normally has a much higher surface recombination velocity than an open surface should have, and which generally covers the entire back surface of the cell.

Two additional features have been incorporated into the solar cell structure. The first is the assumption of a textured front surface, which causes the photons to penetrate under oblique angles into the solar cell structure. This effect is modeled in an idealized manner by assuming all photons to move inside the solar cell at the same penetration angle, which could be visualized as the average of all actual penetration angles. This average angle has been chosen here as 45° from the normal to the solar cell planes, a value which should be close to that resulting, in normal incidence, from the surface structure usually obtained in the common texture etching processes. (Ref. 7)

The second feature is the existence of an optically reflecting surface at the rear of the base region. The existence of this surface feature permits photons which penetrate all the way through the front, depletion, and base regions of the cell, to be reflected forward and have a second chance for absorption and charge carrier generation. For the idealized cell structure, a reflectance of 1.0 has been assumed for the back surface. Together with the textured front surface, the reflecting back surface permits the construction of a thinner solar cell with the same absorption characteristic and a possibly even higher collection efficiency as would otherwise be obtained in a thicker cell structure.

For a sensitivity analysis, the cell configuration which appeared readily practically realizable and gave one of the highest efficiencies, was recomputed with two different values of surface recombination velocity: 10 cm s^{-1} and 100 cm s^{-1}.

RESULTS OF THE COMPUTATIONS

Around a hundred computations were made with different material parameters and device structures to obtain: a) the absolute maximum, or limit efficiency; b) the optimum efficiency obtainable with certain material combinations; and c) the sensitivity to changes in various structure parameters. Only the key results are summarized in Table II and in Figures 4 to 8. These results lead to the following observations:

1. The idealized limit efficiency is still about 25%, the highest value found was 25.13%.

2. There is still a tendency towards higher efficiency at the lower resistivities. (Fig. 4)

3. Very low resistivities, involving impurity concentrations above 10^{18} cm^{-3}, are not needed for achieving the limit efficiency.

4. In consequence of point 3, high doping effects, including degeneracy, serious influence of Auger recombination, band-gap narrowing, etc., can be avoided.

5. The limit efficiency value obtained is, however, determined by the onset of Auger recombination which depresses this efficiency slightly.

6. There is a very wide range of impurity concentrations at which idealized efficiencies above 23.5% are obtainable.

7. Idealized efficiencies above 23.5% are obtained at total wafer thicknesses of 25 to 200 μm, and at junction depths of 2 to 10 μm. This means rather thin cells and large junction depths, in contrast to earlier thinking.

8. The higher the impurity concentration chosen, the smaller the junction depth and the total cell thickness have to be. The limit efficiency has been obtained at a total cell thickness of only 50 μm, with junction depths of 2 to 6 μm.

9. In all cases of high efficiency, the region thickness is small compared to the diffusion length within it. The limit efficiency, however, has been obtained in a case where this statement is only marginally valid.

10. The peak efficiency values are obtained in a design trade-off between collection efficiency and voltage (Fig. 5 to 6). As the cell thickness is decreased, the collection efficiency decreases due to reduced photon absorption, while the voltage increases, based on the reduction of the diode saturation current resulting from the decrease of the form factor with decreasing thickness at low surface recombination velocity.

11. The best efficiencies are obtained with equal impurity concentrations in the front and base regions of the cell. Thus, there is principally no need for an "emitter" in the front region, except that higher doping can help to reduce series resistance.

12. Both the textured surface and the optical internally reflecting back surface are important for obtaining high efficiencies in thin cells, and small cell thickness, in turn, is needed to approach the high conversion efficiency values shown here.

13. The optimum efficiencies are obtained over a rather broad range of material and structure parameters, and the sensitivities to the variation of these parameters are generally small (Fig. 7 to 8).

14. Since greater cell thicknesses and wider ranges of junction depth are available at lower impurity concentrations, these cells will probably find preference for practical reasons (Fig. 4).

15. The sensitivity of the efficiency to low values of surface recombination velocity is also not great (Table II, lines 14 to 15, compared to line 4).

DISCUSSION OF RESULTS

The assumption of low or zero surface recombination velocity at the surfaces, combined with oblique penetration of the photons into the solar cell as results from surface texturing, and with optical internal reflection at the back surface leads to a new approach to solar cell design and optimization. While the earlier thinking was based on obtaining high voltages, and consequently high conversion efficiency, by application of very high impurity concentrations to yield a low diode saturation current, the new approach pursues the same goal of low saturation current by using front and back regions of the solar cell which both are narrow compared to the respective diffusion lengths. Thus, the severe limitations imposed by heavy doping effects are avoided, and high efficiencies still are obtainable. However, this cell design involves a trade-off between the collection efficiency and the cell voltages. This trade-off can not be optimized without the oblique penetration of the photons and the internal optical reflection. In fact, in the highest efficiency case found, in which the base region thickness happens to approach the diffusion length (Table II, Line 11), Fig. 4 shows clearly that a further increase of the base region thickness results in reduced light generated current, as fewer of the minority carriers are collected which were generated from photons which had been internally reflected at the back surface. This case clearly illuminates the importance of the optical internal reflection at the back surface in very thin cells.

Table I repeats a set of numbers which were derived in 1970 as design "goals" for the key performance parameters of silicon solar cells in Airmass 0 sunlight, together with the actual data of contemporary cells and improved cells developed since then. The insights gained with the analysis of a new limit efficiency, described here, indicates that a preliminary reevaluation of the design goals would also be appropriate. The results of such a reevaluation are summarized in Table III, using the data on the idealized, 100 μm thick cell with 4 μm thick front layer of 5.10^{17} cm^{-3} n-type impurity concentration, while the p-type base region contains 5.10^{16} cm^{-3} impurities. These data determine the collection efficiency, the open circuit voltage, and the curve factor. The other parameters correspond essentially to current experience factors on the better cells. The preliminary goal thus found for silicon solar cells is 22% conversion efficiency in Airmass 1, unconcentrated sunlight at 28°C. This goal needs refinement through further investigations to determine to what degree the idealized cell structure and its performance can be approached in real solar cells.

CONCLUSIONS

The new computations on idealized solar cell structures have shown that there is a second "theoretical approach" to obtaining high open circuit and maximum power point voltages, after the first one, relying on high impurity concentrations in the base and front regions of the cell, has been found in-

feasible. This second approach involves the "narrow region" design for both the front and back regions of the solar cell, and relies heavily on low effective surface recombination velocities front and back, as well as a textured front surface and an optical internally reflecting back surface. In fact, using this design, the undesirable effects of high doping can be completely avoided. The idealized limit efficiency of the solar cell, the validity of which had become doubtful as a result of the recent realization of the impacts of high doping effects, is thus reestablished at its earlier value near 25%. The new cell design requires a rather thin cell, in the 50 to 150 μm range, with a thick front region in comparison to contemporary designs. Of paramount importance, however, is obtaining low effective surface recombination velocities both at the front and back surfaces of the cell. These may be approached by the use of drift field, inversion, or window layers. Further investigations in progress are aimed at exploring the degree to which the assumptions made, particularly that of extremely low surface recombination velocity, can be expected to be approached in real solar cell structures. Early results from these investigations indicate, that an amazingly close approach to the performance of the idealized solar cell structure may be possible in real solar cells.

REFERENCES

1. Wolf, M., "A New Look at Silicon Solar Cell Performance", Rec. 8th IEEE Photovoltaic Spec. Conf., IEEE Cat. #70C32ED, pp. 360-371, Aug. 1970; also in: "Solar Cells, Outlook for Improved Efficiency", Nat'l Acad. Sciences, 1972.

2. Wolf, M., "Limitations and Possibilities for the Improvement of Photovoltaic Solar Energy Converters", Proc. IRE 48, pp. 1246-1263, (1960).

   Wolf, M., "The Solar Cell Design Handbook", Rec. 9th IEEE Photovoltaic Spec. Conf., pp. 53-60, IEEE Cat. No. 72 CHO 613-0-ED, (1972).

3. Muser, H.A., Z. Phys. 148, 380 (1957).

   Rose, A., "Photovoltaic Effect Derived from the Carnot Cycle," J. Appl. Phys. 31, 1640 (1960).

   Shockley, W., and Queisser, H.J., "Detailed Balance Limit of Efficiency of pn Junction Solar Cells", J. Appl. Phys. 32, 510-519 (1961).

4. Prince, M.B., "Silicon Solar Energy Converters", J. Appl. Phys. 26, 534-540 (1956).

   Loferski, J.J., "Theoretical Considerations Governing the Choice of Optimum Semiconductor...". J. Appl. Phys. 27, 777-784 (1956).

5. Wolf, M., see ref. 2, item 1.

   Kleinman, D.A., "Considerations on the Solar Cell", Bell. Syst. Tech. J. 40, pp. 85-115, (January 1961).

Wysocki, J.J., and Rappaport, P., "Effect of Temperature on Photovoltaic Solar Energy Converters", J. Appl. Phys. 31, 571-578 (1960).

6. Wolf, M., "Outlook for Si Photovoltaic Devices for Terrestrial Solar-Energy Utilization", J. Vac. Sci. Technol. 12, pp. 984-999, (1975).

7. Haynos, J., et. a., "The COMSAT Non-Reflective Silicon Solar Cell: A Second Generation Improved Cell," Photovoltaic Power Generation, pp. 487-500, Proc. Int'l Conf. Photovoltaic Power Conversion, (DGLR), Kiln (1974).

8. Fischer, H., and Pschunder, W., "Impact of Material and Junction Properties on Silicon Solar Cell Efficiencies", Record 11th IEEE Photovoltaic Spec. Conf., IEEE Cat. No. 75 CHO 948-OED, pp. 25-31 (1975).

9. Godlewski, M.P., et. al., "Effects on High Doping Levels on Silicon Solar Cell Performance", ibid., 32-35 (1975).

Lindholm, F.A., et. al., "Fundamental Limitations Imposed by High Doping on the Performance of PN Junction Silicon Solar Cells", ibid., pp. 3-12.

10. Ralph, E.L., private communications.

11. Wolf, M., see ref. 2, item 2.

12. McKelvey, J.P., "Solid State and Semiconductor Physics", pp. 420-423, Harper and Row, N.Y. (1966).

13. Mandelkorn, J., and Lamneck, H. Jr., "Simplified Fabrication of Back Surface Electric Field Silicon Cells", Rec. 9th IEEE Photovoltaic Spec. Conf., IEEE Cat. No. 72 CHO 613-O-ED, (1972).

14. Fossum, J.G., and Burgess, E.L., "High Efficiency p^+-n-n^+ Back-Surface-Field Silicon Solar Cells", Appl. Phys. Lett. 33(3), pp. 238-240 (1978).

15. Shockley, W., Bell Syst. Tech. J., 28, pp. 435- (1949).

Shockley, W., "Electrons and Holes in Semiconductors", Van Nostrand, Princeton, N.J. (1950).

16. Wolf, M., "Drift Fields in Photovoltaic Solar Energy Converter Cells", Proc. IRE 51, pp. 674-693, (1963).

17. Thekaekara, M.P., Solar Energy 14, pp. 109-127 (1973). Anon, 1974 Annual Book of ASTM Standards, Part 41, E490-73a, pp. 609-615, ASTM, Philadelphia, PA. (1974).

18. Moon, P., J. Franklin Inst. 230, pp. 583-617 (1940).

19. Fossum, J.G., et. al., "Development of High-Efficiency P^+NN^+ Back-Surface-Field Silicon Solar Cells", Rec. 13th IEEE Photovoltaic Spec. Conf., IEEE Cat. No. 78CH1319-3 pp. 1294-1299, (1978).

20. Wolf, H.F., "Semiconductors", p. 276, Wiley-Interscience, NY, 1971.

21. Shockley, W., and Read, W.T., Phys. Rev. 87, pp. 835 (1952).

TABLE I. - PERFORMANCE STATUS OF CURRENT SILICON SOLAR CELLS AND IMPROVEMENT GOALS

Attribute	Goal	Efficiency contribution (1-Loss)			Output values			
		1970 Comm'l. Cell	"Violet" Cell	"Black" Cell		Goal	Black Cell	
Basic Losses	0.45	0.45	0.45	0.45		63.0	63.0	mW cm^{-2}
Collect. Eff'y	0.88	0.71	0.79	0.88	Light generated current	49.0	49.0	mA cm^{-2}
Reflection	0.97	0.905	0.951	0.97		47.5	47.7	mA cm^{-2}
Grid Line Cover	0.96	0.96	0.95	0.95		45.5	45.4	mA cm^{-2}
Voltage Factor	0.61(?)	0.522	0.535	0.531		0.675	0.591	V
Curve Factor	0.86	0.82	0.825	0.822		26.3	22.1	mW cm^{-2}
Add'l Curve Fact.	1.0	0.91	1.0	0.99	Power	26.3	21.8	mW cm^{-2}
Series Resistance	0.97	0.96	0.985	0.984		25.6	21.4	mW cm^{-2}
Efficiency (AMO)	0.19	0.104	0.14	0.153				

TABLE II. - SUMMARY OF RESULTS OF COMPUTATIONS

Line	Wafer Thickness	Region 1 (Base), p-type					Region 2 (Front), n-type						Region 3 (Transition)		Total Cell			
		Impurity Conc.	Diffusion Length	Surf. Recomb Veloc.	Light Gen'd. Curr't	Saturation Curr't	Impurity Conc.	Nom'l Thickness	Diffusion Length	Surf. Recomb Veloc.	Light Gen'd Curr't	Saturation Curr't	Nom'l Thickness	Light Gen'd Curr't	Light Gen'd Curr't	Open Circ't Volt.	Curve Factor (CF)	Conv. Effic'y.
	d	N_A	L_n	S_1	$j_L(1)$	$j_o(1)$	N_D	x_j	L_p	s_2	$j_L(2)$	$j_o(2)$	Δx_j	$j_L(3)$	j_L	V_{oc}		
	μm	cm^{-3}	μm	cm s^{-1}	mAcm^{-2}	A cm^{-2}	cm^{-3}	μm	μm	cms^{-1}	mAcm^{-2}	Acm^{-2}	μm	mAcm^{-2}	mAcm^{-2}	V	--	%
1	150	7.10^{14}	1670	0	14.1	3E-13	5.10^{17}	4	60.3	0	26.0	1E-15	1.18	1.8	41.9	0.665	0.84	23.6
2	100	5.10^{15}	604		9.1	1E-13	5.10^{16}	10	135		31.8	7E-15	0.24	0.08	41.1	0.681		
3		5.10^{16}	226		10.2	7E-14		8	135		30.5	6E-15	0.20	0.15	40.8	0.700	0.85	24.3
4					14.5		5.10^{17}	4	60.3		26.0	1E-15	0.15	0.27		0.701		
5	200				14.9	1E-13									41.1	0.687	0.84	24.0
6	50				13.2	4E-14									39.5	0.717	0.85	24.2
7					8.8	3E-14		8			30.5	2E-15		0.11	39.4	0.719		
8					23.0	4E-14		1			15.5	3E-16		1.0	39.5	0.716		
9	150				24.5	1E-13					15.4				41.0	0.692	0.84	24.1
10					10.6			8			30.3	2E-15						
11	50	5.10^{17}	97.6		13.0	1E-14		4			26.0	1E-15	0.06	0.11	39.1	0.748	0.85	25.12
12					18.0		2.10^{18}	2	21.8		20.7	9E-16	0.05	0.19	38.9	0.747		25.0
13	25	2.10^{18}	34.5		12.7	6E-15		3			23.8	1E-15	0.04	0.10	36.6	0.756		23.8
14	100	5.10^{16}	226	10	14.5	7E-14	5.10^{17}	4	60.3	10	26.0	1E-15	0.15	0.27	40.7	0.700		24.3
15				100	14.3	9E-14				100	25.8	4E-15			40.4	0.69	0.84	23.8

TABLE III. - PRELIMINARY 1979 SILICON SOLAR CELL DESIGN GOALS

Attribute	Performance Factors			Output Values			
	Airmass 0		Airmass 1,	Airmass 0		Airmass 1	
	1970*	1979 Prelim.	1979 Prelim.	1970*	1979 Prelim.	1979 Prelim.	
				59.5	59.5	49.6	mW cm^{-2}
Basic Losses	0.44	0.44	0.50	53.3	53.3	44.3	mA cm^{-2}
Collection Efficiency	0.88	0.93	0.93	46.9	49.4	41.0	mA cm^{-2}
Reflection	0.97	0.97	0.97	45.4	47.9	39.8	mA cm^{-2}
Grid Line Coverage	0.96	0.95	0.95	43.5	45.5	37.8	mA cm^{-2}
Voltage Factor	0.61	0.63	0.63	0.675	0.706	0.701	V
Curve Factor	0.86	0.85	0.85	25.2	27.3	22.4	mW cm^{-2}
Add'l Curve Factor	1.00	1.00	1.00	25.2	27.3	22.4	mW cm^{-2}
Series Resistance	0.97	0.985	0.985	24.5	26.8	22.1	mW cm^{-2}
Efficiency	0.182	0.198	0.221				

*Corrected from previously used Johnson spectrum to the current NASA/ASTM Airmass 0 absolute spectral distribution

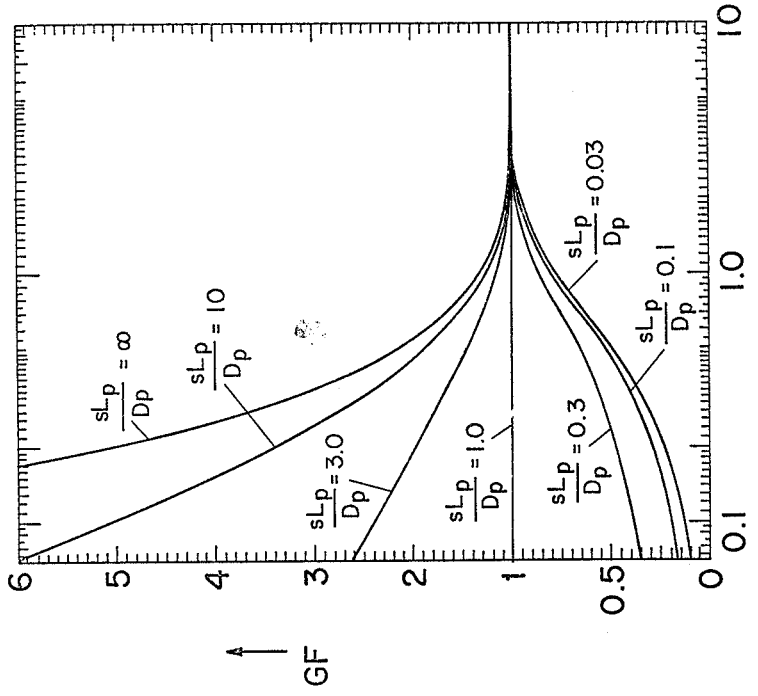

Figure 1

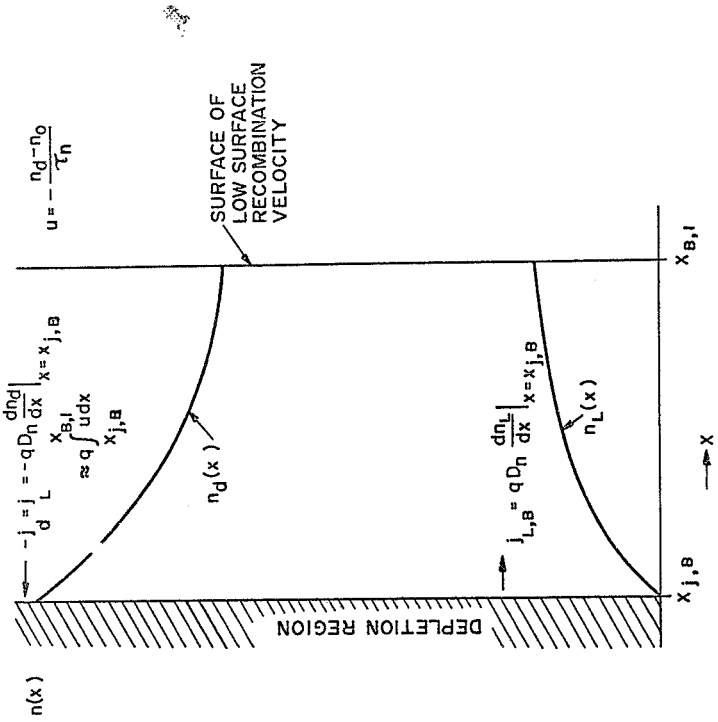

Figure 2

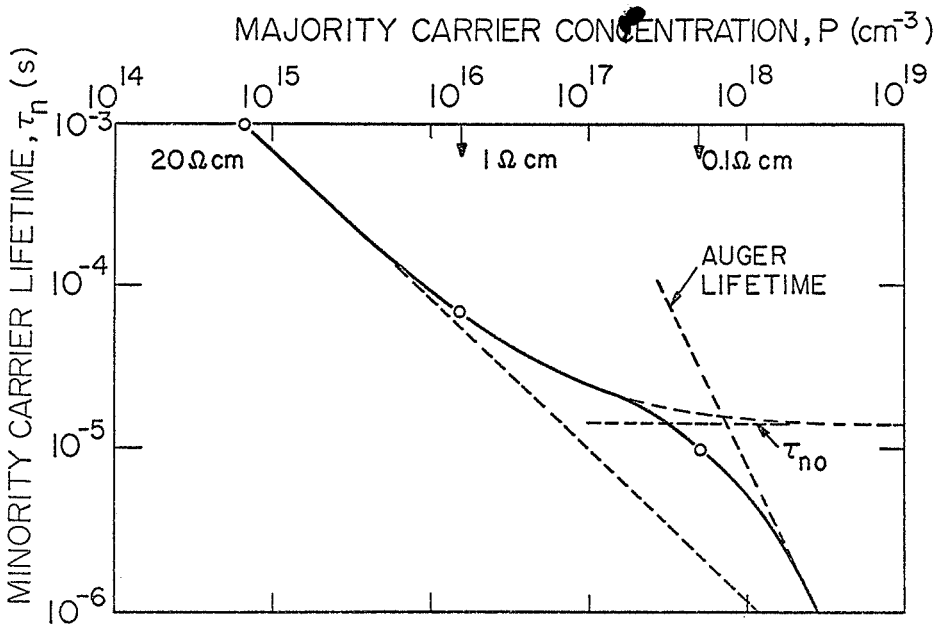

Figure 3

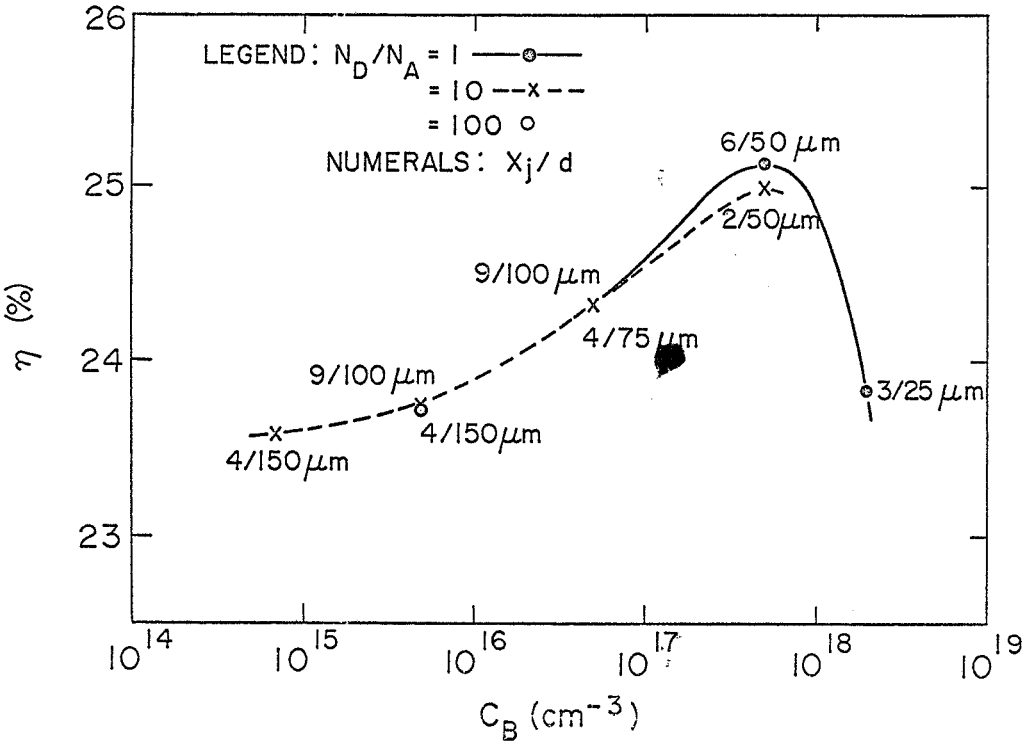

Figure 4

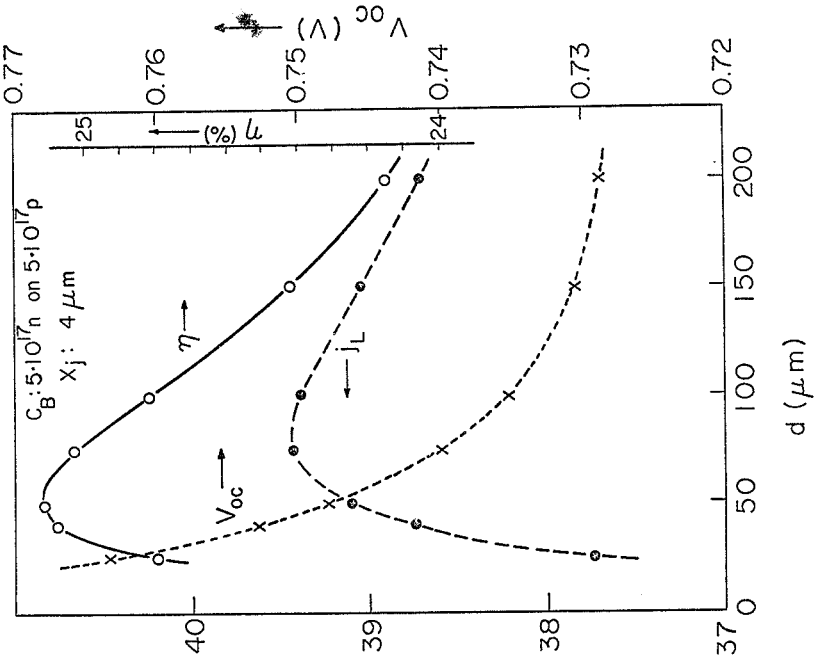

Figure 6

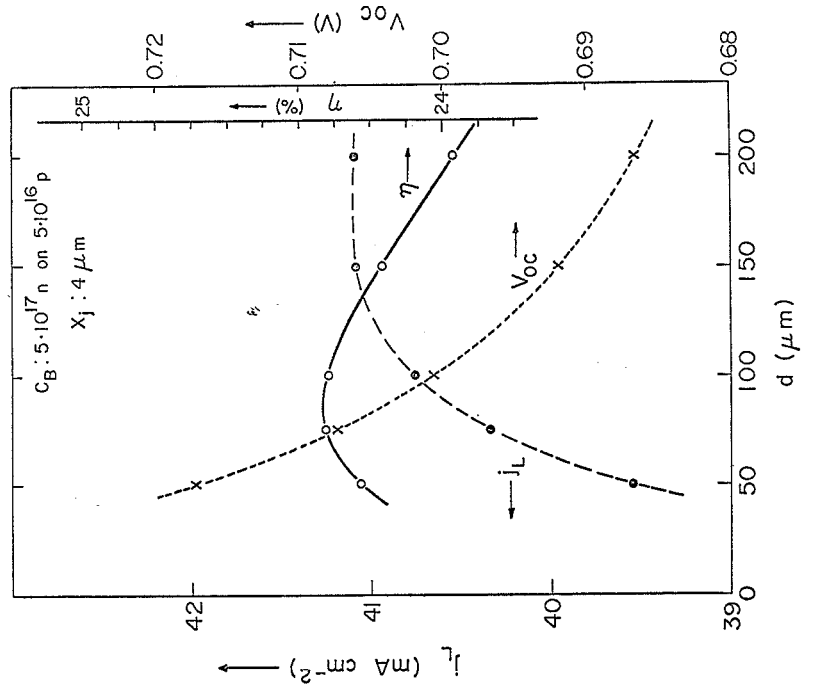

Figure 5

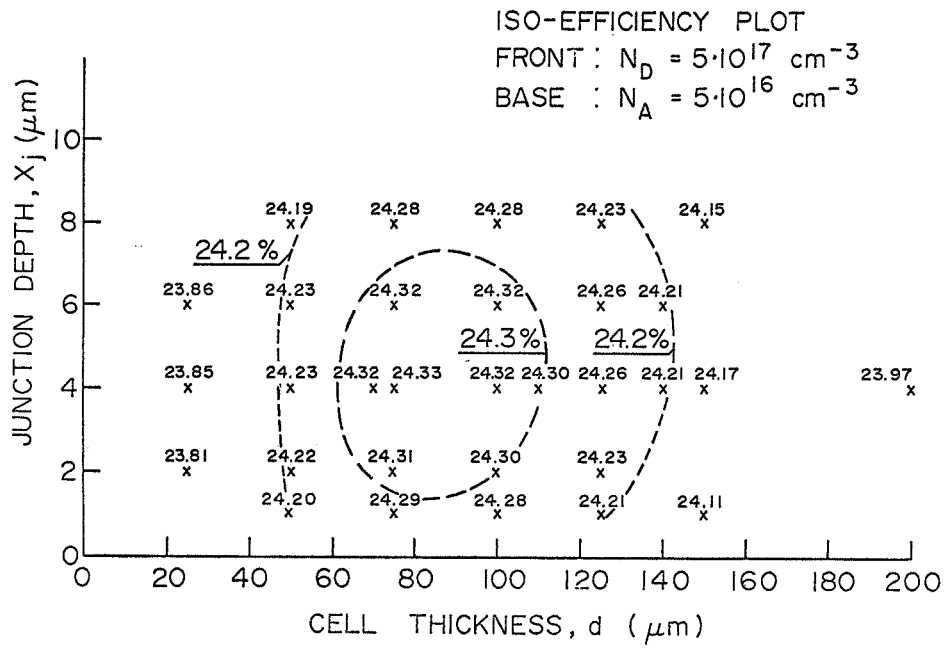

Figure 7

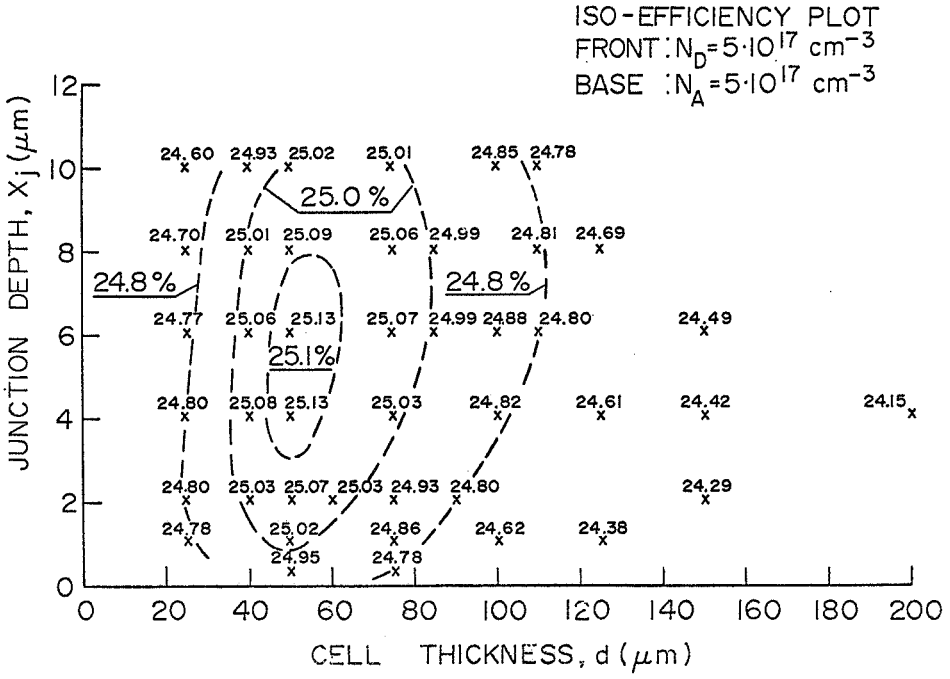

Figure 8

LIMITING PROCESS IN SHALLOW JUNCTION SOLAR CELLS*

A. Meulenberg and E. Rittner
COMSAT Laboratories

In extending the COMSAT violet and non-reflective cell technology to lower resistivities, several processes limiting output power were encountered. The most important was the dark diffusion current due to recombination at the front grid contacts. After removal of this problem by reduction of the silicon-metal contact area (to 0.14 percent of the total area), the electric field enhanced junction recombination current J_r was the main limitation (Figure 1). Alteration of the diffusion profile to reduce the junction field is shown to be an effective means of influencing J_r. The remaining problems are the bulk recombination in the n+ layer and the surface recombination at the oxide-silicon interface; both of these problems are aggravated by band-narrowing resulting from heavy doping in the diffused layer. Experimental evidence for the main limitations is shown in Table 1, where increased diffusion temperature is seen to reduce both the influence of the front grid contacts and the junction electric field by increasing the junction depth. The potential for further significant improvement in efficiency appears to be high.

TABLE 1. 1.2Ω-cm (5-PERCENT CONTACT AREA) CNR CELLS DIFFUSED AT DIFFERENT TEMPERATURES

Temperature	J_{do} (pA/cm^2)	J_r (at P_{max}) (mA/cm^2)	J_{SC} (mA/cm^2)	V_{OC} (mV)
760°C	12 ± 1	27 ± 1	42.5	558
790°C	4.7 ± .15	10 ± 1	42.5	583
820°C	4.5 ± .6	7 ± 3	42.5	588
850°C	3.8 ± .2	4 ± 2	41.8	595

*This extended abstract is based upon work performed at COMSAT Laboratories under the sponsorship of the Communications Satellite Corporation. It is an extension of a more fundamental paper to be published in the Journal of Energy.

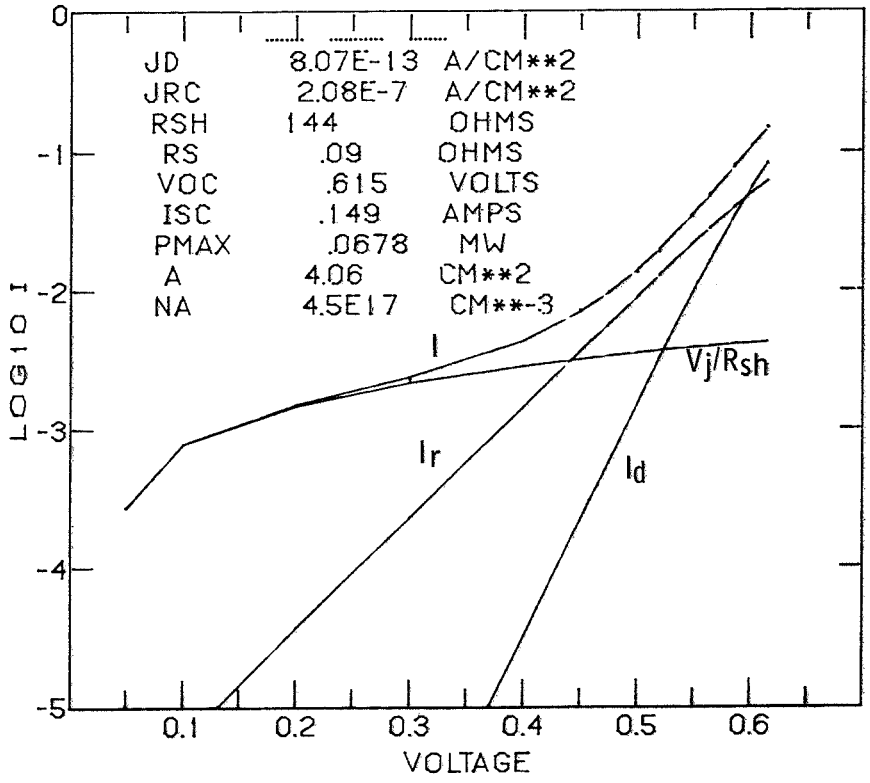

Figure 1. IV Analysis of a Shallow (0.1-μm) Junction 0.1-Ω-cm Solar Cell with Low Contact Area (0.14%)

DESIGN OF HIGH EFFICIENCY HLE SOLAR CELLS FOR SPACE AND TERRESTRIAL APPLICATIONS*

A. Neugroschel and F. A. Lindholm
Department of Electrical Engineering
University of Florida

SUMMARY

A first-order analysis of HLE cells is presented for both beginning-of-life (BOL) and end-of-life (EOL) conditions. Based on this analysis and on experimentally observed values for material parameters, we present design approaches for both space and terrestrial cells. The approaches result in specification of doping levels, junction depths and surface conditions. The proposed structures are projected to have both high V_{OC} and high J_{SC}, and consequently high η.

1. INTRODUCTION

The purpose of this paper is to discuss design approaches for silicon HLE solar cells. Design of cells for radiation and terrestrial environments are considered. Two main types of HLE cells receive attention: (a) the oxide-charge-induced (OCI) HLE cell, and (b) a new HLE cell having a wide p-epitaxial emitter for which the appropriate choices of emitter width and doping levels in the emitter and base are made to yield both high V_{OC} and high J_{SC}.

SYMBOLS

D_a	ambipolar diffusivity (cm^2/sec)
D_n, D_p	electron and hole diffusivities (cm^2/sec)
Q_0	oxide charge density (C/cm^2)
J_{SC}	short circuit current density (A/cm^2)
J_{n0}, J_{p0}	dark electron and hole saturation current density (A/cm^2)
L_n, L_p	electron and hole diffusion length (cm)
Δn,Δp	excess electron and hole concentration (cm^{-3})

*This work was supported by NASA Grant NSG-3018.

n_i	intrinsic carrier concentration (cm^{-3})
n_s, P_s	electron and hole surface concentration (cm^{-3})
$n_s(Q_0)$	oxide charge dependent electron surface concentration (cm^{-3})
N_{DD}, N^+_{DD}	donor concentration in n and n^+ material (cm^{-3})
N_{AA}, N^+_{AA}	acceptor concentration in p and p^+ material (cm^{-3})
q	electronic charge (Coulombs)
S_p	hole surface recombination velocity (cm/sec)
S_{eff}	effective surface recombination velocity (cm/sec)
T	temperature (^oC, ^oK)
V_A	applied voltage (Volts)
V_{OC}	open circuit voltage (Volts)
$(V_{OC})_B$, $(V_{OC})_E$	open circuit voltage established by base and emitter (Volts)
W_E	emitter thickness (cm)
X_j	junction depth (cm)
ρ	resistivity (Ω cm)
τ_n, τ_p	lifetime of minority electrons and holes (sec)
p, p^+	associated with p and p^+ region
n, n^+	associated with n and n^+ region
BOL	beginning-of-life
EOL	end-of-life
E, B	associated with emitter and base

II. OCI-HLE CELL

Fig. 1(a) shows the cross-section of an OCI silicon HLE solar cell. The principles of operation of this cell, which have previously been discussed [1] are illustrated in Figs. 1(a) and 1(b). A positive charge Q_0, achieved by suitable heat treatment [2,3], induces an electron accumulation and an electric field near the silicon surface which reduces the effective surface recombination velocity for holes S_{eff} to [4]

$$S_{eff} \simeq \frac{N_{DD}}{n_s} S_p \qquad (1)$$

By solving the hole continuity equation for the desired case, $W_E < L_p$, and low injection, one determines the hole saturation current J_{PO} to be [4]

$$J_{PO} \simeq \frac{qn_i^2}{N_{DD}} \left[\frac{S_{eff} + \frac{W_E}{\tau_p}}{1 + \frac{S_{eff}}{D_p/W_E}} \right] \tag{2}$$

in which the first term in the numerator accounts for hole recombination at the surface and the second term accounts for hole recombination in the bulk. The current J_{PO} must be small if high V_{OC} is to result.

2.1 Beginning of life - (BOL) Design

For BOL, our experiments [1] show that $S_p < 10^4$ cm/sec can result from the presence of the SiO_2 layer on the illuminated surface. For a wide range of doping levels N_{DD}, the term W_E/τ_p in (2) can be made negligible, and the diffusion velocity D_p/W_E will typically be of the order of 10^4 cm/sec. Thus, if S_{eff} can be made much less than 10^4 cm/sec, then (2) reduces to

$$J_{PO} \simeq \frac{qn_i^2}{N_{DD}} \; S_{eff} \simeq qn_i^2 \; \frac{S_p}{n_s} \tag{3}$$

which also holds for high injection provided D_a/W_E and $W_E/(\tau_n+\tau_p)$ are both small compared with $(S_{eff})_{\text{high injection}} = (n_i/n_s) \exp qV_A/2kT$, as can be shown by solving the ambipolar transport equation for high injection [5]. To show that $S_{eff} < 10^4$ cm/sec is possible, we indicate in Fig. 2, for different values of N_{DD} and Q_0, the resulting values of n_s and S_{eff}. The functional dependence $n_s(Q_0)$ is found from standard MOS theory [6].

Because S_{eff} can be small, we consider now the value of J_{PO} for the limiting case $S_{eff} = 0$. Fig. 1(b) shows the minority hole density in the dark cell, resulting from an applied voltage, for the desired condition, $L_p > W_E$:

$$J_{PO} \simeq qn_i^2 \; W_E(N_{DD}\tau_p)^{-1} \tag{4}$$

To estimate J_{PO}, we use the empirical data of Kendall [7], which gives, for $N_{DD} \geqq 5 \times 10^{16} cm^{-3}$,

$$\tau_p N_{DD} \simeq 3 \times 10^{12} \text{ sec cm}^{-3} \tag{5}$$

Thus, at T = 25°C,

$$J_{p0} \simeq 7 \times 10^{-12} W_E \qquad (6)$$

Thus, if $J_{SC} \simeq 35$ mA/cm^2(AMO), which was seen in OCI-HLE cells, the open-circuit voltage limit, $(V_{OC})_E = kT/q \, \ell n(J_{SC}/J_{p0})$, established by the emitter current J_{p0} is, for example, 800 mV, 780 mV, and 718 mV for W_E = 2 μm, 5 μm, and 50 μm, respectively, independent of N_{DD} (provided low-injection levels are maintained). From a design viewpoint, this demonstrates that $(V_{OC})_E > 700$ mV can be achieved for a wide variety of choices of N_{DD} and W_E provided only that $L_p > W_E$.

2.2 End-of-Life (EOL) Design

Radiation damage increase S_p and Q_0[8]; it will also reduce τ_p[9,10]. As a design approach, we choose W_E small compared with anticipated degraded diffusion length to minimize bulk recombination; that is, we require $W_E < L_p$ (after irradiation). Then (2) still applies, and J_{p0} is determined by the velocities S_{eff}, W_E/τ_p, and D_p/W_E. As a worst-case limit, we consider the case $S_{eff} = \infty$. Then the transit time t_t for holes to cross the emitter is

$$t_t = W_E^2/2D_p \qquad (7)$$

which, for example, is of the order of 10^{-9} sec for $W_E \simeq 2$ μm. Thus, if τ_p after irradiation is larger than 10^{-9} sec, the emitter will be transparent to holes and (2) reduces to

$$J_{p0} = \frac{qn_i^2}{N_{DD}} \frac{D_p}{W_E} \qquad (8)$$

This worst-case dependence suggests that N_{DD} should be large enough, both to assure small lateral series resistance and to decrease J_{p0}, but small enough to avoid heavy-doping degradation. For example, consider a design with W_E = 2 μm, and $N_{DD} = 10^{18}$ cm^{-3}. For T = 25°C and $J_{SC} \simeq 25$ mA/cm^2, $(V_{OC})_E > 640$ mV. For electron fluences up to 10^{15} cm^{-2}, $J_{SC} \simeq 25$ mA/cm^2 is expected if prior to radiation $J_{SC} \simeq 35$ mA/cm^2[10].

2.3 Examples of V_{OC} established by the emitter for BOL and EOL

We have previously discussed $(V_{OC})_E$ for two limiting cases: $S_{eff} = 0$,

which corresponds to the BOL condition, and $S_{eff} = \infty$, which corresponds to the EOL condition. We now remove these limiting-case assumptions by considering intermediate values of S_{eff}, as determined by (1) and the condition that 10^3 cm/sec $< S_p < 10^7$ cm/sec. The lower bound on S_p is easily achieved, as is indicated by our experiments for a surface passivated by SiO_2 [1]. The upper bound is a theoretical limit for a silicon surface [11].

In Fig. 3 we plot $(V_{OC})_E$ as a function of S_p for two values of emitter widths W_E = 2.5 μm and 15 μm and for emitter doping densities of $N_{DD} = 10^{17}$ cm^{-3} and 10^{18} cm^{-3}. Three values of oxide charge densities are considered: (a) $Q_0/q = 4 \times 10^{11}$ cm^{-2}, which is the order of magnitude obtained in thermally grown dry oxides followed by oxygen heat treatment at about 700 C [2,3] before the irradiation; and $Q_0/q = 1 \times 10^{12}$ cm^{-2} and 5×10^{-12} cm^{-3}, which is the range of values expected after irradiation [8]. As shown in Fig. 3 for BOL with $S_p \simeq 10^3$ cm/sec, the emitter recombination is no barrier for achieving $(V_{OC})_E \geqq 700$ mV for variety of emitter doping levels and thicknesses. After irradiation, for EOL, S_p is expected to increase significantly [8], but will not be larger than the order of 10^6 cm/sec [11]. But Q_0/q will also increase, as mentioned above, which will increase n_s [6], and $S_{eff} \simeq N_{DD}\, S_p/n_s\,(Q_0)$ will depend on the ratio $S_p/n_s\,(Q_0)$ after the irradiation. It follows from Fig. 3, consistent with our previous worst-case calculation, that $(V_{OC})_E > 650$ mV is still possible at EOL, if $W_E < (L_p)_{EOL}$.

2.4 V_{OC} established by the base for BOL and EOL

As shown in Fig. 1(b) for the dark case with applied voltage V_A, the quasi-neutral saturation current J_0 in low injection, neglecting heavy-doping effects [12], is $J_0 = J_{p0} + J_{n0}$, and the base saturation current is

$$J_{n0} = \frac{q n_i^2 D_n}{N_{AA} L_n} \tag{9}$$

To minimize J_{n0}, note that, for $N_{AA} \gtrsim 10^{17}$ cm^{-3}, $D_n/N_{AA}L_n$ is a decreasing function of N_{DD} [13], provided heavy doping effects are negligible. As a result, the open-circuit voltage limited by the base $(V_{OC})_B$ is an increasing function of N_{DD} until $N_{AA} \simeq 10^{19}$ cm^{-3} ($\rho_{base} \simeq 0.01$ Ωcm) which is a doping level at which the heavy doping effects in p-type material become important [12], as shown in

Fig. 4. The broken line in Fig. 4 shows an experimental dependence of V_{OC} on N_{AA} [14] which peaks at $N_{AA} \simeq 5 \times 10^{17}$ cm^{-3}. This is a result of the increasing importance of the emitter current J_{pO}, for base dopings larger than about 5×10^{17} cm^{-3}, in conventional cell where the emitter current is not suppressed by an HLE structure such as that present in the proposed device.

3. Design concepts for space and terrestrial applications

Based on the foregoing analysis we present design concepts for two different types of space cells and for a terrestrial cell.

1) n^+-n-p OCI-HLE (diffused HLE) space cell

Fig. 5 shows a cell designed for space applications. The p-type base doping is $N_{AA} \simeq 5 \times 10^{17}$ ($\rho \simeq 0.1$ Ωcm) which appears to be an optimum value which gives L_n in a range of 85-150 μm in a finished cell [15]. This long diffusion length, which will assure collection of most of the generated minority electrons, provides a high value of the short circuit current J_{SC}. The epitaxial emitter is narrow, about 2 μm, and highly doped, $N_{DD} \simeq 10^{17}$ to 10^{18} cm^{-3}, to assure low series resistance. The thinness of the emitter offsets, to a large degree, the effects of significant degradation of lifetime in the n-type material after the irradiation [9]. The H-L emitter junction can be achieved using either OCI induced or diffused n^+ layer [16].

The following conclusions about this structure can be made based on the discussion in the previous sections:

a) $(V_{OC})_E > 650$ mV at EOL, if $t_t < (\tau_p)_{EOL}$.

b) $(V_{OC})_B$ at EOL will depend on the radiation damage [10]. Since the base is the same as in the conventional n on p cell, results obtained for the conventional cell radiation damage [10] also apply here.

c) $(J_{SC})_{EOL} = (J_{SC})_{\substack{\text{conventional} \\ \text{base}}} + (J_{SC})_E$.

d) For an OCI structure, $S_{eff} \simeq N_{DD} S_p/n_s$, where both S_p and n_s increase with radiation, thus tending to keep S_{eff} low. S_{eff} controls $(J_{SC})_E$ and J_{pO}.

e) For BOL, with $S_p \simeq 10^3$ cm/sec, $(V_{OC})_E > 700$ mV, and $(V_{OC})_B$ depends on minimizing $D_n/L_n N_{AA}$. $(V_{OC})_B$ of the order of 700 mV can be expected for $\rho_{base} \simeq 0.1$ Ωcm with $L_n > 75$ μm.

f) For $Q_0/q > 10^{12}$ cm^{-2}, heavy doping effects in the accumulation layer may become important [Fig. 2]. However, since the accumulation layer is very narrow, these effects are expected to be very small [17].

g) A structure with a diffused n^+-region offers larger flexibility in choosing N_{DD} because of the low shunting resistance of the n^+-diffused layer.

2) A wide-emitter p^+-p-n^+ space cell

We propose a new silicon solar cell structure [18] which is projected to have both high J_{SC}(45 mA/cm^2) and high V_{OC}(700 mV) and consequently high η (20%, AM0). The new structure is projected to have good performance in radiation as well as non-radiation environments.

The structure is shown in Fig. 6. The qualitative sketches showing the minority carrier distributions in Fig. 1 are valid for this case, too, with hole and electron profiles reversed.

We emphasize some special features of this structure:

a) The surface is passivated with SiO_2 on top of which a suitable antireflection (AR) coating is deposited. The H-L emitter junction is achieved by a thin ($\sim$0.1 μm) p^+-diffused layer resulting in [4]

$$S_{eff} \simeq S_n \frac{N_{AA}}{(N_{AA}^+)_{eff}} \qquad (10)$$

where $(N_{AA}^+)_{eff} \simeq 10^{19}$ cm^{-3} is the effective doping in the p^+-diffused layer for $N_{AA}^+ \simeq 10^{20}$ cm^{-3} at the surface. An electron recombination velocity at the Si-SiO_2 interface on the order of 10^3 or less can be easily achieved [1]. Therefore, for $N_{AA} = 5 \times 10^{17}$ cm^{-3}, S_{eff} is of the order of 10 cm/sec or less; thus $S_{eff} \simeq 0$ is a reasonable approximation.

b) As a result of $S_{eff} \simeq 0$, and the choice of a 50 μm wide emitter region, about 90% [19] of all available optically generated minority electrons will be collected. Using a 5% loss AR coating and 4% metal coverage the projected AM0 $J_{SC} \simeq 45$ mA/cm^2. P-type material is chosen as a region from which the J_{SC} is collected due to smaller sensitivity to the radiation than seen in n-type material [9].

c) The doping level in the n^+-base is optimized to be about 10^{18} cm^{-3}, which is the onset level for heavy-doping effects [17]. The doping

level in the emitter ($\sim 5 \times 10^{17}$ cm^{-3}) is chosen to minimize $N_{AA}\tau_n$ [13].

d) Using published data for lifetimes for holes and electrons [7,13], we can calculate by use of Eqs. (2) and (9), for structure shown in Fig. 6, that the saturation current $J_0 \lesssim 7 \times 10^{-14}$ A/cm^2, implying $V_{OC} \simeq 700$ mV for $J_{SC} = 45$ mA/cm^2 at 25°C, and implying $\eta \simeq 20\%$ AMO.

e) Significant differences exist between this new cell and a previously proposed epitaxial p^+-p-n cell [20]; these are discussed in detail in Ref. 18.

f) An alternative related structure (p^+-p-n-n^+) can be made, which employs an n-n^+ low-high junction back-surface-field base [4]. This structure will have higher J_{SC} at BOL due to improved collection of minority holes from the n-region of the base.

3) n^+-n-p OCI-HLE terrestrial cell (Fig. 1)

There are two approaches to minimize the base current in this cell, Fig. 7:

a) Choose $\rho_{base} \simeq 0.1$ Ωcm ($N_{AA} \simeq 5 \times 10^{17}$ cm^{-3}). In this case $L_n \gtrsim 70$ μm is required for $(V_{OC})_B \simeq 700$ mV (25°C and $J_{SC} = 35$ mA/cm^2). Such values for L_n can be achieved in finished cells using a low temperature fabrication process [13,15]. Epitaxial growth of the emitter and a high-temperature oxidation required for low S_p [1] may decrease L_n below the 70 μm; this would result in $(V_{OC})_B < 700$ mV. The largest V_{OC} seen experimentally for a cell with $\rho_{base} \simeq 0.1$ Ωcm is 643 mV AMO, at 25°C.

b) A second approach is to use a highly doped p-type (5×10^{18} - 10^{19} cm^{-3}) base. Note that for $N_{AA} = 5 \times 10^{18}$ cm^{-3}, for example, $L_n \simeq 2$ μm is sufficient to achieve $(V_{OC})_B$ of 700 mV. Such values are expected even after the high-temperature fabrication steps. In this second approach, $W_E \simeq 50$ μm, since the base will contribute negligibly to J_{SC}. Such a wide emitter is required to collect about 90% of generated minority holes. In approach (a), W_E can range from about 10 to 50 μm. The largest V_{OC} seen experimentally for a cell with $\rho_{base} \simeq 0.024$ Ωcm ($N_{AA} \simeq 2.5 \times 10^{18}$ cm^{-3}) is 647 mV AMO, at 25°C.

c) Emitter doping can be chosen from range of about 5×10^{16} cm^{-3} to about 5×10^{17} cm^{-3}.

CONCLUDING REMARKS

First order analysis of HLE solar cells for BOL and EOL conditions is presented. Based on this analysis and on experimentally measured material parameters, design concepts for both space and terrestrial cells are discussed. The proposed structures include: n^+-n-p OCI-HLE space cell, wide emitter p^+-p-n^+ space cell, and n^+-n-p OCI-HLE terrestrial cell . All structures are projected to yield both high V_{OC} and J_{SC}.

REFERENCES

1. Neugroschel, A., Lindholm, F. A., Pao, S. C, and Fossum, J. G., "Emitter Current Suppression in a High-Low-Junction Emitter Solar Cell Using An Oxide-Charge-Induced Electron Accumulation Layer," Appl. Phys. Letters, vol. 33, July 15, 1978, pp. 168-170.

2. Deal, B. E., Sclar, M., Grove, A. S., and Snow, E. H., "Characteristics of the surface-state charge (Q_{SS}) of thermally oxidized silicon, J. Electrochem. Soc., vol. 114, March 1967, pp. 266-274.

3. Fu, H. S. and Sah, C. T., "Theory and experiments on surface 1/f noise", IEEE Trans. Electron Devices, vol. ED-19, Feb. 1972, 273-285.

4. Godlewski, M. P., Baraona, C. R., and Brandhorst, H. W., "Low-high junction theory applied to solar cells", in Record of Tenth IEEE Photovoltaic Specialist Conf., 1973.

5. Lindholm, F. A., Fossum, J. G., and Burgess, E. L., "Application of the superposition principle to solar-cell analysis", IEEE Trans. Electron Devices, vol. ED-26, March 1979, pp. 165-171.

6. Kingston, R. H. and Neustandter, S. F., "Calculation of the space charge, electric field and free carrier concentration at the surface of semiconductors, J. Appl. Phys., vol. 26, June 1955, pp. 718-720.

7. Kendall, D., Conf. Physics and Application of Lithium Diffused Silicon, NASA-Goddard Space Flight Center, Dec. 1969.

8. Zaininger, K. H. and Holmes-Siedle "A survey of radiation effects in metal-insulator-semiconductor devices", RCA Rev., vol. 28, 1967, pp. 208-241.

9. Cooley, W. C. and Janda, R. J., "Handbook of space-radiation effects on solar-cell power systems", NASA Report SP-3003, 1963.

10. Tada, H. Y. and Carter, J. R., "Solar cell radiation handbook", JPL Publication 77-56, 1977.

11. Heasell, E. L., "Recombination beneath ohmic contacts and adjacent oxide covered regions", Solid-State Electron., vol. 22, Jan. 1979, pp. 89-93.

12. Dunbar, P. M. and Hauser, J. R., "Theoretical effects of surface diffused region lifetime models on silicon solar cells", Solid-State Electron., vol. 20, August 1977, pp. 697-701.

13. Iles, P. A. and Soclof, S. I., "Effect of impurity doping concentration on solar cell output, in Record of Eleventh Photovoltaic Specialist Conf., 1975, pp. 19-24.

14. Godlewski, M. P., Brandhorst, H. W., and Baraona, C. R., "Effects of high doping levels on silicon solar cell performance", in Record of Eleventh Photovoltaic Specialists Conf., 1975, pp. 32-35.

15. Brandhorst, H. W. and Godlewski, M. P., private communication.

16. Lindholm, F. A., Neugroschel, A., Pao, S. C., Fossum, J. G., Sah, C. T., "Design Considerations for Silicon HLE Solar Cells", in Record of Thirteenth IEEE Photovoltaic Specialists Conf., 1978, pp. 1300-1305.

17. Lanyon, H. P. D. and Tuft, R. A, "Bandgap narrowing in heavily doped silicon", IEDM Technical Digest, Dec. 1978, pp. 316-319.

18. Neugroschel, A. and Lindholm, F. A., submitted for publication to IEEE Trans. Electron Devices.

19. Fossum, J. G., "Computer-aided numerical analysis of silicon solar cells", Solid-State Electron., vol. 19, April 1976, pp. 269-277.

20. D'Aiello, R. V., Robinson, P. H., and Kressel, H., "Epitaxial silicon solar cells", Appl. Phys. Letters, vol. 28, 15 Feb., 1976, pp. 231-234.

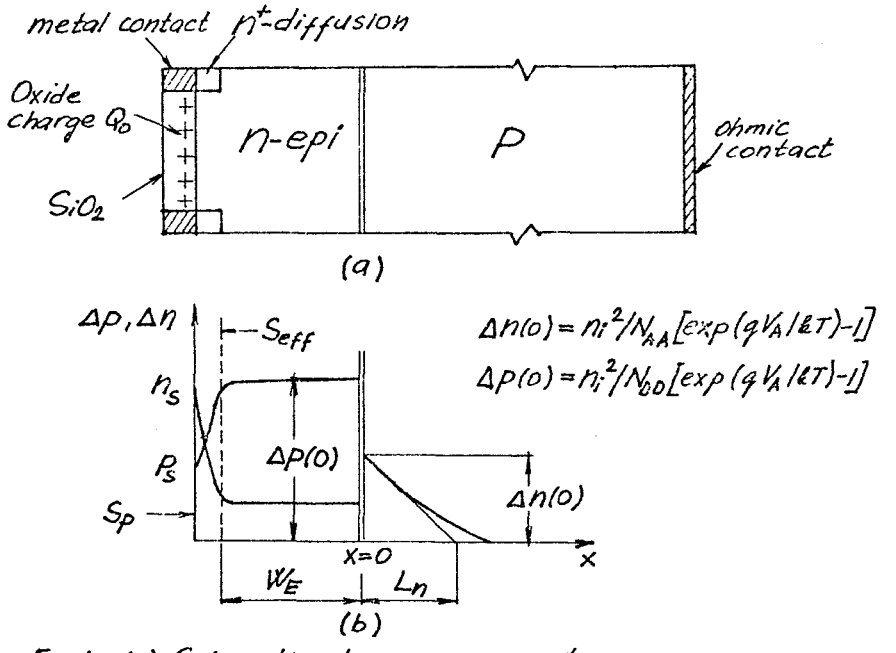

Fig. 1. (a) Schematic diagram of a n^+-n-p OCI-HLE cell.
(b) Qualitative sketches of excess minority carrier distribution in dark with applied voltage V_A.

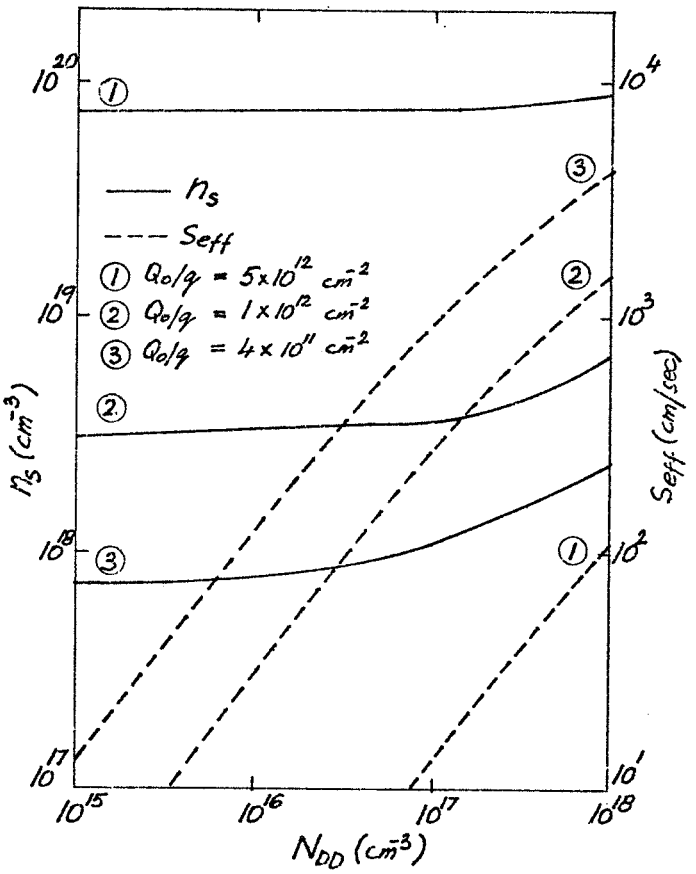

Fig. 2. Dependence of electron surface concentration n_s and effective surface recombination velocity Seff (for $S_p = 10^4$ cm/sec) on emitter doping.

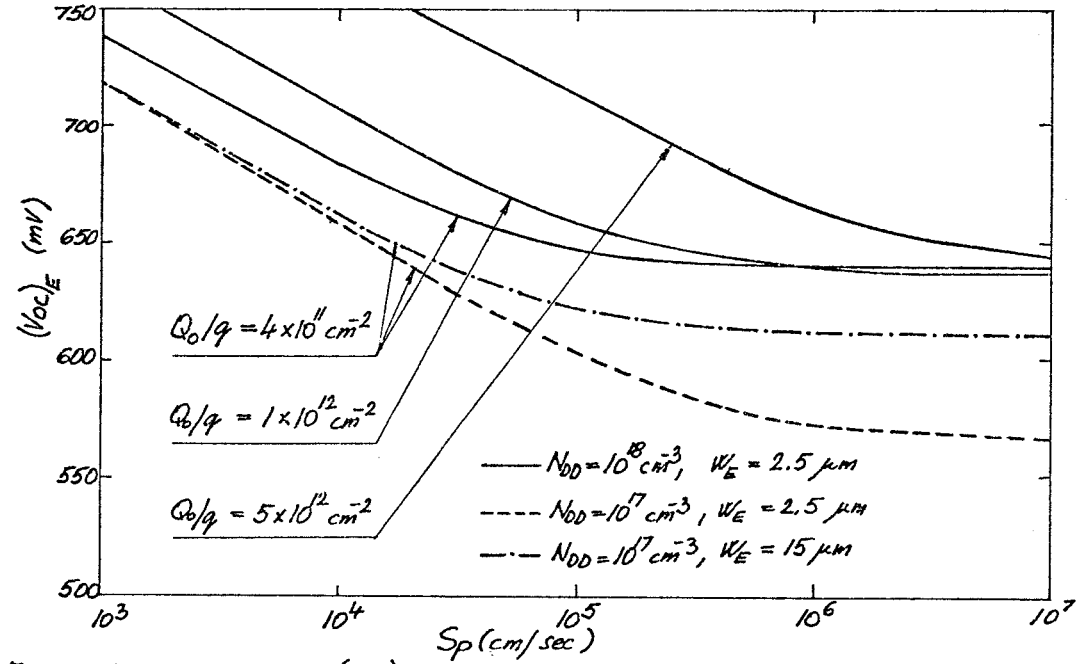

Fig. 3. Dependence of $(V_{OC})_E$ on S_p.

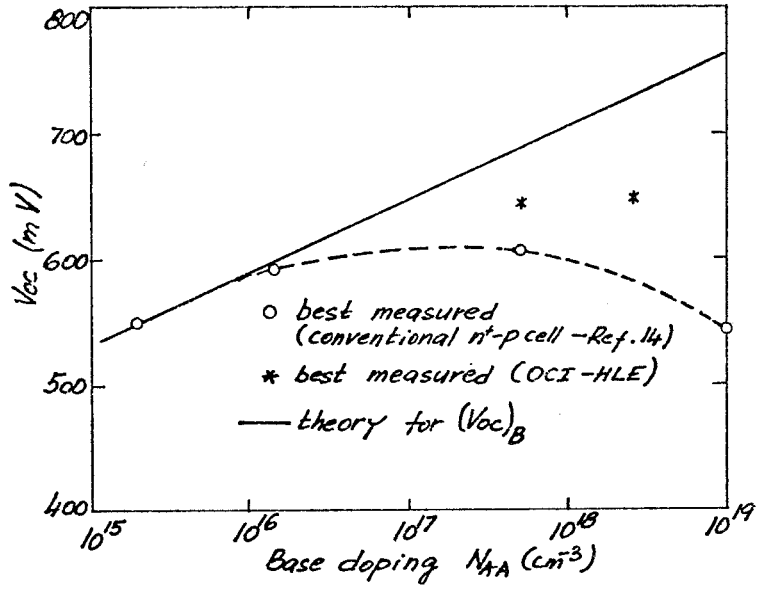

Fig. 4. Experimental and theoretical dependence of Voc on base doping. Best results obtained on OCI-HLE cells are 643 mV for 0.1 Ωcm base resistivity and 647 mV for 0.024 Ωcm base resistivity (measured at NASA Lewis, at 25°C, AMO).

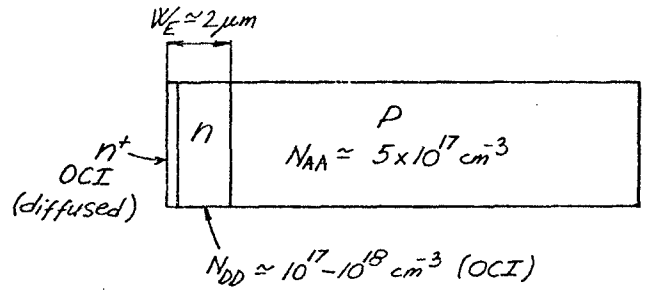

Fig. 5. Schematic diagram of a n^+-n-p OCI-HLE (diffused HLE) space cell.

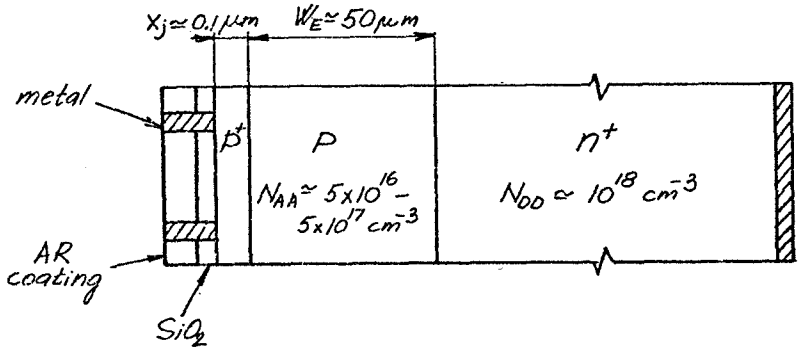

Fig. 6. Schematic diagram of a p^+-p-n^+ space cell.

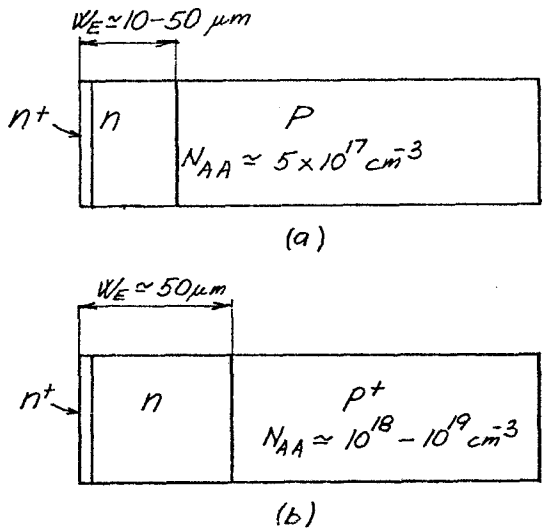

Fig. 7. Schematic diagrams of an OCI-HLE terrestrial cells.
(a) n^+-n-p cell
(b) n^+-n-p^+ cell

APPLICATIONS OF ION IMPLANTATION TO HIGH PERFORMANCE, RADIATION TOLERANT SILICON SOLAR CELLS*

Allen R. Kirkpatrick, John A. Minnucci,
and Keith W. Matthei
Spire Corporation

SUMMARY

Ion implanted silicon solar cells have undergone appreciable development during the past two years. Efficiencies now exceed 14 percent AM0 in structures which have not been optimized. Back surface field effects are reproducibly accomplished by implantation. Special annealing in conjunction with implantation has resulted in 0.1 ohm-cm cell open-circuit voltages to 644 mV. Radiation tolerance is being addressed by development of extremely clean processing to avoid contamination-induced defect formation. Very high efficiency cells with good environmental stability characteristics are expected.

INTRODUCTION

For a number of years the potential advantages of ion implantation for fabrication of silicon solar cells have been recognized. To effectively employ implantation to produce high-performance cell structures, a great deal of preliminary work related to damage annealing requirements and profile deficiency corrections has been necessary. Most of this work has now been completed.

At the time of the first High Efficiency Silicon Solar Cell Review in November 1974, silicon cells with efficiencies of 10-11 percent AM0 could be produced. Operational implanters were standard machines used by the semiconductor industry which allowed only marginally satisfactory parameter selections and had poor throughput capabilities at the dose and ion energy levels being utilized. By the Solar Cell High Efficiency and Radiation Damage Meeting in April 1977, efficiency of implanted silicon cells had increased to 12 percent AM0, development of new annealing technology was in progress and profile deficiencies had been recognized (see ref. 1). A modified production implanter was operational at Spire to allow use of improved implant parameters.

Since April 1977, substantial progress has been made. Efficiencies above 14 percent AM0 are now being achieved in implanted spacecraft and terrestrial cell configurations (see ref. 2). Advanced thermal and pulsed-energy-beam transient process annealing techniques are available, as described in references 3, 4 and 5. Much has been learned regarding effective utilization of implant processing. Implanted junctions are still rather deep, typically 0.25 μm or more, and texturized surfaces have not yet been exploited. Inadequacies still exist in the structures of implanted cells. Major improvements remain to be made, but expectations of very high performance can be justified. Solar cell production implantation equipment now exists, and implanters for future high-volume terrestrial cell production have been designed (see ref. 2).

*This work is supported in part under NASA Lewis Research Center contracts NAS3-20823 and NAS3-21276.

PRESENT STATUS OF ION IMPLANTED SILICON SOLAR CELLS

One set of implant and thermal anneal parameters is used at Spire for standard processing of most N/P silicon cells with base resistivity of 1 ohm-cm or higher. At present these parameters are as follows:

Junction Implant: 5 keV $^{31}P^{+}$
$2x10^{15}$ cm^{-2}

Back Surface Implant: 25 keV $^{11}B^{+}$
$5x10^{15}$ cm^{-2}

Anneal: 550°C - 60 minutes
850°C - 15 minutes
550°C - 60 minutes
In nitrogen

Dopant profiles resulting with these conditions are shown in figure 1. In the past, implant damage annealing was usually performed as a one-step operation at the high temperature needed for electrical activation. Resulting profiles were approximately the same. The two 550°C steps which have been added to the annealing procedure have significant effects upon the performance of resulting cells. The initial 550°C step causes effective epitaxial regrowth of the damaged silicon lattice (see refs. 6 and 7). The final 550°C step is believed to improve minority-carrier lifetime in the silicon bulk.

The listed implantation/anneal conditions now being utilized still result in cell structures which are far from optimized. Using these parameters, efficiencies up to 14.2 percent AM0 are observed in 7.6-cm-diameter cells of 10-ohm-cm (100) silicon. Figure 2 shows performance parameter distributions measured on a group of five hundred 7.6-cm cells prepared using 550/850/550°C annealing (see ref. 8).

DEVELOPMENT IN PROGRESS

Over the past few years the deficiencies of ion implantation for solar cell junction purposes have been corrected. Work is now in progress to improve cell structure, performance and radiation tolerance. Development is being conducted as a number of separate elements which will, as they become available, be later combined to produce highest overall performance and stability. Activities at Spire include:

(i) Development of effective back surface preparation by implantation

(ii) Investigation of junction processing to achieve high V_{oc} in low-resistivity cells

(iii) Investigation of improved radiative tolerance, which may be accomplished by processing with low contaminant introduction.

IMPLANTED BACK SURFACE LAYERS

Although the standard processing now being employed for preparation of ion implanted cells involves implants into both cell surfaces, little has been done toward optimization of the back surface. Examination of the open-circuit voltages of the 10-ohm-cm cells of figure 2 shows that reasonably effective back surface fields are being introduced.

Recently, a test was conducted by OCLI and Spire in which back fields were introduced by $^{11}B^{+}$ implantation or by aluminum paste alloying into quantities of otherwise identical 10-ohm-cm diffused junction cells (see ref. 9). The implanted-back-layer cells exhibited open-circuit voltages approximately 8 mV lower than those of the aluminum-alloyed-layer cells (average 585 versus 593 mV). Open-circuit voltage distribution of the implanted-back cells was narrower. Very tight V_{oc} distributions are a consistent characteristic of implanted layer cells. The secondary ion mass spectroscopy (SIMS) examinations shown in figure 3 of the alloyed and implanted back layers indicate a deeper and monotonically declining profile from the alloyed aluminum. The implanted boron was apparently inadequately distributed by the processing employed. Correction can be made by direct process variations.

Back layers by implantation have advantages in simplicity and reproducibility. The quality of the implanted surface is substantially better than that of the reprocessed alloyed surface, which should be beneficial for future incorporation of additional back surface optimizations. Figure 4 shows scanning electron microscope (SEM) views of alloyed-aluminum and implanted-boron silicon wafer surfaces. The implanted surface retains its original bright-etch quality.

HIGH OPEN-CIRCUIT VOLTAGE CELLS

It is generally accepted that if high open-circuit voltages approaching 700 mV are to be achieved in cells of low base resistivity, junction characteristics must be improved. Consideration must be given to dopant level and profile, to minority-carrier lifetimes and mobilities and to recombination characteristics of the junction layer surface. Implantation offers the control, reproducibility and flexibility necessary to investigate effects of junction parameter variations upon open-circuit voltage.

Improved open circuit voltages are now being achieved in 0.1-ohm-cm cells with implanted junctions. Figure 5 shows the AM0 I-V characteristic of a 2x2-cm cell with 644-mV V_{oc} at 25°C. Comparable results are easily reproduced.

The implant and anneal parameters employed to prepare the cell of figure 5 were as follows:

Junction Implant: 5 keV $^{31}P^{+}$
$2x10^{15}$ cm^{-2}

Anneal: 550°C - 2 hours
850°C - 30 minutes
550°C - 2 hours
Oxidizing atmosphere

An oxide grown on the junction layer surface during annealing was left on the cell to serve as surface passivation and as an antireflection coating. The rather modest I_{sc} exhibited in figure 5 is attributed at least in part to the inadequacy of the low-index SiO_2 coating.

Figure 6 shows a SIMS examination of the phosphorus profile produced by the implant and anneal/oxidize conditions listed above. The sharp peak at the immediate surface of the silicon is believed to contribute to the V_{oc} produced.

RADIATION TOLERANT CELLS

It is recognized that radiation tolerance of the silicon solar cell may be limited by radiation-induced defects associated with impurities in the silicon introduced during crystal growth or during device processing. If very high quality silicon, characterized by low content of spurious impurities, is utilized for solar cell fabrication, its quality will be compromised by processing-induced contaminants which cannot be avoided when conventional techniques including thermal procedures are employed. This shortcoming is generally true for ion implantation and thermal annealing. Substantial amounts of carbon and oxygen are known to be introduced by standard implantation procedures (see refs. 10 and 11). However, specialized implantation and energy-beam transient annealing can be combined to fabricate cells with very low introduction of spurious impurities.

In the case of processing by normal implantation, contaminants are introduced by knock-on recoil effects. Incoming ions which impact with surface contaminant atoms can transfer appreciable energy to these atoms, causing them to recoil into the silicon lattice. They may later be redistributed by thermal annealing. The atoms which are introduced in this manner can originate from processing or handling residues, from native oxides and from vacuum system diffusion-pump oil deposits.

Under NASA Contract NAS3-21276, Spire is preparing special processing capability to avoid contaminant introduction. An ion implanter is being modified to replace its process station diffusion pump by a cryogenic pump, to minimize carbon introduction during implantation. The implanter will be operated in a mode in which precleaned wafer surfaces will be in situ sputter-cleaned immediately prior to dopant introduction. Transient annealing by pulsed electron beam and pulsed laser methods (see refs. 3, 4 and 5) under clean environmental conditions will be used to anneal implant damage without thermal elevation of the silicon bulk. It is expected that C and O atom introduction by this processing will be reduced approximately four orders of magnitude from existing levels.

Some preliminary testing of silicon solar cells fabricated by good implantation and annealing techniques prior to preparation of the special capabilities described above has shown promise of improved radiation tolerance (see ref. 12). Controlled preparation of cells from silicon of best available quality may result in substantial improvements.

PLANNED DEVELOPMENT

Present activities will soon cause the efficiency of ion implanted silicon cells to rise above 15 percent AM0 and could provide capability for achieving improved radiation tolerance. During the next phase of development of ion implanted cells, total device optimization will have to be addressed. Most of the requirements can now be defined. Among the needed component elements are the following:

- Higher open-circuit voltages by optimization of implantation and anneal procedures
- Higher current densities by use of texturized front surfaces and advanced back layer structures
- Further reduction of contaminant levels and of structural imperfections by improved utilization of transient processing methods

REFERENCES

1. Minnucci, J. A.; and Kirkpatrick, A. R.: Proceedings of Solar Cell High Efficiency and Radiation Damage Conference. Lewis Research Center, April 1977, p. 99.

2. Kirkpatrick, A. R.; Minnucci, J. A.; Greenwald, A. C.; and Josephs, R. H.: Proceedings of 13th IEEE Photovoltaic Specialists Conference. Washington, June 1978, p. 706.

3. Greenwald, A. C.; Little, R. G.; and Minnucci: J. A., IEEE Trans. Nucl. Sci. NS-26(1), 1683 (1979).

4. Greenwald, A. C.; Kirkpatrick, A. R.; Little, R. G.; and Minnucci, J. A. J. Appl. Phys. 50(2), 783 (1979).

5. Greenwald, A. C.; and Little, R. G. Solid State Tech. 22(4), 143 (1979).

6. Csepregi, L.; Mayer, J. W.; and Sigmon, T. W. Appl. Lett. 29(2), 92 (1976).

7. Csepregi, L.; Shu, W. K.; Muller, H.; Mayer, J. W.; and Sigmon, T. W.; Radiat. Eff. 28, 227 (1976).

8. Cells fabricated for delivery to Jet Propulsion Laboratory under LSA Project Contract 954786.

9. Minnucci, J. A.; Kirkpatrick, A. R.; Iles, P. A.; and Khemthong, S.: Presentation at Electrochemical Society Meeting, Boston, 8 May 1979.

10. Moline, R. A.; and Cullis, A. G. Appl. Phys. Lett. 26(10), 551 (1975).

11. Tsai, M. Y.; Streetman, B. G.; Blattner, R. J.; and Evans, C. A. J. Electrochem. Soc. 126(1), 98 (1979).

12. Drevinsky, P. J.; Schott, J. T.; DeAngelis, H. M.; Kirkpatrick, A. R.; and Minnucci, J. A.: Proceedings of 13th IEEE Photovoltaic Specialists Conference. Washington, June 1978.

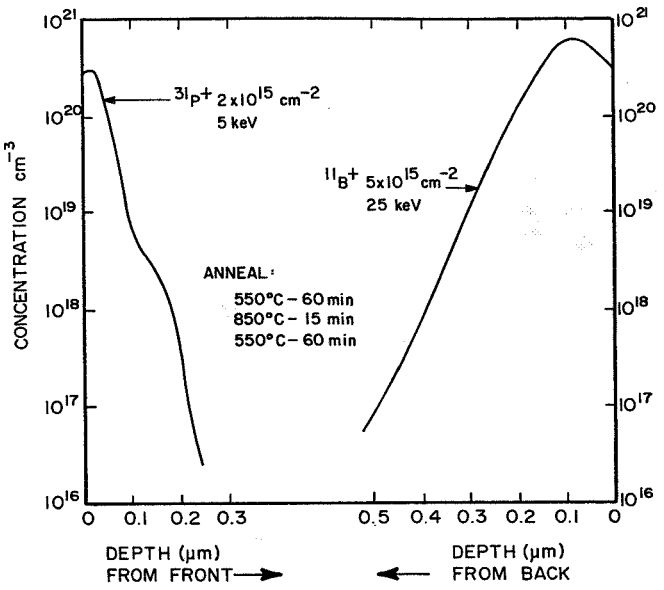

FIGURE 1. MEASURED DOPANT PROFILES FROM STANDARD IMPLANT/ANNEAL CONDITIONS

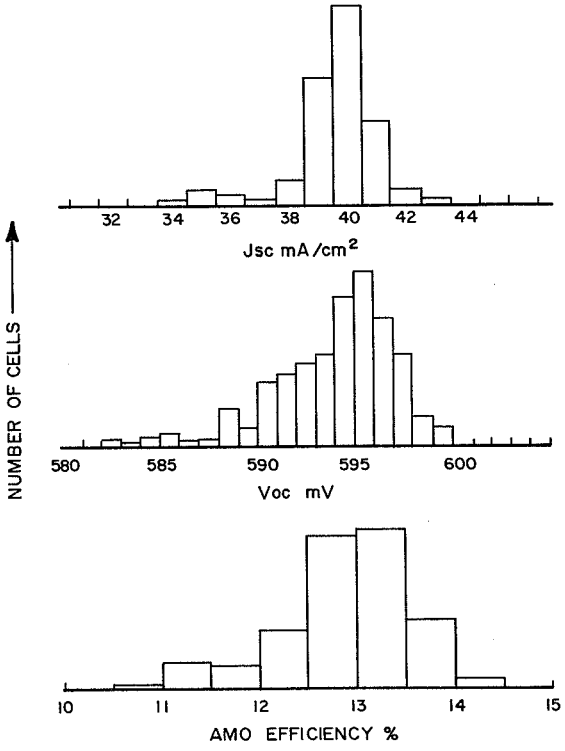

FIGURE 2. 25°C AM0 PERFORMANCE DISTRIBUTIONS OF 500 IMPLANTED $N^{+}PP^{+}$ 3-INCH CELLS

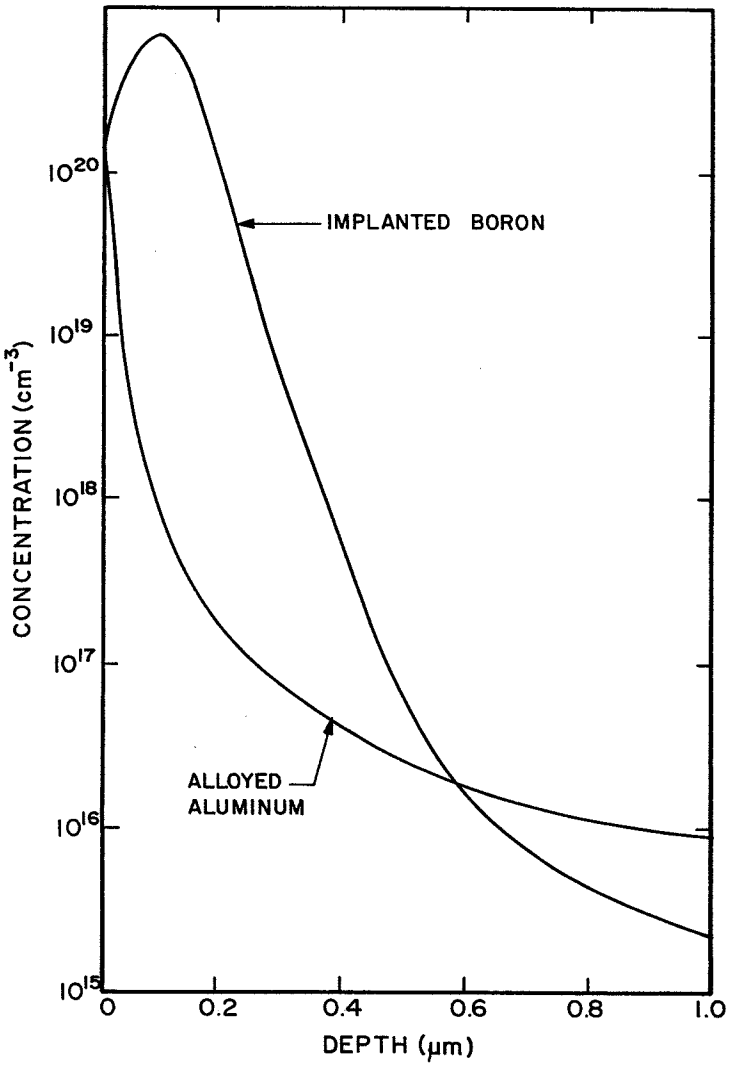

FIGURE 3. BACK LAYER PROFILES DETERMINED BY SIMS

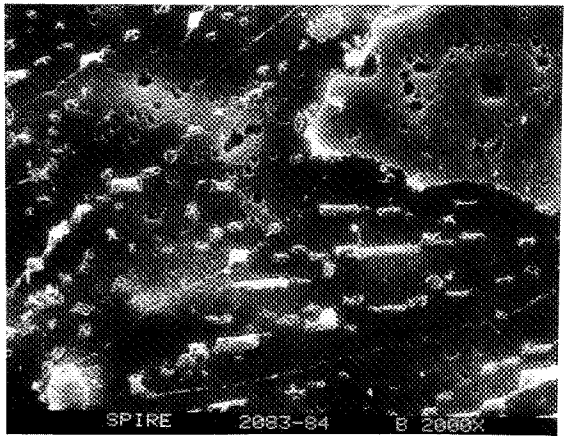

(A) Back Surface After Thick-Film Aluminum Alloy (2,000X)

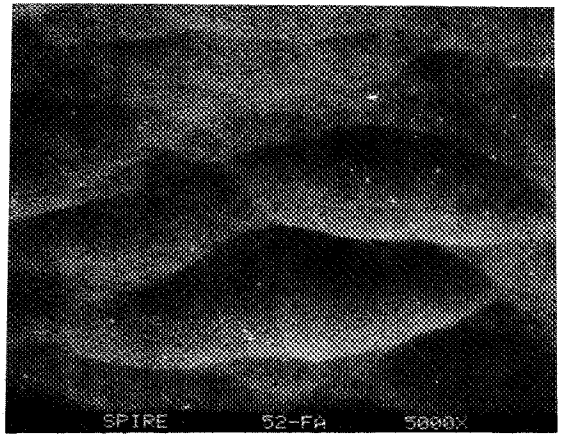

(B) Back Surface After Ion Implantation and Furnace Anneal (5,000X)

FIGURE 4. SEM MICROGRAPHS OF TWO BSF PROCESSED SURFACES

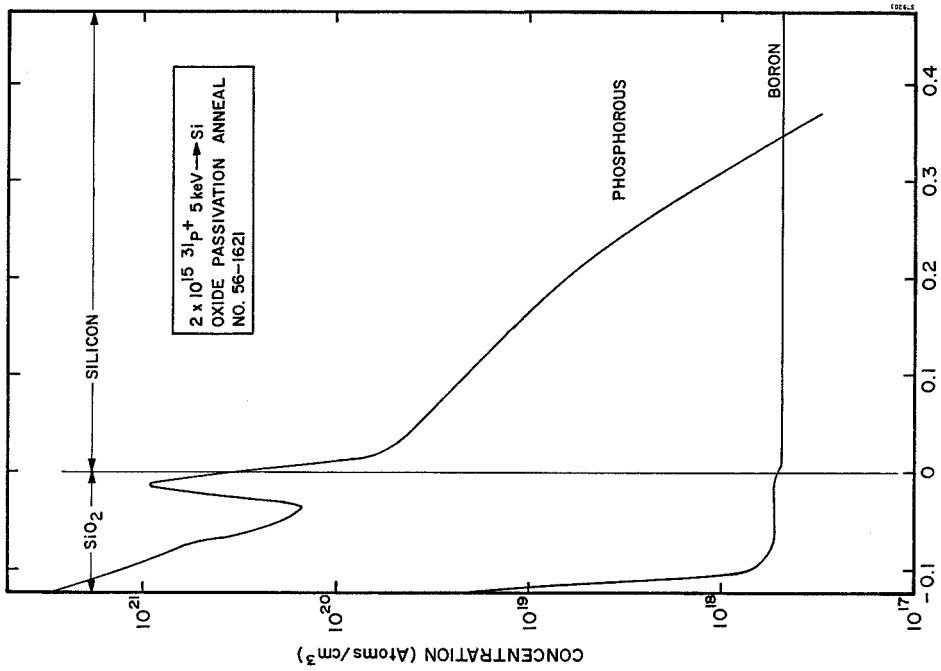

FIGURE 6. SIMS PROFILE OF PHOSPHORUS IN IMPLANTED CELL WITH PASSIVATING OXIDE

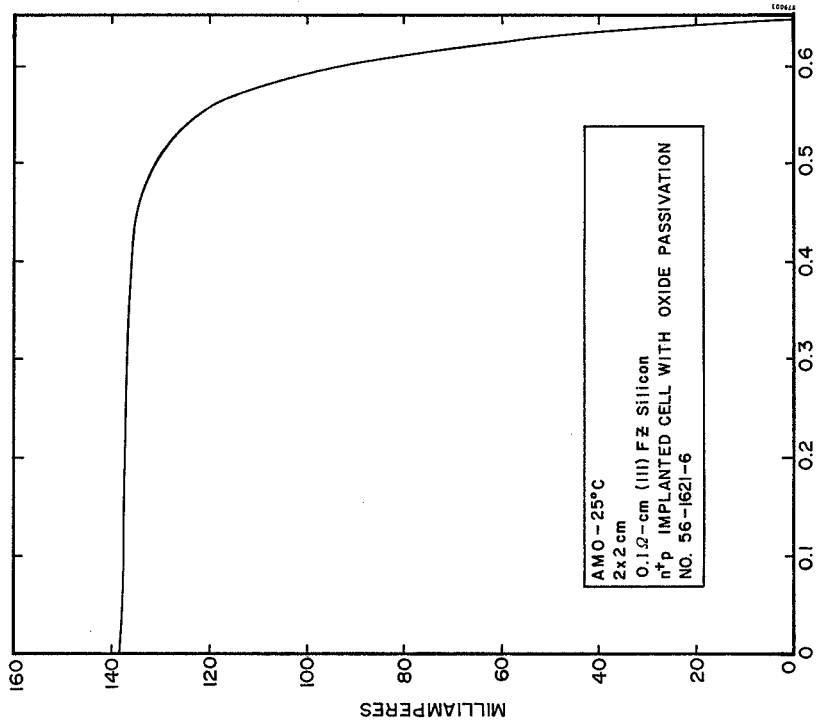

FIGURE 5. AM0 I-V CHARACTERISTIC OF HIGH V_{oc} CELL

OPEN-CIRCUIT VOLTAGE IMPROVEMENTS IN LOW-RESISTIVITY SOLAR CELLS

Michael P. Godlewski, Thomas M. Klucher, George A. Mazaris
and Victor G. Weizer
National Aeronautics and Space Administration
Lewis Research Center

The Lewis Research Center has been engaged in an attempt to identify the mechanisms limiting the open-circuit voltage in 0.1-ohm-cm solar cells. In the course of this work it was found that a rather complicated multistep diffusion process could produce cells with significantly improved voltages. Concurrent with the Lewis effort, several other laboratories have been pursuing alternative approaches under various NASA contracts. The best Lewis results to date and the best results from other laboratories are compared in figure 1. Together with the Lewis results, the figure shows the air-mass-zero (AMO) open-circuit voltage as a function of the short-circuit current for the University of Florida's charged-oxide, high-low emitter cell and for the Spire Corporation's ion-implanted emitter cells and published results for the University of New South Wales' metal-insulator-seminconductor (MIS) cell (ref. 1). To compare the voltage capabilities of these cells, independent of their absorption and collection efficiencies, we must compare them on the basis of their saturation currents or, equivalently, compare their voltage outputs at a constant current-density level. If we arbitrarily choose 25 mA/cm^2 or, as plotted in figure 1, 100 mA/4 cm^2 as the reference current density and assume ideal diode characteristics, we see that the highest voltage (648 mV) is obtained from the Florida cell. The Lewis cell and the Spire cell yield about 637 millivolts, and the New South Wales cell about 632 millivolts. The open-circuit voltage is defined throughout this paper as the voltage obtained at a current density of 25 mA/cm .

The Lewis multistep fabrication schedule is described in figure 2, along with a list of processing conditions that have resulted from a partial optimization effort. The schedule consists of three steps, all of which have been found to be necessary. The first step is a relatively deep diffusion. This primary diffusion is followed by an acid-etch removal of the emitter surface such that the final sheet resistance is in the 10- to 12-ohm/ range. The etching step is then followed by a short, low-temperature secondary diffusion. Final junction depths ranged from 1 to 4 micrometers.

As stated, the schedule has not been completely optimized. Consider, for example, the time of the primary diffusion. As shown in figure 3, we have found a direct correlation between the primary diffusion time and the open-circuit voltage. As can be seen, the highest voltage was obtained for the longest diffusion time (i.e., 637 mV for a 65-hr diffusion).

As the diffusion time is lengthened, cell fabrication becomes increasingly cumbersome. It was decided, therefore, for experimental expediency, to investigate the mechanisms associated with the increase in diffusion time that lead

to improved voltages. The identification of these mechanisms should permit us to achieve the increased voltages in more conventional structures.

The first step in the investigation was to determine which region of the cell was responsible for voltage control (i.e., base, emitter, or depletion region). Since the cells fabricated by the multistep technique exhibit ideal diode characteristics, depletion region effects were ruled out.

To determine the degree of control exercised by the base and emitter components of the saturation current, several experiments were performed. In figure 4 the open-circuit voltage is plotted as a function of the base diffusion length as measured by the X-ray technique for cells receiving a 4-hour, 950° C primary diffusion. The other fabrication conditions for these cells are as indicated in figure 3. Superimposed on the data in figure 4 are those calculated curves that have been fit to the data at the point indicated. The upper curve is what would be expected if the base component of the saturation current were only 10 percent of the total saturation current as calculated at the fit point. Also shown are what would be expected for 40 and 100 percent base control. The closest fit occurs when we assume complete base control.

A similar plot for cells diffused at 950° C for 41 hours is given in figure 5. The voltages in this plot are generally higher than those in figure 4, an indication of reduction of the base saturation current with increasing diffusion time. A similar set of calculated curves on this plot indicate base control, although there is now some evidence of emitter influence. Best agreement with the experimental data is obtained for the case where, at the fit point, the base contributes 80 percent of the device saturation current and the emitter 20 percent.

These two plots correlate with the results of the spectral response measurements made both with 0.5-micrometer-wavelength light, which is absorbed completely in the emitter, and 0.9-micrometer-wavelength light, which is absorbed mostly in the base. Figure 6 shows the relationship between the open-circuit voltage and the monochromatic 0.5- and 0.9-micrometer spectral responses for cells fabricated with 4-hour, 950° C primary diffusions. The parameters that affect the current output from a given region of the cell (i.e., base or emitter) should also affect the value of the saturation current from that region. If, therefore, the base component of the saturation current were controlling the voltage, we would expect a positive correlation between the base current (0.9-μm response) and the open-circuit voltage. That figure 6 shows such a correlation is further evidence that the base is voltage controlling in these cells.

These arguments apply in a similar fashion to the emitter region. The lack of correlation between the voltage and the emitter current (0.5-μm response) is consistent with the notion of base control.

These current-voltage arguments, although convincing, are not absolutely conclusive. It is conceivable that some emitter current - such as the diffusivity, which does not affect the emitter current - is actually controlling the cell voltage. However, to be consistent with the data, this emitter parameter would have to be fortuitously correlated with the base current - a situation which, although possible, is very unlikely. These data, therefore, along with

those presented in figures 4 and 5, strongly suggest that the open-circuit voltage of the Lewis multistep diffusion cell is controlled by the base component of the cell saturation current.

Similar spectral response - voltage plots for a limited sampling of Florida high-low emitter cells and Spire ion-implanted cells are shown in figure 7. The red response-voltage correlation for the Spire cells indicated probable base control. The data for the Florida cells, on the other hand, are not very conclusive. There does not appear to be the same correlation with red response as for the other cells, a possible indication of emitter control. The results of 1-MeV-electron irradiation experiments performed at Lewis (ref. 2) on these three cell types support the above conclusions (i.e., base control for the Lewis and Spire cells and emitter control for the Florida cells).

The preceding data suggest strongly that the open-circuit voltage in the Lewis diffused cells is controlled by the base component of the saturation current. It remains now to identify which parameter in that component is being influenced by the primary diffusion time in such a way as to yield increased voltages as the time is lengthened.

Assuming a high recombination velocity at the rear surface of the cell, the base saturation current, I_{OB}, is given by the well-known expression:

$$I_{OB} = \frac{qn_i^2 D}{N_A L} \coth \frac{d}{L} \tag{1}$$

where q is electronic charge, n_i is intrinsic carrier concentration, D is diffusivity, N_A is acceptor impurity concentration, L is diffusion length, and d is base-region width. In an attempt to isolate the voltage-controlling parameter, three cells were selected that had widely different open-circuit voltages but nearly identical base diffusion lengths, thicknesses, and rear surface treatments. The primary diffusion times for these cells were 4, 16, and 41 hours. Again, these cells and all the cells discussed in this paper exhibited ideal, diffusion-controlled current-voltage characteristics. It was reasoned that the voltage differences between these cells must be due to differences in either the boron concentration and/or profile or the base minority carrier diffusivity.

The electrically active boron concentration profiles in these three cells were determined indirectly through a SIMS measurement of their phosphorus profiles. The SIMS data are shown in figure 8, along with other data for these cells. The diffusion lengths in these cells were the same to within a few percent, as were their thicknesses. In the figure the phosphorus concentration is plotted as a function of distance from the junction. The profiles near the depletion region are unexpectedly similar. In fact, they appear to be identical. This anomalous result is due to an unexplained retardation of the phosphorus diffusion front that intensifies as the diffusion time is increased. Although such retardation phenomena have been reported in the literature (ref. 3), the mechanisms involved are still unclear.

The net, or electrically active, boron concentration on the base side of the junction can be obtained by subtracting the measured phosphorus concentration from the prediffusion boron concentration. Since these cells were all fabricated from the same silicon ingot, the calculated postdiffusion net boron concentration profiles must be identical.

We can conclude, therefore, that because the net boron profiles, the base diffusion lengths, the thicknesses, and the rear surface recombination velocities of these cells are identical, the observed voltage differences must be due to differences in the remaining variable (i.e., the base minority carrier mobility). To explain the observed voltage increases, one would have to invoke a reduction in the electron mobility in the base as the diffusion time is increased.

The validity of these conclusions could be tested through a measurement of the base mobility of these three cells. Theoretically this could be done by making independent measurements of the diffusion length and the lifetime and employing the well-known relation

$$L = (D\tau)^{1/2} \tag{2}$$

where L is diffusion length and τ is minority carrier lifetime. Unfortunately, attempts to measure τ in the above cells using a transient open-circuit-voltage decay technique were unsuccessful because of ambiguities in the interpretation of the decay curves. We can, however, present some evidence to attest to the existence of large changes in minority carrier mobility with diffusion time.

The data presented in figure 9 were obtained at Lewis several years ago during a study of shallow-junction, 10-ohm-cm devices. It can be seen that as the diffusion time was increased, the diffusion lengths decreased significantly. However, contrary to what would be expected, as the diffusion lengths decreased, the open-circuit voltages increased. The lifetimes of these cells were measured using an open-circuit voltage decay (OCVD) technique, and the diffusivities calculated using equation (2). The results, shown in figure 9, indicate a large drop in the value of D as the diffusion time was increased from 30 minutes to 2 hours. The decrease in the diffusivity in this case was apparently sufficient to overcome the effects of the decreasing diffusion length and to produce an increase in voltage, even though the diffusion length was severely degraded. These effects are very similar to what has been observed for the present Lewis low-resistivity cells. It appears reasonable, therefore, on the basis of the data presented above, to ascribe the voltage limiting role in the Lewis low-resistivity cells to the electron mobility (diffusivity) in the cell base.

In summary, it appears that for both the Lewis diffused emitter cell and the Spire ion-implanted emitter cell the base component of the saturation current is voltage controlling. The evidence for the University of Florida cells, although not very conclusive, suggests emitter control of the voltage in this device. The data suggest further that the critical voltage-limiting parameter for the Lewis cell is the electron movility in the cell base. The mechanisms involved in the observed mobility changes, however, await further study.

REFERENCES

1. Godfrey, R. B.; and Green, M. A.: 655 mV Open-Circuit Voltage, 17.6% Efficient Silicon MIS Solar Cells. Appl. Phys. Lett. vol. 34, no. 11, June, 1979, pp. 790-793.

2. Weinberg, Irving; Swartz, Clifford K.; and Weizer, Victor G.: Radiation Damage in High-Voltage Silicon Solar Cells. Solar Cell High Efficiency and Radiation Damage - 1979, NASA CP-2097, 1979.

3. Matsumoto, S.; et al.: Effects of Diffusion-Induced Strain and Dislocation on Phosphorus Diffusion into Silicon. J. Electrochem. Soc., vol. 125, no. 11, Nov. 1978, pp. 1840-1845.

COMPARISON OF VOLTAGE IMPROVEMENTS IN 0.1 OHM-CM SILICON CELLS.

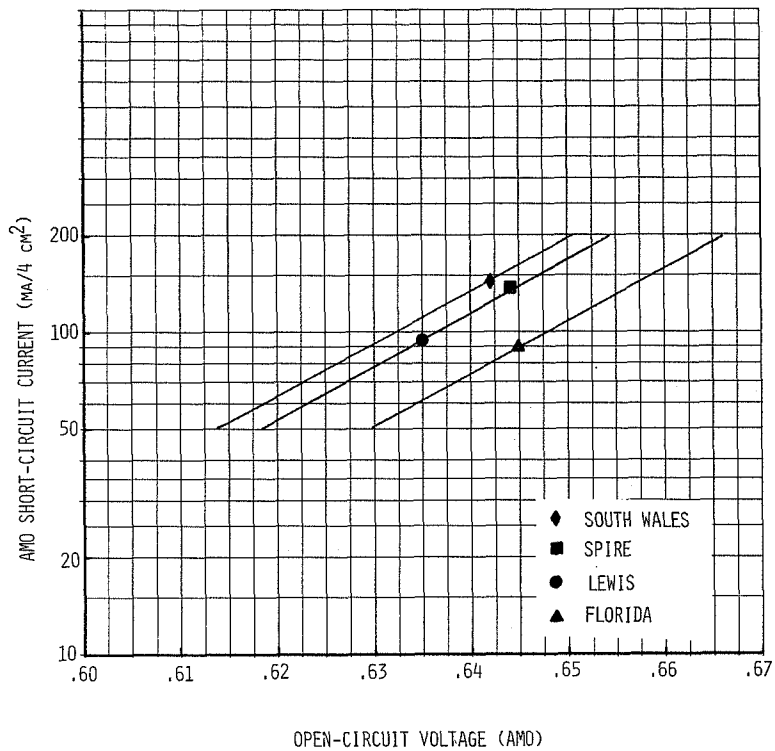

FIGURE 1

LEWIS CELL FABRICATION SCHEDULE

1. PRIMARY DIFFUSION

SURFACE CONCENTRATION	1×10^{20} CM^{-3}
TEMPERATURE	950° C
TIME	$\geqslant$ 65 HRS.

2. EMITTER ETCH

SHEET RESISTANCE	10-12 OHM/□

3. SECONDARY DIFFUSION

SURFACE CONCENTRATION	2×10^{20} CM^{-3}
TEMPERATURE	750° C
TIME	15 MIN.

FIGURE 2

OPEN-CIRCUIT VOLTAGE AS A FUNCTION OF PRIMARY DIFFUSION TIME

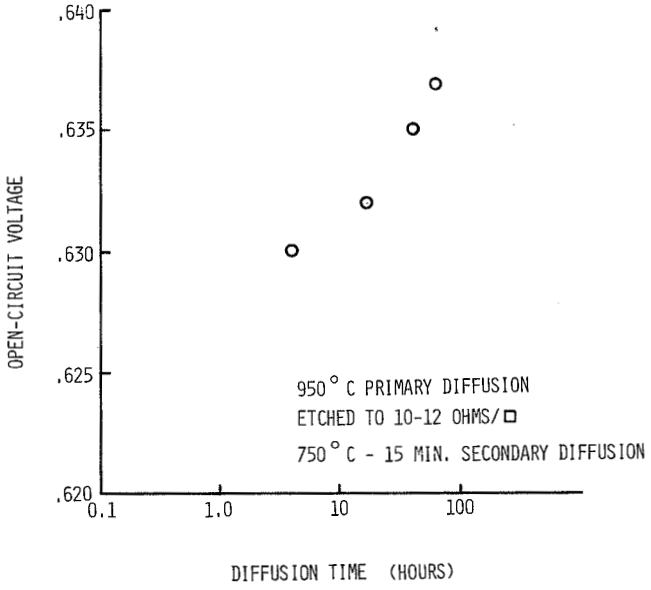

FIGURE 3

INFLUENCE OF BASE DIFFUSION LENGTH ON VOLTAGE

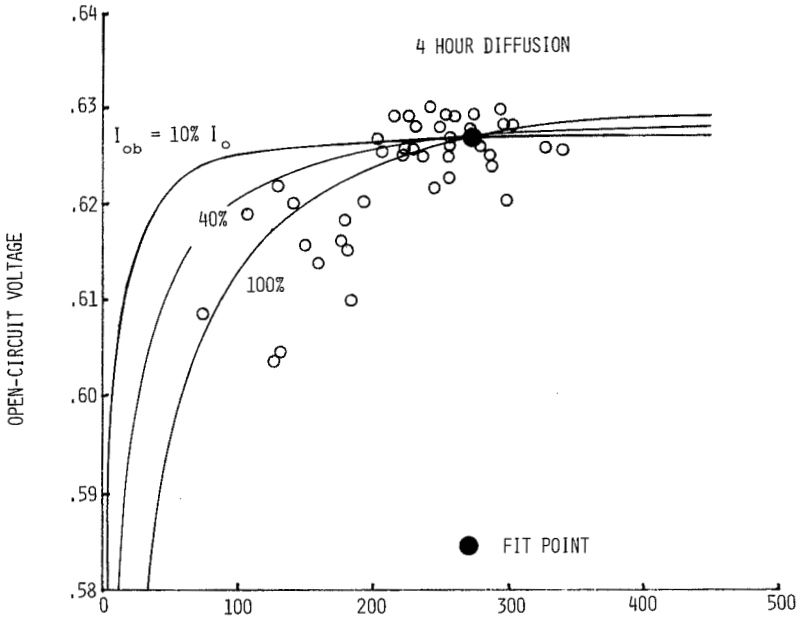

FIGURE 4

INFLUENCE OF BASE DIFFUSION LENGTH ON VOLTAGE

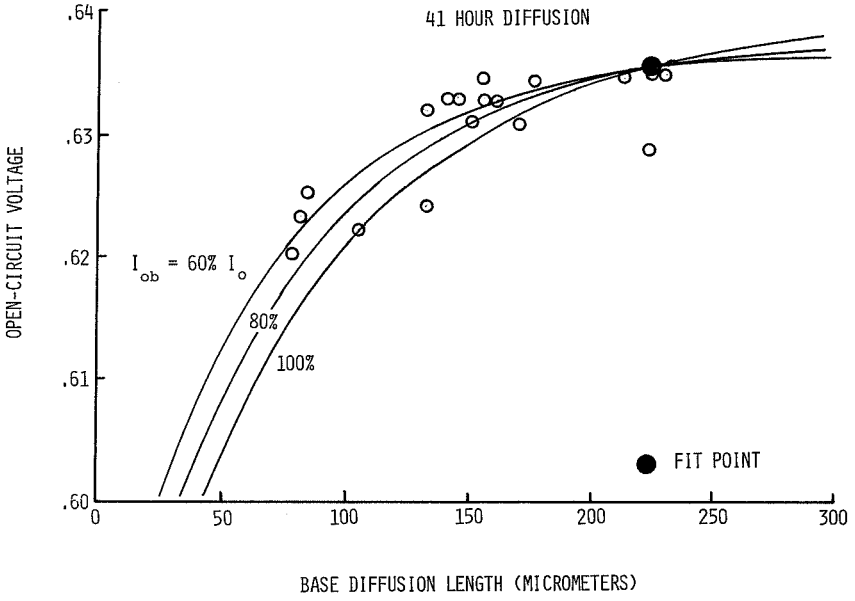

FIGURE 5

CORRELATION BETWEEN VOLTAGE AND CURRENT FOR SELECTED WAVELENGTHS

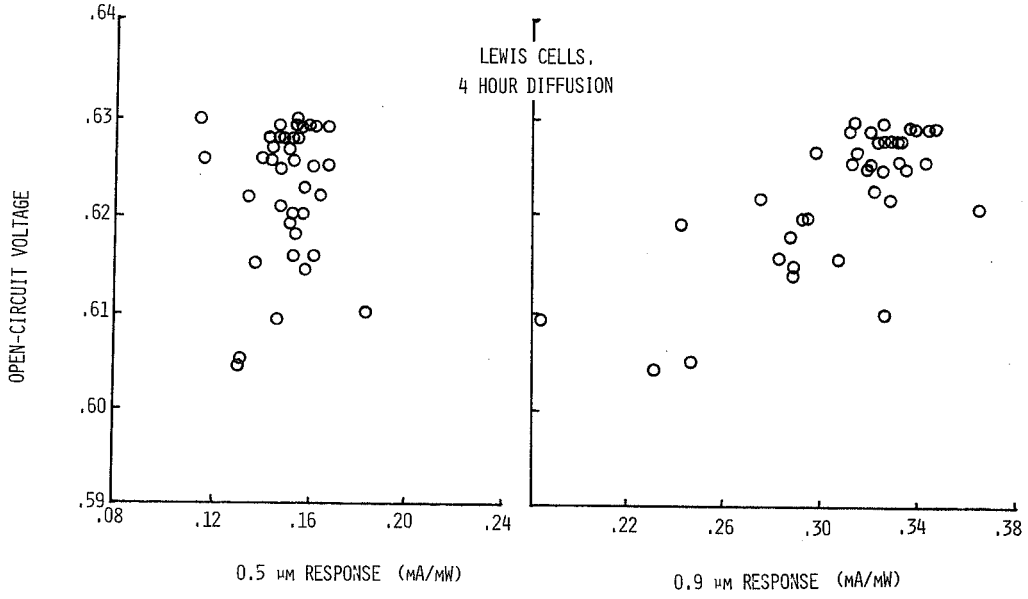

FIGURE 6

CORRELATION BETWEEN VOLTAGE AND CURRENT FOR SELECTED WAVELENGTHS

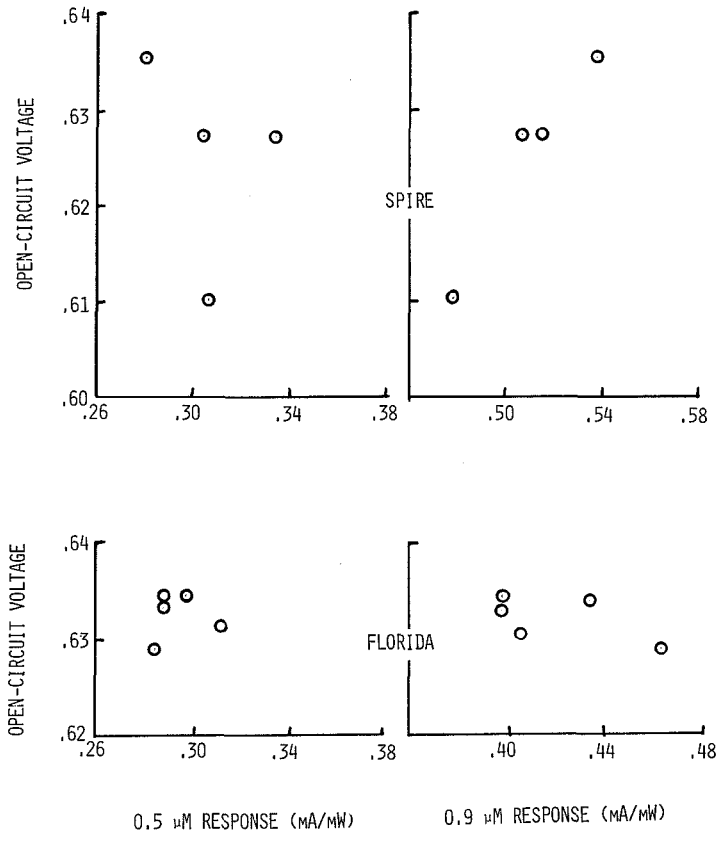

FIGURE 7

EFFECT OF PRIMARY DIFFUSION TIME ON PHOSPHORUS CONCENTRATION PROFILE (SIMS)

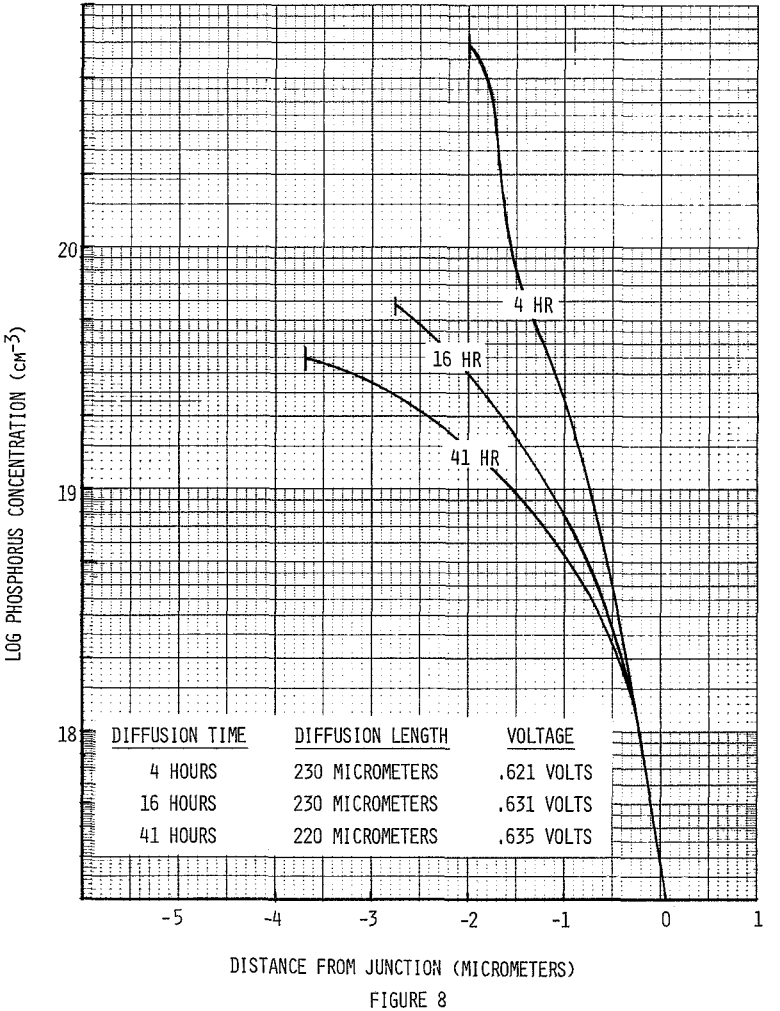

FIGURE 8

EFFECT OF DIFFUSION TIME ON MINORITY CARRIER DIFFUSIVITY

DIFFUSION CONDITIONS	V_{OC}^{25}	$L^{(A)}$	$\tau^{(B)}$	$D(\tau)$
750 - 30 MIN	.523 V	120 μM	2.0 μSEC	72.0 $\frac{CM^2}{SEC}$
750 - 60 MIN	.524 V	70 μM	2.0 μSEC	24.5 "
750 - 120 MIN	.527 V	36 μM	2.3 μSEC	5.6 "

(A) X-RAY TECHNIQUE

(B) OCVD TECHNIQUE

FIGURE 9

A NEW METHOD FOR MODELING MULTILAYER SOLAR CELL STRUCTURES

M. Wolf and Y. H. Wu
University of Pennsylvania

ABSTRACT

With the current trend to the use of drift fields (BSF) and high-low junctions in both front and base regions of the solar cell, the need arises for the relatively simple modeling of solar cell structures with at least three layers in each region. A beginning of this had been made in this author's paper of 1963[1], which treated a one-dimensional, two-layer model in closed form and showed an expansion to a third layer for a simple case. The direct expansion of the closed-form method to additional layers would be very cumbersome, but the expansion method used gave a hint to an approach of layer-by-layer modeling. The important aspect is the representation of current densities across the layer interfaces by the product of the density and a transport velocity. The only basic conditions are that the interface be chosen at a location where the carrier density and the current are continuous across the interface; that is, no surface charge and no surface recombination exists at the interface. In addition, the treatment is greatly eased if the interface is chosen in a space-charge, quasi-neutral region of the cell.

In the case of low-level injection, space-charge quasi-neutrality, and spatially constant material parameters, including an electrostatic field within a layer, the individual layer can be treated analytically, and its basic solar cell performance parameter contributions evaluated by three equations. The first represents the transformation of the transport velocity across the layer from the other boundary, which may be an open surface with a given surface recombination velocity. The second determines the light-generated current output from this layer, under the influence of the transport velocities at both layer boundaries and of bulk recombination. The third equation describes the flow of this current across other layers. In certain cases where not all the conditions are met for a given layer, an analytical approach may still be possible. Otherwise, numerical methods may have to be applied for a given layer.

The power of the approach is that it permits analysis of the solar cell's performance layer by layer, that it gives a clear picture of the individual layer's influence on the cell efficiency, and that it greatly eases the cell design optimization task.

The principles of the methodology and results of its application will be discussed, including implications on future high-performance solar cell structures.

---

[1] Wolf, M.: Drift Fields in Photovoltaic Solar Energy Converter Cells. Proc. IEEE 51, 1963, pp. 674-693.

MODELING OF THIN, BACK-WALL SILICON SOLAR CELLS

Cosmo R. Baraona
National Aeronautics and Space Administration
Lewis Research Center

SUMMARY

The performance of silicon solar cells with p-n junctions on the nonilluminated surface (i.e., upside-down or back-wall cells) was calculated. These structures consisted of a uniformly shaped p-type substrate layer, a p^+-type field layer on the front (illuminated) surface, and a shallow, n-type junction on the back (nonilluminated) surface. A four-layer solar cell model was used to calculate efficiency, open-circuit voltage, and short-circuit current. The effect on performance of p-layer thickness and resistivity was determined. The diffusion length was varied to simulate the effect of radiation damage. The results show that peak initial efficiencies greater than 15 percent are possible for cell thicknesses of 100 micrometers or less. After 10 years of radiation damage in geosynchronous orbit, thin (25 to 50 μm thick) cells made from 10- to 100-ohm-cm material show the smallest decrease (~10 percent) in performance.

INTRODUCTION

A back-wall, or upside-down, solar cell (ref. 1) is a conventional n^+-p-p^+ device with its collecting p-n junction on the nonilluminated bottom side of the device. The p^+ side is covered with a gridded contact; the n^+ region has full area metallization. Back-wall cells are similar to certain high-voltage cell designs that have collecting p-n junctions 25 or more micrometers from the illuminated surface (ref. 2) or to interdigitated back-contact cells (refs. 3 and 4). The interdigitated cells that are most similar to the back-wall cell design are those with a front-surface field. Structures like these have been prepared for space use; hence, it is of interest to assess their performance in a radiation environment.

The present work explores analytically the performance of a range of back-wall cell structures. The performance trends of these back-wall cell designs are calculated by using a four-layer solar cell model. This model has been used previously (refs. 5 to 8) to calculate solar cell performance and has shown good agreement with experiment. The influence of the back-wall cell thickness, the bulk resistivity, and the radiation damage coefficient on performance was determined. The ranges of parameters used in the model can be achieved with present technology. These calculations are intended to give the scope of the problem and to illustrate performance trends. Experimental data were not available for comparison.

THEORETICAL MODEL

The solar cell model used for these calculations has been described elsewhere (refs. 5 to 8). The model is based on a four-layer, homojunction semiconductor solar cell. Layer widths, impurity concentrations, surface properties, and material properties can be specified. Exponential impurity distributions are assumed so that drift field strengths within each layer are constant.

The equations used in the model were derived by solving the continuity equation: The current transport equation and appropriate boundary conditions were used to solve for the diode saturation current density J_0 and for the short-circuit current density J_{sc}. The open-circuit voltage V_{oc}, maximum power P_{max}, curve factor CF, and air-mass-zero (AMO) efficiency were calculated in reference 8. In calculating the curve factor, a diode quality factor of 1 and a series resistance of zero were assumed. For most cells, this represents about a 3 percent overestimate of power and curve factor. Data in this paper were not adjusted for that overestimate. The AMO solar constant used was 135.6 mW/cm^2.

Some of the values used in the calculations are shown in figure 1. Zero optical reflection and lower front-surface recombination velocity ($S \leq 10$ cm/sec) were used to improve cell performance. The p^+ front-surface field region was about 1 micrometer deep. The carrier concentration, mobility, and diffusion length were characteristic of an alloyed or heavily doped diffused region. The n^+ and n regions were 0.25 micrometer deep and had properties characteristic of a shallow diffused junction. The surface recombination velocity at the back wall (under the full-area metallization) was 10^8 cm/sec.

Both front- and back-surface recombination velocities were assumed to be constant and independent of radiation fluence. If S increased with irradiation, additional degradation in cell performance would be predicted by the four-layer model. Complete collection of carriers was assumed within the depletion region.

The p-region bulk of the cell was a uniformly doped, field-free region from 25 to 100 micrometers thick. The p-region resistivities, corresponding to initial diffusion lengths and radiation damage coefficients for 1-MeV electrons (ref. 9) used in the calculations are shown in table I. The initial diffusion lengths chosen correspond to reasonable minority carrier lifetimes for the various resistivities. The diffusion length after a given fluence was calculated with the usual equation (ref. 9).

RESULTS AND DISCUSSION

Efficiency is shown as a function of fluence for 25-, 50-, and 100-micrometer-thick, 10-ohm-cm back-wall cells in figure 2. Almost all the loss in efficiency is due to loss in J_{sc}. The initial unirradiated efficiencies are about 15.2 percent for 25- and 50-micrometer-thick cells and about 14.1 percent for 100-micrometer-thick cells. This demonstrated that high beginning-of-life (BOL) efficiencies are possible for back-wall cells. Figure 2 also shows that thin back-wall cells degrade less rapidly than thicker cells.

A fluence of $4x10^{14}$ electrons/cm^2 corresponds to about 10 years in geosynchronous orbit and is defined herein as the end-of-life (EOL) condition. At end of life the 25-micrometer-thick cell is 13.4 percent efficient and the 50- and 100-micrometer thick cells are 11.3 and 6.2 percent efficient, respectively. Thus, acceptable end-of-life efficiencies may be possible if back-wall cells are made ultrathin.

Similar calculations were performed for back-wall cells made from 1- and 100-ohm-cm material. These calculations, along with those for 10-ohm-cm cells, are shown in figure 3. Efficiency is plotted as a function of resistivity for three cell thicknesses. The beginning-of-life results (fig. 3(a)) show that 15 percent efficiencies can be achieved with several conbinations of thickness and resistivity. However, 100-micrometer-thick cells made from 1- and 10-ohm-cm material are less efficient because the diffusion length is reduced. The end-of-life results (fig. 3 (b)) show that 50-micrometer-thick, 100-ohm-cm back-wall cells and 25-micrometer-thick, 10- and 100-ohm-cm back-wall cells can achieve an efficiency of 13 percent. This represents only about a 10 percent loss in performance over the life span, compared with 15 to 20 percent for conventional cell designs. Therefore, using thin, high-resistivity material appears to yield both high BOL and high EOL performances in the back-wall cell design.

SUMMARY OF RESULTS

Calculations of back-wall silicon solar cell performance with a four-layer model gave the following results:

1. Back-wall cells can achieve 15 percent air-mass-zero beginning-of-life efficiency.
2. Air-mass-zero, end-of-life efficiency of 13 percent is possible with 50-micrometer-thick, 100-ohm-cm material or with 25-micrometer-thick, 10- or 100-ohm-cm material.

REFERENCES

1. Brandhorst, H. W., Jr.: Back Wall Solar Cell. U.S. Patent 4,131,486, Dec. 1978.

2. Neugroschel, A.; and Lindholm, F.A.: Design of High Efficiency HLE Solar Cells for Space and Terrestrial Applications. Solar Cell High Efficiency and Radiation Damage - 1979. NASA CP-2097, 1979.

3. Carbajal, B. G.: High Efficiency Cell Development. (TI-03-79-16, Texas Instruments, Inc.; NASA Contract NAS7-100.) NASA CR-158581, 1979.

4. Anspaugh, Bruce E.; Miyahira, Tetsuo F.; and Scott-Monck, John A.: Electron Irradiation of Tandem Junction Solar Cells. Solar Cell High Efficiency and Radiation Damage - 1979. NASA CP-2097, 1979.

5. Wolf, M.: Drift Fields in Photovoltaic Solar Energy Converter Cells. Proc. IEEE, vol. 51, May 1963, pp. 674-693.

6. Godlewski, M. P.; Baraona, C. R., and Brandhorst, H. W., Jr.: The Drift Field Model Applied to the Lithium-Containing Silicon Solar Cell. Tenth Photovoltaic Specialists Conference, Institute of Electrical and Electronics Engineers, Inc., 1974, pp. 378-383.

7. Godlewski, M. P.; Baraona, C. R.; and Brandhorst, H. W., Jr.: Low-High Junction Theory Applied to Solar Cells. Tenth Photovoltaic Specialists Conference, Institute of Electrical and Electronics Engineers, Inc., 1974, pp. 40-49.

8. Baraona, C. R.; and Brandhorst, H. W., Jr.: Analysis of Epitaxial Drift Field N on P Silicon Solar Cells. Twelfth Photovoltaic Specialists Conference, Institute of Electrical and Electronics Engineers, Inc., 1976, pp. 9-14.

9. Srour, J. R.; et al.: Damage Coefficients in Low Resistivity Silicon. (NRTC-75-23R, Northrup Research and Technology Center, NASA Contract NAS3-17849.) NASA CR-134768, 1975.

10. Miyahira, T. F.; and Anspaugh, B.: Electron Radiation Degradation of Recent Solar Cell Designs. Thirteenth Photovoltaic Specialists Conference, Institute of Electrical and Electronics Engineers, Inc., 1978, pp. 463-464.

TABLE I. - BACK-WALL CELL MODELING PARAMETERS

Resistivity, ohm-cm	Initial diffusion length, μm	Damage coefficient, electron^{-1}
1	100	2.0×10^{-10}
10	200	4.5×10^{-11}
100	600	1.0×10^{-11}

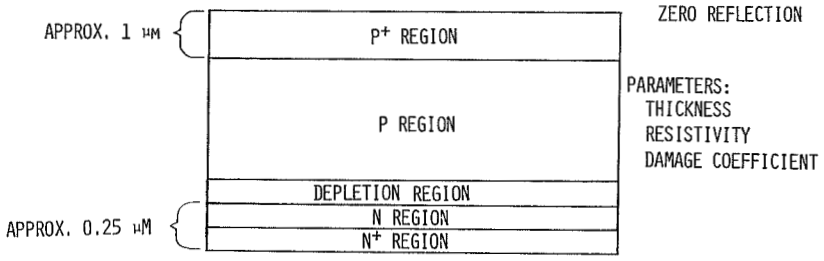

Figure 1.- Cross section of thin, four-layer backwall cell. Air-mass-0 illumination.

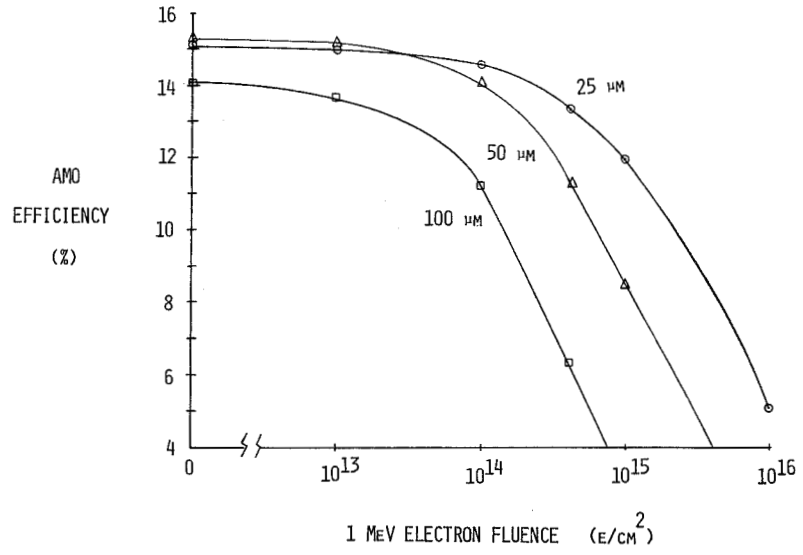

Figure 2.- Efficiency as function of fluence for 10-ohm-cm backwall cells.

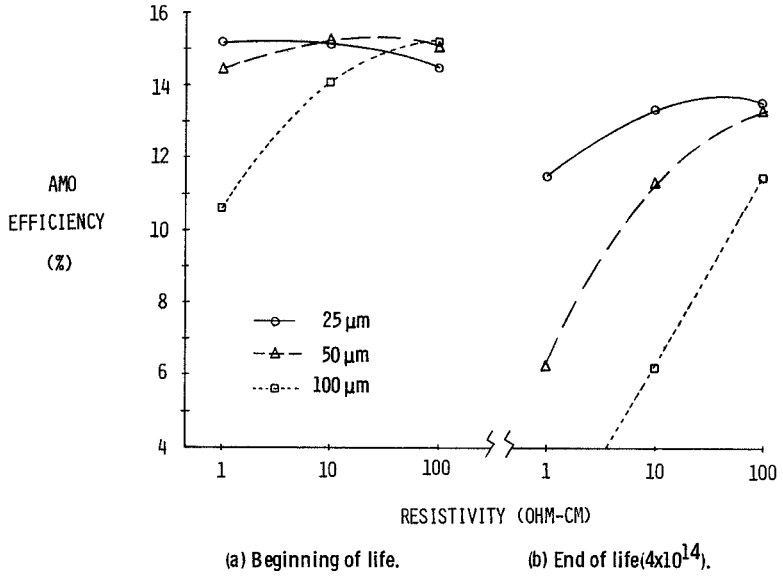

(a) Beginning of life. (b) End of life(4×10^{14}).

Figure 3. - Efficiency as function of resistivity for backwall cells.

DESIGN CONSIDERATIONS FOR THE TANDEM JUNCTION SOLAR CELL*

W. T. Matzen, B. G. Carbajal, and R. W. Hardy
Texas Instruments, Inc.

SUMMARY

Structure and operation of the Tandem Junction Cell (TJC) are described. The impact of using only back contacts is discussed. A model is presented which explains operation of the TJC in terms of transistor action. The model is applied to predict TJC performance as a function of physical parameters.

INTRODUCTION

The Tandem Junction Solar Cell (TJC) is a back contact cell which has exhibited high efficiency in terrestrial applications (ref. 1,2). A model has been presented which explains operation of the TJC and provides general design criteria (ref. 3). The model is applied here to predict TJC performance in terms of physical parameters.

SYMBOLS

The International System of Units is used throughout.

D	Diffusion coefficient
$G(X)$	Generation rate for carriers as a function of depth
I_{CS}	Saturation current for collector-base junction
I_{SC}	Short-circuit current
I_{λ}	Total photon generated current
$I_{\lambda C}$	Photon generated current at collector-base junction
$I_{\lambda E}$	Photon generated current at emitter-base junction
J_{SC}	Short-circuit current density
kT	Thermal energy
L	Diffusion Length
$N(X)$	Minority carrier concentration as a function of distance
$N'(X)$	Gradient of minority carrier concentration as a function of distance
q	Magnitude of electronic charge
X	Distance normal to surface
X_E	Emitter junction depth
W	Base width
V_{OC}	Open circuit voltage
τ	Minority carrier lifetime
α_N	Normal (forward) current transfer ratio
α_I	Inverse current transfer ratio
γ_E	Injection efficiency of emitter-base junction

* This work was partially supported by the Low-Cost Solar Array Project, Jet Propulsion Laboratory, California Institute of Technology, sponsored by the U.S. Department of Energy through an interagency agreement with NASA.

TJC STRUCTURE

As illustrated in the cross section of Figure 1, the TJC consists of a P-type base with a thin N+ region at the front surface and interdigitated P+ and N+ regions at the back. The front N+ region is uncontacted. Current is collected at the N+ and P+ contacts at the back of the cell. The front surface is texturized. Refraction of incident light and reflection at the back surface give a long optical path so that a high percent of the light is absorbed, even in very thin cells.

Benefits of using contacts on only the back surface include:

- o Elimination of metal shadowing
- o Potential of low series resistance
- o Convenience of interconnect

Additionally, high short circuit current and open circuit voltage have been achieved in very thin cells. An inherent limitation of back contact cells is that good performance is dependent upon high lifetime.

TRANSISTOR MODEL FOR THE TJC

Operation of the TJC is explained by the basic transistor model shown in Figure 2. In the cross section of Figure 2(a), the front N+ region corresponds to the emitter, the P-region to the base, and the back N+ region to the collector. The current sources $I_{\lambda E}$ and $I_{\lambda C}$ in Figure 2(b) result from carrier generation in the vicinity of emitter-base and collector-base junctions, respectively.

Generation and flow of carriers is illustrated in Figure 3. When carriers are generated in the emitter, holes diffuse to the base region. For short-circuit conditions, the holes move by fields through the base to the P+ contact. To maintain charge neutrality, a potential is built up across the junction such that electrons are injected from emitter to base in approximately equal quantities. Carrier generation in the base also contributes to the emitter-base junction potential; a boundary condition for base-generated carriers is that net flow of electrons across the emitter-base junction is zero (assuming emitter injection efficiency is unity, as discussed in a later section).

From the equivalent circuit of Figure 2(b), the short circuit current is

$$I_{SC} = \alpha_N \; I_{\lambda E} + I_{\lambda C} \qquad (1)$$

where α_N is the forward (normal) current transfer ratio. Most of the current is generated very close to the surface. As a first order approximation, the total photon-generated current I_λ is at the emitter junction so that

$$I_{SC} \cong \alpha_N I_\lambda. \tag{2}$$

Open circuit voltage determined from the Ebers-Moll relationship (ref. 4), is

$$V_{OC} = \frac{kT}{q} \ln \frac{I_{SC}}{I_{CS}(1-\alpha_N\alpha_I)} \tag{3}$$

where I_{CS} is the saturation current of the collector-base junction. In principle, V_{OC} can be made quite high if forward and inverse current transfer ratios, α_N and α_I, approach unity.

High measured values of short circuit current, open circuit voltage, and good response at short wavelength are consistent with the transistor model.

DESIGN CONSIDERATIONS

The transistor model provides a familiar frame of reference for optimizing the TJC structure and estimating performance. Short circuit current, in Equation 2, is related to physical parameters of the cell by expressing current transfer ratio as

$$\alpha_N = \gamma_E \frac{1}{\cosh \frac{W}{L}} \tag{4}$$

where W is base width, L is diffusion length for minority carriers in the base, and γ_E is injection efficiency for the emitter-base junction. Values of γ_E near unity can be obtained using heavily-doped emitters.

From equations 2 and 4, short circuit current is approximated as

$$I_{SC} = I_\lambda \frac{1}{\cosh \frac{W}{L}} \tag{5}$$

A more accurate calculation has been carried out using the carrier continuity equation

$$qD \frac{d^2N}{dX^2} - \frac{q}{\tau} N + G(X) = 0 \tag{6}$$

The carrier generation function, G(X), has been adapted to the TJC by including the effects of refraction and reflection. The continuity equation is solved by a computer routine to obtain short-circuit current due to carriers generated in the base. Boundary conditions are

$$N'(X_E) = 0 \qquad \text{(assuming } \gamma_E = 1.0\text{)}$$

$$N\ (X_E + W) = 0$$

where X_E is emitter junction depth and W is base width. Emitter generation current is obtained from the transistor model.

Short-circuit current density is plotted in Figure 4 as a function of base width for several constant values of diffusion length. The solid lines are results from the computer solution; the transistor approximation from Equation 5 is shown by the dotted lines. For small values of W/L the two are essentially coincident. The transistor model deviates for large values of W/L but still gives a useful engineering estimate. Measured values for several cells are shown in Figure 4. These follow predicted trends and are within limits of lifetime measurement.

Dependence of open circuit voltage on cell parameters can be calculated from Equation 3, using values of short-circuit current density obtained from Figure 4.

SUMMARY

A conceptual model has been described which explains operation of the Tandem Junction Cell. Structural optimization follows transistor design principles.

Short-circuit current density has been calculated in terms of the physical parameters of the cell. Estimates from the basic transistor model are quite close to values determined from a computer solution. Measured results follow predicted trends and are within reasonable accuracy of physical constants.

The transistor model can also be used to caluclate open circuit voltage.

Measured values of TJC parameters after exposure to a simulated space environment will be presented in the next session by Bruce Anspaugh.

REFERENCES

1. Chiang, S.Y.; Carbajal, B.G.; and Wakefield, G.F.: Thin Tandem Junction Solar Sell. Thirteenth IEEE Photovoltaic Specialists Conference, Washington D.C., June 1978.

2. Chiang, S.Y.; Matzen, W.T.; Carbajal, B.G.; and Wakefield, G.F.; Concentrator Solar Cell Assembly. 1978 Annual Meeting, American Section of the International Solar Energy Society, Denver, Aug. 1978.

3. Matzen, W.T.; Chiang, S.Y.; and Carbajal, B.G.: A Device Model for the Tandem Junction Solar Cell. IEDM (Late News), Washington, D.C., Dec. 1978.

4. Pritchard, R.L.: Electrical Characteristics of Transistors, P. 88, McGraw-Hill, 1967.

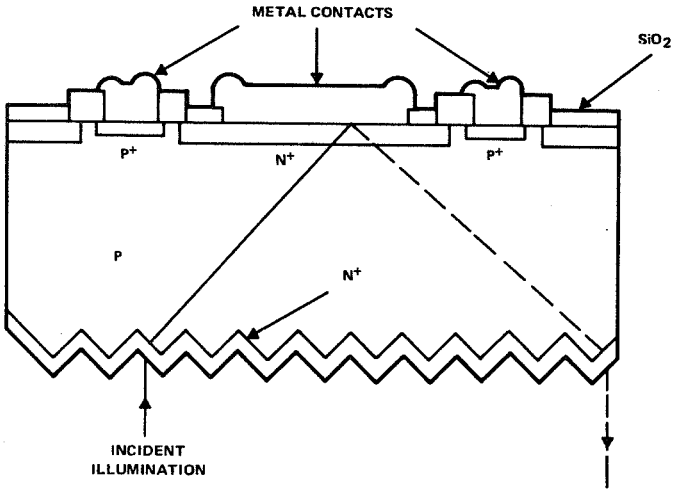

FIGURE 1 SKETCH OF TANDEM JUNCTION SOLAR CELL

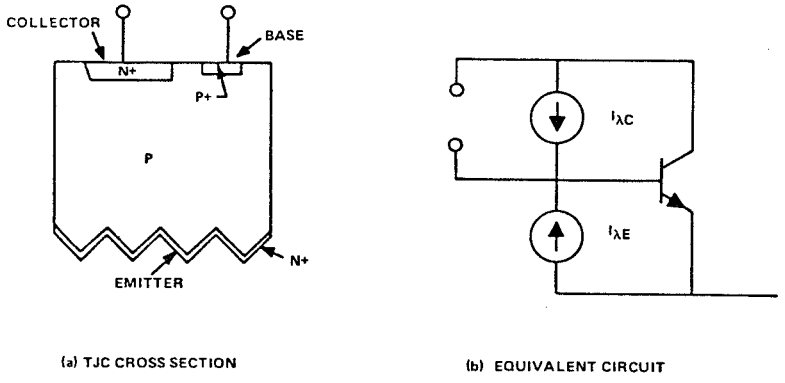

FIGURE 2 REPRESENTATION OF TJC AS TRANSISTOR STRUCTURE

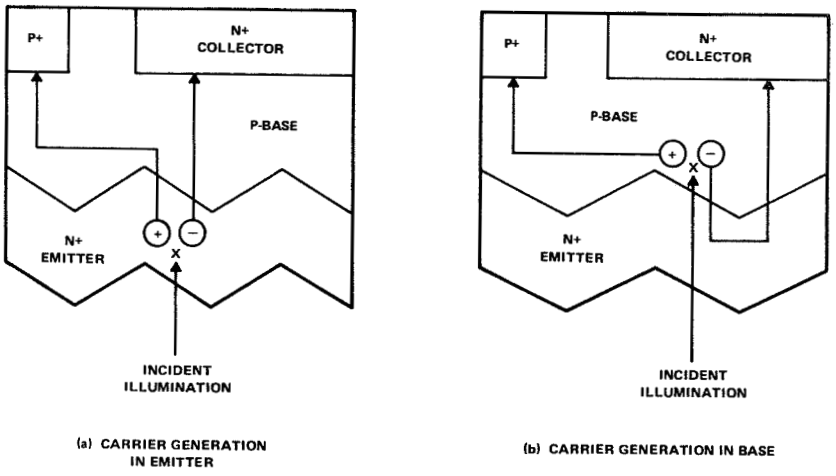

FIGURE 3 SCHEMATIC REPRESENTATION OF CARRIER FLOW IN TANDEM JUNCTION CELL

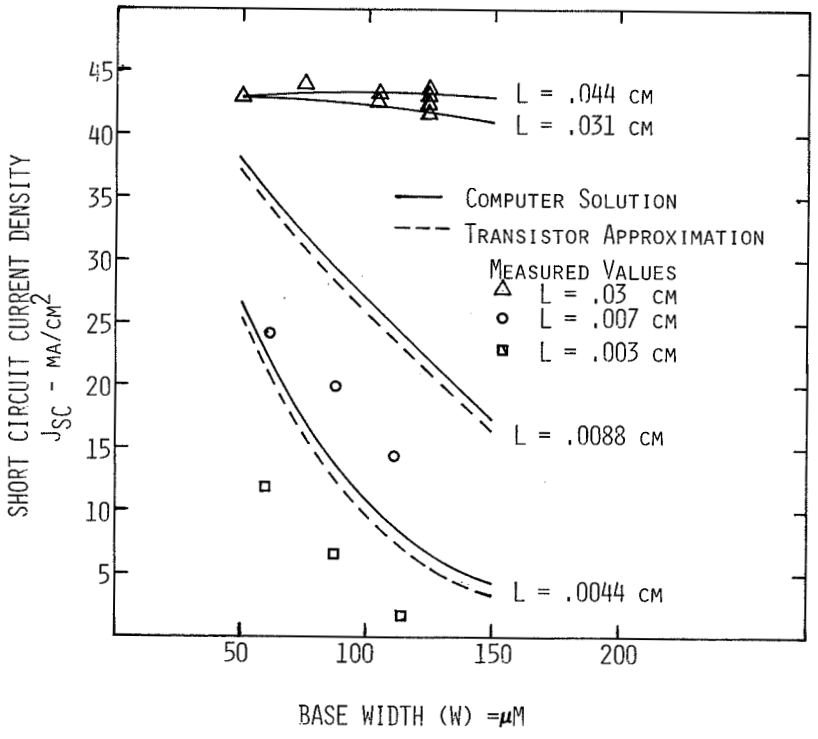

FIGURE 4

SHORT CIRCUIT CURRENT DENSITY (AMO) FOR THE TANDEM JUNCTION CELL AS A FUNCTION OF BASE WIDTH FOR CONSTANT VALUES OF MINORITY CARRIER DIFFUSION LENGTH, L.

THIN CELLS FOR SPACE*

G. Storti, J. Wohlgemuth, and C. Wrigley
Solarex, Inc.

ABSTRACT

Research and pilot line production efforts directed towards the fabrication of high efficiency ultrathin silicon solar cells (50 um) are reported. The research efforts have resulted in conventional ultrathin cells with AMO efficiencies exceeding 14% and coplanar back contact cells with AMO efficiencies up to 11.7%. The primary mechanisms limiting efficiency have been determined in both types of cells, and they are discussed within the context of further improving efficiency. Results of pilot line production of conventional ultrathin cells are also presented. Average AMO efficiencies of 12% have been readily achieved for 2000-cell production runs.

INTRODUCTION

A significant advance in silicon solar cell technology for space applications has been the fabrication of high efficiency ultrathin (50 μm) cells that are nearly independent of base resistivity (Ref.1,2). This includes the conventional ultrathin cell which incorporates a high-low p^+ - p junction at the rear of the cell and the coplanar back contact cell which has high-low p^+ - p junctions both on the front and on certain regions at the back of the cell. As a consequence of the new technology, the power to mass ratio has increased dramatically over that of conventional, 200 μm thick space cells. In addition, conventional ultrathin cells have been found to be particularly resistant to radiation damage because the distance that the minority carrier must travel to the collecting junction is relatively short.

No less important have been the breakthroughs in manufacturing technology that have resulted in highly producible conventional ultrathin cells (Ref. 3). Solarex has fabricated several thousand of this type of cell.

* Work performed for Jet Propulsion Laboratories, Contract 954883 and NASA Lewis Research Center, Contract NAS3-21250.

In this paper, we present results of research efforts on both the conventional and coplanar back contact cells and of the pilot line production efforts on the conventional cells. Also, we discuss the principal loss mechanisms affecting cell efficiency in both types of cells.

RESEARCH EFFORTS

a. Conventional Ultrathin Cells - The basic processing sequence is seen in Figure 1. Silicon wafers are thinned down and textured using NaOH and KOH-isopropanol etches, respectively. The slices are then diffused at 860°C using PH_3 as the diffusant source. Aluminum paste is then silk screened on one side, cured at 90°C for one-half hour and fired at 850°C for approximately thirty seconds. After cleaning up the alloy residue, standard Ti-Pd-Ag contacts and a Ta_2O_5 AR coating are deposited on the cells. Using this process technique, cells having AMO efficiencies greater than 13% at AMO are consistently obtained. Figure 2 shows the I-V characteristics of the best of these cells (η = 14.1% at 25°C). For comparison purposes, the I-V curve of a non-textured thin cell which had evaporated aluminum as a source for back surface field formation is shown. As can be seen in the figure, texturing in a junction with an effective back surface field produces a significant increase in current because of a reduction in reflection and the generation of minority carriers closer to the junction.

This is further seen in Figure 3, where the spectral response of the two cells is shown. The major difference in the two curves is the reflection, although at long wavelengths ($\lambda > .85$ μm) there is additional current collection because of the refraction of the entrant light.

Textured cells having open circuit voltages greater than 600 mV have been fabricated when Al pastes have been the source for back surface field formation. This is considerably better than the open circuit voltages obtained when evaporated Al is used as the source. At present, the material processes responsible for the difference are not known.

b. Coplanar Back Contact Cell - In another program, Solarex has been fabricating coplanar back contact cells - that is, cells in which the contacts to both the n^+ and p^+ regions are located on the back of the cells. The motivation for the development of this type of cell is the high cost associated with solar cell assembly.

The process sequence for this cell is seen in Figure 4. After thinning with a NaOH etch, a boron doped silicon dioxide layer is deposited on the front of the slice and an un-doped oxide layer on the back. In a series of photolithography steps, portions of the back oxide are removed for phosphorus diffusion and high-low p^+ - p junction formation with evaporated Al as the source. The resultant n^+ and p^+ regions are then metallized with Ti-Pd-Ag to provide contacts to the cell. The front oxide is then removed and a Ta_2O_5 anti-reflection coating applied.

Figure 5 shows the basic pattern of the n^+, -p, and p^+ regions at the back of the cells. With a step and repeat of 20 mils, the n^+ region is 16 mils wide and the p^+ region 2 mils wide. The two regions are separated by p-regions that are 1-mil in width.

The best cell that has been produced after five months of fabrication effort is seen in Figure 6. The AMO efficiency of this planar cell is 11.7% at 25°C. Resistivity of the base silicon is approximately 5Ω-cm. Current densities are presently limited by less than optimum optical coupling and by low minority carrier diffusion length. A spot scan has shown minima in the current output over the p^+ regions.

The diffusion length in the silicon is a critical parameter for high efficiency coplanar back contact cells. Table I shows the influence of diffusion length on the current density for a 16-1-2-1 mask configuration and for three cell thicknesses. Reflection is assumed to be zero, and the recombination velocities at the p and p^+ surfaces are indicated. Not surprisingly, when the diffusion length decreases to the same order as the cell thickness or the distance between the center of p^+ region and the edge of the n^+ region, the current density is strongly affected.

PILOT LINE FABRICATION EFFORTS

In conjunction with research efforts on conventional ultra-thin cells, Solarex has been producing non-textured 50 μm thick cells in a pilot line effort. Several thousand cells have been fabricated. The results of the most recent production runs as seen in Figure 7, representing a total of five thousand cells. The significant increase in output power that occurred during the second quarter was due to controlling cell flexure during high temperature processing. The high power levels seen in some cells during the fourth quarter was to a large extent due to effective back surface fields formed from evaporated aluminum.

In the coming year, pilot line production of textured cells using Al pastes for back surface field formation is planned. A substantial increase in average cell efficiency is expected as a consequence.

LOSS MECHANISMS

The current density and fill factor of the conventional ultrathin cells have been maximized. The open circuit voltage remains at considerably less than theoretically expected values because the emitter recombination current is high. Increased open circuit voltages can be expected with the incorporation of a high-low emitter as has recently been done by Neugroschel, et al. (Ref. 4).

For the coplanar back contact cell with front surface field, better optical coupling and larger minority carrier diffusion lengths are needed to maximize the current density. Fill factors are at satisfactory levels. Open circuit voltages are low for the same reason as with the conventional thin cells. High-low emitter regions should considerably improve the open circuit voltage.

SUMMARY AND CONCLUSIONS

Ultrathin high-efficiency conventional and coplanar back contact cells have been fabricated. Conventional cell efficiencies have exceeded 14%, and coplanar back contact cell efficiencies have reached 11.7%. Non-textured, conventional ultrathin cells have been produced in pilot line quantities. Average efficiencies of these cells have reached 11.6%.

Major increases in efficiency must come by increasing the open circuit voltage of both types of cells. Further work in optimizing optical coupling and maintaining high minority carrier diffusion length is required for high short circuit current densities in coplanar back contact cells.

Thin cells offer substantial advantages with respect to high power to mass ratios. Also, the great flexibility of the cells allows for compact launch configurations of lightweight arrays.

REFERENCES

1. C. F. Gay, "Thin Silicon Solar Cell Performance Characteristics," Proc. 13th IEEE Photovoltaic Specialists Conference, Washington, D.C., 1978.

2. J. Lindmayer, C. Wrigley, and G. Storti, "Development of an Improved High Efficiecy Thin Silicon Solar Cell," JPL Contract No. 954883, Fifth Quarterly Report, January 1979.

3. J. Lindmayer, C. Wrigley, and G. Storti, "Development of a High Efficiency Thin Silicon Solar Cell, JPL Contract No. 954883, Pilot Line Report, November 1978.

4. A.Neugroschel, F. A. Lindholm, S. C. Pao and J. G. Fossum, Appl. Phys. Lett., Vol 33, p. 168, 1978.

TABLE 1. EFFECT OF DIFFUSION LENGTH ON THE SHORT CIRCUIT CURRENT DENSITY OF COPLANAR BACK CONTACT CELLS OF DIFFERENT THICKNESSES

	J_{sc} (mA/cm^2)		
Ln (μm)	t = 50 μm	75 μm	125 μm
1000	42.	43	43
500	42.	43	42
300	42	42	40
200	41	40	35½
150	39½	37½	31
100	36½	32	22
50	25½	17	7

MASK CONFIGURATION: 16 mil - n^+; 1 mil - p; 2 mil - p^+
1 mil - p

ASSUMPTIONS:

1. PLANAR FRONT SURFACE
2. NO REFLECTION
3. $V_s(p)$ = 1000 cm/s
4. $V_s(p^+)$ = 100 cm/S

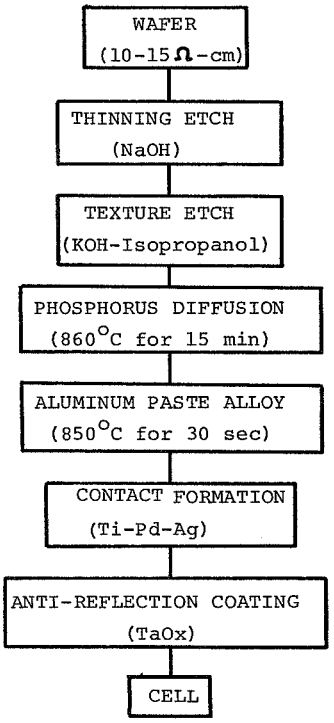

FIGURE 1: PROCESS SEQUENCE FOR CONVENTIONAL, TEXTURED ULTRATHIN CELL

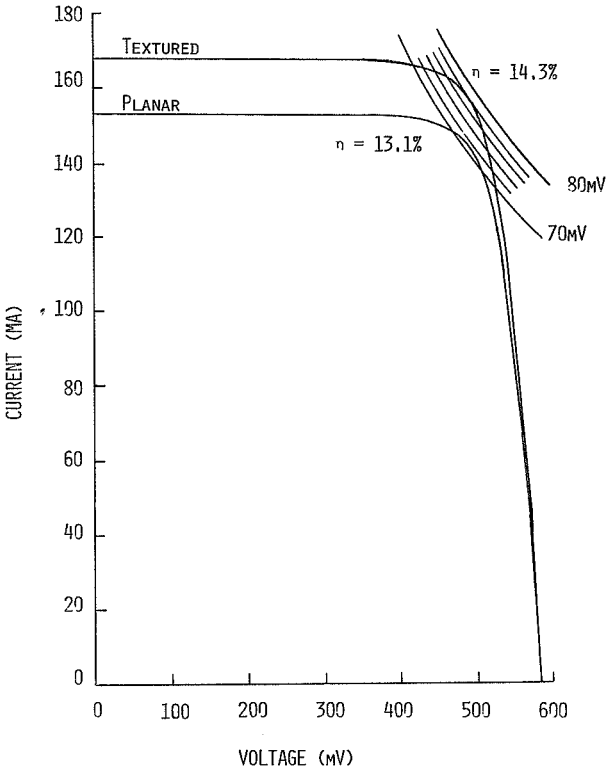

FIGURE 2: I-V CHARACTERISTICS OF PLANAR AND TEXTURED 50μM THICK SILICON CELLS. CELL AREA IS $4CM^2$.

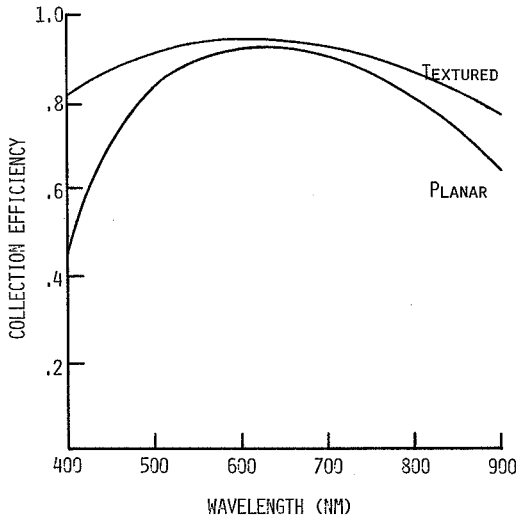

FIGURE 3: SPECTRAL RESPONSE OF PLANAR AND TEXTURED 50μM THICK SILICON CELLS.

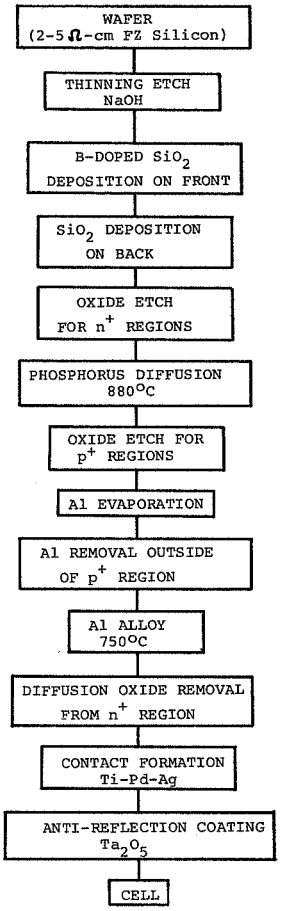

FIGURE 4: PROCESS SEQUENCE FOR THE COPLANAR BACK CONTACT CELL

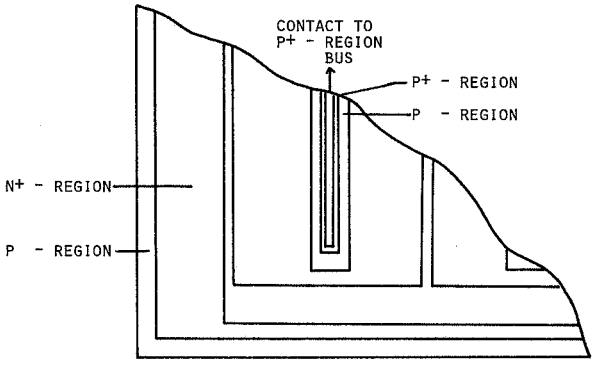

N+ - REGION WIDTH: 16 MILS (406μM)
P+ - REGION WIDTH: 2 MILS (51μM)
P - REGION WIDTH: 1 MIL (25μM)

FIGURE 5: DIFFUSED REGION AND CONTACT CONFIGURATION OF COPLANAR BACK CONTACT CELL.

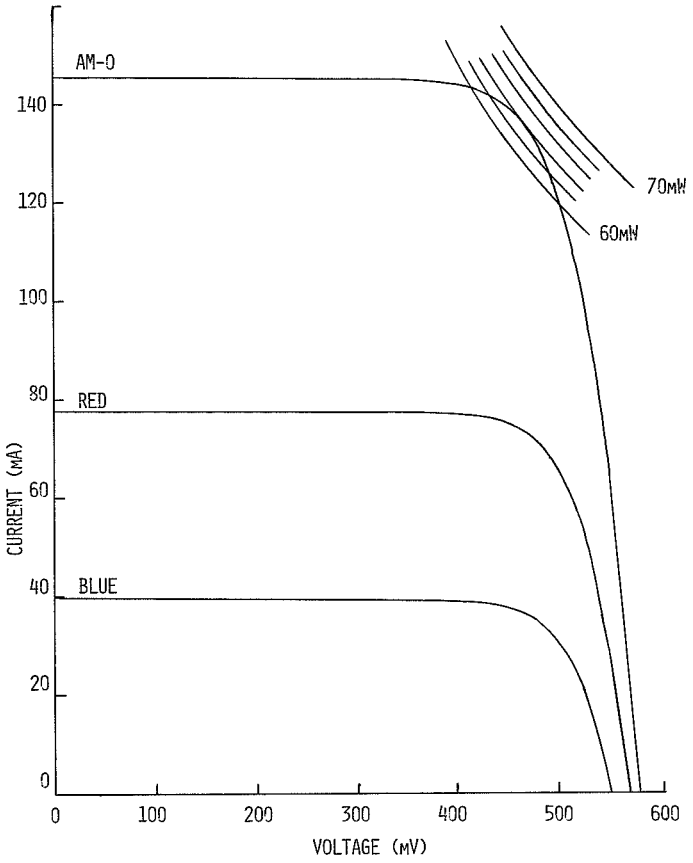

FIGURE 6: I-V Characteristics at 25°C of the Best 50µm Thick Coplanar Back Contact Cell.

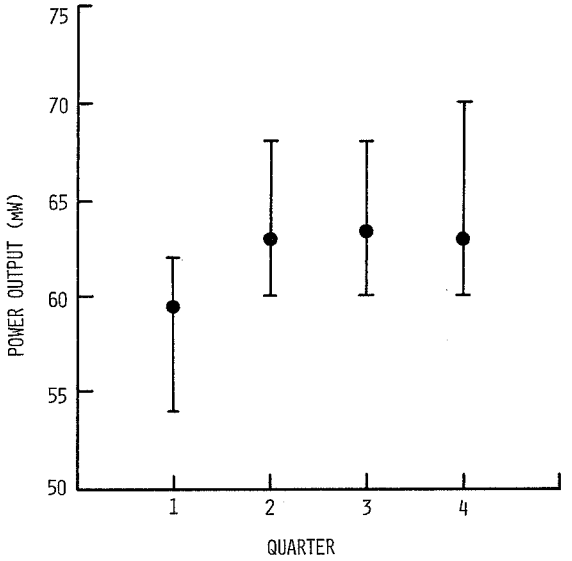

FIGURE 7: AM0 Power Output at 25°C as a Function of Quarterly Pilot Line Production Efforts for Planar, 50µm Thick Silicon Cells. Cells Area is 4cm^2

HIGH EFFICIENCY CELL GEOMETRY

R.N. Hall
General Electric Company

SUMMARY

A new silicon solar cell is described which has an array of small-area conduction paths to transport current directly through the wafer to metal electrodes on the back. This design eliminates grid shadowing and many of the other losses inherent in conventional cells. Early experimental units without texturing or antireflection coatings have shown 13.3% efficiency under AM1 insolation.

INTRODUCTION

The front surface grid of a conventional solar cell causes losses in efficiency due to shadowing and series resistance along the grid lines. Furthermore, it requires high-resolution patterning and yields a non-planar front surface. These problems are eliminated in the "Polka Dot Cell" described below in which the current collected at the front junction is carried through the cell via an array of small-area interconnects to a junction of the same type which covers most of the rear surface.

DESCRIPTION

The geometry of this cell is shown in figure 1, which illustrates the N^+P configuration. The cells are made by patterning the backs of <100> silicon wafers and anisotropically etching to produce pyramidal indentations which barely penetrate through the front surface. The wafer is diffused to produce a thin N^+ junction on the front surface and a deeper one over the back except for areas which are masked and ion implanted P^+ to make contact with the substrate. The cell is completed by depositing metallization over the entire back of the cell and patterning it to separate the N^+ and P^+ contact areas. The front can be textured and AR coated to reduce reflection losses.

The power delivered by the cell, expressed as $P = I_{sc}V_{oc}f$, is expected to be increased relative to that of a conventional cell through improvements in each of these cell coefficients. The short-circuit current I_{sc} will be increased by elimination of grid shadowing. A larger open-circuit voltage V_{oc} due to improved emitter efficiency is expected through elimination of the $S = \infty$ boundary condition that would exist under a metallized grid area. The

absence of junction degradation caused by impurities coming from the grid metallization should further increase both of these parameters. The rear junction is made deep enough to avoid such degradation.

The fill factor f is mainly determined by the product R_sA, where R_s is the series resistance of the cell and A is its area. R_s has two principal components, one caused by spreading resistance in the front N^+ region around the interconnect openings, and the other associated with lateral current flow in the substrate.

SERIES RESISTANCE ANALYSIS

The spreading resistance can be evaluated by imagining the cell to be divided into squares of side "a" surrounding each interconnect opening, as illustrated in figure 2. These openings are squares of side "b". We will approximate the performance of this subcell by that of a circular cell of the same area, so its inner and outer radii are $b/\sqrt{\pi}$ and $a/\sqrt{\pi}$ respectively. We assume that photocurrent density J is generated uniformly over the surface of the subcell and flows radially inward to the interconnect opening through the N^+ layer which has a sheet resistance $\rho_\square$. R_s will be evaluated by expressing the power lost in the N^+ region in the form, $P = I^2R_s$. The power dissipated in each circular zone of length dr is caused by photocurrent collected in the annular area outside r, so the total power lost in each subcell is given by

$$P = \int \left[\pi J \left(\frac{a^2}{\pi} - r^2\right)\right]^2 \frac{\rho_\square dr}{2\pi r}$$

$$= \frac{\rho_\square J^2 a^4}{2\pi} \left[\ln \frac{a}{b} - \frac{3}{4} + \frac{b^2}{a^2} - \frac{b^4}{4a^4}\right]$$

from which R_s can be evaluated. Multiplying by a^2 to get the R_sA product, we find

$$R_sA \approx (\rho_\square a^2/2\pi)[\ln(a/b) - 3/4]$$

To indicate the magnitude to be expected for this resistance loss, we take a 0.6 mm (appropriate for a 200 μ thick cell), a/b = 20, and $\rho_\square$ = 200 ohm/square, which gives R_sA = 0.26 ohm-cm^2. This loss would reduce the output of a silicon cell by less than 2%.

The loss due to current flow in the substrate can be calculated similarly. For a wafer of thickness t and resistivity ρ having an array of parallel line contacts a distance d apart, we find

$$R_sA = \rho d^2/12t$$

Substrate contacts could conveniently be placed between every other interconnect row, giving d = 2a. However, for initial experiments we have chosen to omit every 8th row and place the contacts there, corresponding to d = 8a. For a wafer resistivity of 0.25 ohm-cm this gives R_sA = 0.24 ohm-cm^2.

The combined effect of these two R_s components would be to reduce the fill factor from its ideal value of 0.83 to 0.80, assuming V_{oc} = 0.6 volts and J_{sc} = 40 mA/cm^2.

EXPERIMENTAL RESULTS

Early experimental cells have been made by T.J. Soltys of this laboratory in both the N^+P and P^+N configurations. Cells made without texturing or antireflection coatings have shown J_{sc} = 29.3 mA/cm^2, V_{oc} = 0.588 volts, and f = 0.77 under 100 mW/cm^2 of AM1 illumination, corresponding to a conversion efficiency of 13.3%.

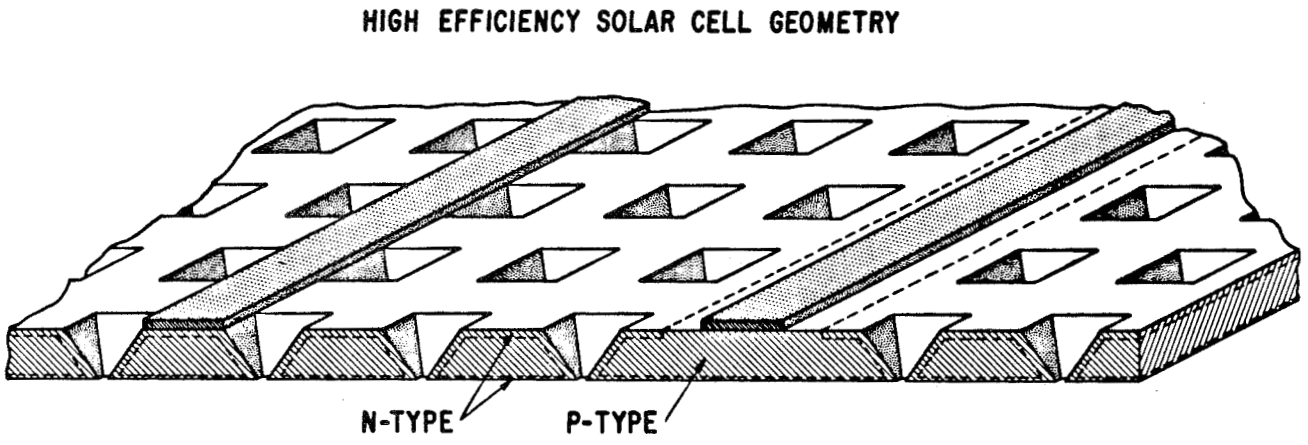

Figure 1. Cross-section of the Polka Dot solar cell, shown upside down. The N^+ metallization actually covers most of the back surface of the cell.

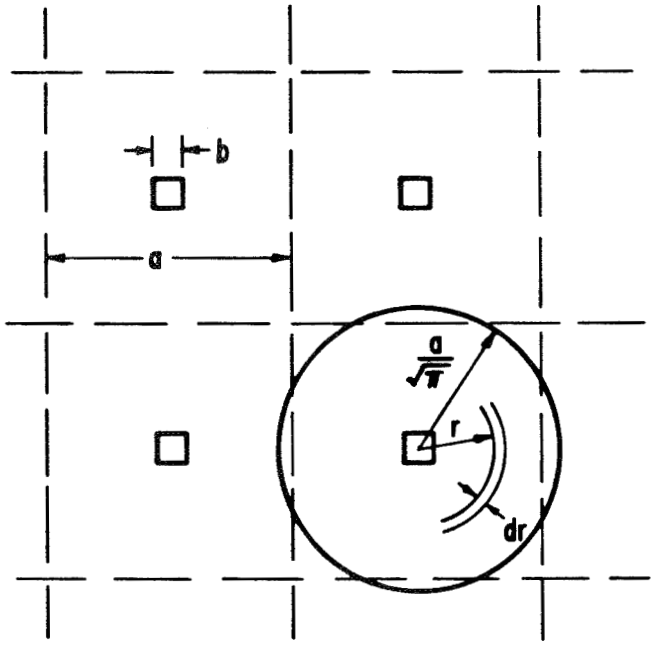

Figure 2. Subcell used for calculating series resistance.

SILICON SOLAR CELLS FOR SPACE USE: PRESENT PERFORMANCE AND TRENDS

P.A. Iles, F.F. Ho and S. Khemthong
Photoelectronics Corporation of America

FABRICATION METHODS

Much of modern silicon device technology has been applied to make current space cells. This technology includes the use of large single crystals (up to 10 Kg), sliced by advanced ID saws, mechanized polishing methods and cleaning, and diffusion in microprocessor-controlled furnaces. Contacts and coatings are deposited in large evaporators using electron beam-heated sources, and with semi-automatic control of layer properties. Cells are processed through most of this sequence in large slice ($\sim$3") form. The combination of these processes has been shown to retain proven levels of space worthiness and quality control.

BASIC PRODUCTION CELL DESIGN

The surface finish is either polished or textured. The back surface may be of high reflectance (BSR) or include an electric field (BSF). Slice thicknesses are generally 8-12 mils, and resistivities 2-10 ohm-cm are used mostly. The grid pattern designs are determined with aid of computer programs and using photolithographic (or shadow masking) methods, well controlled patterns of narrow, close-spaced lines of high conductance are obtained.

PRESENT PERFORMANCE

AMO Output (Pm)

Values above 21.5 mW/cm^2 ($\sim$16%) have been achieved. For production runs, cells in the range 19-20 mW/cm^2 are specified with increased frequency, although cells in the range 15-17 mW/cm^2 are still required. These output values are those measured at controlled temperatures (25-28°C). Recently, more attention has been paid to the orbital output, determined largely by the value of solar absorptance for the cell.

Solar Absorptance (α_S)

The highest output cells (textured surface) have retained high α_S values (>0.87 even with BSR). Recently significant decrease in α_S (down to 0.72) have been achieved for production non-textured cells with high output, obtained by an effective BSF, and the output of such cells can exceed 95% of that of textured cells. Specially designed cells have had α_S values down to

0.66. The same α_S control has been extended to thin cells ($\sim$2 mils), and in fact the optimum combination of Pm and α_S has been achieved for such cells. Figure 1 shows the Pm (measured at 25°C) versus achieved values of α_S for various production cells. Typical Pm and α_S ranges are indicated. The circles indicate the orbital power output for the Pm and α_S values at the centroid of the dashed rectangle.

Radiation Resistance

The radiation resistance is controlled by the bulk resistivity, and to a lesser extent by the cell design. The resistivity used is between 2 and 10 ohm-cm, where the best combination of BOL and EOL performance is realized. A major influence on radiation resistance is the cell thickness, and dramatic increases in radiation resistance have resulted from use of silicon slices thinner than 4 mils.

Thin Cell Development

The cell processes which give high output have been successfully applied to thin slices. Mechanical yields have improved significantly, and the electrical output has increased to within 95% of that of similarly processed thicker cells, with considerable increase (16-23%) in radiation reistance; in fact the highest power output after fluences $\sim 10^{15}$ 1 Mev electrons/cm^2 is obtained for 2 mil-thick cells. Also the power-to-weight ratios have increased from 0.35 W/g to 1.7 W/g (for cells with contacts).

PRESENT DEVELOPMENT TRENDS

The thin cell advances have led to several associated trends, including the development of suitable array-formation methods, and increased study of reverse-illuminated structures (interdigitated contacts, tandem junction cells).

Efficient cells for use with concentrators (up to 16% at 40 AMO suns) have been made, and are ready for space-use if required. These cells combine much of current space cell technology with modifications (such as computer aided grid design) required for operation at higher insolation levels. Cells with enhanced IR output are also available for combination in high performance tandem cell concentrator systems.

Several contact variations are available, including some with improved high temperature performance (for use in laser-hardening, ES bonding or possible annealing of radiation damage), or with both contacts on the back surface (wraparound or reverse illuminated). Also present cell technology can be adjusted to allow good bonding by soldering or by several different welding techniques.

The increased voltage available from highly doped silicon is being evaluated to check the overall effect on output, and the extent of the increased sensitivity to radiation damage. Technology is also available to compare VMJ cells directly with 50 μm cells.

INCREASED CAPACITY, LOWER COST ARRAYS

Although much of the present low cost terrestrial cell technology is not yet ready for space-use, the present production capacity using the methods listed above can accommodate cell production schedules for multi-100 KW missions. There is associated promise of space cell costs below $30/watt (for slight relaxation in non-technical specifications but no reduction in performance) even before additional automation is introduced.

Thus, in summary, silicon solar cell technology has continued to develop, and provides a sound base for present and projected future space missions.

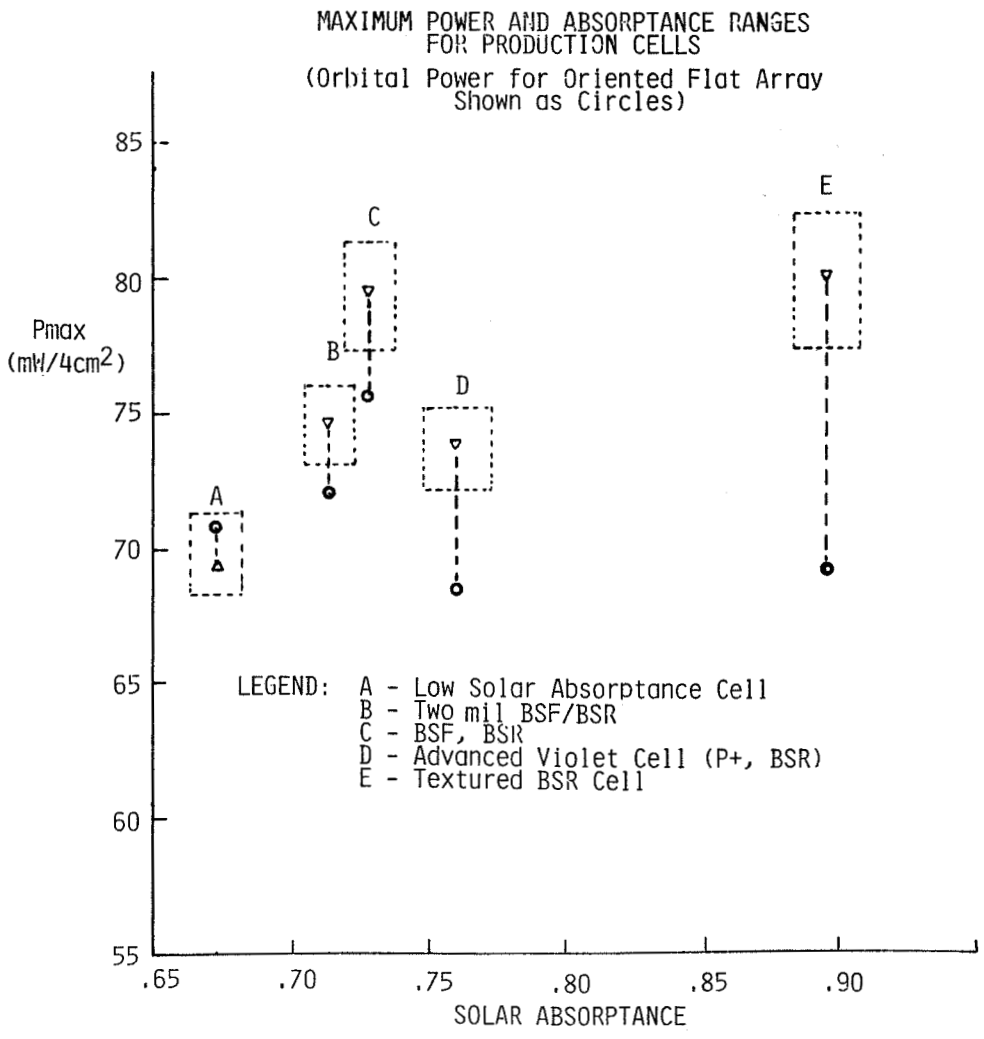
MAXIMUM POWER AND ABSORPTANCE RANGES
FOR PRODUCTION CELLS
(Orbital Power for Oriented Flat Array
Shown as Circles)
Pmax
(mW/4cm2)
85
80
75
70
65
60
55
A
B
C
D
E
LEGEND: A - Low Solar Absorptance Cell
B - Two mil BSF/BSR
C - BSF, BSR
D - Advanced Violet Cell (P+, BSR)
E - Textured BSR Cell
.65
.70
.75
.80
.85
.90
SOLAR ABSORPTANCE

Figure 1

LASER TECHNIQUES IN PHOTOVOLTAIC RESEARCH*

R. T. Young, R. F. Wood, R. D. Westbrook, J. Narayan, and C. W. White
Solid State Division, Oak Ridge National Laboratory

SUMMARY

High-power laser pulses are being used to replace the conventional high temperature furnace processing for the p-n junction formation step in high-speed, low-cost solar cell fabrication. Three different approaches to junction formation have been used: (1) laser annealing of ion-implanted Si in which laser radiation is used to remove the radiation damage and to recover the electrical activity in the implanted layer; (2) a process in which a thin film of dopant is first deposited on the substrate and then incorporated into the near-surface region by laser-induced diffusion; and (3) a process in which a heavily doped amorphous silicon layer is deposited on the Si substrate and epitaxially regrown from the melted substrate layer by laser radiation. We have demonstrated that all three methods provide suitable candidates for high efficiency Si solar cells.

INTRODUCTION

Approximately two years ago at the photovoltaic conference in Luxembourg, we described the use of high-power laser pulses to anneal the lattice damage in ion-implanted Si solar cells (ref. 1). We demonstrated that pulsed laser annealing is superior to conventional thermal annealing for the removal of lattice damage, for the recovery of electrical activity, and for the preservation of the minority carrier lifetime in the substrate, and we showed that this superiority resulted in improved solar cell performance. Pulsed laser annealing is now understood (ref. 2) to take place by a mechanism involving the ultrarapid melting of the entire damaged layer and subsequent liquid-phase epitaxial regrowth from the underlying perfect substrate. The dopant profiles are usually broadened considerably by pulsed laser annealing and this can be readily explained quantitatively by dopant diffusion in the molten state. An understanding of the importance of near-surface melting by laser heating led to the development (refs. 3-6) of two other laser-assisted junction formation techniques, i.e., laser-induced diffusion of dopant films and laser-induced recrystallization of doped amorphous films to form epitaxial junctions. These techniques are important because they are much simpler and more easily automated processes than either thermal diffusion or ion implantation. This is

*Research sponsored by the Division of Materials Sciences, U. S. Department of Energy under contract W-7405-eng-26 with the Union Carbide Corporation.

particularly advantageous for solar cells which require high-volume, low-cost fabrication processes to become economically competitive in terrestial applications. In this paper we review and compare the three laser-assisted junction formation techniques and discuss their applications to solar cell fabrication. Throughout this work, the laser annealing was performed in air with the Q-switched output of a ruby laser (λ = 0.694 μ, τ = 15-60 nsec). After the samples were exposed to the laser pulses, the perfection of the emitter regions was studied by transmission electron microscopy (TEM), and their electrical parameters were determined by van der Pauw measurements. The dopant profiles were obtained by secondary ion mass spectrometry (SIMS) or anodic oxidation and stripping technique. The resulting junction characteristics were studied by I-V and C-V measurements on mesa diode structures. Finally solar cells were fabricated and tested under AM1 illumination.

JUNCTION FORMATION BY ION IMPLANTATION AND LASER ANNEALING

In this method, energetic dopant ions are allowed to impinge on a Si substrate and laser radiation is used to remove the radiation damage and to bring the dopant ions into electrically active substitutional sites. The resulting dopant profile and junction depth are determined by the as-implanted profile, which is controlled by the stopping power for the dopant particles in silicon and the implantation energy, and by the duration of the laser-induced surface melting which is controlled by the laser parameters such as energy density and pulse duration time. The influence of the laser energy density on the dopant profile behavior is given in figure 1 which shows results for samples implanted with ^{11}B (35 keV, 1 x 10^{16} cm^{-2}) and subsequently annealed with laser pulses in the energy density range of 0.64 J/cm^2 to 3.1 J/cm^2. At a laser energy density $\sim$.6 J/cm^2, the boron profile is indistinguishable from that of the as-implanted specimen. Evidence that the annealing was incomplete in this sample was obtained from van der Pauw measurements and from TEM which showed that only $\sim$ 30% of the expected electrical activity had been obtained, and that significant damage in the form of dislocation loops remained. Complete annealing was achieved with energy densities of 1.1 J/cm^2 and greater; the profiles were then almost flat topped in the surface region with the penetration depth increasing as the energy density was increased. Figure 2 gives the comparison of dopant profiles obtained from samples implanted with boron at 5 keV and 35 keV and annealed with laser pulses of 1.7 J/cm^2. These results indicate that in order to obtain a defect-free shallow junction by the ion-implantation, laser-annealing technique, the implantation energy should be kept low and the laser energy just high enough to melt the surface layer which contains the damaged region. Solar cells with conversion efficiencies of 14-15% can be routinely fabricated by this technique. Parameters of a typical cell made from Si implanted with $^{75}As^+$ (5 keV, 2 x 10^{15} cm^{-2}) and annealed with one pulse of a ruby laser are I_{SC} = 33.6 ma/cm^2, V_{OC} = 565 mV and FF = 0.76 and a resulting conversion efficiency of 14.5%. The cells were fabricated with single-layer Ta_2O_5 antireflection coatings and no back surface fields.

JUNCTION FORMATION BY LASER-INDUCED DIFFUSION

In this technique, thin (50-100 Å) films of dopants such as boron and aluminum are first vacuum-deposited on the substrate and then driven into the near-surface region by laser-induced surface melting and diffusion. Transmission electron microscopy and electrical measurements show that the dopants are dissolved in the silicon lattice and electrically activated. Resultant emitter regions with appropriate sheet resistivities (30-100 Ω/□) for solar cell applications can be obtained and the dopant profiles are nearly ideal for high efficiency cells. Figure 3 gives the boron concentration profile after laser irradiation with pulses of 1.5 J/cm^2. This profile has a high dopant concentration near the surface region and an intermediate region decreasing toward the junction. The high potential barrier near the surface will reflect the minority carriers from the surface and minimize surface recombination losses. The results of I-V and reversed-biased C-V measurements on Al-deposited, laser-annealed mesa diodes are given in figure 4. The near unit value of A, the small reverse-bias current and the good agreement between the measured and expected junction potentials suggest that a defect-free junction was obtained. Solar cells were fabricated and tested and the efficiencies were found to be comparable to or slightly lower than those of the ion-implanted laser-annealed cells. The effects on cell performance of impurities in the dopant source and of surface contamination during deposition are not clear at the present time.

FORMATION OF EPITAXIAL p-n JUNCTION BY PULSED-LASER RADIATION

In a more recent study, we have demonstrated that laser radiation can be used for epitaxial regrowth of a doped amorphous silicon layer deposited on a silicon substrate. A single pulse from a ruby laser with an energy density of 1.8 J/cm^2 was sufficient to recrystallize, with almost perfect crystallinity, an As-doped amorphous silicon layer deposited on a (100) substrate to a depth of about 3000 Å. Junction characteristics determined by I-V and C-V measurements showed that a perfect junction with a low leakage current was achieved. Use of this technique for junction formation provides many advantages normally attributed to ion implantation, such as relatively easy control of dopant concentration and junction depth. Figure 5 shows dopant profiles measured by Hall effect measurements in combination with anodic oxidation and stripping techniques for the cases of 1000 Å and 2000 Å deposited layers annealed with pulses of 1.55 J/cm^2 and 1.78 J/cm^2, respectively. The dopants have spread deeper into the substrate in a manner very similar to dopant redistribution in As-implanted laser-annealed samples (ref. 2). The solid line in the figures are calculated profiles using techniques described in reference 2. The liquid phase diffusion of As was calculated from ideal as-deposited profiles (dotted lines) without considering the possible complications due to thin interfacial oxygen layers between the substrate and deposited layers. The agreement between the experimental and calculated profiles is very good. From these results, it appears that junction parameters can easily be controlled with this method by a variation of the dopant concentration in the evaporant source, the thickness of the deposited layer, and

the energy density of the laser radiation. Solar cells have not yet been fabricated with this technique. However, from the results described above, we anticipate that it should provide another alternative method for high efficiency solar cell fabrication. Extensive studies of the effects of substrate orientation on recrystallization, interfacial problems such as the presence of SiO_2 or hydrocarbons, and the influence of the various dopant impurities and residual gas atoms (such as H_2, N_2, and O_2) on the regrowth behavior are currently underway.

CONCLUSIONS

In conclusion, high-quality p-n junctions can be formed by the use of laser pulses to anneal radiation damage, induce diffusion, alloying, and regrowth of films deposited on silicon substrates. Due to the simplicity and low cost of this type of processing, we expect that the methods discussed here, after further development, will be extremely useful in the large-volume fabrication of high-efficiency solar cells.

REFERENCES

1. Young, R. T.; White, C. W.; Clark, G. J.; Narayan, J.; and Christie, W. H.: Laser Annealed Boron Implanted Silicon Solar Cells. Photovoltaic Solar Energy Conference, Proceedings of the International Conference, Luxembourg, September 27-30, 1977, Reidel, Boston, 1978, p. 861.

2. Wang, J. C.; Wood, R. F.; Pronko, P. P.: Theoretical Analysis of Thermal and Mass Transport in Ion Implanted, Laser Annealed Silicon. Appl. Phys. Lett., Vol. 33, 1978, p. 455.

3. Fairfield, J. M. and Schwuttke, G. H.: Silicon Diodes Made by Laser Irradiation. Solid State Electron., Vol. 11, 1968, p. 1175.

4. Harper, F. I. and Cohen, M. I.: Properties of Si Diodes Prepared by Alloying Al Into n-Type Si with Heat Pulses From a Nd:YAG Laser. Solid State Electron., Vol. 13, 1970, p. 1103.

5. Narayan, J.; Young, R. T.; Wood, R. F.; and Christie, W. H.: p-n Junction Formation in Boron-Deposited Silicon by Laser-Induced Diffusion. Appl. Phys. Lett., Vol. 33, 1978, p. 338.

6. Young, R. T.; Narayan, J.; Westbrook, R. D.; and Wood, R. F.: Transmission Electron Microscopy and Electrical Properties Measurements of Laser Doped Silicon and GaAs. Proceedings of Laser-Solid Interactions and Laser Processing Symposium, Boston, Massachusetts, Nov. 28 - Dec. 1, 1978, p. 579.

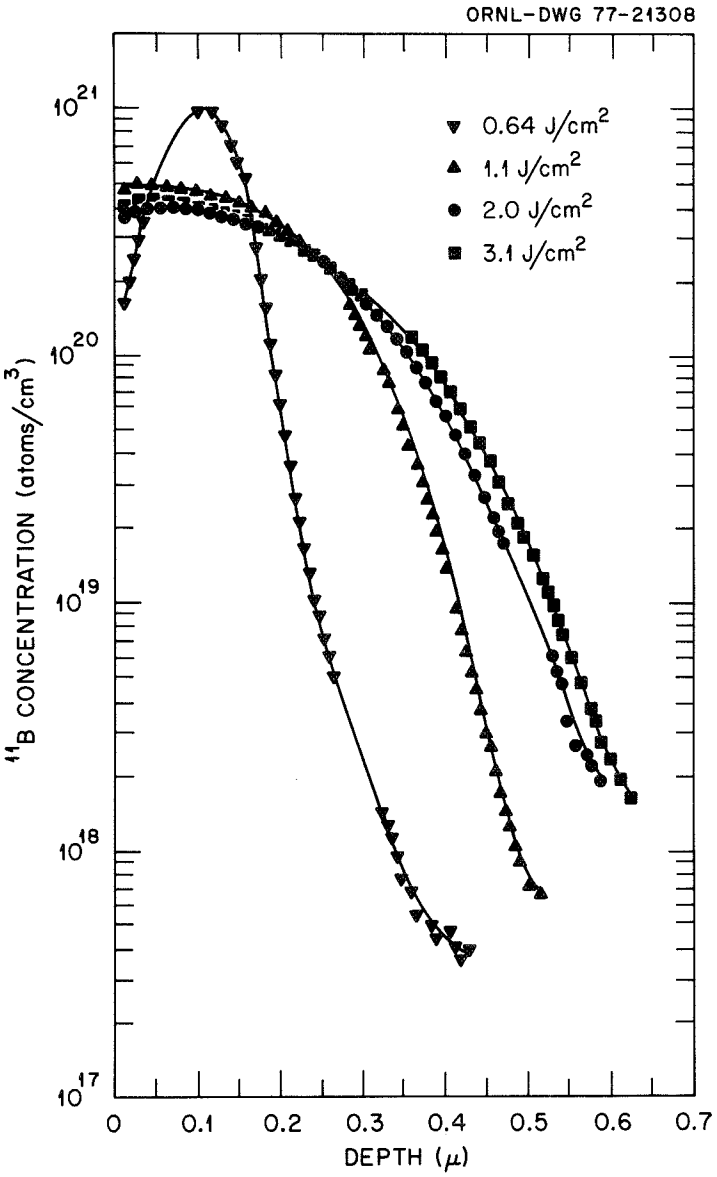

Figure 1. Comparison of ^{11}B (35 keV, 1 x $10^{16}/cm^2$) profiles annealed by different laser energy densities.

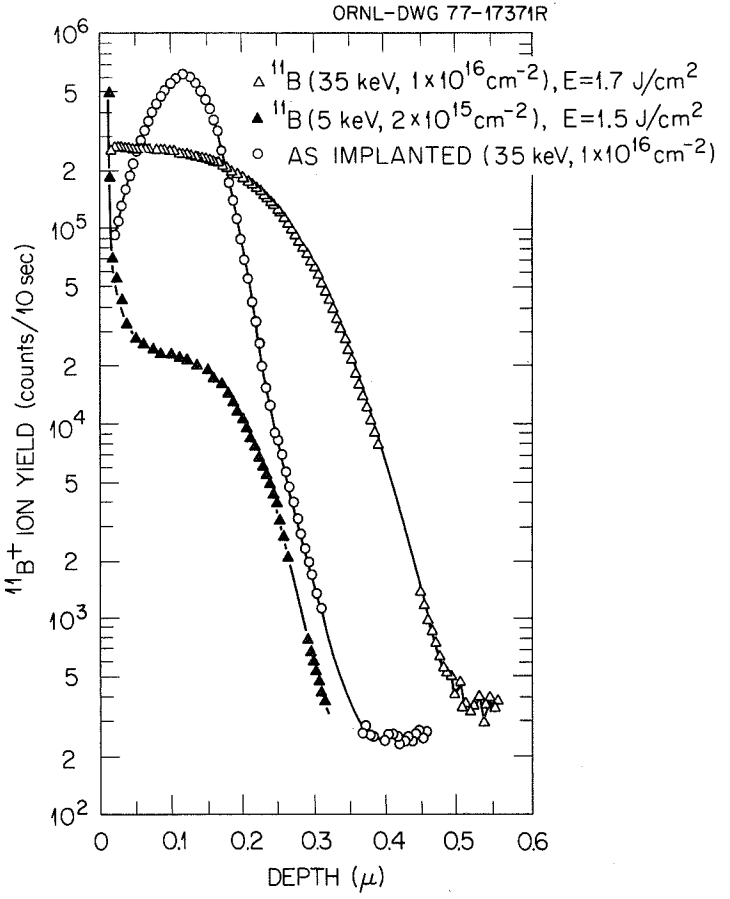

Figure 2. Comparison of ^{11}B (35 keV) and ^{11}B (5 keV) profiles annealed by laser energy density of 1.7 J/cm^2.

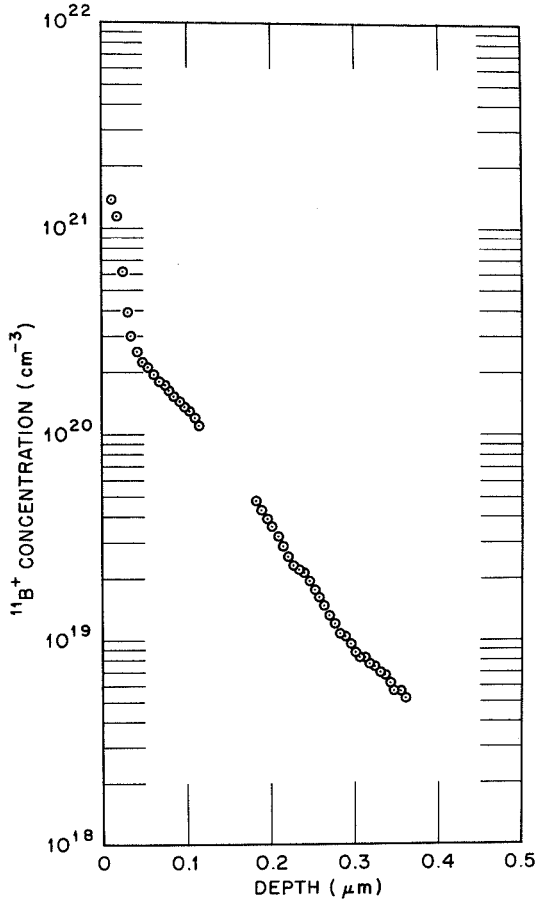

Figure 3. Depth profiles for boron-deposited, laser-annealed Si.

ORNL-DWG 79-11899

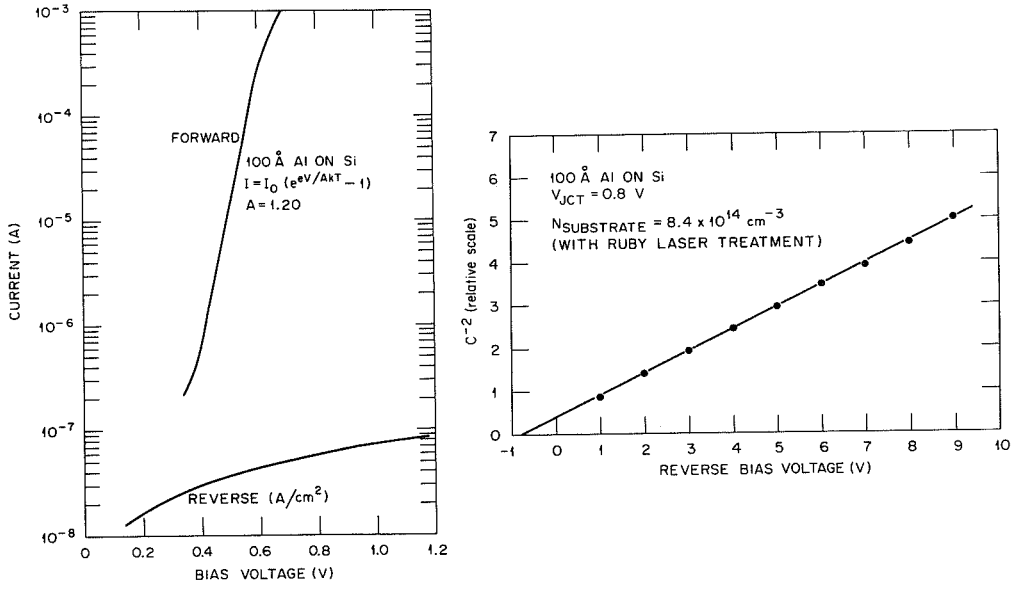

Figure 4. Dark I-V and reverse-biased C-V measurement on Al-deposited laser-annealed Si mesa diodes.

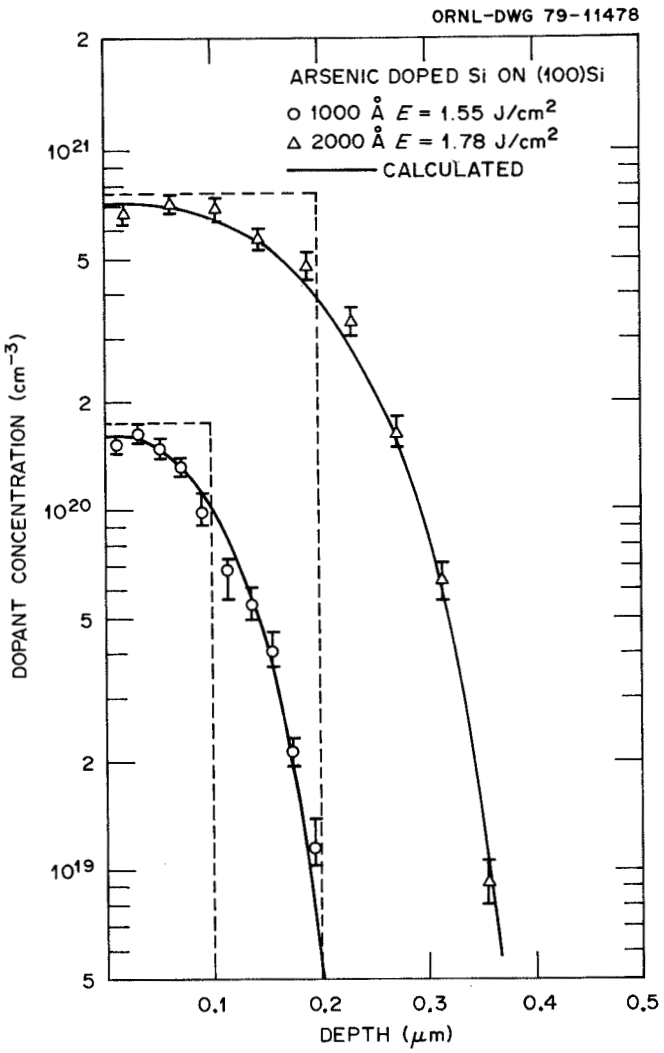

Figure 5. Comparison of experimental and calculated dopant profiles on 1000 Å and 2000 Å deposited layers after laser irradiation.

SUMMARY OF SILICON HIGH EFFICIENCY SOLAR CELL WORKSHOP

Henry W. Brandhorst, Jr.
National Aeronautics and Space Administration
Lewis Research Center

It was agreed that the maximum practical silicon solar cell efficiency was 20 percent (AMO) with the hopes that 18 percent could be achieved by the end of CY80. (The role played by a NASA RFP that sought to develop an 18-percent cell by that same time in this assessment may never be known.) It was agreed that open-circuit voltage was the final limiting barrier to achievement of this goal. The list of voltage limiting mechanisms was not shortened; in fact, additions such as the need to match dopant to lattice, minority carrier diffusivity, and band narrowing due to junction field were made to the mechanisms outlined at previous workshops. The growing list of mechanisms underscored the need for a focussed attack on the problems. The participants did believe that 0.7 V is still a reasonable goal.

The quality of the available silicon material was thought to be adequate to achieve 18 percent efficiency now. However, before 20 percent could be achieved, improvement in minority carrier lifetime and in reduction of unwanted impurities such as carbon and oxygen would have to be made.

A number of device structures thought capable of achieving 18 percent efficiency surfaced. It is clear in any of these structures that the design of emitters and base structures must be carefully controlled to achieve high performance. The use of 0.1 Ω-cm material with or without back surface field was still recommended, although concerns were expressed about the radiation resistance of this structure. The use of n^+-p-p^+ structures with p-base resistivities above 0.1 Ω-cm were thought to also be practical. However, care must be taken in both design of the emitter (including HLE structures) and in achieving a perfect p^+ layer before these structures can reach 18 percent. Also, the use of thin cells (∿50 μm) was an integral part of this discussion. Perhaps the cell that culminated this trend was the thin n-i-p cell (50 μm) that should have the aforementioned advantages of the n^+-p-p^+ structures plus radiation resistance due to the use of intrinsic silicon. In addition to these somewhat con-

ventional structures, both the interdigitated back contact with either a tandem junction or a front surface field and the vertical junction cell under development by the U.S. Air Force were felt capable of achieving 18 percent AMO efficiencies.

One high performance cell design that was discussed incorporated the following features: use material of about 20 Ω-cm resistivity with a 1.0-msec lifetime and thickness <100 μm; form an n^+-n-p-p^+ structure keeping all surface concentrations below 10^{19} cm^{-3}; process with "cool" processing steps — i. e., those that do not require long times at high temperatures — such as various pulsed processing procedures; use a mirror back surface; passivate surface with a charged oxide or silicon oxide-nitrides; use low metal coverage on the surface (<1 percent coverage). This structure served to focus the discussion and led to surfacing of the variety of mechanisms and approaches listed previously. Whether the design is feasible or not is speculative at this time. Most of the basic features of this structure were aimed at eliminating the adverse mechanisms and effects thought to limit the performance of present devices.

It was agreed that high beginning-of-life efficiency and high end-of-life efficiency were not incompatible. Specific cell designs that might encompass both of these diverse demands were the n-i-p cell and the vertical junction cell.

Several R&T areas were surfaced. The need to develop low carbon and oxygen silicon (with concentrations below 10^{15} cm^{-3}) was stressed. The need for a materials repository that could serve as a common, controlled source of materials for investigators was also noted. As mentioned previously, there is a need to develop "cool", clean processes that do not harm the lifetime in the good material. The absorptivity problem leading to increased orbital temperatures was highlighted as a need that could be solved by the development of better antireflection coatings. As a corollary, a means for comparing competing cell designs by determining performance at orbital temperatures was desired so that the benefits of an improved technology could be realized in flight. Finally, the need for a measurement round-robin was surfaced. An error of 5 percent in performance measurement spells the difference between an 18-percent cell and

a 17-percent cell. Thus, verification of the achievement of an 18-percent cell will require a careful measurement program. The round-robin was envisioned as a first step in this process.

WORKSHOP QUESTIONS

HIGH EFFICIENCY SILICON SOLAR CELLS

- WHAT IS MAXIMUM PRACTICAL EFFICIENCY (AMO) OF SILICON SOLAR CELLS?
- WHAT MECHANISM(S) IS PRIMARILY LIMITING THE VOLTAGE?
- DO WE SEE ANOMALIES SUGGESTING A NEW MECHANISM?
- DO WE NEED HIGHER QUALITY SILICON TO ACHIEVE 18% EFFICIENCY?
- WHAT APPROACHES LOOK BEST TO ACHIEVE 18% BEGINNING OF LIFE EFFICIENCIES?
- CAN WE GET BOTH 18% BOL AND HIGH END-OF-LIFE EFFICIENCY?
- WHAT RESEARCH ON OTHER SILICON DEVICES HAS A POTENTIAL IMPACT ON SILICON SOLAR CELLS?
- WHAT AREAS OF RESEARCH OR TECHNOLOGY SHOULD GET MORE ATTENTION?

Figure 1

AN INTERIM REPORT ON THE

NTS-2 SOLAR CELL EXPERIMENT*

Richard L. Statler and Delores H. Walker
Naval Research Laboratory

SUMMARY

Solar cell modules on the NTS-2 satellite have experienced more than 642 days of orbital time in a planned 3 year mission in a 20,190 km (10,990 NM) circular orbit at an inclination of 63.5 degrees. Complete I-V curve data are obtained from the fourteen solar cell modules together with a record of panel temperature and sun inclination. The data are corrected for sun angle, solar intensity, and cell temperature effects. No instrumental problems have occured, and only one solar cell module has failed completely.

INTRODUCTION

The Navigation Technology Satellite-Two (NTS-2) is the second in a series of developmental satellites that are forerunners of the DOD NAVSTAR Global Positioning System (GPS). NAVSTAR GPS is being developed to provide extremely accurate navigation information on a 24 hour basis with worldwide coverage in all types of weather conditions. NTS-2 was launched on 23 June 1977 into a circular orbit of altitude 20,190 km at an inclination of 63.5°.

The purpose of the solar cell experiment is to obtain flight data on (1) state-of-the-art solar cell configurations which embody improvements in solar cell efficiency through new silicon surface and bulk technology, (2) improved coverslip materials and coverslip bonding techniques, and (3) short and long-term effects of ultraviolet rejection filters vs. no filters on the cells. In addition, it is deemed important to obtain (4) comparative degradation data on a developmental type of liquid epitaxy gallium-aluminum-arsenide solar cell, and (5) confirmation of the predicted space radiation effects in this orbit.

DESCRIPTION OF EXPERIMENTS

The NTS-2 solar cell experiment contains 13 modules of

*This work is supported by the Space Applications Branch of the Naval Research Laboratory, by the Air Force Aero Propulsion Laboratory, and by the Space and Missile Systems Organization.

silicon cells and 1 module of gallium-arsenide solar cells. Each module consists of five 2 x 2 cm cells connected in series. The modules are mounted on two 1/4-inch thick aluminum homeycomb panels, as shown in Figure 1. There is also an experimental blocking diode which is a 1 x 2 cm planar device with a polished aluminized surface. Experiment 12 is comprised of this diode in series with experiment 11. The panels are thermally isolated from the spacecraft structure; therefore, in order to allow for heat dissipation which can only be accomplished by thermal radiation from the front panel surface, the modules were evenly spaced on the panel and the intervening regions were coated with a white thermal control coating, Dow Corning 92007, which covers 52 percent of the panel surface.

Temperatures are monitored at the rear surface of four cells by means of three thermistors and one wire resistance thermometer. The thermistors are accurate to within $\pm$ 3 degrees C up to 100 degrees C, and the wire thermometer is accurate to within $\pm$ 2 degrees C to above 120 degrees C.

The experimental panels are continuously illuminated by the sun (except during the biannual eclipse season of 25 days). The experiment is mounted on the satellite surface which faces the direction of travel about the earth, and twice during each orbit the satellite is rotated 180 degrees in yaw so that the paddles (and experiment) face the sun. Figure 2 shows the location of the panels on the spacecraft.

Table I gives a brief description of the experiments showing the type and thickness of the solar cell, the type and thickness of the coverslip, the nature of the coverslip to cell bonding, the interconnect material, and the beginning-of-life (BOL) cell efficiency.

EXPERIMENTAL RESULTS

This report includes data through 642 days in orbit. This period began 7 July 1977 until 14 April 1979.

The current-voltage characteristics of the solar cell arrays are telemetered in real time as the satellite passes over the tracking station at Blossom Point, Maryland. The electronic circuit measures the I-V curve for each module in sequence reading out current-voltage values for evenly-spaced points from I_{sc} to V_{oc}. Each cell module is short-circuited except when it is being stepped through the I-V curve. The average value of I_{sc} measured in space on the first day of exposure agreed with the solar simulator values to 1.41 $\pm$ 0.99 percent. The agreement between V_{oc} on initial space exposure and the solar simulator values was 1.24 $\pm$ 2.02 percent. The average error between P_m measurements on the ground and the first day in orbit was 3.33 $\pm$ 3.17 percent.

Unpredicted Module Degradation

Several modules exhibited unusual and unpredictable behavior in orbit. The first observation was in the I-V curve of the gallium-arsenide module on the first day in orbit. It was observed that the P_M had decreased 12.3 percent from the pre-launch value, as V_{OC} had dropped 6.8 percent. Because of the good agreement among the other modules with ground data, we did not think this was due to measurement error. We believed there was a possibility for physical change in the cell module in the time between the last ground calibration with a solar simulator and the space measurement (145 days). Between day 1 and day 80 in orbit the GaAs cell module showed a significant amount of P_M and V_{OC} recovery, which we believe is related to the method of interconnection of the GaAs cells. They were series-connected by means of a metal-filled epoxy, rather than by soldering or welding a metal interconnect. Figure 3 shows the space performance of the GaAs module. The performance of Hughes gallium arsenide cell has generated a great deal of interest. The gallium arsenide cell is a high-efficiency solar cell whose efficiency is less affected by high temperature than are silicon cells. GaAs is expected to be harder to radiation and is therefore ideal for space applications. The problems of surface recombination and low lifetime in the diffused region are largely overcome by the addition of a GaAlAs window.

Three experiments have sustained unpredictably large degradations. The first of these, the Solarex Space Cell, Experiment 8, experienced an open-circuit of the module on the 69th day, causing the complete loss of subsequent data. Fortunately this failure occurred during a time while data were being recorded, allowing the abrupt manner in which it failed to be observed. Analysis of the data acquisition system showed that no single point failure of the data system could result in both voltage and current data loss. Therefore it is presumed the module open-circuited.

A second anomaly was the sudden onset of increased degradation rate in the Solarex vertical junction cell, Experiment 7 (Figure 4). At this time there have been four sudden drops in the maximum power output of the vertical junction cells. These large decreases have occurred around day 20 in orbit, near day 180, then day 300, and finally day 540. Investigations performed at AFAPL suggest that these unusually large losses in maximum power are the result of cell surface disintegration due to thermal cycling of adhesive-bonded coverslipped cells. The data in Figure 4 seem to support this hypothesis. The abnormal drops in power occur at approximately the same time as the maximum duration of the eclipse. As the cells experience increasingly longer periods of extreme cold, more of the junction is destroyed resulting in power loss. The breakdown of the junction is thought to be related to the type of adhesive used to bond the coverslip. Following each drop in P_M the power output stabilizes quite well until the next maximum

duration of the eclipse. The decrease in P_M output of the vertical junction cell by day 642 was 66.6 percent.

The third unusual occurrence is the large degradation rate for Experiment 5, the COMSAT CNR cell covered with a 12 mil (0.305 cm) fused silica coverslip which has no ultraviolet cut-off filter. The COMSAT textured cell was flown both with and without an ultraviolet rejection filter in order to evaluate the effect of the filter. The P_M of this cell has decreased to 37.6 mW after 642 days, while Experiment 6, an identical module except for the addition of the ultraviolet cut-off filter on the coverslip, has a P_M of 53.8 mW (Fig. 5). Laboratory measurements at COMSAT Laboratories did not show a substantial difference with or without a filter. If the degradation seen in the I_{SC} of these cells were caused by particle radiation in the cell, the V_{OC} would be severely degraded. Also, the curve fill factor would be smaller than it is for the less damaged cell. However the V_{OC} of the cells with and without the uv filter is not markedly different, and the fill factor at day 642 is identical at 100 degrees C. Therefore we conclude that coverslide adhesive darkening may be a prime cause in this degradation. The degradation appears to be caused by an optical transmission loss factor, not a p-n junction effect.

Predictable Radiation Degradation of Solar Cell Modules

The remaining eleven cell modules have operated very satisfactorily; the rate of degradation which we attribute primarily to radiation damage has been greater than was predicted from several trapped radiation models. We have made estimates of the space radiation fluence based upon solar cell parameter degradation in four modules, namely Experiment 1, the OCLI conventional cell; Experiment 2, the Spectrolab Helios cell; Experiment 3, the Spectrolab textured hybrid cell and Experiment 10, the OCLI violet cell.

Among the experiments of primary interest is the Spectrolab "Helios" back field cell, Experiment #2. This cell was space qualified as one of the experiments aboard the NTS-1 satellite. The "Helios" cell is presently in use as the main power source on NTS-2 and is in use in other satellite programs. As of day 642, the maximum power output of the Spectrolab Helios cell (NTS-2) has decreased by 23.3 percent. Interestingly, although the Spectrolab Helios cell degraded less than a conventional cell in I_{SC} and P_M, it has degraded more in V_{OC}. This behavior has been reported previously for solar cells with a p^+ layer at the back contact in laboratory studies.The power output of the Helios p^+ solar cell, Experiment 2, is plotted along with the predicted degradation in Fig. 6. It is readily observed that the cells are degrading slightly faster than predicted.

The 1-MeV electron equivalent fluence shown in Table 2 was obtained by fitting solar cell parameter to radiation damage curves

(ref. 1) for generic types of solar cells. The equivalent fluence values obtained from this experiment are all substantially higher than the equivalent fluence listed in reference 1, which bases fluence calculation on the AE4 trapped electron model. For 12 mil fused silica shielding and infinite backshielding, reference 1 lists a 2 MeV electron equivalent fluence of $3.3 \times 10^{13} e/cm^2$-year.

Experiments 3 and 4 were designed to distinguish between cell degradation effects due to adhesive bonding vs. FEP Teflon bonding. There is an improvement with the Teflon bonded coverslip (17.6 percent P_M degradation) using "as sawn fused silica" instead of the traditional polished and uv filtered Corning 7940 fused silica (degradation in P_M 20.6 percent). These data are presented in Figure 7.

Another coverslip evaluation is made in Experiments 1 and 13 which use an OCLI conventional cell, Experiment 1 with an adhesive bonded Corning 7940 fused silica coverslip and Experiment 13 with an electrostatic bonded Corning 7070 glass coverslip. There was a substantial initial loss in BOL P_M with the electrostatic bonding technique at the time the module was fabricated. A direct comparison between the final results is therefore not valid.

A more complete listing of parametric data as a function of radiation fluence may be obtained in reference 2. An abridged data table is included as Table III.

In experiments of this type, there is a compelling urge by the observer to make an overall comparison and a list of cells in the order of their "best performance". Best performance cannot be simply defined to be a universally acceptable criterion. What we have done is prepare a bar graph (Fig. 8) which shows the maximum power of each cell type as measured on the solar simulator before launch and space data after 642 days. The cells are arranged in decreasing order according to power at day 642. It is readily seen that this does not imply that the original efficiency of the cells is in the same order.

CONCLUSIONS

The overall performance of the flight experiment and the data acquisition system continue to be excellent. Several important conclusions which have been reached concerning the new cell technologies are listed below.

1. The Spectrolab Helios p^+ (Exp. 2) cell with an adhesive-bonded 0.0254 cm ceria microsheet coverslip is an excellent solar cell for the GPS natural environment. The Spectrolab textured hybrid cell (Exp. 4) with an FEP bonded 0.0152 cm "as-cut" quartz coverslip is equally satisfactory for this orbit.

2. There are three other types of silicon cells which can be classed as production cells, or nearly production, whose P_M exceeds the Helios (Exp. 2) and hybrid (Exp. 4) output. These are in ascending order of P_M: the Spectrolab textured HESP, no p^+ (Exp. 14) with adhesive-bonded 0.030 Corning 7940 coverslip; the OCLI violet cell (Exp. 10) with an adhesive-bonded 0.030 cm Corning 7940 coverslip; and the Spectrolab textured Helios p^+ (Exp. 9), with a back surface reflector and an FEP bonded 0.030 cm as cut quartz coverslip.

3. The FEP Teflon bonded "as-cut" quartz coverslip permits very high cell power output, with no evidence of any problems, performing as well as adhesive-bonded Corning 7940 with uv filter for radiation shielding and optical transmission.

4. The GaAs cell (Exp. 15) is fourth in rating of power output at day 642. Despite the difficulty with low V_{OC} and P_M during the first month after launch, it has recovered sufficiently to show its value in this radiation environment. However more reliable interconnect than epoxy is obviously needed.

5. Lithium-doped p-on-p solar cells show better P_M output than 2 ohm-cm n-on-p cells in this space electron environment. This was not expected, since p/n (Li) cells have not annealed as well for electron exposures in the laboratory as they have for heavy particle exposures such as protons and neutrons. The high panel temperature (100 degrees C) may have produced partial annealing of the radiation damage.

Some unresolved findings that are of sufficient importance to justify further investigation are:

1. Unexpectedly large I_{SC} loss in the COMSAT CNR cell with the adhesive bonded coverglass of Corning 7940 having no uv filter.

2. Thermal cycling damage in the vertical junction solar cell.

REFERENCES

1. H. Y. Tada and J. R. Carter, Jr., "Solar Cell Radiation Handbook," Pasadena, CA; Jet Propulsion Lab., JPL Pub. 77-56, November 1977.

2. D. H. Walker and R. L. Statler, "Results of the Solar Cell Experiments Aboard the NTS-2 Satellite After 447 Days in Orbit," NRL Memorandum Report 3935, 9 March 1979.

Table I — NTS-2 Solar Cell Experiments

Exp. No.	Cell Type	Thick-ness (cm)	Coverslip (cm)	Coverslip Bond (cm)	Interconnect	Efficiency 28°C (%)
1	OCLI Conventional, 2 ohm-cm	0.025	Corning 7940, AR and UV, (0.030)	R63-489	Cu/Ag	10.7
2	Spectrolab "Helios" p^+ 15-45 ohm-cm	0.0228	Ceria microsheet w/o AR, (0.025)	DC 93-500	Moly/Ag (.0025)	11.5
3	Spectrolab Hybrid Sculptured 7-14 ohm-cm	0.020	Corning 7940, AR and UV, (0.0152)	DC 93-500	Moly/Ag (.0025)	10.5
4	Spectrolab Hybrid Sculptured 7-14 ohm-cm	0.020	Corning 7940, w/o AR or UV, (0.0152)	FEP Teflon (0.0051)	Moly/Ag (.0025)	11.1
5	Comsat Non-Reflecting, p^+ Textured, 1.8 ohm-cm	0.025	Corning 7940, AR, w/o UV (.030)	R63-489	Ag, thermo-compression bonding	14.5
6	Comsat Non-Reflecting, p^+ Textured, 1.8 ohm-cm	0.025	Corning 7940, AR and UV (.030)	R63-489	Ag; thermo-compression bonding	14.6
7	Solarex Vertical Junction, p^+, 1.5 ohm-cm	0.030	Ceria microsheet w/o AR (.0152)	Sylgard 182	Ag mesh	13.0
8	Solarex Space Cell, p^+ 2 ohm-cm	0.025	Ceria microsheet w/o AR (0.0152)	Sylgard 182	Ag mesh	12.8
9	Spectrolab "Helios" p^+ Sculptured, BSR, 10 ohm-cm	0.030	Corning 7940 (.030) w/o AR or UV	FEP teflon (.003)	Ag mesh (.003)	14.2
10	OCLI Violet, 2 ohm-cm	0.025	Corning 7940 (.030) AR and UV	R63-489	Cu/Ag	13.5
11	Spectrolab P/N Li-doped 15-30 ohm-cm, Al contacts	0.020	Corning 7940, AR and UV, (0.015)	Silicone	Aluminum (.0025) Ultra-sonic welding	10.8
12	Spectrolab Planar Diode in series with Exp. 11	NA	NA	NA	NA	NA
13	OCLI Conventional, 2 ohm-cm	0.025	Corning 7070 (.028)	Electrostatic bonding	Cu/Ag	10.2
14	Spectrolab HESP, no p^+, Sculptured, 2 ohm-cm	0.030	Corning 7940, AR and UV (0.0305)	R63-489	Moly/Ag (.0025)	13.6
15	Hughes Gallium-Aluminum Arsenide	0.0305	Corning 7940, AR and UV, (0.0305)	DC 93-500	Aluminum GPD (.0025), epoxy	13.6

Table II.– NTS-2 Equivalent Fluence (1 - MeV e/cm^2) Predictions*

OCLI Conventional 2 Ω-cm, 10 mil cell, 12 mil FS Coverslip

BOL		Fluence at 200 days	Fluence at 1 yr	Fluence at 3 yr
I_{sc}	136.0 mA	1.5×10^{14}	2.7×10^{14}	8.2×10^{14}
V_{oc}	548 mV	3×10^{13}	5.5×10^{13}	1.6×10^{14}
P_m	56.5 mW/4 cm^2	1.3×10^{14}	2.4×10^{14}	7.1×10^{14}
Spectrolab Helios, 10 Ω-cm, 9 mil cell, 10 mil Ceria Coverslip				
BOL		Fluence at 200 days	Fluence at 1 yr	Fluence at 3 yr
I_{sc}	154 mA	1.3×10^{14}	2.4×10^{14}	7.1×10^{14}
V_{oc}	545 mV	1×10^{13}	1.8×10^{13}	5.5×10^{13}
P_m	60.5 mW/4 cm^2	9×10^{13}	1.6×10^{14}	4.9×10^{14}
Spectrolab Textured Hybrid, 8 mil cell, 6 mil FS Coverslip				
BOL		Fluence at 200 days	Fluence at 1 yr	Fluence at 3 yr
I_{sc}	156 mA	5.0×10^{14}	9.1×10^{14}	2.7×10^{15}
V_{oc}	522 mV	5.0×10^{14}	9.1×10^{14}	2.7×10^{15}
P_m	53.8 mW/4 cm^2	3.3×10^{14}	6.0×10^{14}	1.8×10^{15}
OCLI Violet				
BOL		Fluence at 200 days	Fluence at 1 yr	Fluence at 3 yr
I_{sc}	166 mA	1×10^{13}	1.8×10^{14}	5.5×10^{14}
V_{oc}	552 mV	2×10^{13}	3.7×10^{13}	1.1×10^{14}
P_m	67.5 mW/4 cm^2	7.5×10^{13}	1.4×10^{14}	4.1×10^{14}

*Cell data at 50°C

Table III. NTS-2 SOLAR CELL EXPERIMENT

EXP NO.	CELL TYPE	MAXIMUM POWER (MW)* PRE-LAUNCH	DAY 1	DAY 642	% LOSS FROM PRE-LAUNCH	FILL FACTOR AT 100 C
1	OCLI 2 ohm-cm	53.1	56.3	40.2	24.3	.674
2	SPECTROLAB Helios (NTS-2)	57.9	60.6	44.4	23.3	.644
3	SPECTROLAB Text. Hybrid	52.4	53.5	41.6	20.6	.595
4	SPECTROLAB Text. Hybrid, FEP	54.6	55.4	45.0	17.6	.637
5	COMSAT CNR No filter	72.8	74.7	37.6	48.4	.672
6	COMSAT CNR	70.1	72.0	53.8	23.3	.672
7	SOLAREX VJ	63.1	62.2	21.1	66.6	.435
9	SPECTROLAB Text. Helios BSR	66.6	70.0	51.6	21.8	.690
10	OCLI Violet	67.5	66.6	50.8	24.7	.645
11	Lithium, P/N	53.2	55.8	42.5	20.1	.682
13	OCLI 2 ohm-cm ESB coverslide	47.0	46.8	37.0	21.3	.559
14	SPECTROLAB HESP	63.3	63.8	47.0	25.8	.677
15	HRL AlGaAs	70.0	61.4	50.0	28.6	.752

*The power data are corrected to 50°C and one sun intensity air mass zero.

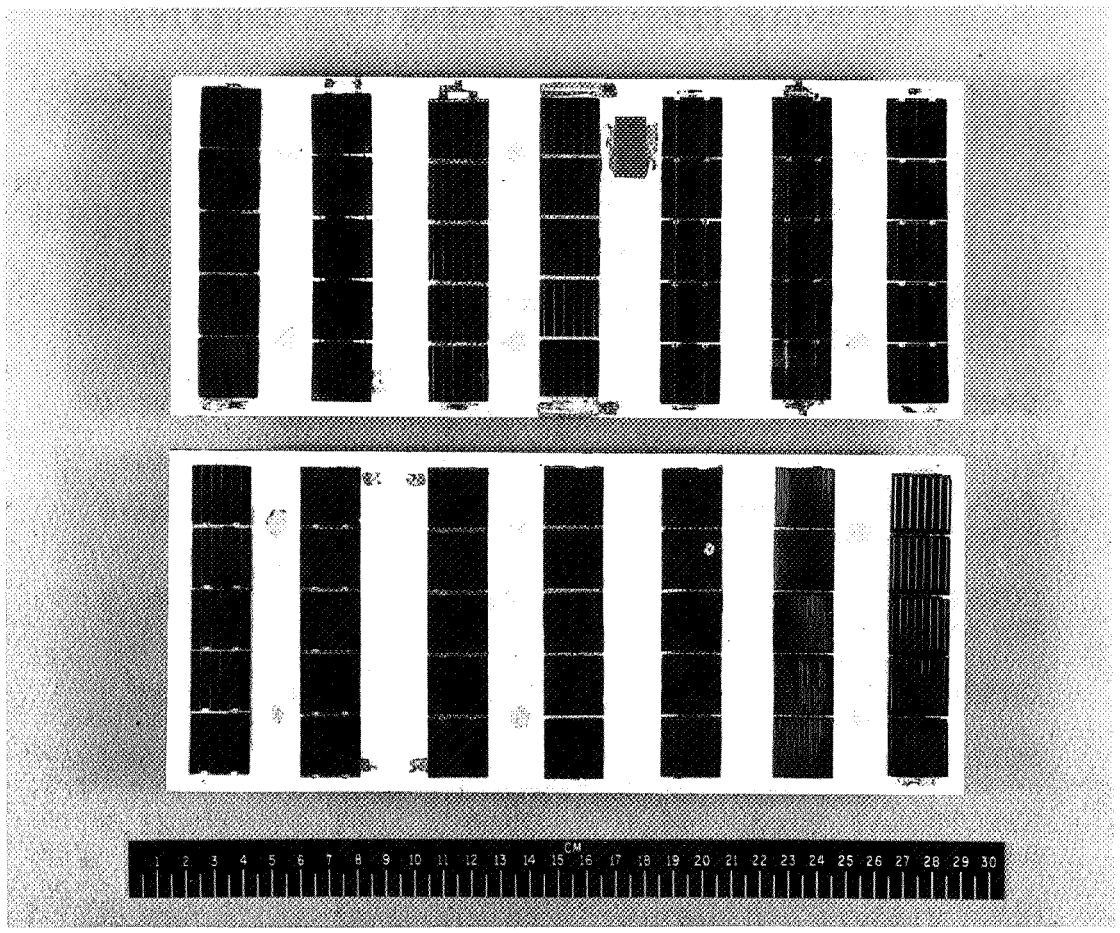

Figure 1. The NTS-2 solar cell experiment modules mounted on aluminum honeycomb panels.

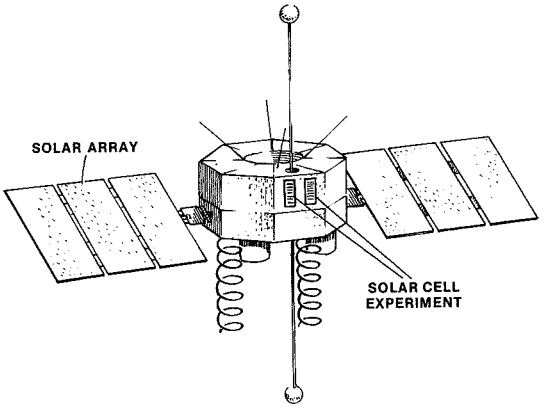

Figure 2. The NTS-2 satellite with solar arrays deployed.

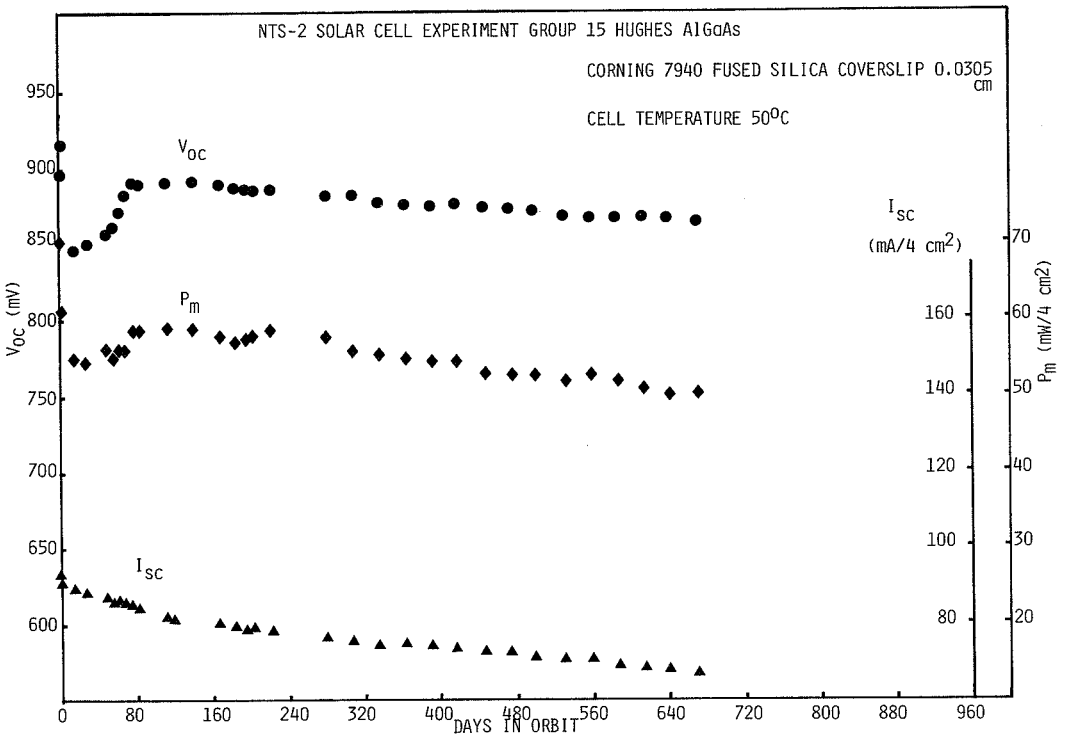

Figure 3. Maximum power, short-circuit current, and open-circuit voltage degradation of the Hughes gallium arsenide solar cell.

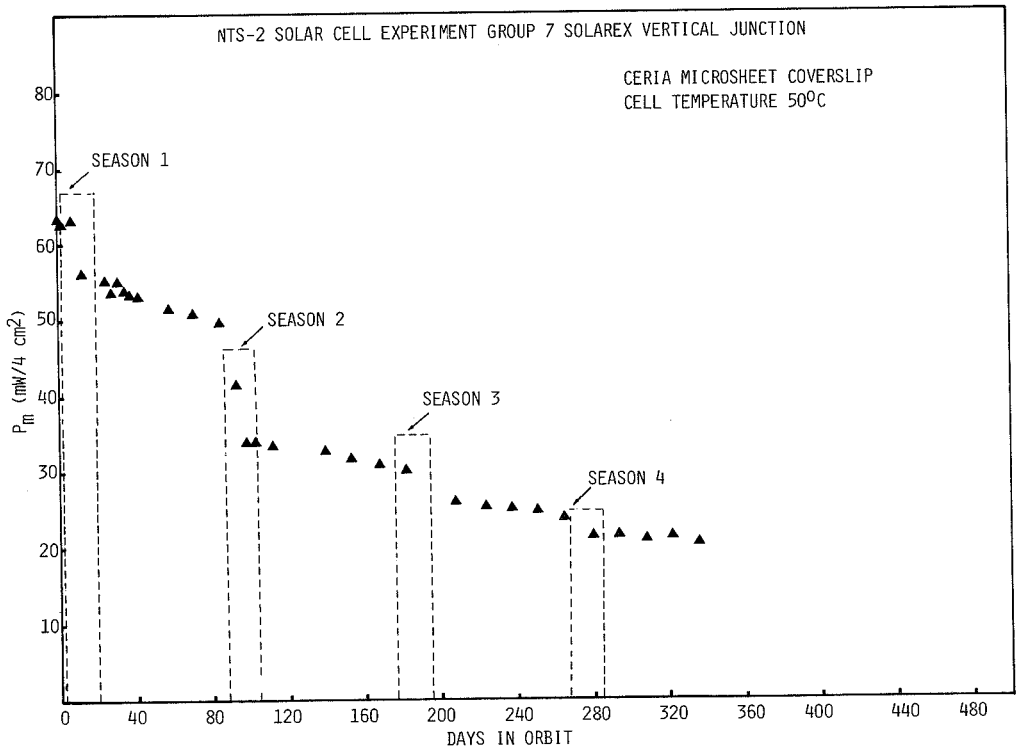

Figure 4. Maximum power, short-circuit current, and open-circuit voltage degradation of the Solarex vertical junction solar cell.

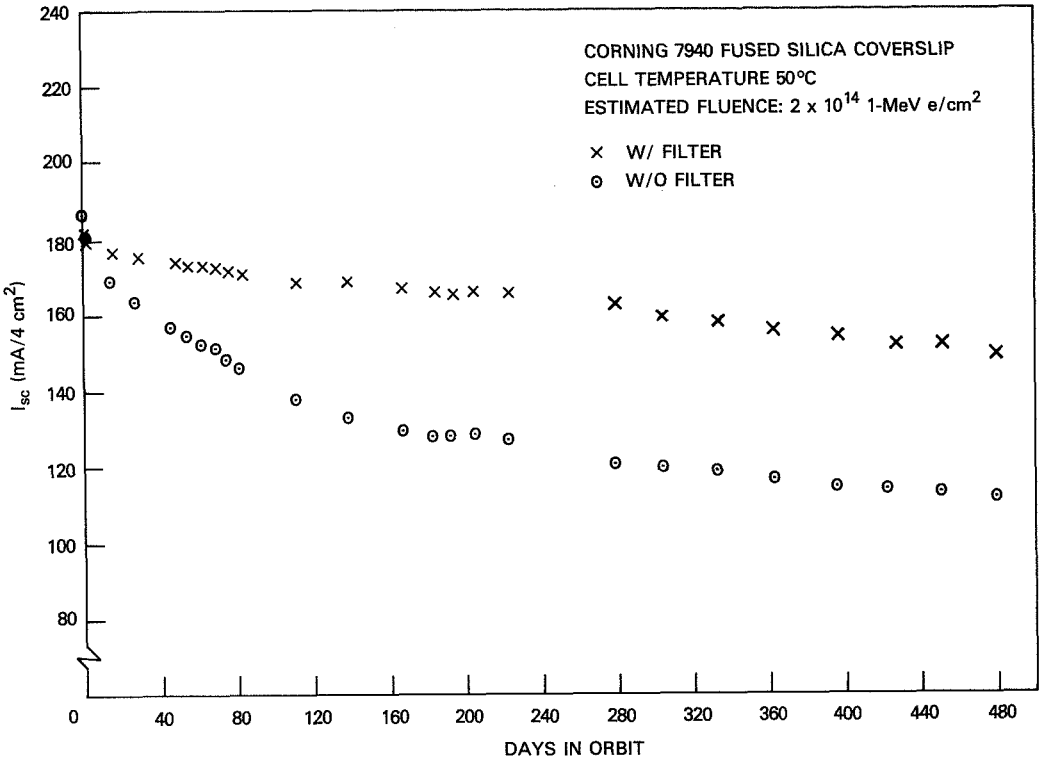

Figure 5. Short-circuit current of the COMSAT non-reflective cell, with and without an ultraviolet filter.

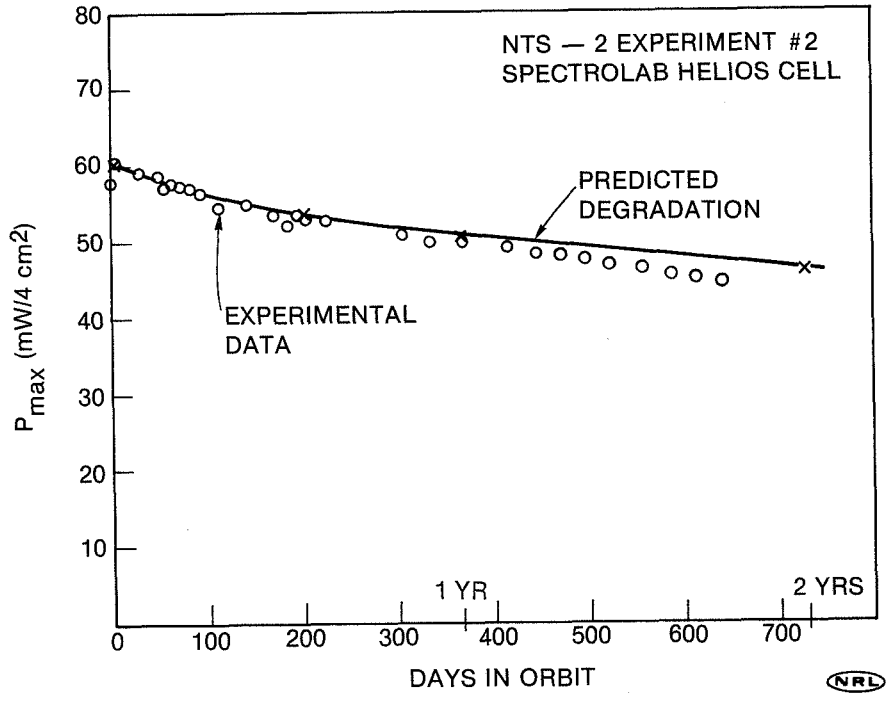

Figure 6. Maximum power degradation of the NTS-2 Spectrolab Helios solar cell.

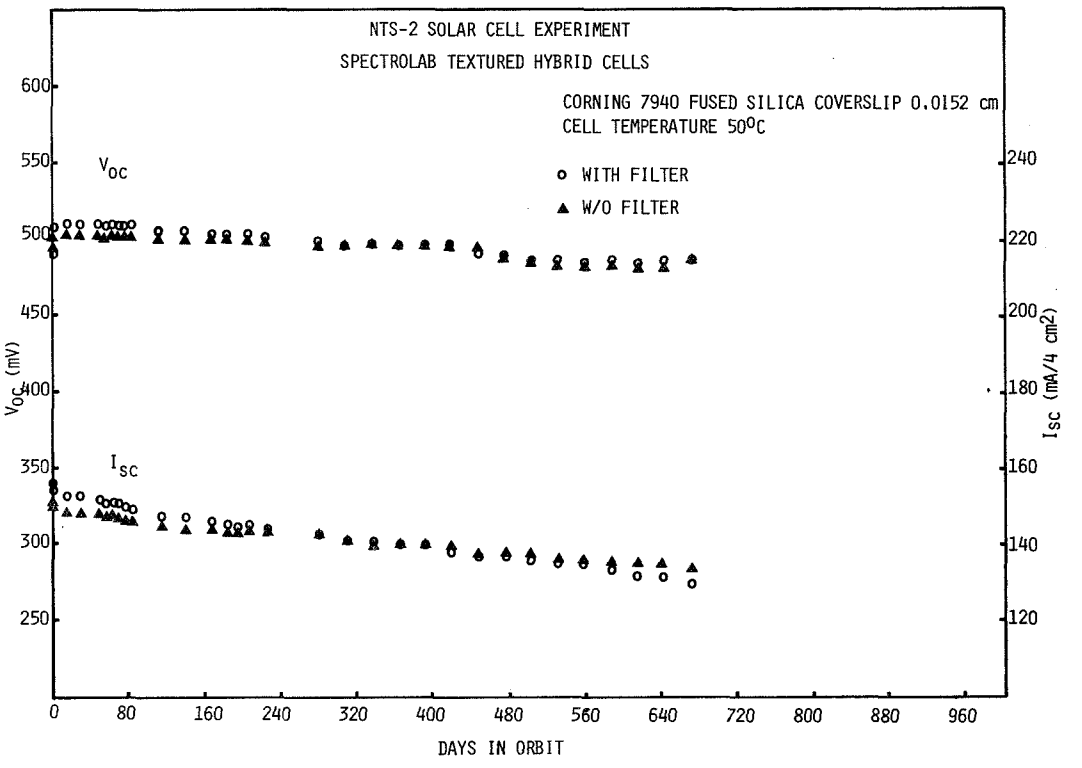

Figure 7. Short-circuit and open-circuit voltage degradation of the Spectrolab textured hybrid solar cells (Exp. 3 and 4).

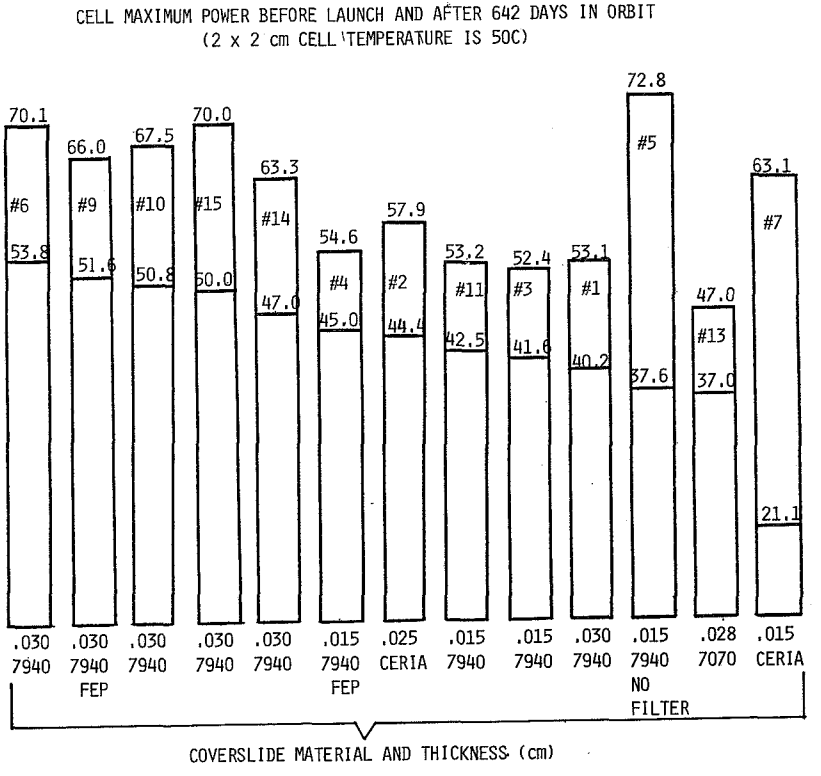

Figure 8. Maximum power before launched and after 642 days in orbit, corrected to 50°C and 1 sun AMO.

ELECTRON IRRADIATION OF TANDEM JUNCTION SOLAR CELLS*

Bruce E. Anspaugh, Tetsuo F. Miyahira and John A. Scott-Monck
Jet Propulsion Laboratory
California Institute of Technology

SUMMARY

The electrical behavior of 100 micron thick tandem junction solar cells manufactured by Texas Instruments has been studied as a function of 1 MeV electron fluence, photon irradiation, and 60°C annealing. These cells are found to degrade rapidly with radiation, the most serious loss occurring in the blue end of the cell's spectral response. No photon degradation was found to occur, but the cells did anneal a small amount at 60°C.

INTRODUCTION

The Texas Instrument tandem junction solar cell (ref. 1) is constructed with a junction on the front surface and a junction on the rear surface in an n^+pn^+ configuration. The front surface, usually textured, has no grid lines or contacts of any kind. An n^+ layer is diffused in a fingerlike pattern on the rear surface which leaves both n^+ and p material exposed for purposes of contact deposition. This construction, with contacts only on the rear surfaces permits simplified cell interconnection during panel construction. An additional advantage is that these cells have worked quite well at thicknesses down to 100 microns. Their performance after 1 MeV electron irradiation, annealing, and photon exposure is the subject of this paper.

We have irradiated and measured three TI tandem junction cells using the JPL Dynamitron as a source of 1 MeV electrons. I-V curves and spectral response measurements were made as a function of fluence, photon irradiation and 60°C anneal. All three cells had textured, contactless front surfaces. They were furnished mounted on thin ceramic substrates. Cell 20-2 was made of 3 ohm-cm CZ silicon, 100 microns thick, area 4 cm^2, and cells 34-1 and 38-1 were 6 ohm-cm CZ silicon, 110 microns thick, area 4 cm^2. P contacts were Al-Ti-Pd-Ag and n contacts were Ti-Pd-Ag. All junction depths front and back were reported to be approximately 0.25 to 0.3 microns deep.

---

*The research described in this paper was carried out at the Jet Propulsion Laboratory, California Institute of Technology, under NASA Contract NAS7-100.

IRRADIATION

The results of the irradiated data are plotted in figures 1 to 3, showing I_{sc}, V_{oc} and P_{max} vs. 1 MeV electron fluence. All measurements are AMO, 28°C, made with an Aerospace Controls Model 302 filtered xenon simulator. The cells were annealed for 16 hours at 60°C after the cumulative fluence reached $2x10^{14}$ e/cm^2. The values after annealing are used in the plots. The changes in I_{sc} and P_{max} are dramatic. After 10^{15} e/cm^2, cells which began with efficiencies of 11.84%, 8.96%, and 13.47% have been reduced to 0.67%, 1.99%, and 0.81%, respectively. Cell 20-2 made of 3 ohm-cm material is seen to be the most vulnerable. It dropped to an efficiency of 1.69% after $2x10^{13}$ e/cm^2, then decreased in output slowly with fluence. The two 6 ohm-cm cells did not decrease as rapidly until exposed to somewhat greater fluences, but when they fell their output coincided with that of the 3 ohm-cm cell. The V_{oc} behavior of all three cells has roughly the same trend as shown by Figure 2, but the undulations in the cell 38-1 curve could possibly be due to a thermal contact problem involving the cell/ceramic structure.

ANNEALING AND PHOTON EFFECTS

All three cells were annealed at 60°C after higher fluence exposures. All cells showed positive annealing after this treatment in all cases, with the 6 ohm-cm cells showing a greater effect than the 3 ohm-cm cell (this duplicates the behavior of conventional structure cells). The annealed 6 ohm-cm cells showed improvements in I_{sc} of between 7 and 27%, in P_{max} between 9 and 37% and in V_{oc} between 0.7 and 4.8%. The annealing in the 3 ohm-cm cell was between 1.5 to 5% in I_{sc}, 5 to 17% in P_{max} and 1.2 to 2.5% in V_{oc}.

Cell 20-2 was subjected to a 3-day exposure to tungsten light following the 10^{15} e/cm^2 fluence and to a 35 hour light exposure following the 10^{16} e/cm^2 fluence. No reverse annealing was observed, but there was evidence of damage recovery of roughly 2% in I_{sc} and V_{oc} and 5-10% in P_{max}.

SPECTRAL RESPONSE

The spectral response measurements are taken using a chopped monochromatic light beam as an excitation source. Cell output goes to a lock-in amplifier tuned to the light chopper frequency. This permits flooding the solar cell under test with a dc light level to check for injection level effects. (Standard space quality cells do not normally show injection level effects either before or after electron irradiation).

Figures 4 and 5 show the spectral responses of cells 20-2 and 38-1 as a function of radiation fluence. Both cells also exhibit a bandwide injection dependence which, although not shown, nearly disappears after exposure to fluences greater than $1x10^{14}$ e/cm^2. Figure 6 shows the spectral response of

cell 34-1. Its injection dependence is remarkably strong and remains important until fluences of nearly 10^{16} e/cm^2 have been reached. All curves shown in figure 6 would be shifted upward but by a decreasing amount as the fluence increases. It appears then quite probable that these cells have large concentrations of trapping levels.

Figures 4-6 show that as radiation fluence is increased, spectral response is diminished all across the band, but most importantly they exhibit complete loss in the blue end of the spectrum after fluences of only 10^{14} e/cm^2. This contrasts strongly with the behavior of standard cells where the loss occurs only in the red end of the spectrum and the blue response remains unchanged.

CONCLUSIONS

While it is usually dangerous to draw far-reaching conclusions based on so small a sample size, certain general statements can reasonably be made concerning the cells we have studied.

1. Although these cells are attractive for their possible ease in panel assembly, they are not yet suitably developed for use in a radiation environment.

2. Varying but strong concentrations of trapping levels appear to be introduced in these cells.

3. TI has shown that the presence of the front junction is necessary for the high initial performance of these cells. The mechanism introduced by the junction must act to force either majority or minority carriers toward the rear surface of the cell for collection by the rear junction. Whatever the force is, it is readily destroyed by relatively low electron fluences. One possible mechanism for producing such a force is the existence of charged surface states on the front surface. These surface states are highly affected by 1 MeV electron irradiation and will probably be affected by electrons having energy below the displacement threshold. The surface state hypothesis may easily be tested by irradiation with electrons having energies below 100 keV.

4. Following initial loss of the force mechanism, the cells exhibit a more gradual loss in spectral response (primarily blue) which is consistent with a decreasing diffusion length and loss in the ability of carriers to traverse the thickness of the cell.

REFERENCES

1. Chiang, S., Carbajal, B. G., and Wakefield, G.F.: Thin Tandem Junction Solar Cell. Thirteenth IEEE Photovoltaic Specialists Conference, June 1978, p. 1290.

FIGURE 1. I_{SC} VS 1 MeV ELECTRON FLUENCE FOR TANDEM JUNCTION SOLAR CELLS (AMO, 28°C)

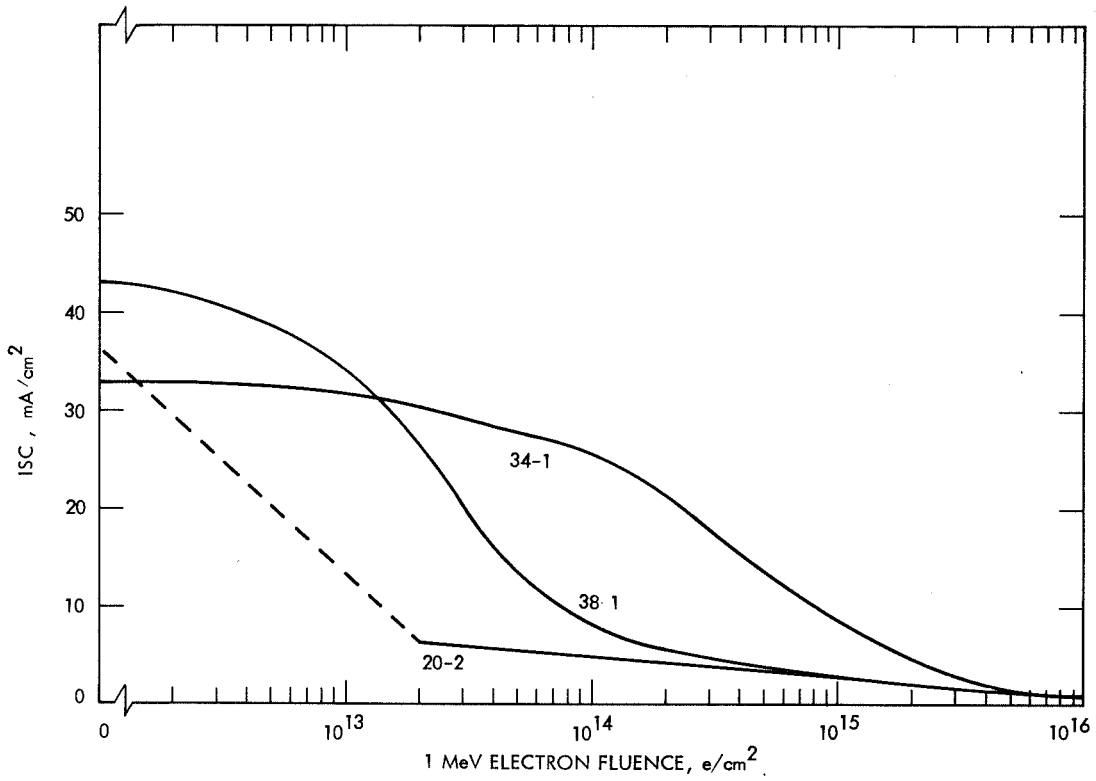

FIGURE 2. V_{OC} VS 1 MeV ELECTRON FLUENCE FOR TANDEM JUNCTION SOLAR CELLS (AMO, 28°C)

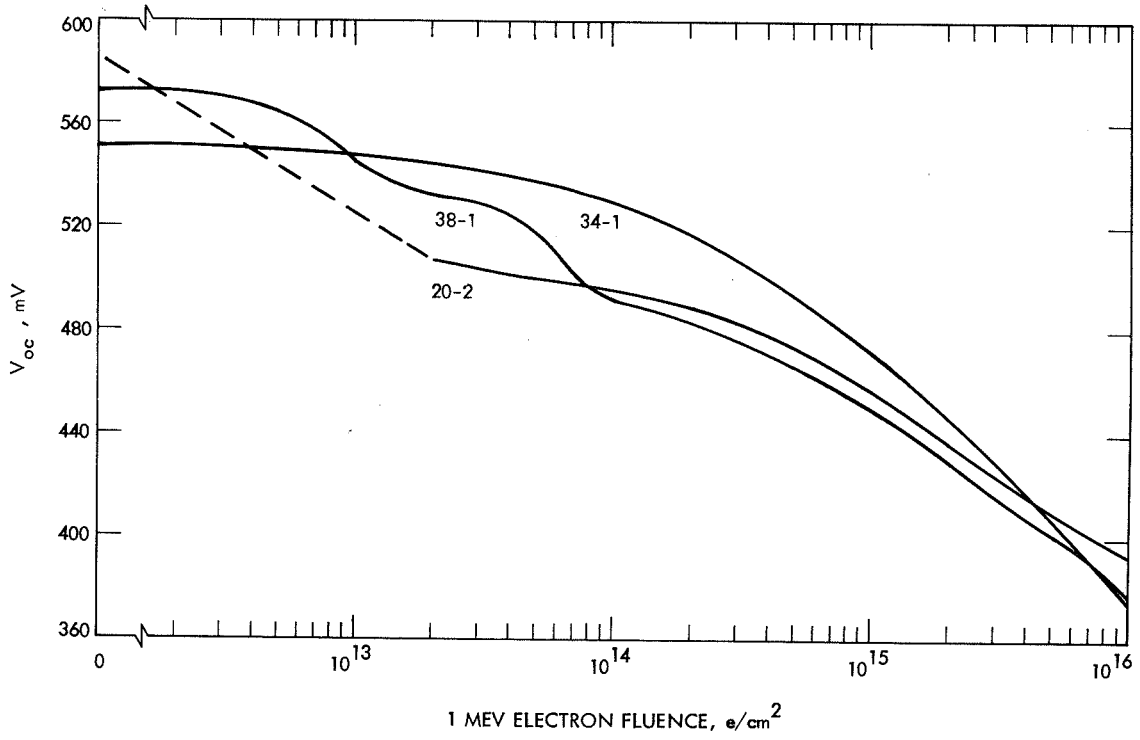

FIGURE 3. P_{MAX} VS 1 MeV ELECTRON FLUENCE FOR TANDEM JUNCTION SOLAR CELLS (AMO, 28 °C)

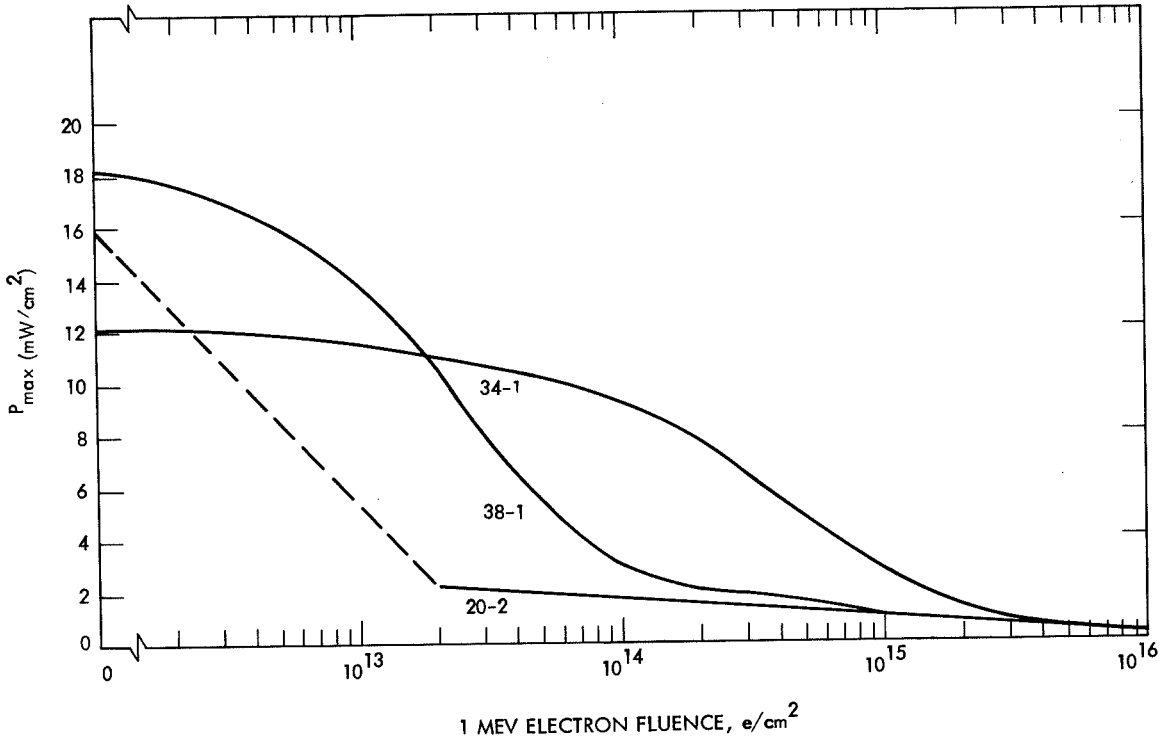

FIGURE 4. SPECTRAL RESPONSE OF CELL 20-2

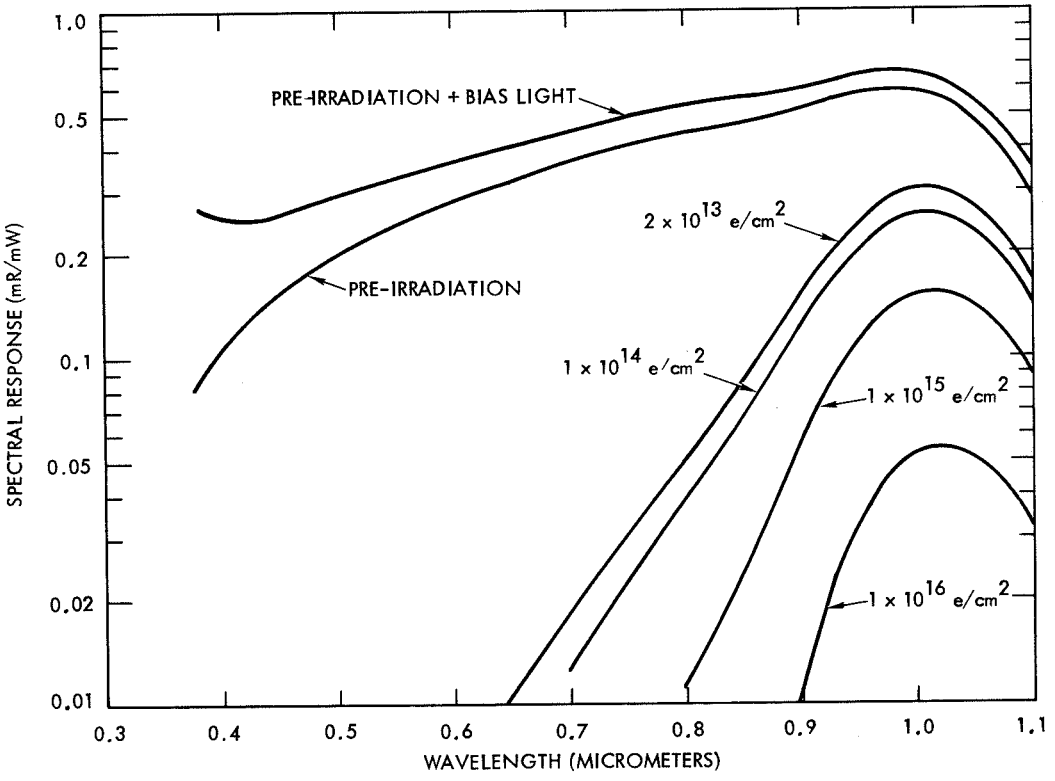

FIGURE 5. SPECTRAL RESPONSE OF CELL 38-1

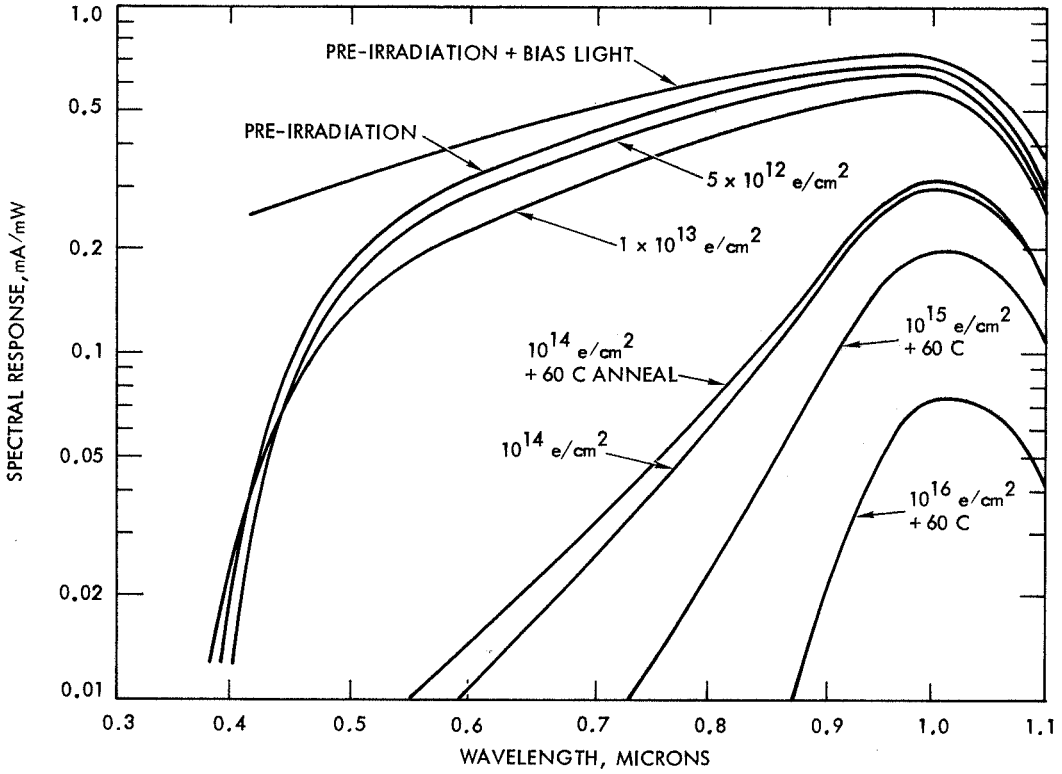

FIGURE 6. SPECTRAL RESPONSE OF CELL 34-1

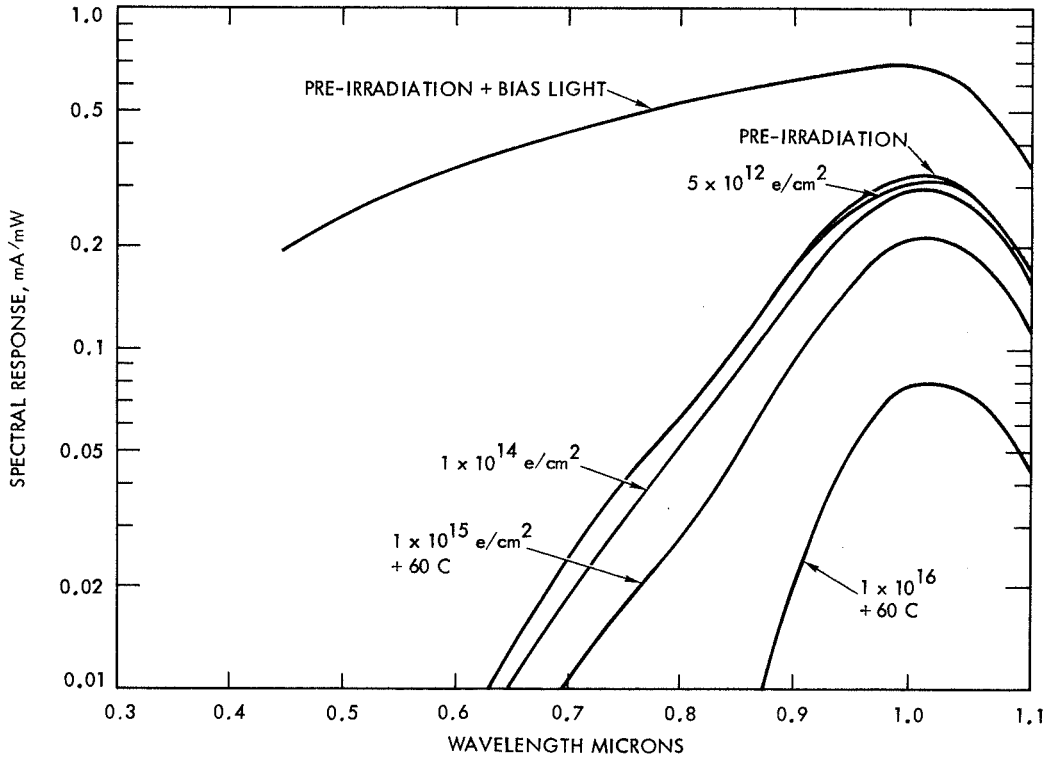

RADIATION DAMAGE IN HIGH-VOLTAGE SILICON SOLAR CELLS

Irving Weinberg, Clifford K. Swartz, and Victor G. Weizer
National Aeronautics and Space Administration
Lewis Research Center

During the past several years, the NASA Lewis Research Center has conducted a program to achieve high open-circuit voltage V_{oc} in silicon solar cells. To date, three cell designs have been developed under this program and air-mass-zero (AMO) open-circuit voltages of approximately 645 millivolts have been achieved. Although the program has been directed primarily toward demonstrating increased V_{oc}, the effects of the particulate space radiation environment on cell performance are an ever present concern. Hence, we have determined the performance, after exposure to 1-MeV-electron irradiations, of the three cell designs emerging from this program.

EXPERIMENTAL PROCEDURE

The salient features of the cells are given in table I. The ion-implanted and high-low emitter (HLE) cells have thermally grown silicon dioxide (SiO_2) on their front surfaces; the diffused cells have no front-surface oxide. The oxide on the HLE cells was formed by using a temperature-time schedule that results in a net positive charge, in the oxide, near the oxide-silicon interface (ref. 1). The positive oxide charge induces an accumulation layer at the silicon surface and thus establishes the n^+n high-low emitter junction.

Preirradiation AMO parameters are listed in table II. Diffusion lengths were measured by an X-ray excitation technique with 250-keV X-rays (ref. 2); the AMO-current-voltage measurements were obtained with a xenon-arc solar simulator. Spectral response data were obtained by using a filter-wheel solar simulator (ref. 3). Both X- and electron irradiation result in changes in oxide charge (refs. 4 and 5). Therefore, only one of each pair of oxide-coated cells was exposed to X-irradiation for diffusion length measurement. However, all cells were exposed to 1-MeV-electron irradiations to a maximum fluence of 10^{15} cm^{-2}.

RESULTS AND DISCUSSION

A typical data plot used to determine the diffusion-length damage coefficient is shown in figure 1. Table III summarizes the damage coefficients obtained for each cell design. Comparison with previous damage coefficient evaluations (ref. 6) indicates that the damage coefficients obtained for the present high-V_{oc} cells are typical of 0.1-ohm-cm p-type silicon.

Plots of normalized short-circuit current I_{sc} and V_{oc} as a function of 1-MeV-electron fluence are shown in figures 2 and 3, respectively. Data for a 10-ohm-cm cell are included for comparison. This cell showed a decrease

in output typical of that resistivity. In general, performance degradation under irradiation was highest for the HLE cells, with the greatest degradation being noted for the X-rayed HLE cell. For the ion-implanted cells, there was no measurable difference between the X-rayed and non-X-rayed cell performance. Both diffused and ion-implanted cell designs degraded at approximately the same rate. The I_{sc} and V_{oc} degradation data for the HLE cells appear to be anomalous because the diffusion-length damage coefficient K is approximately the same for all cell designs. However, K is largely a measure of the degradation occurring in the cells base region. Hence, in attempting to understand the observed increased degradation of the HLE cells, we must consider damage occurring in the emitter and oxide in addition to that occurring in the base region.

The sources of I_{sc} degradation are clarified by plots of the normalized short- and long-wavelength spectral response shown in figures 4 and 5. Since significant I_{sc} degradation of the HLE cells occurs at both long- and short-wavelengths, we concluded that I_{sc} degradation of the HLE cells occurs in both p-type base and n-type emitter. On the other hand, I_{sc} degradation of the ion-implanted and diffused cells occurs predominantly at long wavelengths and therefore predominantly in the base region. This tends to explain the observed, relatively higher I_{sc} degradation in the HLE cells despite the approximate equality of K values for all cell designs.

Calculations are in progress to determine the cell region in which V_{oc} degradation occurs. Preliminary results indicate that V_{oc} degradation occurs predominantly in the emitter region for the HLE cells and in the base region for the ion-implanted and diffused cells.

For the HLE cells, one source of the increased I_{sc} and V_{oc} degradation under irradiation is the use of a relatively deep (10 μm), n-type emitter. The damage coefficient for n-type silicon is an order of magnitude greater than that for p-type silicon (ref. 7). Since about 75 percent of the incoming optical radiation is absorbed in the 10-micrometer-wide HLE n-region, the increased susceptibility of n-type silicon to radiation damage is reflected in the increased degradation noted for the HLE cells under 1-MeV-electron irradiation. Thus, a large loss in the blue spectral response would be expected and was observed.

Another source of increased degradation of the HLE cells is the use of a charged oxide. It has been established that ionizing radiation affects the charge state of SiO_2 (refs. 4 and 5). Hence, so that the effects of the X-irradiation on the charged oxide cells could be explored, an additional HLE cell was exposed to 250-keV X-rays for 5 minutes, and its performance parameters were determined as a function of time after irradiation for times to 54 days (fig. 6). At this time, V_{oc} had degraded by 2.3 percent and I_{sc} by approximately 7 percent. These results clearly show that the X-irradiation causes performance degradation over and above that caused by electron irradiation. Since X-rays do not damage the silicon but are known to damage the oxide (refs. 4 and 5), the performance degradation shown in figure 6 is clearly attributable to oxide degradation.

The I_{sc} degradation shown in figure 6 is insufficient to account for the difference in total short-circuit-current degradation between the X-rayed and

non-X-rayed cells after irradiation by 1-MeV electrons (fig. 2). One source of the added I_{sc} degradation could be synergism between the effects of X- and electron irradiations. Another possible source of the added degradation could be a difference in the quality of the silicon constituting the emitters of the two HLE cells of figure 2.

CONCLUSIONS

The results of the NASA Lewis Research Center program to achieve high V_{oc} in silicon solar cells show that cells with a relatively deep n-type emitter (high-low emitter (HLE) design) are more susceptible to radiation damage than other high-V_{oc} cell designs. Use of diffused or ion-implanted junctions leads to high-V_{oc} cell designs that are less susceptible to radiation damage. These latter two types of cells show degradations that are typical of the 0.1-ohm-cm material from which they are fabricated. Furthermore, exposure to ionizing radiation causes oxide degradation and decreased cell performance in cells that depend on a charged oxide to achieve significant cell properties. Hence, the combination of a charged oxide and a relatively deep n-type emitter is not recommended for incorporation into a cell designed for use in the particulate radiation environment of space.

REFERENCES

1. Sah, C. T.; Ning, T. H.; and Tschopp, L. L.: The Scattering of Electrons by Surface Oxide Charges and by Lattice Vibrations at the Silicon - Silicon Dioxide Interface. Surface Sci., vol. 32, 1972, pp. 561-575.

2. Rosenzweig, W.: Diffusion Length Measurement by Means of Ionizing Radiation. Bell Sys. Tech. J., vol. 41, no. 5, Sept. 1962, pp. 1573-1588.

3. Mandelkorn, J.; Broder, J. D.; and Ulman, R. P.: Filter Wheel Solar Simulator. NASA TN D-2562, 1965.

4. Collins, D. R., and Sah, C. T.: Effects of X-Ray Irradiation on the Characteristics of Metal-Oxide-Silicon Structures. Appl. Phys. Lett., vol. 8, no. 5, Mar. 1966, pp. 124-126.

5. Zaininger, K. H.: Electron Bombardment of MOS Capacitors. Appl. Phys. Lett., vol. 8. no. 6, Mar. 1966, pp. 140-142.

6. Srour, J. R., et al.: Damage Coefficients in Low Resistivity Silicon. (NRTC-75-23R, Northrup Research and Technology Center; NASA Contract NAS3-17849.) NASA CR-134768, 1975.

7. Downing, R. G.: The Energy Dependence of Electron Damage in Silicon. Proceedings of the Fourth Photovoltaic Specialists Conference, Vol. 1: Radiation Effects on Solar Cells and Photovoltaic Devices. (PIC-SOL-209/5, Pennsylvania Univ.; NASA Contract NASR-191.) NASA CR-58680,1964, pp. A-5-1 to A-5-33.

TABLE I. - TYPES OF HIGH-OPEN-CIRCUIT-VOLTAGE CELLS

[Base resistivity ≈ 0.1 ohm-cm; all cells n on p.]

	Ion implanted	High-low emitter	Diffused
Oxide	SiO_2	SiO_2 + charge near interface	None
Oxide depth, μm	0.1	0.01	----
n-layer depth, μm	0.2 - 0.3	10	1.5 - 2
Cell thickness, μm	300	260	200

TABLE II. - PRE-ELECTRON-IRRADIATION AMO CELL PARAMETERS

Cell type	Open-circuit voltage, V_{oc}, mV	Short-circuit current, I_{sc}, mA/cm^2	Maximum power, P_{max}, mW/cm^2	Fill factor, percent	Pre-irradiation diffusion length, L_0, μm	X-irradiated	
						Yes	No
Ion implanted	636	34.4	14.4	65.8	---		X
	636	35.5	14.5	64.1	158	X	
Diffused	626	20.3	9.3	73.3	279	X	
	623	19.8	9.2	74.4	158	X	
HLE	634	31.2	13.5	68	---		X
	640	28.6	14	76.5	47	X	

TABLE III. - DIFFUSION-LENGTH DAMAGE COEFFICIENTS

(a) Present data

Cell type	Diffusion-length damage coefficient, K
Ion implanted	8×10^{-10}
Diffused	9×10^{-10}
HLE	10×10^{-10}

(b) Previous data - 0.1-ohm-cm cells

Research	Diffusion-length damage coefficient, K
Srour, et al. (ref. 6), 1974	7×10^{-10} to 8×10^{-10}
Lewis data (unpublished), 1973	9×10^{-10}

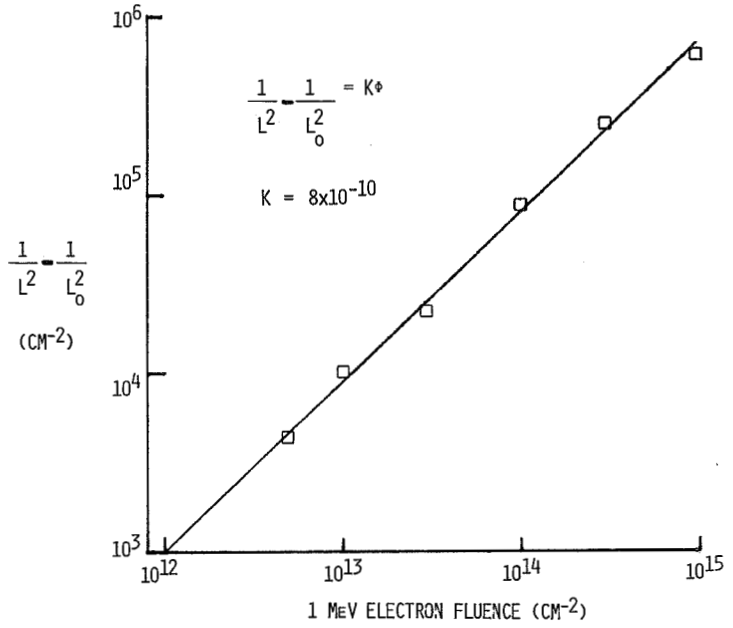

Figure 1. - Diffusion length as function of fluence for ion-implanted cell.

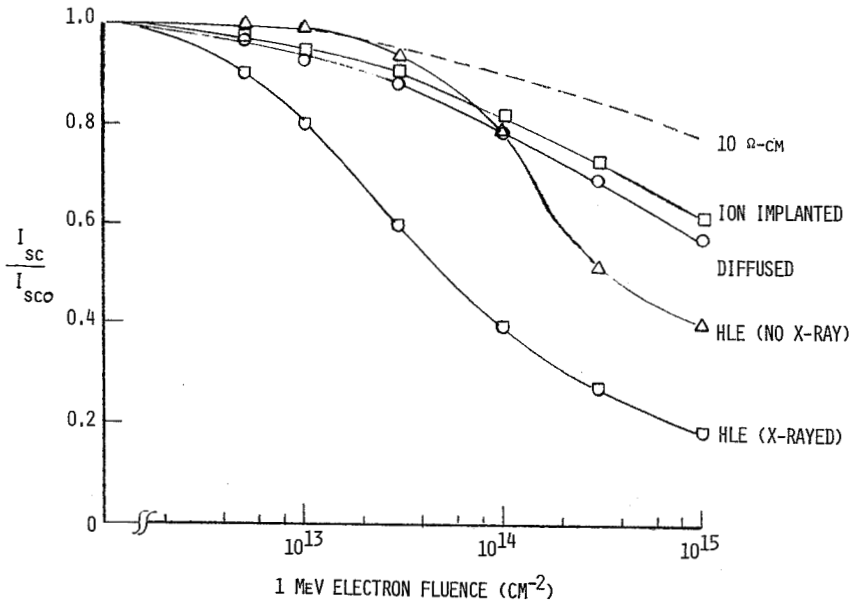

Figure 2. - Normalized I_{sc} versus electron fluence.

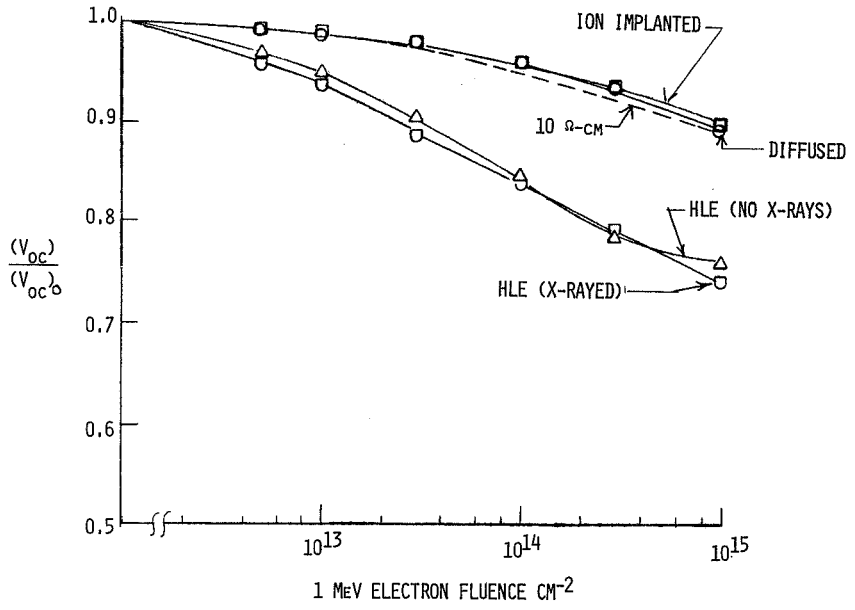

Figure 3. - Normalized V_{OC} electron fluence.

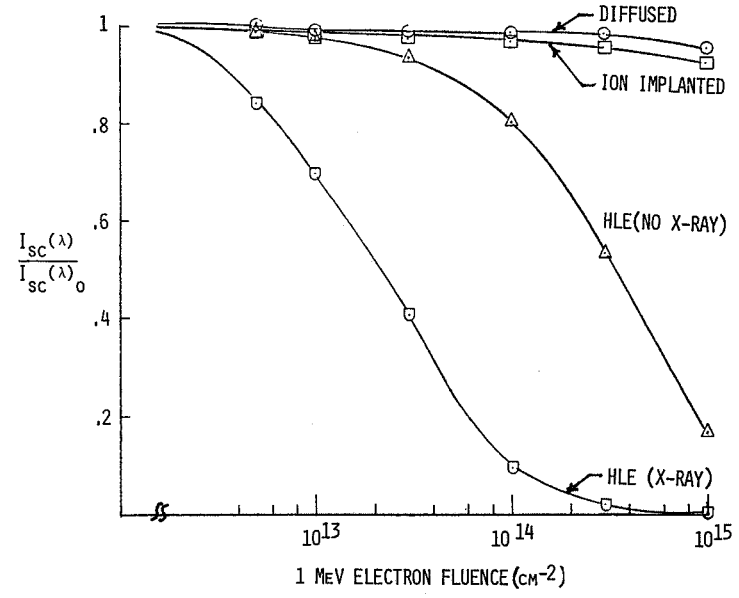

Figure 4. - Normalized spectral response at short wavelength. Wavelength, 0.45 micrometers.

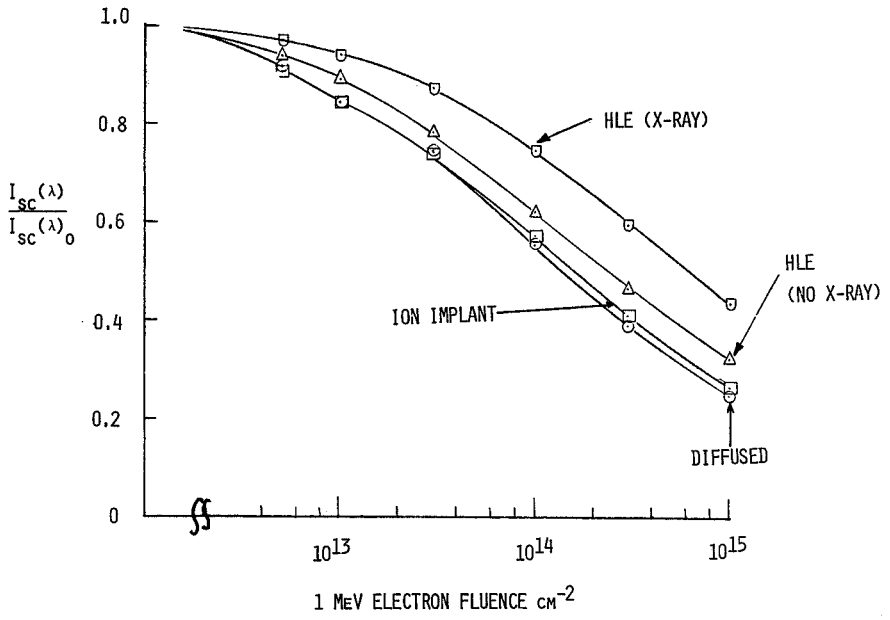

Figure 5. - Normalized spectral response at long wavelength (0.9 μm) after irradiation with 1-MeV electrons.

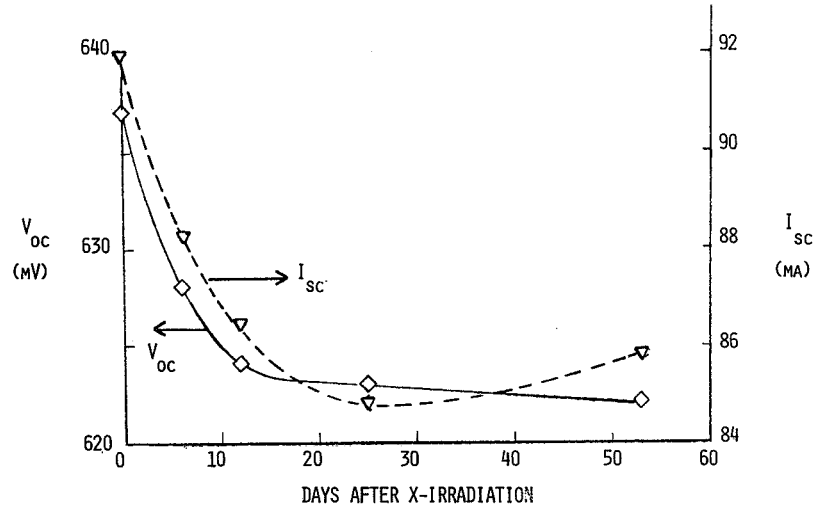

Figure 6. - Voltage and current decay in HLE cell exposed to x-irradiation only.

CO_2 LASER ANNEALING OF 50- μm-THICK SILICON SOLAR CELLS

Frank E. Walker
Boeing Aerospace Company

SUMMARY

A test program is currently being conducted to determine thin solar cell annealing effects using a laser energy source. A CO_2 continuous-wave (CW) laser has been used in annealing experiments on 50- μm-thick silicon solar cells after proton irradiation. Test cells were irradiated to a fluence of 1.0×10^{12} protons/cm^2 with 1.9 MeV protons. After irradiation, those cells receiving full proton dosage were degraded by an average of 30% in output power. In annealing tests laser beam exposure times on the solar cell varied from 2 seconds to 16 seconds reaching cell temperatures of from 400°C to 500°C. Under those conditions annealing test results showed recovery in cell output power of from 33% to 90%.*

INTRODUCTION

Past investigations have shown positive annealing effects when radiation damaged silicon solar cells were heated to above 400°C for longer than 10 minutes (ref. 1 and 2). More recently, manufacturing process induced defects in semiconductors have been annealed using directed beam energy to obtain the desired annealing time and temperature (ref. 3). The coherent beam of a laser may provide an ideal energy source for solar cell annealing space applications

*This work has been supported by NASA under Contract NAS9-15636.

where annealing ovens or array enclosures (ref. 4) might not be practical. A laser provides the added benefit of directing the annealing beam to any portion of a large array when required (such as a Solar Power Satellite). This would allow the annealing device to scan the array continuously without disrupting panel power generation as only a small segment of the array is affected. In-situ annealing of solar arrays in space has been a topic of technical scrutiny for some time.

BACKGROUND

Preliminary laser annealing studies were conducted to determine feasibility of laser annealing principles as applied to the annealing of radiation damage in silcon solar cells.* These studies showed positive annealing results for uncovered solar cells annealed with a scanned DC electron beam (fig. 1) and with a pulsed Nd:YAG laser (fig. 2). Glass covered solar cells with electrostatically bonded (ESB) Corning 7070 cover glasses were annealed using a CO_2 laser (fig. 3). These early solar cell laser annealing tests involved exposure periods of from 10 μsec for the electron beam to 2 sec for the CO_2 laser. No attempt was made to optimize beam parameters or to determine what effect, if any, the short duration, high intensity laser exposure had on the cell or the annealing process (ref. 5).

LASER ANNEALING OF THIN CELLS

Further testing of solar cell annealing using a CO_2 laser has been conducted to address the questions of laser beam effects on solar cells and reproducibility of laser annealing in an individual cell. In particular, 50-μm-thick solar cells were tested as a low mass advanced cell with potential for application in the development of large space power generating systems. Solar cell types used in the annealing tests are described in table 1.

---

*This work was performed by Spire Corp., Bedford, MA, under contract to Boeing Aerospace Company, Seattle, WA.

Initial laser annealing test parameters were derived from thermodynamic analysis of a 50- μm-thick silicon solar cell with a 50- μm-thick integral-glass cover. This steady state thermodynamic model shows in figure 4 the laser beam energy density required to maintain a desired annealing temperature. The amount of time required for a laser beam to raise the temperature of a solar cell, as a function of laser beam energy density, from room temperature (28°C) to an annealing temperature of 500°C is plotted in figure 5. Although early theoretical analysis was done for a 50- μm-thick cell with 50-μm-thick integral-glass cover, unglassed 50- μm-thick solar cells were used in these annealing tests as integral-glass covers on thin cells are not completely developed.

TEST PROCEDURES

Figure 6 shows schematically the test set-up. A CO_2 laser capable of greater than 150 watts CW was used as the laser source. A mechanical shutter was used which utilizes two knife edge shutter leaves and a light emitting diode, photo cell to generate a pulse of laser radiation and an electrical timing pulse, respectively. The electrical pulse was measured with a counter to determine the exact laser beam pulse length. With the shutter held open, a sampling mirror was placed in the beam to deflect the beam into the reference power transducer which was used to measure the total raw beam power as a reference.

A zinc selenide lens with a 5.0 inch focal length was used to spread the beam. Distance C in figure 6 was adjusted to give the required power density at the test plane.

The beam travels through a motor-driven mirror arrangement which was computer controlled and can be used for aligning and centering the beam and for scanning the beam across the aperture plate (2mm aperture) to provide power density profile maps of the beam. The laser test facility and Coherent Optics, Everlase 150 laser with the test set-up on the work table above the laser cabinet are pictorially illustrated in figure 7.

Electrical parameters of each cell are measured before and after every test to provide comparative test parameters. A Spectrolab X-25 Mark II solar simulator provides illumination on the test cell during electrical measurements.

Each cell is electrically degraded by irradiation of 1.9 MeV protons to a fluence of 1.0×10^{12} protons/cm^2 at Boeing's Radiation Effects Laboratory.

EVALUATION OF ELECTRICAL DEGRADATION IN UNIRRADIATED TEST CELLS DUE TO LASER EXPOSURE

Before formal laser annealing tests began, 50- μm-thick solar cell test specimens were subjected to various laser intensities and exposure durations to determine the mechanical effects of thermal shock during laser irradiation. Unglassed 50-μm-thick solar cells were found to physically deform in an unpredeterminable fashion above 300°C when subjected to a laser beam. Upon measuring electrical characteristics (figs. 8 and 9) of test cells after a 5 second, 100 watt CO_2 laser exposure that raised the cell temperature to 500°C, no reduction in the solar cells' electrical characteristics was apparent within measurement tolerances.

RESULTS AND DISCUSSION

Figures 10 through 16 illustrate laser annealing of charged-particle irradiated Solarex and O.C.L.I. 50- μm-thick solar cells. Each cell was to be irradiated with 1.9 MeV protons to a fluence of 1.0×10^{12} protons/cm^2; however cells No. 18, 19, 31 and 32 did not receive full irradiation fluence due to a malfunction of the proton source during the irradiation portion of the test sequence. Cells No. 18 and 32 had reduced outputs after the laser anneal portion of the test due to cell damage. Cell No. 18 was broken and 25% of the cell was lost. Cell No. 31 curled during laser exposure to such an extent that accurate measurement in our solar simulation test facility was not possible.

The average cell degradation in output power due to irradiation was 30%. Recovery of output power as measured at the maximum power point varied from 33% to 90% after laser annealing. Cells that were moderately degraded appeared to recover more completely than those more severely damaged. There was some indication that longer exposure to the annealing temperature was beneficial.

Figure 17 illustrates repeated annealing under the same test conditions as applied to those solar cells depicted in figures 10 through 16. Note that this cell did not recover as completely after the second annealing as it did after the first.

Figure 18 is a summary of output power variations, at the maximum power point, after each step of the annealing test sequence for all cells except cells No. 18 and 32 which were damaged during laser exposure.

Test cells were exposed to temperatures greater than 500°C for various time periods; however, no annealing data was obtained as cells tested above 500-600°C were broken as a result of severe mechanical deformation of the cell. The suspect cause of this effect is thermal expansion differences between the silicon of the cell and the metal of the cell back contact. This back contact covers the entire back of the cell having a greater effect than the metal grid on the front cell surface.

CONCLUSIONS

Laser annealing of thin cells shows promise; however, basic design alterations are required to minimize thermal shock effects of short duration, high intensity laser pulses on the 50- μm-thick solar cell. Further studies of annealing temperature and duration of laser annealing on thermo-mechanically stable thin cells are suggested.

REFERENCES

1. Fang, P. H.: Thermal Annealing of Radiation Damage in Solar Cells. Astronautica Acta, Vol. 13, No. 2, pg 147-157, 1967

2. Faraday, B. J., Statler, R. L., and Tauke, R. V.: Thermal Annealing of Proton-Irradiated Silicon Solar Cells. Proceedings of the IEEEE, Vol. 56, No. 1, pg 31-37, January 1968

3. Young, R. T., and Narayun, J.: Laser Annealing of Diffusion-Induced Imperfections in Silicon. Appl. Phys. Lett., 33(1), pg 14-15, 1 July 1978

4. Fang, P. H., Meszaros, G.; and Gdula, W. G.: Recovery of Radiation Damaged Solar Cells Through Thermal Annealing. Patent No. 3,597,281, Aug. 3, 1971

5. Minucci, J. A.; Matthei, K. W.; Kirkpatrick, A. R.; and Oman, H.: In-Situ Annealing of Space Radiation Damage. Thirteenth IEEE Photovolatic Specialists Conference, pg 586-589, 1978

6. Walker, F. E.: Silicon Solar Cell Annealing Test. NASA Report No. D180-25037-4 under Contract NAS9-15636, 1979

MANUFACTURER	THICKNESS (μm)	CELL DIMENSIONS (cm)	SURFACE FINISH	BASE RESISTIVITY	JUNCTION DEPTH	A. R. COATING	BACK SURFACE FIELD	ELECTRICAL CONTACTS	MEASURED MEAN EFF. (%)
SOLAREX	50	2 x 2	Chemical Etch	2Ωcm	2-3μm	Ta_2O_5	Compensated Back Surface Field	Ti-Pd-Ag Chevron	10.22
O.C.L.I.	50	2 x 2	Chemical Etch	2Ωcm	2-3μm	OCLI Multi-layer Coating	Back Surface Field	Ti-Pd-Ag Grid	10.28

Table 1 ; Test Sample Description

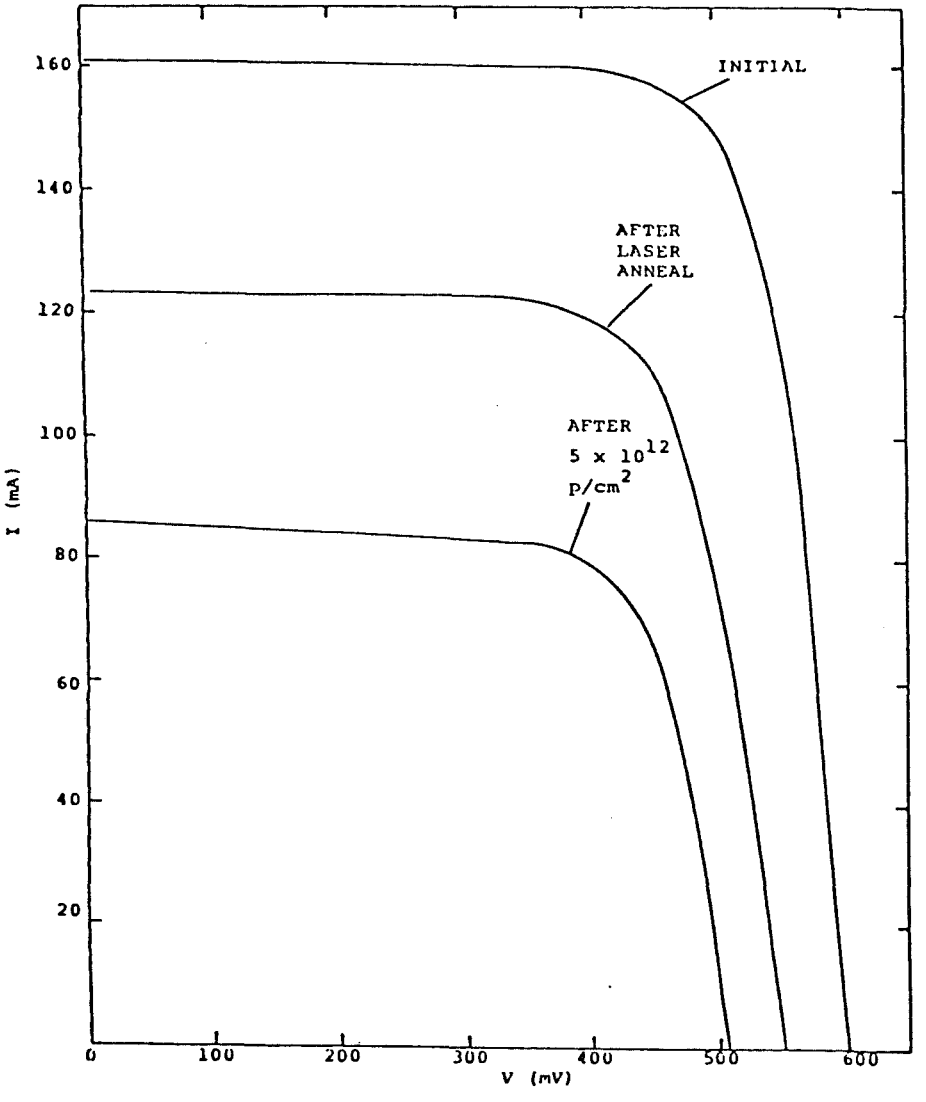

Figure 1 ; The Effect of Pulsed Laser Anneal on Violet Cell 12E

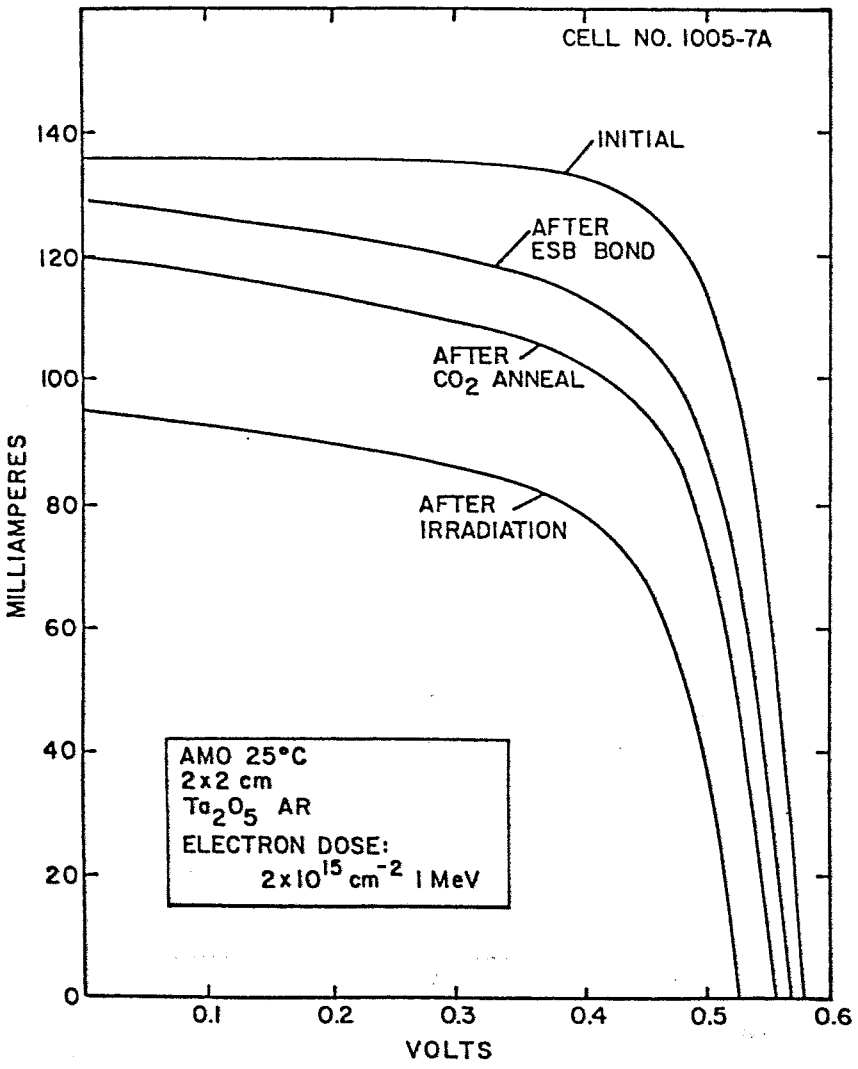

Figure 2; I-V Characteristics of Cells with ESB 7070 Coverglass After Electron Irradiation and After CO_2 Laser Anneal

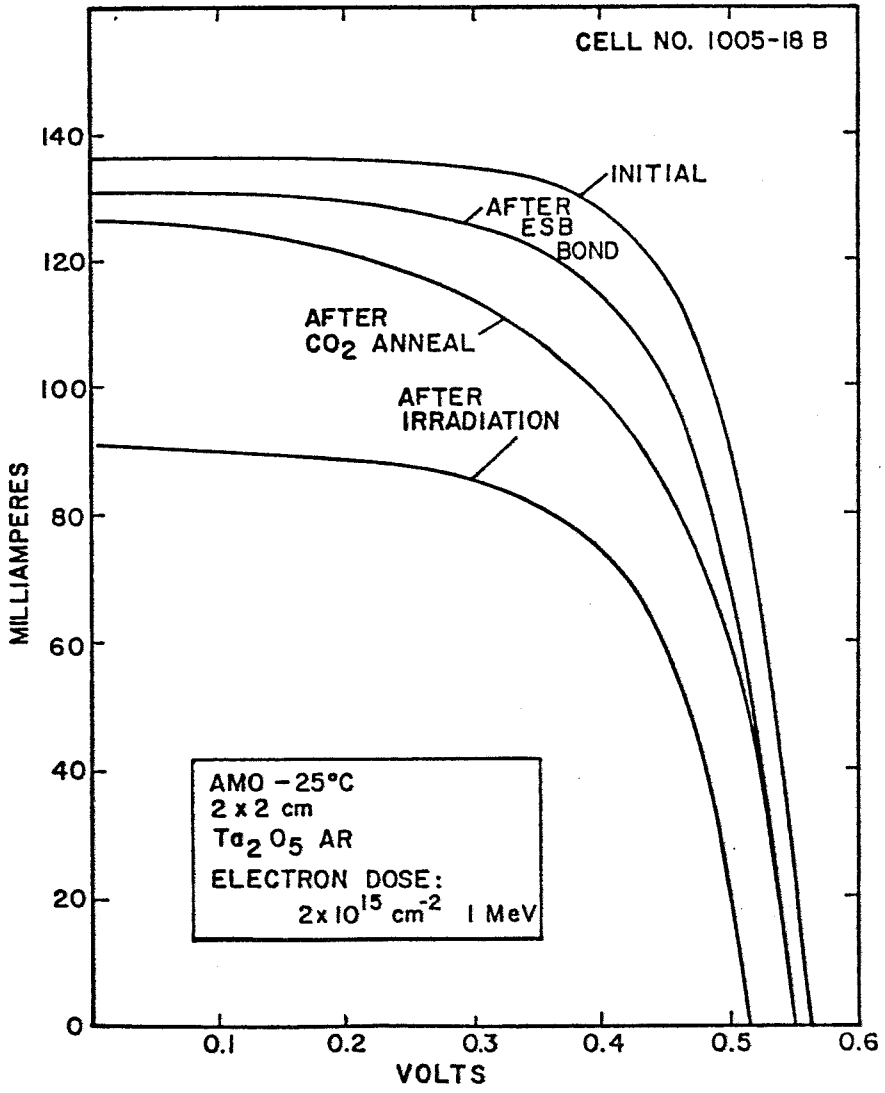

Figure 3; I-V Characteristics of Cell with ESB Coverglass After Electron Irradiation and After CO_2 Laser Anneal

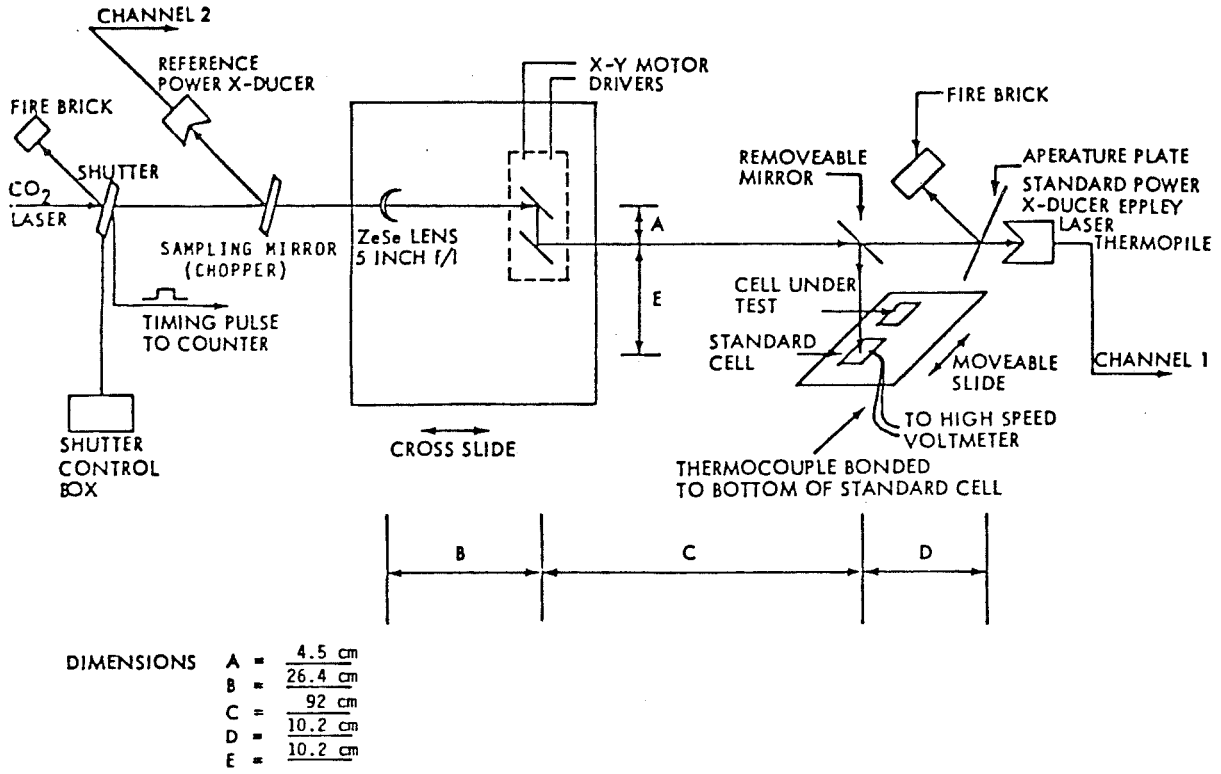

Figure 4; Laser Annealing of Solar Cells — Test Schematic

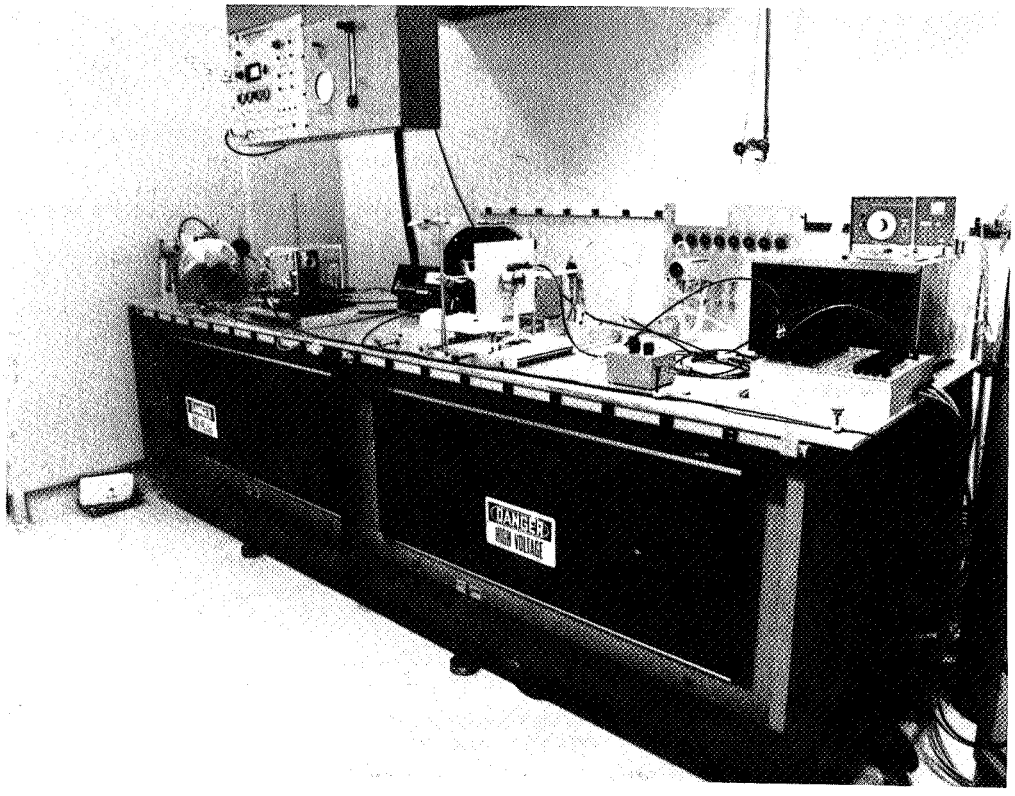

Figure 5; Laser Annealing Test Setup With Coherant Optics Everlase 150 CO_2 Laser

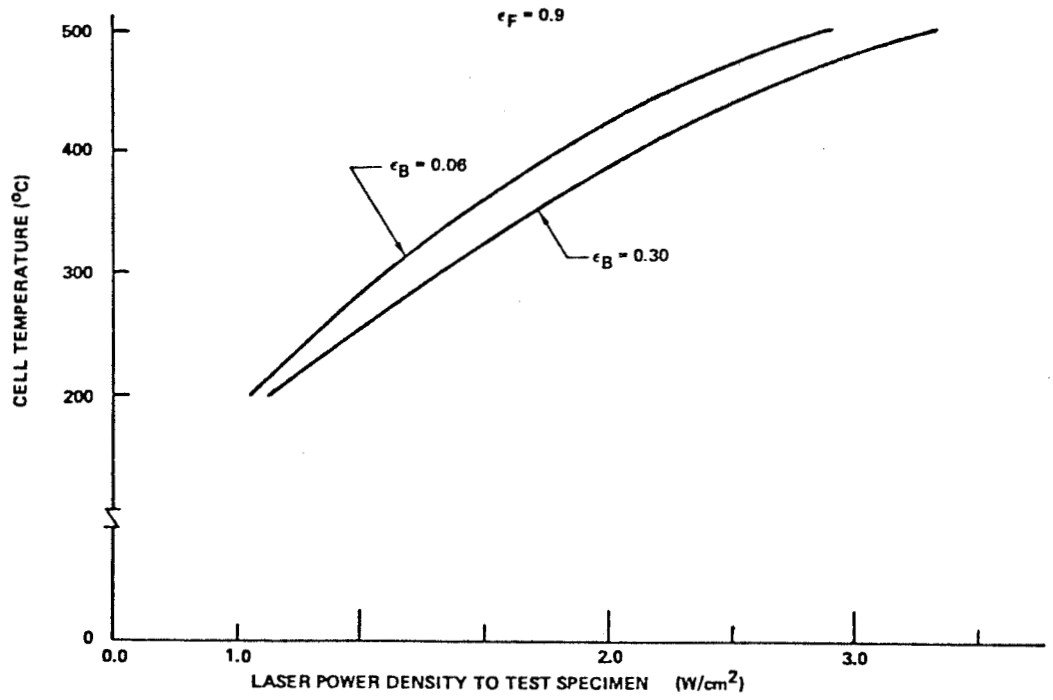

Figure 6; Steady State Temperature Resulting From Different Energy Densities in a 50-μm-Thick Solar Cell With 50-μm-Thick Integral Glass Cover

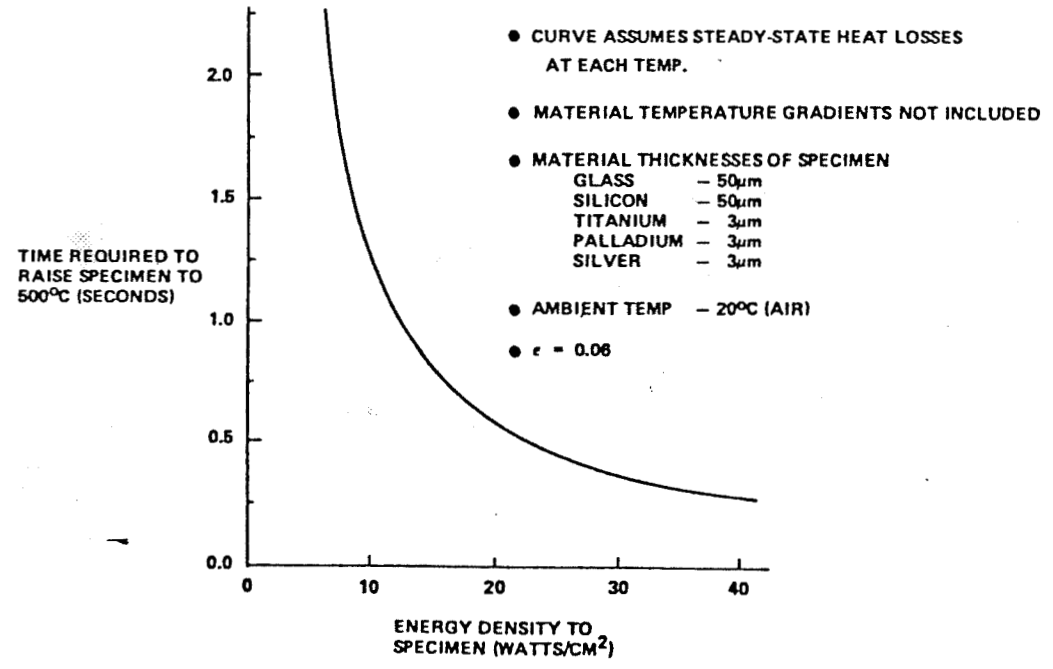

Figure 7; Time to Temperatore (500°C) Curve For Different Energy Densities In A 50-μm-Thick Silicon Solar Cell With 50-μm-Thick Integral Glass Cover

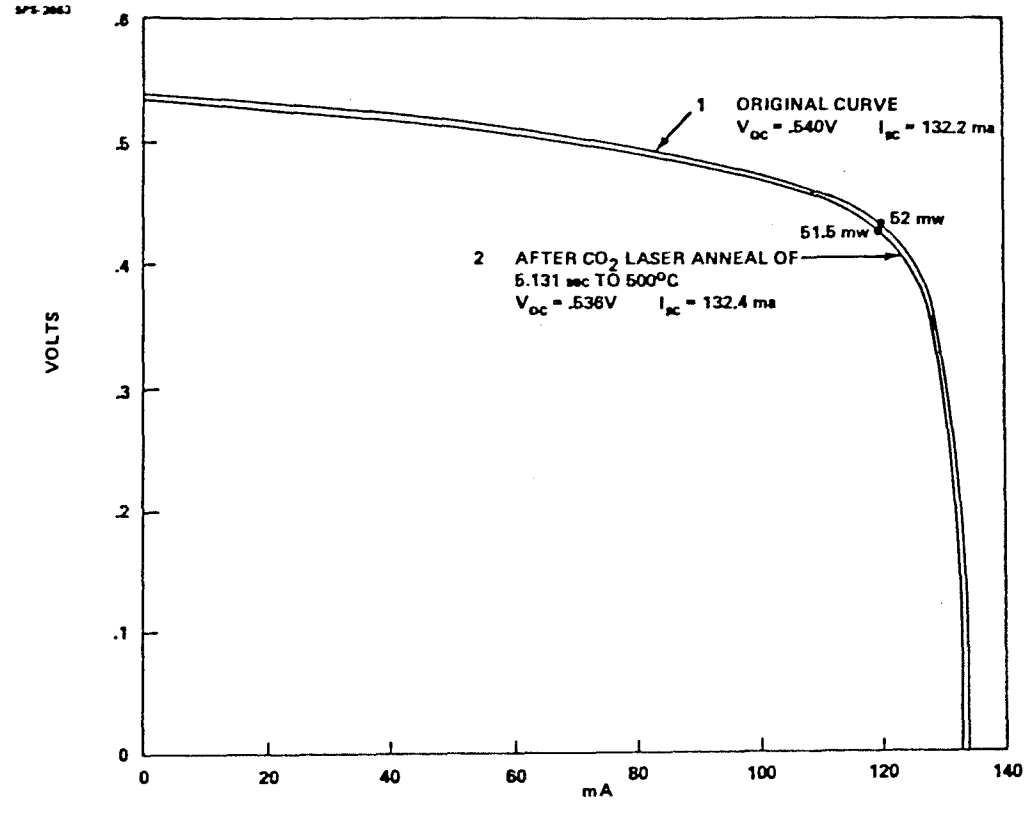

Figure 8 ; CO_2 Laser Annealed Solar Cell Without Coverglass, Solarex Cell No. 44

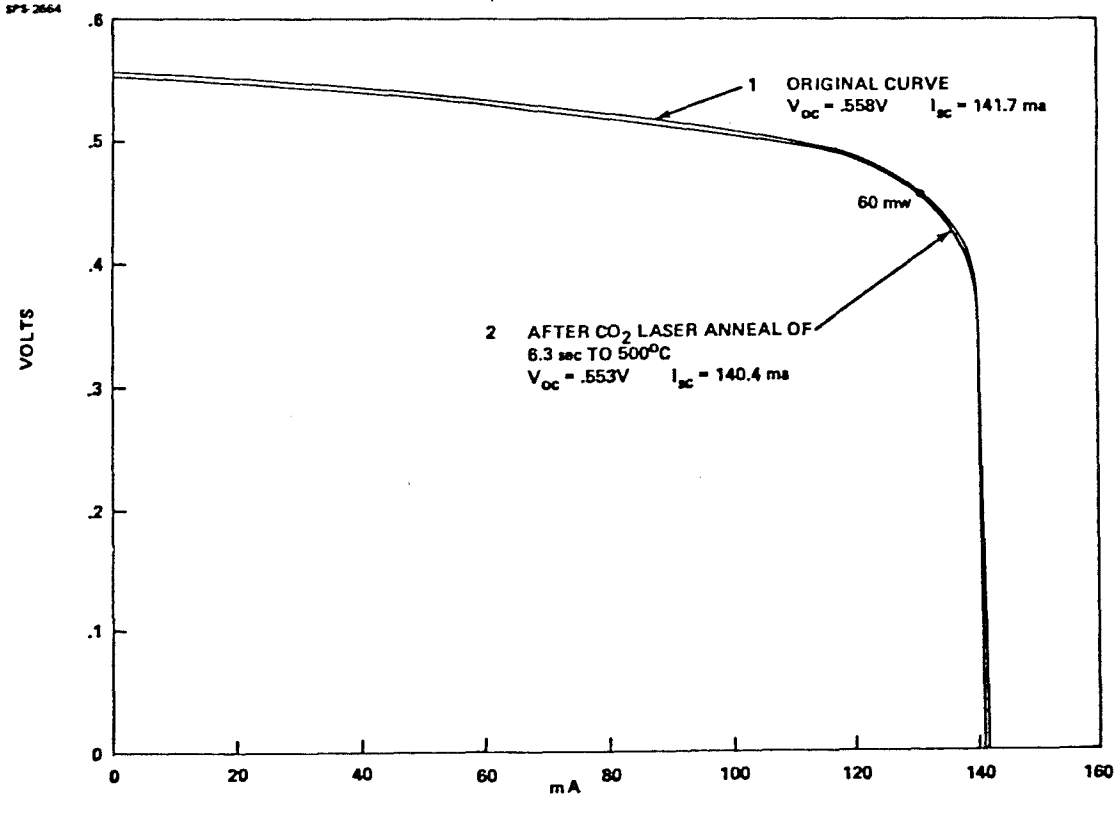

Figure 9 ; CO_2 Laser Annealed Solar Cell Without Coverglass, Solarex Cell No. 45

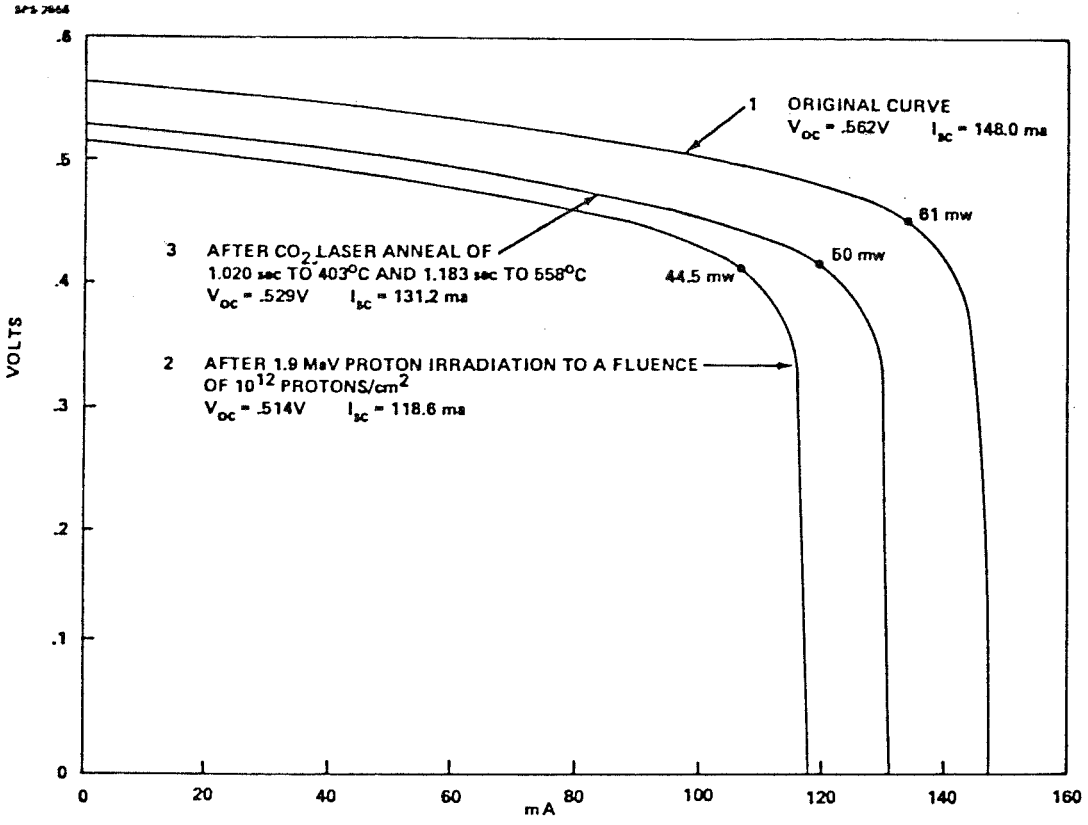

Figure 10; CO_2 Laser Annealed Solar Cell Without Coverglass, Solarex Cell No. 16

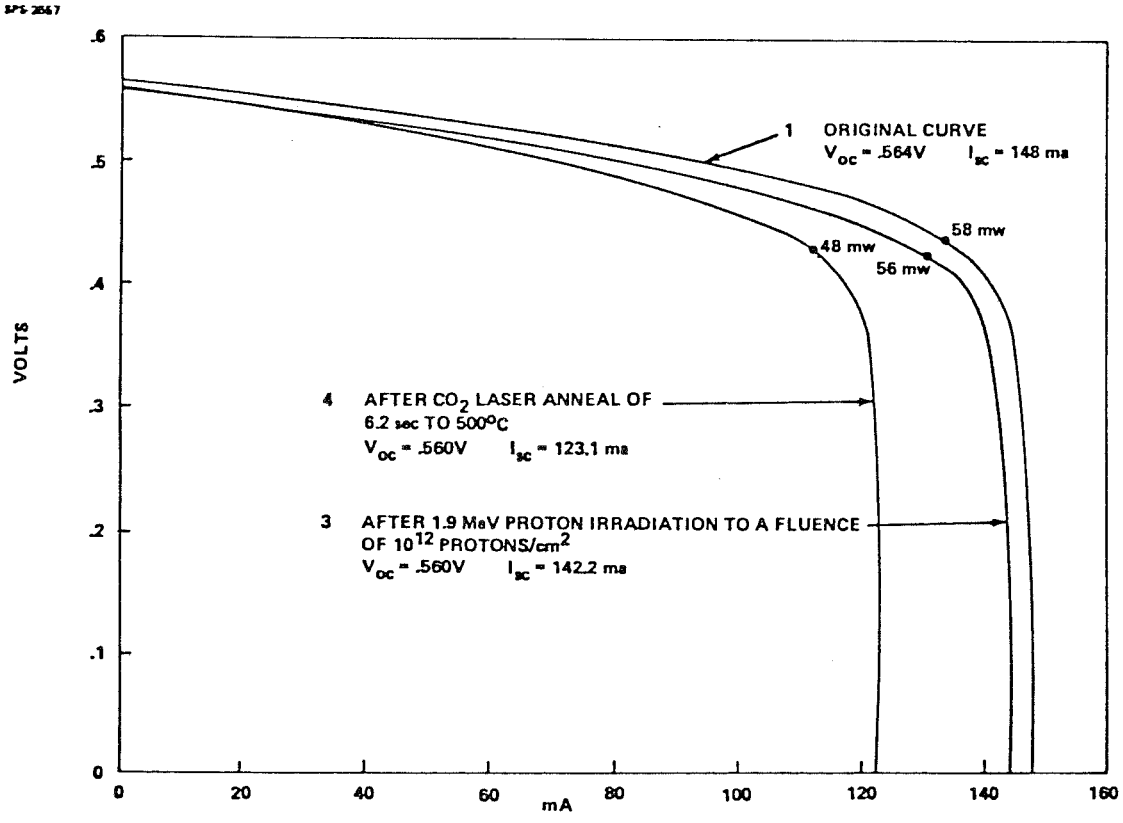

Figure 11; CO_2 Laser Annealed Solar Cell Without Coverglass, Solarex Cell No. 18

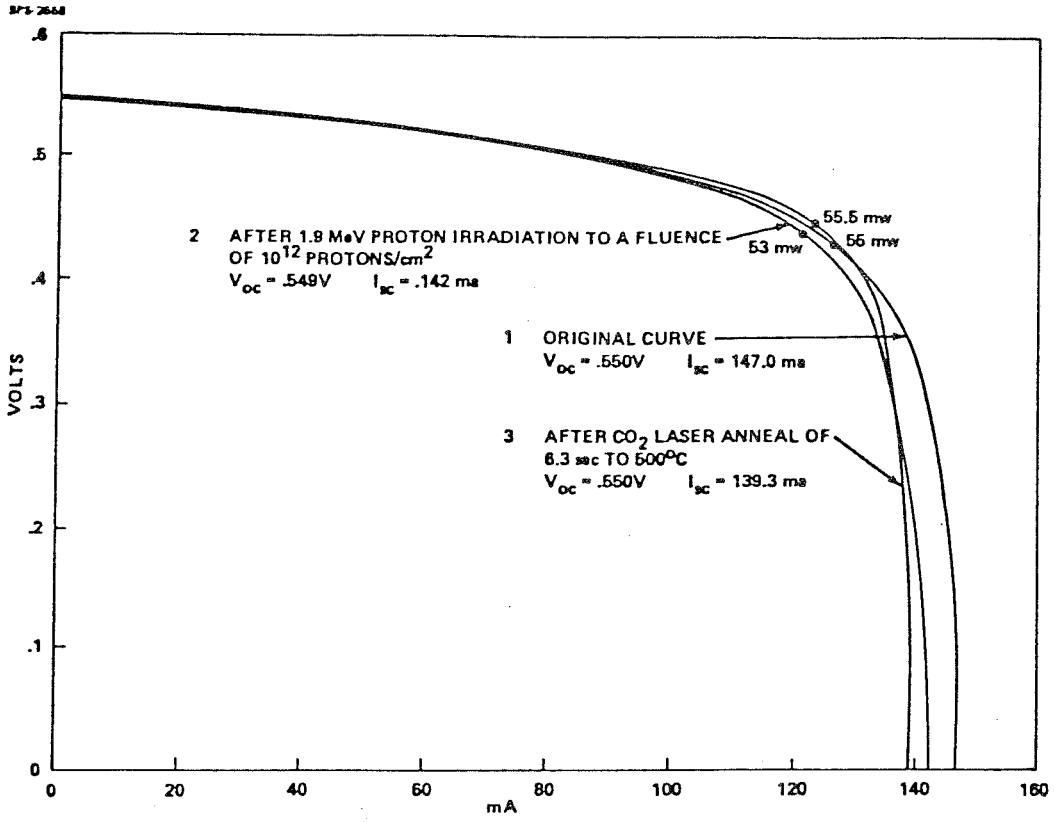

Figure 12; CO_2 Laser Annealed Solar Cell Without Coverglass, Solarex Cell No. 19

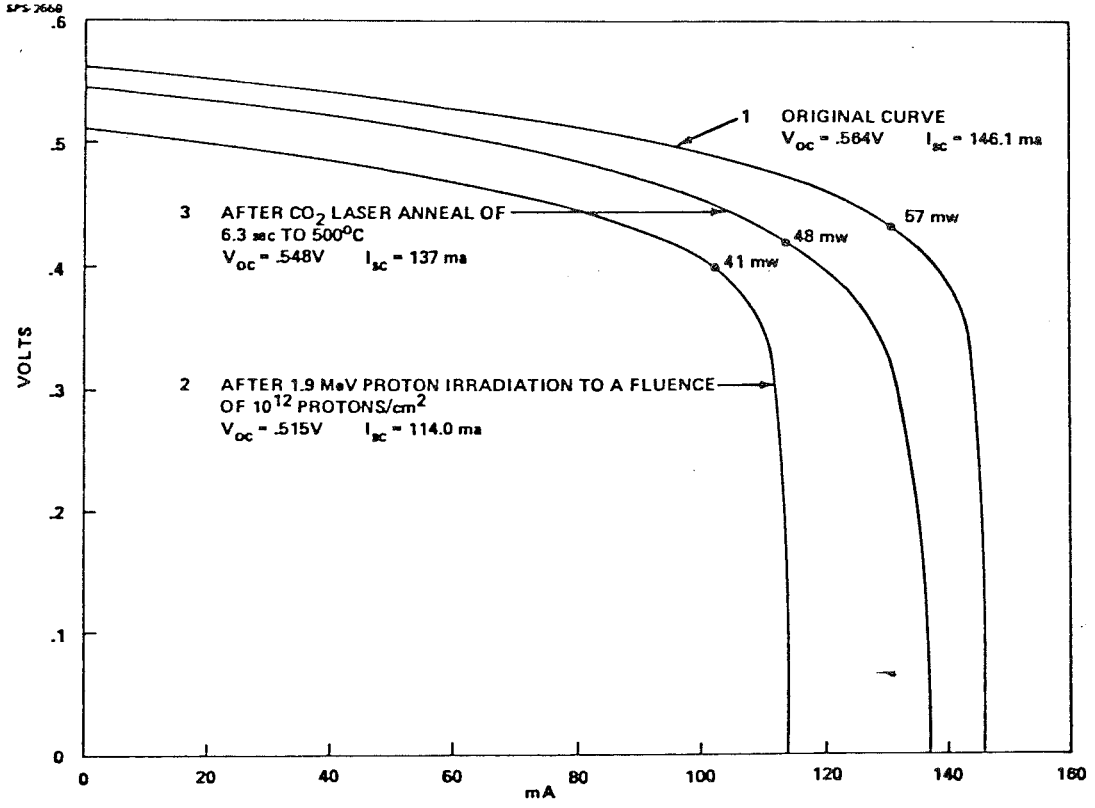

Figure 13; CO_2 Laser Annealed Solar Cell Without Coverglass, Solarex Cell No. 20

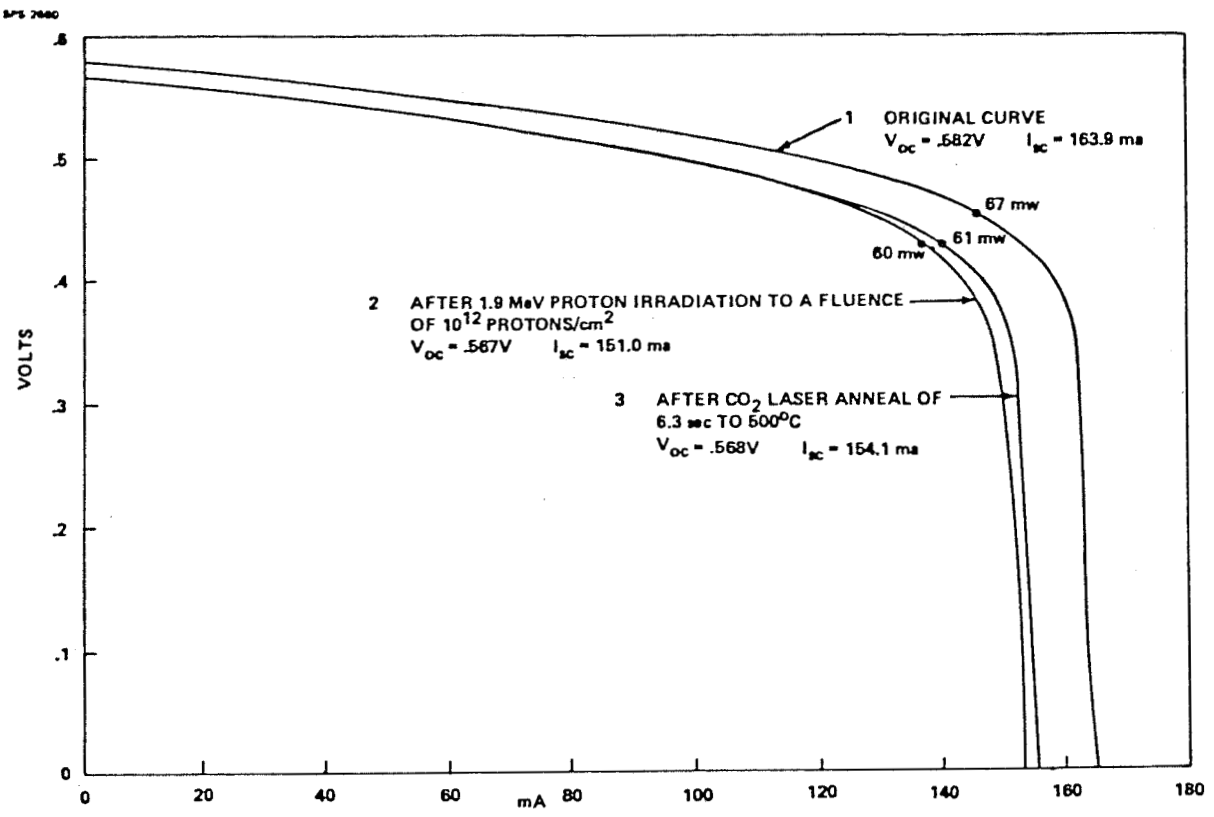

Figure 14; CO_2 Laser Annealed Solar Cell Without Coverglass, O.C.L.I. Cell No. 31

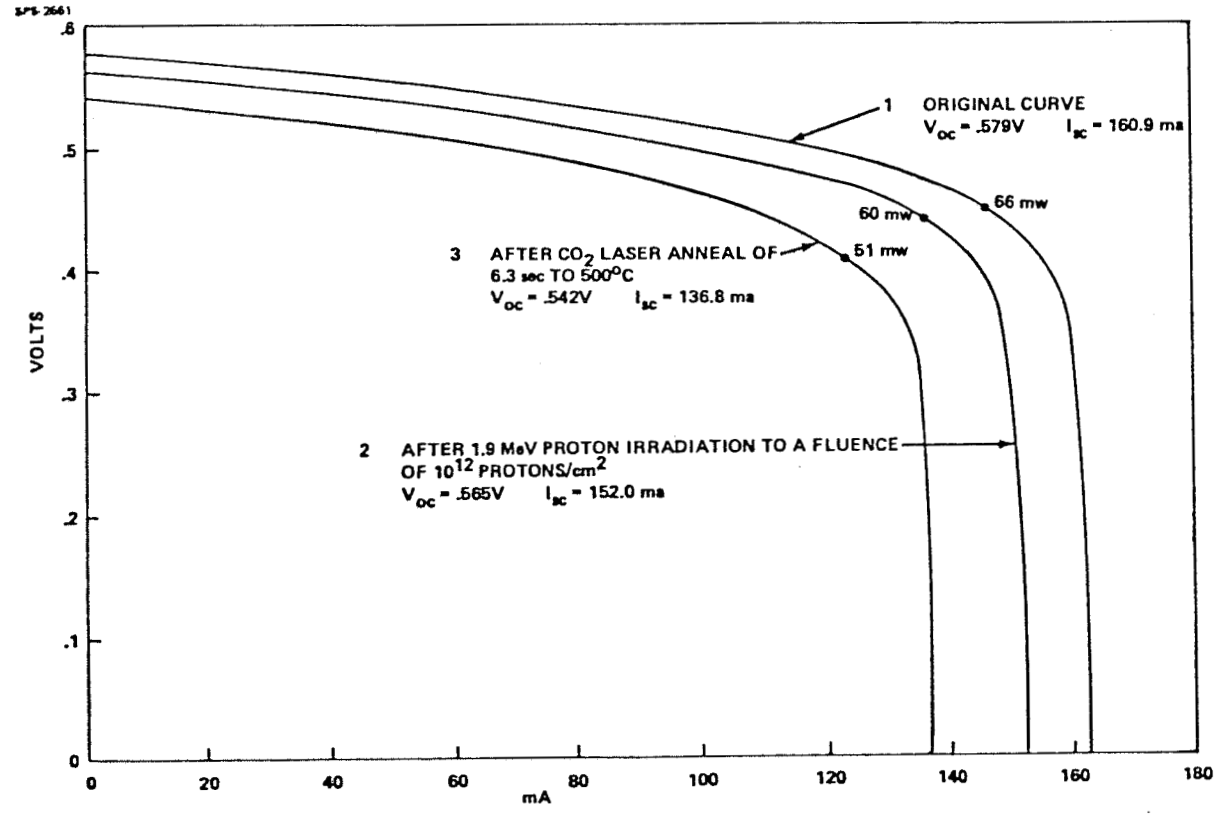

Figure 15; CO_2 Laser Annealed Solar Cell Without Coverglass, O.C.L.I. Cell No. 32

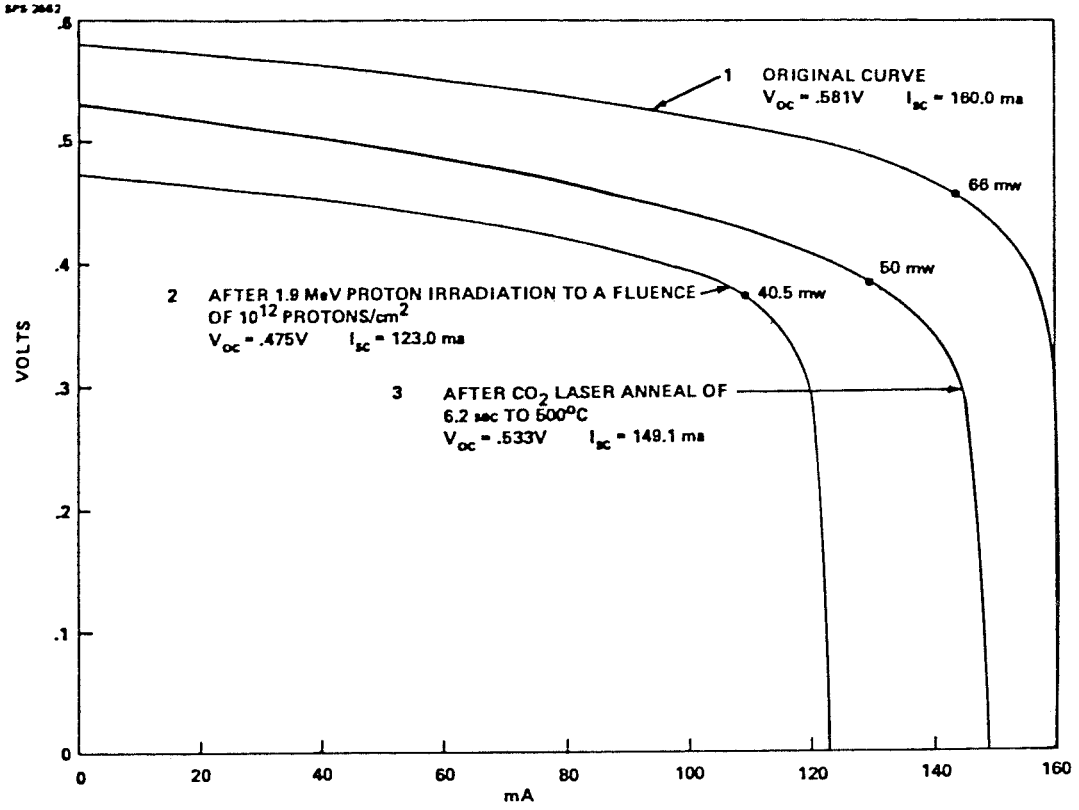

Figure 16; CO_2 Laser Annealed Solar Cell Without Coverglass, O.C.L.I. Cell No. 33

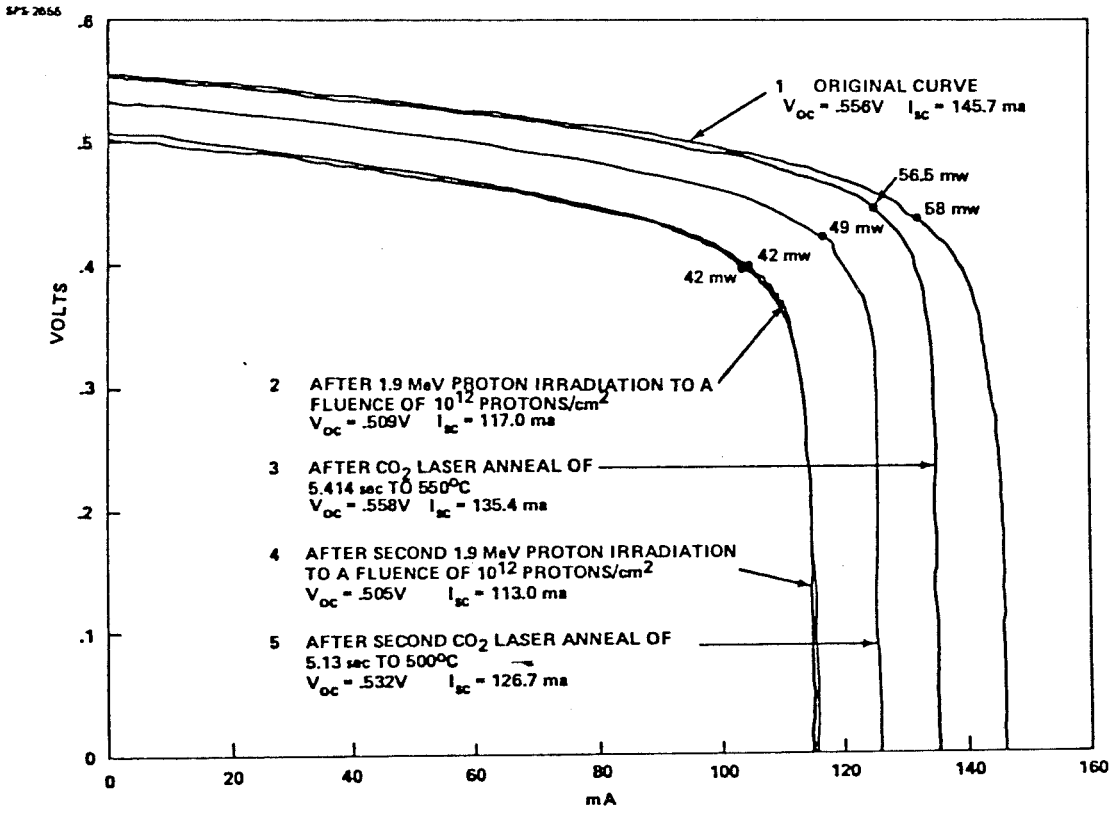

Figure 17; CO_2 Laser Annealed Solar Cell Without Coverglass, Solarex Cell No. 13

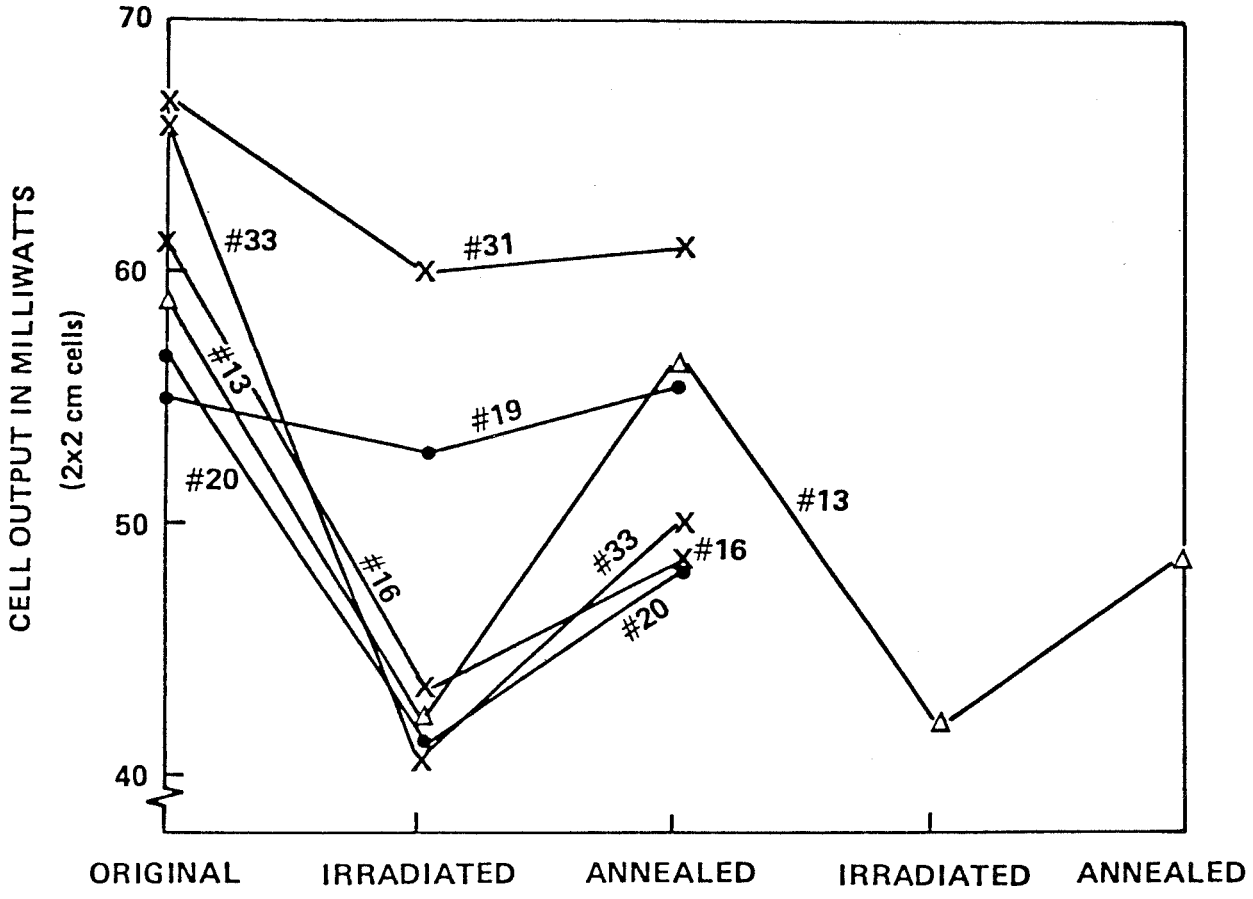

Figure 18; Degradation and Recovery of Maximum Power for Laser Annealed Solar Cells

REVERSE ANNEALING IN RADIATION-DAMAGED, SILICON SOLAR CELLS

Irving Weinberg and Clifford K. Swartz
National Aeronautics and Space Administration
Lewis Research Center

INTRODUCTION

The phenomenon of reverse annealing has been observed in bulk silicon (ref. 1) and in silicon solar cells (refs. 2 and 3). To date, however, attempts to understand this detrimental effect, in terms of the defects formed by particulate radiation, have been unsuccessful. Recently, however, sensitive instrumental techniques have been used to gain increased insight into the behavior of defects formed in p-type silicon by particulate radiation (refs. 4-7). Hence, in the present work, we report results using relatively new information regarding defect formation in boron doped silicon (refs. 6 and 7) in calculations which tend to clarify and explain the reverse annealing effects we observe in silicon solar cells.

EXPERIMENTAL

Irradiations and isochronal annealing were performed on n^+p silicon solar cells with 0.1 and 2 ohm-cm boron doped base resistivities. Starting material for the 2 ohm-cm cell was Czochralski grown while the starting material for the .1 Ω-cm cell was vacuum float zone single crystal silicon. The cells were irradiated by 1 Mev electrons to a fluence of 10^{15} cm^{-2}. After irradiation, the cells were isochronally annealed in 50° C steps, the cells being held at each fixed temperature point for 20 minutes. Minority carrier diffusion lengths and AMO I-V measurements were obtained at room temperature before and after irradiation and after each step in the isochronal anneal. Diffusion lengths were measured by an X-ray excitation technique (ref. 8), while the AMO I-V measurements were obtained using a xenon-arc solar simulator. Isochronal annealing data are shown in figure 1 where it is seen that reverse annealing occurs for the 2 ohm-cm cell at temperatures above 150° C, but is absent in the 0.1 ohm-cm cell's data.

In order to understand these results in terms of properties of the radiation induced defects, we used a combination of our diffusion length measurements and defect data obtained from Deep Level Transient Spectroscopy (DLTS), (ref. 7). The pertinent diffusion length data for the cells of figure 1 are shown in figure 2, where L_T^{-2} is reciprocal diffusion length squared, measured at room temperature after isochronal anneal at temperature T, while L_{IRR}^{-2} is

reciprocal diffusion length squared measured at room temperature after irradiation and before annealing. The DLTS, isochronal annealing data for a 2 ohm-cm n^+p silicon solar cell are shown in figure 3, while figure 4 shows the DLTS data for a 0.3 ohm-cm cell (ref. 7). In figures 3 and 4, E_v is energy at the top of the valence band, while E_c is energy at the bottom of the conduction band. Regarding the cells used to obtain the DLTS data (ref. 7), starting material for the 2 Ω-cm cell was Czochalski grown boron-doped silicon, while that for the 0.3 Ω-cm cell was vacuum float zone boron-doped silicon.

THEORY

Derivation of Working Equation

To obtain an equation relating the present diffusion length data to defect parameters, such as carrier capture cross sections and relative defect concentrations, we use the Shockley-Read-Hall (SRH) theory of recombination (refs. 9 and 10). Our starting point is the SRH expression for τ_i the carrier lifetime due to the i^{th} single level defect. For low injection conditions we have (refs. 9 and 10)

$$\frac{1}{\tau_i} = \frac{N_i}{\frac{1}{v_p \sigma_{pi}}\left(\frac{n_o+n_1}{n_o+p_o}\right) + \frac{1}{v_n \sigma_{ni}}\left(\frac{p_o+p_1}{n_o+p_o}\right)} \tag{1}$$

Where N_i is the concentration of the i^{th} defect, n_o and p_o are equilibrium electron and hole concentrations, v_n and v_p are thermal velocities for electrons and holes, σ_{pi} and σ_{ni} are hole and electron capture cross sections for the i^{th} defect and n_i and p_i are calculated from the relations

$$n_1 = N_c \exp\left(\frac{E_i - E_c}{kT}\right) \tag{2a}$$

$$p_1 = N_v \exp\left(\frac{E_v - E_i}{kT}\right) \tag{2b}$$

Where N_c and N_v are the density of states for the conduction and valence bands k is the Boltzmann constant and Ei is the energy level of the i^{th} defect. The thermal velocities are obtained from the relations

$$v_p = \left(\frac{3kT}{m_h}\right)^{1/2} \tag{3a}$$

$$v_n = \left(\frac{3kT}{m_e}\right)^{1/2} \tag{3b}$$

Where m_h and m_e are hole and electron effective masses respectively.

For P type silicon p_o is measured and n_o calculated from the relation

$$n_o p_o = n_I^2 \tag{4}$$

Where n_I is the intrinsic carrier concentration.

Using equations 2, 3 and 4, we find for the defects in figures 3 and 5 that

$$\frac{p_o + p_1}{n_o + p_o} \approx 1$$

$$\frac{n_o + n_1}{n_o + p_o} \ll 1 \text{ , and}$$

$$v_n \approx v_p \approx 2 \times 10^7 \text{ cm/sec.}$$

Hence equation 1 simplifies to

$$\frac{1}{\tau_i} \approx N_i \sigma_{ni} v_n = N_{max} R_i \sigma_{ni} v_n \tag{5}$$

Where R_i is the relative concentration of the i^{th} defect with

$$R_i = \frac{N_i}{N_{max}} \tag{6}$$

N_{max} being the maximum defect concentration measured by DLTS during the isochronal anneal. For example in figure 3, N_{max} is obtained from the peak amplitude of the E_v + .38 defect (ref. 7).

Since

$$\frac{L_T^{-2}}{L_{IRR}^{-2}} = \frac{\left(\frac{1}{\tau}\right)_T}{\left(\frac{1}{\tau}\right)_{IRR}} = \frac{\left(\sum_i \frac{1}{\tau_i}\right)_T}{\left(\sum_i \frac{1}{\tau_i}\right)_{IRR}} \tag{7}$$

We obtain the required relation

$$\frac{L_T^{-2}}{L_{IRR}^{-2}} \approx \frac{\left(\sum_i R_i \sigma_{ni}\right)_T}{\left(\sum_i R_i \sigma_{ni}\right)_{IRR}} \tag{8}$$

Capture Cross Section

The capture cross sections obtained from DLTS (ref. 7), are listed in Table 1. Since the electron capture cross section σ_n for only one defect (E_c-0.27 eV) is available from DLTS, we cannot calculate diffusion length ratios from equation 8 using only this DLTS result. We have therefore obtained the necessary additional σ_n values by other methods.

With respect to the defects at E_v+0.38 and E_v+0.23, temperature dependent lifetime studies in 1.5 ohm-cm p-type silicon yield values for the ratio σ_n/σ_p from which σ_n is calculated (ref. 11). From reference 11, for the E_v+0.38 defect $\sigma_n/\sigma_p \approx 150$ and for the defect at E_v+0.23, $\sigma_n/\sigma_p \approx 1300$ from which the σ_n values for these defects shown in Table 2 are calculated. For the remaining defects, values for σ_n were computed by fitting equation 8 to the diffusion length data of figure 2 at 250 and 300° C using R_i values from figure 3. In this way, the electron capture cross sections for the defects at E_v+0.30 and E_v+0.26 were obtained. Thus, the required cross sections for all but the defect at E_v+0.2 eV are obtained for use in equation 8. Since we cannot evaluate σ_n for this latter defect, it is arbitrarily assumed that it can be ignored in subsequent calculations. Similar considerations apply to the E_v+0.48 defect in 0.3 ohm-cm p-silicon (fig. 4) i.e., since we cannot evaluate σ_n for this defect it is omitted from the calculations.

RESULTS

The L^{-2} ratios, for the 2 Ω-cm cell, calculated from equation 8, using relative concentrations from figure 3 and capture cross sections from Table 2 are shown in figure 5. From the figure it is seen that the calculated and measured values are in reasonable agreement. From these results, the defect responsible for the reverse annealing in 2 ohm-cm p-type silicon is identified as the defect at E_V+0.30 eV. Additional calculations were performed after conceptually removing this defect, using the remaining cross sections of Table 1 and the remaining relative concentrations of figure 3. The result is shown in figure 6.

Calculated values for the 0.3 ohm-cm cell using the data of Table 2 and figure 4 are shown in figure 7. These results indicate the absence of reverse annealing in this low resistivity cell and are in qualitative agreement with our data for the 0.1 ohm-cm cell. Removal of the E_V+0.30 defect results in calculated values shown by the dotted line of figure 7. Since no DLTS data are available for 0.1 ohm-cm p-type silicon, we interpret these 0.3 ohm-cm results as an indication of trends when going to lower resistivity p-type silicon.

DISCUSSION

The good agreement between our experimental and calculated values indicates the correctness of the mathematical relationship (equation 8) derived from the SRH theory. Our results indicate that the defect at E_V+0.30 eV is responsible for the observed reverse annealing. Furthermore, its removal could result in significant annealing at 200° C for the cells investigated. Since the E_V+0.30 defect always appears when the E_C-0.27 defect disappears (ref. 7) the two defects are related in the sense that the E_C-0.27 defect can be called the "parent" to the E_V+0.30 defect. Hence, the atomic constitution of both defects is of importance.

The defect at E +0.30 has been tentatively identified as a boron-oxygen-vacancy complex (ref. 7). The E_C-0.27 defect increases in concentration with increasing boron concentration and has been identified as a boron interstitial-oxygen interstitial complex (ref. 7). An alternate identification asserts that the E_C-0.27 defect is composed of a boron interstitial-boron substitutional pair (ref. 12). A firmer identification of the E_V+0.30 defect is required as well as additional research directed at choosing between competing identifications for the E_C-0.27 parent defect. Such identifications would be an invaluable guide to processing efforts aimed at decreasing the concentration of these radiation induced defects.

REFERENCES

1. Hasiguti, R. R.; and Ishino, S.: Defect Mobility and Annealing in Irradiated Germanium and Silicon. Seventh International Conference on the Physics of Semiconductors, Radiation Damage in Semiconductors, Vol. 3, P. Baruch, ed., Academic Press, N.Y., 1964, pp. 259-273.

2. Fang, P. H.; and Liu, Y. M.: Temperature Dependence of Radiation Damage in Silicon. Phys. Lett., vol. 20, no. 4, Mar. 1, 1966, pp. 344-346.

3. Fang, P. H.: Thermal Annealing of Radiation Damage in Solar Cells. NASA TM X-55399, 1965.

4. Miller, G. L.; Lang, D. V.; and Kimerling, L. C.: Capacitance Transient Spectroscopy. Annual Review of Materials Science, Vol. 7, R. A. Huggins, ed., Annual Reviews, Inc., 1971, pp. 377-448.

5. Lee, Y. H.; et al.: EPR and Transient Capacitance Studies on Electron-Irradiation Silicon Solar Cells. Solar Cell High Efficiency and Radiation Damage, NASA CP-2020, 1977, pp. 179-186.

6. Lee, Y. H.; Corbett, J. W.; and Browner, K. L.: EPR of a Carbon-Oxygen-Divacancy Complex in Irradiated Silicon. Phys. Stat. Sol., A, Vol. 41, 1977, pp. 637-647.

7. Mooney, P. M.; et al.: Defect Energy Levels in Boron-Doped Silicon Irradiated with 1-MeV electrons. Phys. Rev. B, vol. 15, no. 8, Apr. 15, 1977, pp. 3836-3843.

8. Rozenzweig, W.: Diffusion Length Measurements by Means of Ionizing Radiation. Bell Syst. Tech. J., vol. 41, no. 5, Sept. 1962, pp. 1573-1588.

9. Hall, R. N.: Electron-Hole Recombination in Germanium. Phys. Rev., vol. 87, no. 2, July 15, 1952, p. 387.

10. Shockley, W.; and Read, W. T., Jr.: Statistics of the Recombinations of Holes and Electrons. Phys. Rev., vol. 87, no. 5, Sept. 1, 1952, pp. 835-842.

11. Srour, J. R.; et al.: Radiation Effects on Semiconductor Materials and Devices. NRTC-73-46 R, Northrup Corp., 1973, p. 126. (HDL-TR-171-4, AD-776420)

12. Kimerling, L. C.: Defect States in Electron-Bombarded Silicon: Capacitance Transient Analysis. Radiation Effects in Semiconductors, N. B. Urli and J. W. Corbett, eds., Institute of Physics Conference Series No. 31, Institute of Physics (London), 1977, pp. 221-230.

TABLE I. - CAPTURE CROSS SECTIONS FROM DLTS

DEFECT ENERGY LEVEL (eV)	CAPTURE CROSS SECTIONS (cm^2)	
	σ_P	σ_N
E_V+0.38	$2x10^{-16}$	--
E_C-0.27	--	$2x10^{-13}$
E_V+0.23	$3x10^{-16}$	--
E_V+0.30	$2x10^{-16}$	--
E_V+0.26	--	--
E_V+0.2	--	--

TABLE II. - ELECTRON CAPTURE CROSS SECTIONS

ENERGY LEVEL OF DEFECT eV	ELECTRON CAPTURE CROSS SECTION (cm^2)	METHOD FOR OBTAINING CROSS SECTION
E_C-0.27	$2x10^{-13}$	DLTS
E_V+0.38	$3x10^{-14}$	*$\sigma_N/\sigma_P \sim 150$
E_V+0.23	$3.9x10^{-13}$	*$\sigma_N/\sigma_P \sim 1300$
E_V+0.30	$3.6x10^{-13}$	FIT OF $\frac{1}{L^2}$ RATIO TO DLTS (250° C)
E_V+0.26	$9.5x10^{-14}$	FIT OF $\frac{1}{L^2}$ RATIO TO DLTS (300° C)

*COMPUTED FROM σ_N/σ_P RATIOS FOR 1.5 Ω-cm P-TYPE (FZ) FROM SROUR, CURTIS, OTHMER, CHIU & DEOKAR: REPORT HDL-TR-171-4-U.S. ARMY

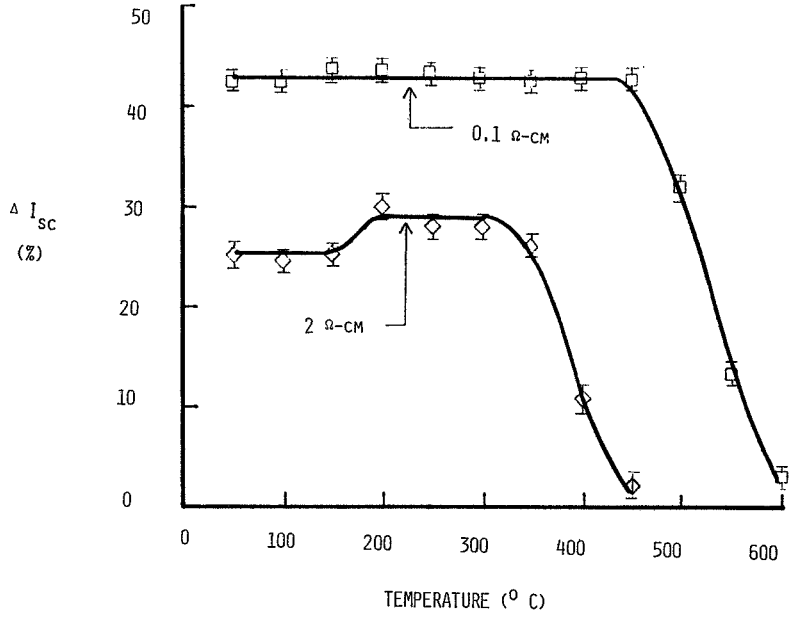

Figure 1. - Isochronal anneal of n^+p silicon solar cells after 1-MeV-electron irradiation. $\varphi = 10^{15}/cm^2$; time at temperature, 20 min.

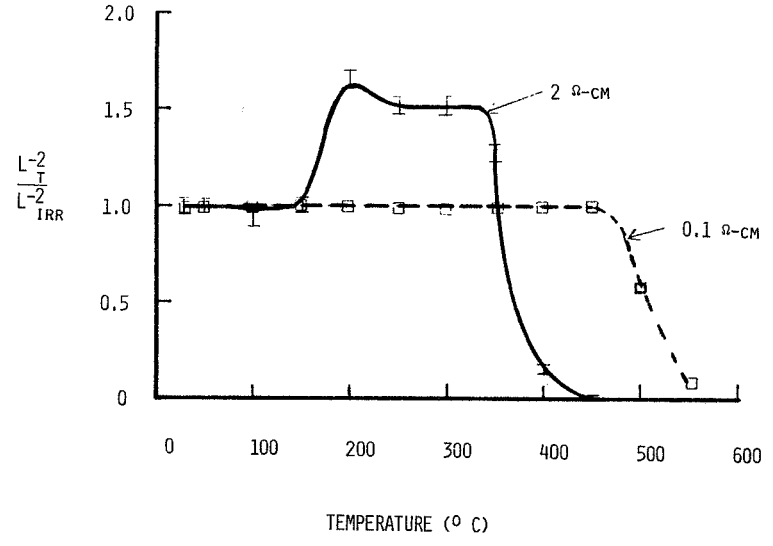

Figure 2. - $1/L^2$ ratios from diffusion lengths measured during isochronal anneal.

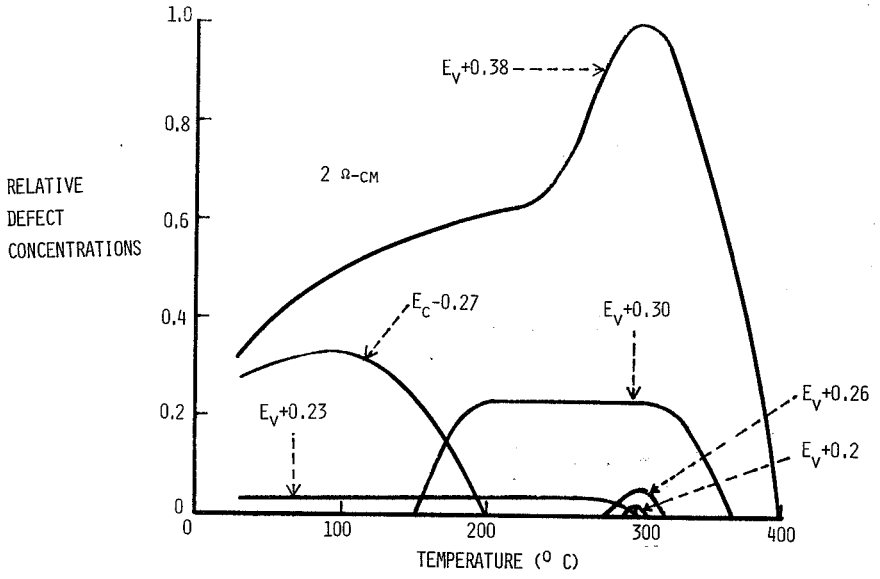

Figure 3. - Relative defect concentrations from DLTS.

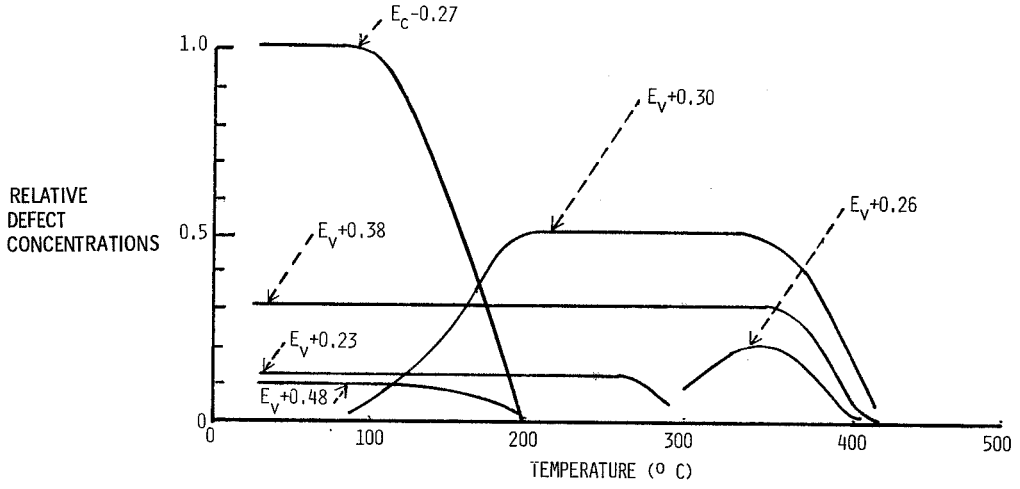

Figure 4. - DLTS data for 0.3 ohm-cm P-Si.

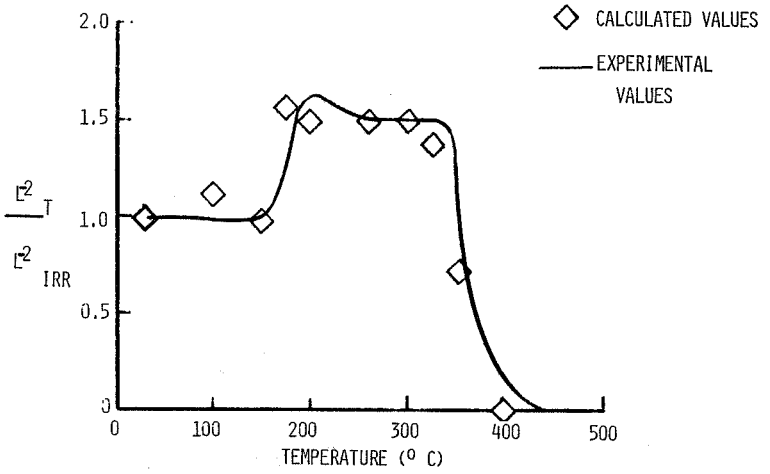

Figure 5.- Calculated and measured $1/L^2$ ratios for 2 ohm-cm cells.

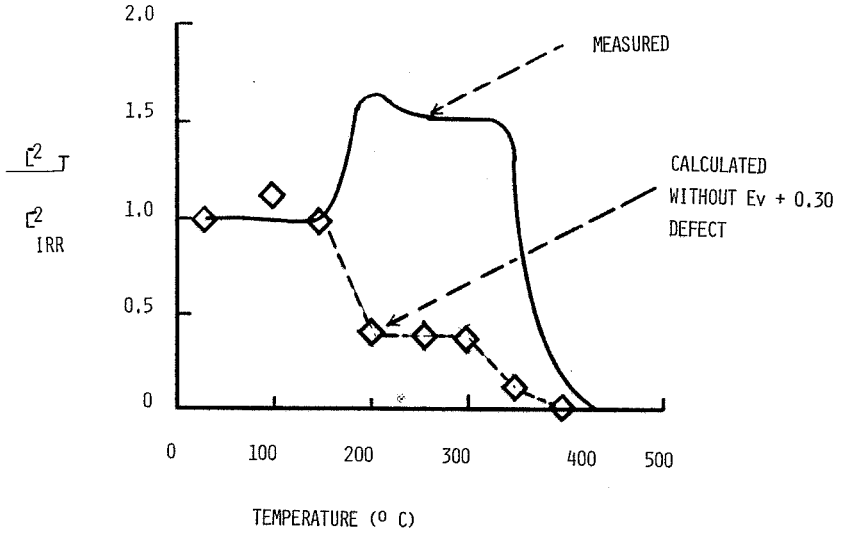

Figure 6.- Calculated and measured $1/L^2$ ratios, omitting E_v + 0.30 effect.

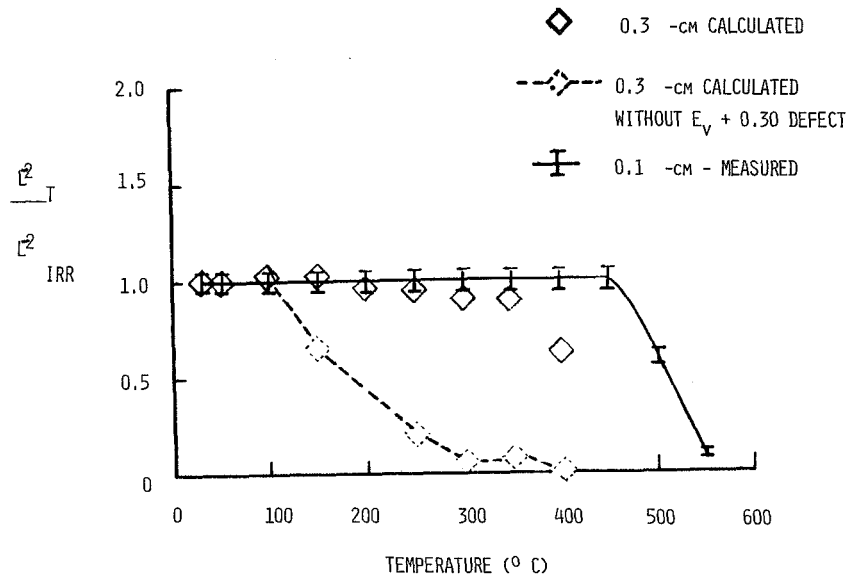

Figure 7. - Calculated and measured $1/L^2$ ratios for low-resistivity P-Si.

EFFECT OF DOPANTS ON ANNEALING PERFORMANCE OF SILICON SOLAR CELLS*

John A. Scott-Monck and Bruce E. Anspaugh
Jet Propulsion Laboratory
California Institute of Technology

SUMMARY

Silicon solar cells doped with boron or gallium and ranging in resistivity from 0.1 to 20 ohm-cm were irradiated with 1 MeV electrons to fluences up to $1x10^{15}$ e/cm^2. The cells were then thermally annealed over the range 60-450°C in order to study their recovery characteristics. Spectral response, minority carrier diffusion length and light I-V data were obtained and used to develop a preliminary model to explain the various annealing stages observed.

INTRODUCTION

There has been renewed interest in thermal annealing of solar cells as a technique for extending satellite operating lifetime and as a means of increasing the feasibility of certain advanced mission concepts. Low thrust propulsion systems are being considered for transferring large solar panels from low earth to geosynchronous orbit. One of the primary obstacles to be overcome is the severe degradation that would be experienced by the solar panels due to exposure to the radiation environment encountered during transfer.

Once in geosynchronous orbit, the panels would still be exposed to sufficient radiation such that their electrical performance would be significantly degraded over a period of years. This problem is presently addressed by oversizing panels, a solution which increases cost and mass, to accommodate the reduction in power during mission lifetime. It is doubtful that this solution can be tolerated for concepts such as SPS which are designed to produce and deliver power. Therefore the idea of recovering radiation induced power losses in solar panels by thermal annealing becomes an attractive possibility for solving this problem.

The purpose of this study was to establish the optimum annealing parameters of time and temperature for producing cell output recovery. A variety of cells representing all space solar cell suppliers as well as advanced experimental samples were investigated. Included in this survey were devices made from gallium doped and boron doped silicon. The cells ranged in resistivity from 0.1 to 20 ohm-cm and in thickness from 50 to 250 μm.

*The research described in this paper was carried out at the Jet Propulsion Laboratory, California Institute of Technology, under NASA Contract NAS7-100.

EXPERIMENTAL METHOD

Approximately 80 n on p-type silicon solar cells were investigated in twenty-one separate annealing experiments. The preliminary phase used 2 ohm-cm, 250 μm thick violet cells manufactured by OCLI. In subsequent tests, cells from Spectrolab, Inc. and Solarex Corp. were included, as well as advanced experimental gallium doped solar cells received from WPAFB. Spectral response, minority carrier diffusion length (L_n) using the method of reference 1, and I-V data, taken under AMO conditions at 28°C, were initially recorded.

The samples were then irradiated with 1 MeV electrons, in vacuum, using the JPL Dynamitron. Fluences employed were generally $1x10^{14}$ or $1x10^{15} e/cm^2$. A complete description of the facility and experimental technique is given in reference 2. After irradiation, spectral response and L_n data were taken on a sampling basis, while I-V curves under AMO at 28°C were obtained for all cells.

Thermal annealing was done in dry nitrogen with the cells mounted on a quartz boat within the constant temperature zone of a diffusion furnace. Typical annealing times were 30 minutes, although in some experiments cells were annealed for up to 64 hrs at a given temperature. Initial annealing was begun at 200°C in most cases and after retesting the samples, heating was increased in 50°C increments up to a final temperature of 450°C. For annealing temperatures below 200°C the cells were mounted to a temperature controlled heater block in vacuum and I-V data was obtained using the solar simulator that is part of the JPL Dynamitron test facility as described in reference 2. I-V data was obtained after each annealing step, and when appropriate it was supported with spectral response and L_n measurements. Unirradiated control cells were included in the annealing tests to guarantee that factors such as antireflection coating transmission changes or contact punchthrough were not influencing the data taken.

RESULTS AND DISCUSSION

The experiments reveal a complicated recovery pattern for both gallium and boron doped silicon solar cells. There are marked differences between the two dopants at annealing temperatures of 60°C. Extremely low resistivity (0.1-0.2 Ω-cm) gallium and boron doped silicon cells display a unique form of recovery as compared to higher base resistivity devices. Based on our investigations of isochronal and isothermal behavior of these samples, it appears that significant recovery of radiation induced degradation does not take place until exposure to a temperature of at least 350°C for a period greater than 30 minutes.

The data presented here is in terms of short circuit current, although open circuit voltage and maximum power were also monitored. Unfortunately, many of the cells made with titanium-palladium-silver contacts showed evidence of shunting due to contact punchthrough at annealing temperatures of 400°C, which compromised all but the short circuit current data. Fortunately, the

spectral response and minority carrier diffusion length measurements were not influenced by this problem. Cells which had chromium-gold-silver or tantalum-palladium-silver contact systems did not show any signs of shunting even after 30 minutes at 450°C.

The annealing behavior of cells made from gallium and boron doped silicon is shown in figures 1 through 3. The data is given in terms of the unannealed fraction of short circuit current, I_o-I_t/I_o-I_ϕ, versus annealing temperature, where I_o is the current prior to irradiation, I_t is the current being annealed at temperature t, and I_ϕ is the current after irradiation. Positive annealing is defined as a reduction in the unannealed fraction, while negative or reverse annealing is an increase in the unannealed fraction. Figure 1 shows the effect of 30 minute heat treatments over the range 200 to 450°C for 0.10-0.20 ohm-cm gallium and boron doped cells, while figures 2 and 3 provide data for 2 ohm-cm and 10 ohm-cm gallium and boron doped cells over the range 60 to 450°C. Additional data was obtained for 20 ohm-cm gallium doped cells, but it is not given since it matched precisely the information derived from 10 ohm-cm gallium doped cells. These plots represent a number of individual experiments involving in most cases, at least three cells of each type. Due to the significance of the measurements made at 60°C, these data are included, although it represents 16 hrs at temperature while the other points are for 30 minutes at temperature.

Onset of Annealing

The lowest temperature for which there is substantial data is 60°C. We observed positive annealing in all boron doped samples tested regardless of base resistivity. This has been reported previously (ref. 3). However, with gallium doped silicon solar cells the type of annealing (positive or negative) was related to base resistivity, with 2 ohm-cm cells losing additional output, 10 ohm-cm cells remaining the same, while 20 ohm-cm devices showed a slight increase in output. Both back surface field and conventionally processed samples performed similarly. Additional experiments comparing 2 ohm-cm gallium and boron doped silicon solar cells confirmed the original results with respect to the type of annealing produced at 60°C. In the latter experiments the samples were held at 60°C for 64 hrs after they had been irradiated with $1x10^{15}$ 1 MeV electrons/cm^2. Table 1 summarizes the information taken from all experiments.

Intermediate Annealing Stage

The original annealing experiments began at 200°C for an arbitrarily selected time of 15 minutes. Significant reverse annealing was observed in 2 ohm-cm boron doped cells regardless of manufacturer or thickness (50-250 μm). The output of the samples was now lower than after the irradiation. Spectral response and minority carrier diffusion length measurements confirmed our electrical data. Other experiments using 10 ohm-cm samples did not show evidence of reverse annealing under these conditions. Cell output remained the same as after the irradiation. Further, more detailed investigations revealed that the onset of reverse annealing in 2 ohm-cm boron doped silicon took place

somewhere between 120 and 140°C and was extremely rapid (less than one minute). In another test, samples of 10 ohm-cm boron doped silicon were irradiated to $1x10^{14}$ e/cm^2 and then heated for 16 hrs at 200°C. Although in absolute terms the amount of reverse annealing observed was small (1.4 mA average), relative to the amount of initial loss in current from the irradiation (3.2 mA average), it was very significant (>40 percent). Thus it appears that heating cells that had been irradiated to 200°C led to an additional loss in output, a situation not unlike photon induced degradation in irradiated float zone silicon solar cells (ref. 4).

The data given in figure 3 appears to be in conflict with our observations concerning reverse annealing in 10 ohm-cm silicon, but it should be noted that these samples received a 60°C soak for 16 hrs, which according to our model, discussed in a later section, would modify the cell's behavior at 200°C. Further discussion of reverse annealing in 10 ohm-cm samples will be found in the section entitled "Additional Observations".

There is no additional significant change in cell output for 2 and 10 ohm-cm boron doped samples until a temperature of 350°C is reached. Our work indicates that the next annealing stage is located very close to 350°C in point of fact. In one annealing experiment the cells were inadvertently heated to only 340°C for 30 minutes, and they did not show any signs of recovery. The gallium cells by comparison show a gradual recovery of output over this temperature range as can be seen in figures 2 and 3.

The behavior of the low resistivity samples is in sharp contrast (fig. 1). The amount of reverse annealing appears to increase with temperature, peaking at 300°C for gallium and 350°C for boron doped silicon cells. The fact that neither group was originally heated at 60°C is regrettable in light of our proposed model.

Final Recovery Stage

With the exception of the 0.1 ohm-cm sample, all cells showed a significant amount of positive annealing at 350°C, and at 450°C had recovered from 75 to 90 percent of the radiation induced degradation in output. The absolute amount of recovery appears to be related to base resistivity for both dopants, with the higher resistivity cells displaying the greatest recovery.

Since the purpose of this work is to define practical parameters for producing recovery from the effects of radiation, we feel that a minimum temperature of 350°C is required. New investigations are necessary in order to determine if longer exposures at temperatures such as 350°C can duplicate the effects of shorter times at more elevated temperatures. Table 2 shows the correlation between L_n and electrical output for a typical annealing experiment. Figure 4 shows the spectral response variation over this same run.

Additional Observations

A series of experiments was performed to observe the effect of increasing the annealing time at a particular temperature. It was found that over fifty percent of the original degradation caused by $1x10^{14}$ e/cm^2 could be eliminated by heating the cells for approximately one hour at 350°C. In some cases there were only relatively small improvements in output after 30 minutes, but one hour seemed to maximize recovery at that temperature. Since many cells showed evidence of contact punchthrough at ∿400°C, we were reluctant to try the same test above 400°C.

The behavior of boron doped two ohm-cm back surface field devices was similar to that seen for conventional cells. The ten ohm-cm boron doped field cells appeared to display a greater amount of output recovery at a given temperature than did 10 ohm-cm conventional samples. Hopefully more data of higher resistivity boron doped field cells will be available in the near future.

The absolute magnitude of the strong reverse annealing described in two ohm-cm boron doped cells irradiated and then heated to 200°C for 30 minutes does not seem to be a function of fluence, which offers additional support for our proposed model. The average additional degradation in current measured for a population of 12 cells was 7.0 mA when irradiated to $1x10^{14}$ e/cm^2. Another group of 14 cells irradiated to $1x10^{15}$ e/cm^2 degraded by an average of 7.7 mA after being heated to 200°C for 30 minutes.

Proposed Model

Our observations can be explained in a qualitative manner by postulating a pair of competing mechanisms to account for the low temperature reverse annealing seen in most boron and gallium doped silicon solar cells. Still another mechanism dominates at higher temperatures (350°C and greater) to complete this model. It is assumed that one of the mechanisms, defined as B, allows migrators to couple with radiation induced recombination sites thus increasing or enhancing their capture cross sections. This would tend to reduce minority carrier diffusion length. The new recombination complex is postulated to be thermally stable up to temperatures of ∿350°C.

In competition with this mechanism is another mechanism, defined as G, which provides migrators that seek out the very same recombination sites, and if the recombination site has not been already enhanced, the G-type migrator couples with it in such a manner as to reduce or neutralize its capture cross section. This would result in an increase in minority carrier diffusion length. As with the B-type complex, the G-type complex is thermally stable up to temperatures of ∿350°C. Once a recombination site has become G or B-type, it is no longer susceptible to further coupling with either migrator.

We assume that the B-type migrator is associated with the dopant itself while the G-type migrator is some other species contained within the crystal. The concentration of both migrators is postulated to be relatively small with respect to the concentration of radiation induced defects, and depending on

the temperature at which B-type migrators are triggered, the relative concentrations of B and G-type migrators is fairly similar.

Examining the data reported for boron doped samples it can be argued that the positive annealing that takes place at 60°C is due to G-type migrators. However, when a temperature sufficient to trigger B-type occurs, they now dominate, which is what has been seen, namely an abrupt additional loss in diffusion length at a temperature of ∿120-140°C. The magnitude of reverse annealing is greater for 2 ohm-cm as compared to 10 ohm-cm cells, which is explained by arguing that B-type migrators are related to dopant concentration. The fact that heating 10 ohm-cm cells at 60°C prior to heat treatment at 200°C mitigates reverse or negative annealing is explained by arguing that type-G migrators have had sufficient time to occupy nearby recombination sites, thus preventing type-B, which does not exist in very high concentrations, from becoming fully activated. The saturation in reverse annealing over the range of 250 to 350°C is also explained by arguing that both types of migrators have now occupied as many recombination sites as they can reach. The idea that the concentration of type-B migrators is less than the number of recombination sites available also might account for the relative constant loss of 7-8 mA observed in 2 ohm-cm cells exposed to fluences of $1x10^{14}$ and $1x10^{15}$ e/cm^2.

The gallium doped cell behavior at 60°C can be explained by arguing that B-type migrators are triggered at a lower temperature, and do not enhance the capture cross section of radiation induced recombination centers as greatly as do B-type migrators in boron doped silicon. However, the B-type are still related to the dopant concentration, thereby accounting for the reverse annealing in 2 ohm-cm cells and the slight positive annealing in 20 ohm-cm gallium doped cells at 60°C. With higher temperatures the G-type migrators dominate and saturate, explaining the slow positive annealing observed in both 2 and 10 ohm-cm gallium doped samples.

At 350°C, a new dominant mechanism is triggered which breaks up the B and G-type complexes and also begins eliminating the radiation induced recombination centers. This explained the similarity in behavior of 2 and 10 ohm-cm gallium and boron doped samples over the annealing range of 350 to 450°C.

This model must also account for the behavior of the very low resistivity cells doped with boron and gallium in order to be worthy of further consideration. The boron doped sample showed a very high etch pit count (10^6 per cm^2) indicating a high dislocation density. The gallium doped samples exhibited striations caused by the method used to incorporate the dopant. It is proposed that the dislocations and striations acted to pin or impede the triggering of type-B migrators until sufficient additional thermal energy allowed them to be released. It is significant that the peak reverse annealing observed for low resistivity samples showed the same trend as for other samples, namely gallium doped at lower temperatures. In addition, the difference in triggering temperatures between the two dopants was ∿50°C, very close to the difference observed in higher resistivity cells.

CONCLUSIONS

The model we have proposed to account for our experimental findings is extremely unsophisticated. It is hoped that future work will yield sufficient information to allow the identification of the B and G-type migrators. This effort has yielded a great deal of practical information concerning annealing which will assist us in establishing techniques for providing on panel heating in order to reduce or eliminate radiation damage to solar cells. A great deal of work remains to determine whether there is any relationship between fluence and annealing which could be useful in an engineering sense, e.g. are there advantages to annealing after lower fluences. Of even greater importance is the need for detailed information on the annealing characteristics of proton irradiated solar cells. The greatest challenge still has yet to be addressed, that is designing a solar panel which can still function effectively after being thermally annealed.

REFERENCES

1. Rosenzweig, W.: Diffusion Length Measurements by Means of Ionizing Radiation. Bell Sys. Tech. Journ. Vol. 41, p. 1573, Sept. 1962.

2. Anspaugh, B. E. and Miyahira , T. F.: Electron Irradiation of Modern Solar Cells. Solar Cell High Efficiency and Radiation Damage Conference Proceedings, NASA Conf. Publication 2020, p. 207, May 1977.

3. Scott-Monck, J.; Gay, C.; Stella, P.; and Uno, F.: High Efficiency Solar Panel (HESP), AFAPL-TR-77-36, July 1977.

4. Crabb, R. L.: Photon Induced Degradation of Electron Irradiated Silicon Solar Cells. Conf. Record of the Ninth IEEE Photovoltaic Specialists Conference, p. 329, May 1972.

CHANGE IN IRRADIATED (ϕ = $1x10^{15}$ e/cm^2) ELECTRICAL PARAMETERS AFTER 60°C HEATING

Cell Type	Sample Size	Time (hrs)	ΔI_{sc} (mA)	ΔV_{oc} (mV)	ΔP_{max} (mW)
2 Ω-cm Ga	6	16	(3.5)	(3.0)	(1.7)
2 Ω-cm Ga	6	64	(3.4)	(3.2)	(1.5)
10 Ω-cm Ga	6	16	0.1	0.5	-
20 Ω-cm Ga	6	16	0.5	0.6	0.7
2 Ω-cm B	2	16	2.0	3.3	1.2
2 Ω-cm B	2	64	1.1	3.4	0.7
10 Ω-cm B	2	16	2.7	3.0	1.3

( ) - loss

TABLE 1

CORRELATION BETWEEN CELL OUTPUT AND DIFFUSION LENGTH

Condition	Isc (mA)	Voc (mV)	P_{max} (mW)	L_n (μm)
Pre-irradiation	148.2	594	69.3	96.8
ϕ = 1 x 10^{14}	137.7	571	60.6	61.9
200°C 15 min.	131.3	560	57.9	42.3
200°C 45 min.	130.5	560	57.5	-
250°C 15 min.	130.2	561	57.4	-
300°C 15 min.	129.8	562	57.6	-
350°C 15 min.	135.1	573	60.9	61.0
350°C 45 min.	144.0	589	66.5	83.2
6 samples 2 ohm-cm boron doped, 250 μm thick				

TABLE 2

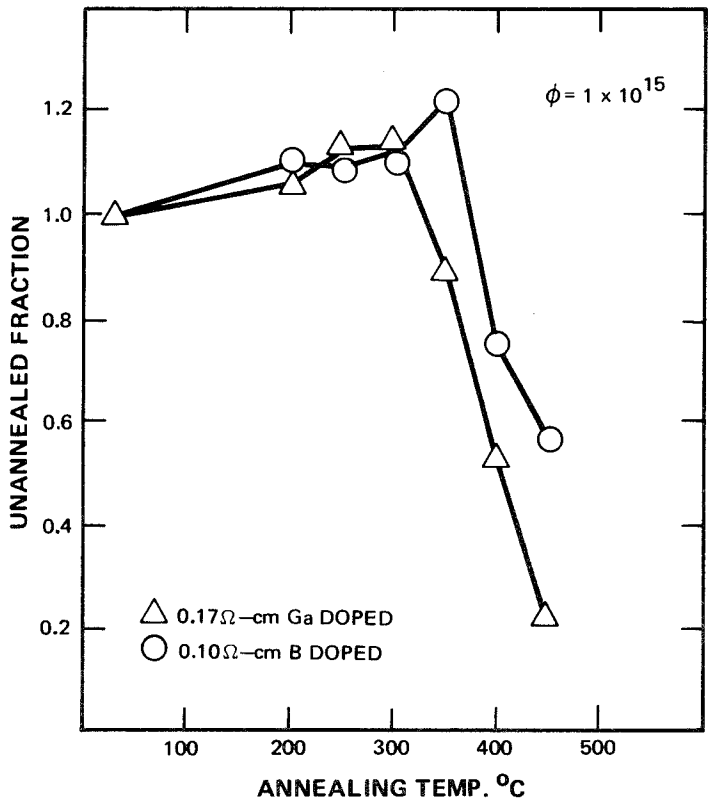

FIGURE 1

I_{SC} RECOVERY IN ELECTRON IRRADIATED
0.1-0.2 Ω-CM SILICON

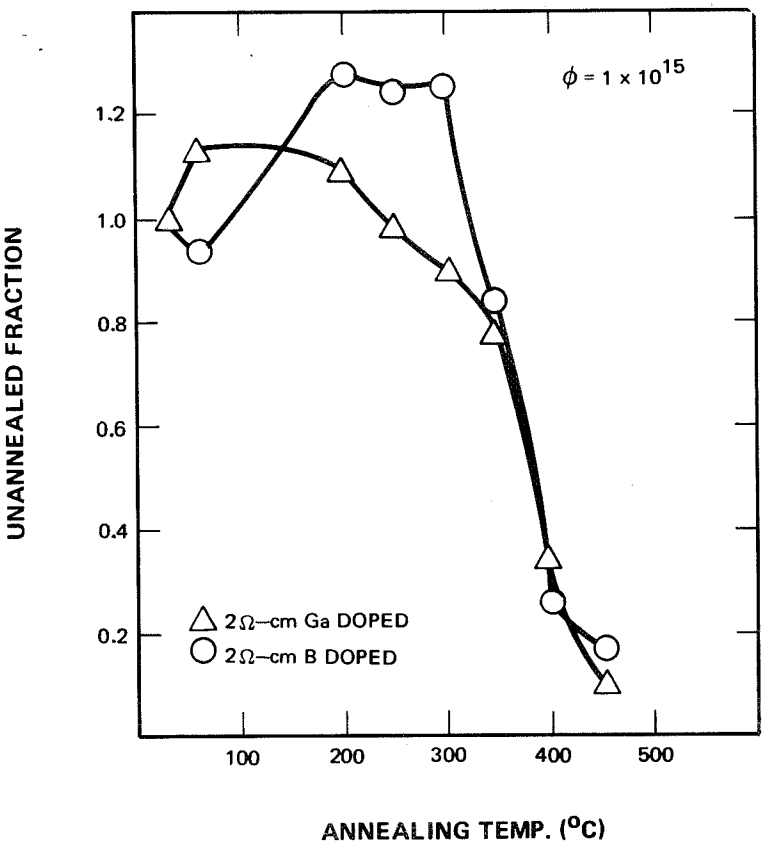

FIGURE 2

I_{SC} RECOVERY IN ELECTRON IRRADIATED
2 Ω-CM SILICON

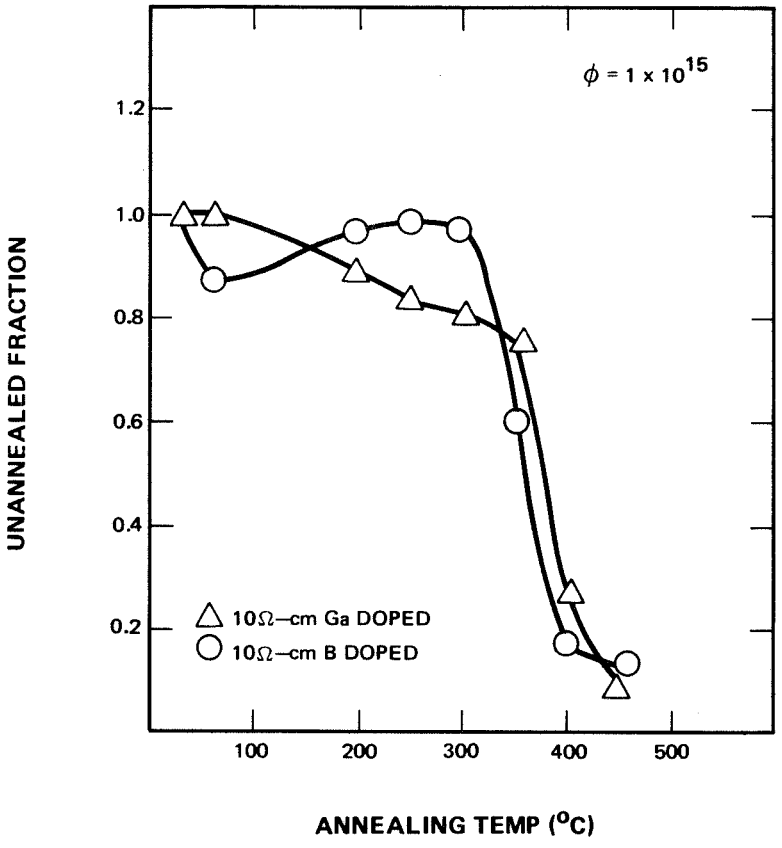

FIGURE 3

I_{SC} RECOVERY IN ELECTRON IRRADIATED 10 Ω-CM SILICON

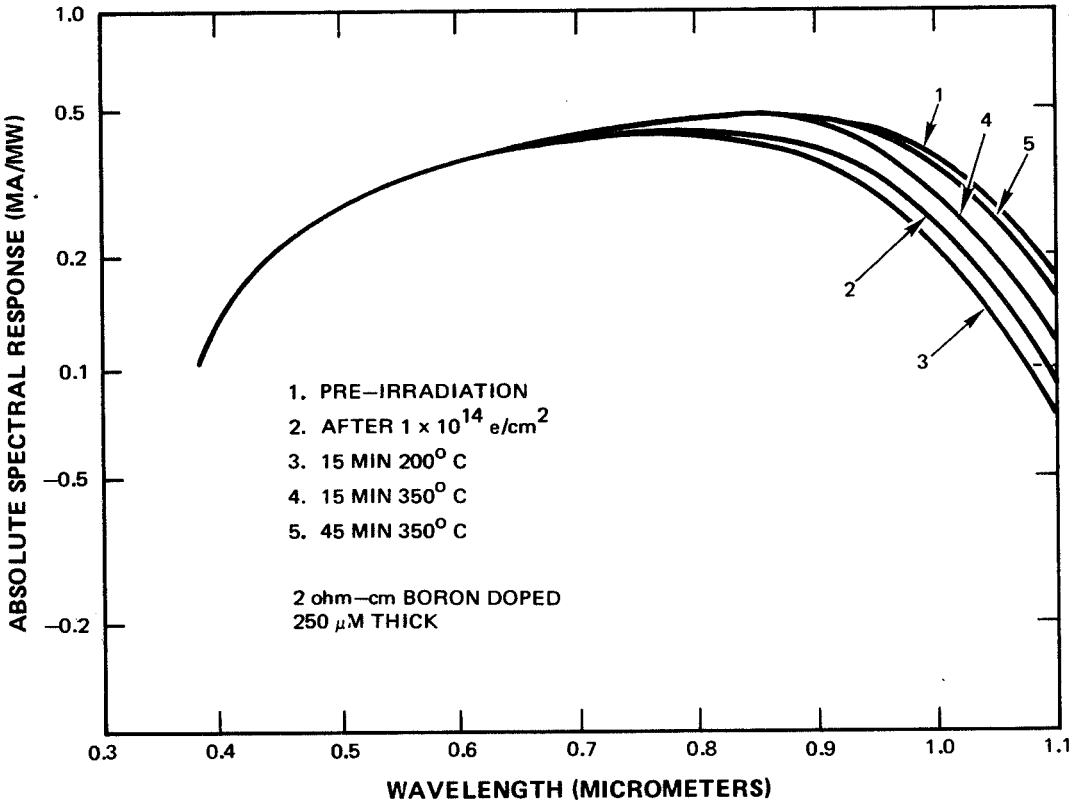

FIGURE 4

SPECTRAL RESPONSE OF IRRADIATED AND ANNEALED
2 Ω-CM BORON DOPED SILICON

HIGH-ENERGY ELECTRON-INDUCED DAMAGE PRODUCTION AT ROOM TEMPERATURE IN ALUMINUM-DOPED SILICON

J. W. Corbett, L.-J. Cheng*, A. Jaworowski, J. P. Karins, Y. H. Lee†, L. Lindström‡, P. M. Mooney§, G. Oehrlein, and K. L. Wang‖

Institute for the Study of Defects in Solids
Department of Physics
State University of New York at Albany

ABSTRACT

DLTS and EPR measurements are reported on aluminum-doped silicon that has been irradiated at room temperature with high-energy electrons. Comparisons are made to comparable experiments on boron-doped silicon. Many of the same defects observed in boron-doped silicon are also observed in aluminum-doped silicon, but we have observed several not observed, including the aluminum interstitial and aluminum-associated defects. Damage production modeling, including the dependence on aluminum concentration, will be presented.

INTRODUCTION

The radiation-induced defects in silicon responsible for the deterioration of solar cells are mainly impurity-associated defects such as the vacancy-oxygen-carbon complex (the K-center) (ref. 1). One way to improve the radiation tolerance of silicon cells is to remove the undesired impurities, especially oxygen and carbon from the starting material and to prevent their introduction during the cell fabrication processes. Alternatively, a way to reduce the importance of such impurities is to introduce sinks which would act as recombination centers for vacancies and self-interstitials to reduce the chance of the primary defects interacting with the impurities, or perhaps, to introduce an impurity which would trap a vacancy or self-interstitial to form

---

*Present address: Jet Propulsion Laboratory, Pasadena, CA 91103, USA
†Present address: IBM-Thomas J. Watson Research Center, Yorktown Heights, New York 10598, USA
‡Permanent address: Försvaret Forskningsanstalt, S-140 50 Stockholm 80, Sweden
§Permanent address: Department of Physics & Astronomy, Vassar College, Poughkeepsie, New York, 12601 USA
‖General Electric Corporate Research & Development Center, Schenectady, New York 12301, USA

an electronically inactive complex which would not then reduce the minority carrier lifetime in the device. So that we may produce such radiation resistant silicon it is important to understand the damage production mechanisms and defect interactions in electron irradiated silicon. Sutdies which lead to defect characterization and identification and an understanding of defect interactions, particularly of interstitial defects, are in progress. This paper describes some preliminary results of our work in aluminum-doped silicon. This material is interesting because unlike the boron interstitial which is mobile at room temperature, the aluminum interstitial is not mobile at room temperature, and hence, its role in damage production should be different.

EXPERIMENTAL RESULTS

Both EPR and DLTS measurements have been made on electron irradiated aluminum-doped silicon to characterize and identify the defects produced. In all samples oxygen and carbon impurities were present in concentrations of 10^{16}-$10^{18}cm^{-3}$. Diodes were fabricated from float zone and Czochralski grown silicon of 1 Ωcm and 10 Ωcm resistivity irradiated with 1.0 and 1.5 MeV electrons. Most of the diodes were Schottky barrier diodes in which only majority carrier traps are observed although we did observe the minority carrier traps in diffused diodes made from 1 Ωcm material. Figure 1 shows the DLTS spectrum for a diffused diode. The spectrum shows the divacancy peak (H_2) and the K-center peak (H_4 and H_5) both of which are also present in boron doped silicon. In addition, a peak at E_v + 0.17 eV (H_1) is observed and also a minority carrier peak at E_c - 0.29 eV (E_1). The peak E_1 occurs at nearly the same energy as a boron defect, tentatively identified as $B_I + O_I$ (ref. 2), but the peak intensity is considerably smaller. This could be an aluminum complex and further study is needed to identify this defect.

Figure 2 shows a DLTS spectrum for 10 Ωcm aluminum-doped silicon, in this case a Schottky barrier diode. Again, we observe H_1 but here the intensity compared to the divacancy peak is much smaller, indicating that the concentration of the trap has decreased as has the aluminum concentration. This data plus the absence of this defect in boron-doped material leads to the conclusion that this is an aluminum associated defect. H_3 is the carbon interstitial which anneals at room temperature to form the carbon-oxygen-vacancy complex as was observed in boron-doped silicon (ref. 2,3).

Figure 3 shows the DLTS spectrum for a 1 Ωcm aluminum-doped Schottky diode showing that the peak labeled H_4 and H_5 is resolved into two peaks if the pulse width is reduced sufficiently. At low fluence we believe only the carbon-oxygen-vacancy complex at E_v + 0.33 eV (H_4) is present, but that a defect at E_v + 0.44 eV (H_5) appears as the fluence is increased. This is observed as a shift of the apparent energy level of the peak toward higher energy as the fluence is increased. We believe this second defect is also present in boron-doped material where we have measured two different capture cross

sections for this peak. We have not yet identified the defect corresponding to the H_5 peak. This spectrum also shows a defect at E_v + 0.55 eV (H_6) which occurs in many aluminum-doped samples. We did not observe this defect in boron doped samples which suggests that it too is an aluminum associated defect.

Isochronal annealing for 20 minute periods was performed on Schottky barrier diodes to study the annealing behavior of these defects. A new DLTS peak appeared at E_v + 0.48 eV (H_7) which appears after annealing at 100°C, continues to grow after the 145°C anneal and then decreases after the 200°C anneal and is essentially gone after a 250°C anneal. Another additional peak is observed after annealing at 400°C at E_v + 0.22 eV (H_8) which increases after a 445°C anneal after which another very small peak at E_v + 0.20 eV also appears. We are continuing to study these new peaks.

EPR measurements in aluminum-doped silicon show that, in addition to the divacancy (G6) (ref. 4), and the carbon interstitial (G12) (ref. 5) which anneals at room temperature to form the carbon-oxygen-vacancy complex (G15) (ref. 3,6), aluminum interstitials (G18) (ref. 7,8) are observed as well as aluminum-vacancy pairs (G9) (ref. 8). The aluminum interstitial was observed to anneal at 200°C by thermal processes forming an aluminum substitutional-aluminum interstitial pair (G19,G20) and a third spectrum (G21) (ref. 9). The aluminum interstitial anneals by an ionization enhanced process at 100°C (Troxell, Chatterjee, Watkins and Kimerling, to be published).

We have not always observed the Al_I defect in our DLTS samples. Although its energy position in the band gap is E_v + 0.17 eV, the DLTS peak is observed at the apparent energy position of E_v + 0.26 eV because of the strong temperature dependence of the capture cross section (ref. 10). We believe it is buried in our carbon-oxygen-vacancy peak and would be more easily observed in samples with low carbon and oxygen content. Table I lists the defects observed by DLTS measurements in both boron-doped and aluminum-doped electron irradiated silicon.

DEFECT PRODUCTION MODELING

In a previous paper we presented results of a computer model for defect production by electron irradiation in boron doped silicon containing carbon and oxygen as impurities and showed that the presence of a defect recombination center could reduce damage produced at a given fluence (ref. 11). The model used is a simplified one described by means of a system of rate equations for defect interactions. Free mobile single vacancies, free mobile self-interstitial atoms and immobile divacancies are created at constant rates during irradiation. We have calculated defect production in boron-doped silicon of different resistivities assuming no other impurities are present, and also for aluminum-doped silicon with the same assumptions. The primary difference in these two systems is that the boron interstitial,

created by the Watkins replacement mechanism, is mobile at room temperature, whereas the aluminum interstitial, created in the same way, is not.

We assume the following defect reactions in boron-doped silicon:

$$I + V \rightarrow \text{recombination} \tag{1}$$

$$I + B_S \rightarrow B_I \quad \text{(ref. 12)} \tag{2}$$

$$B_I + V \rightarrow B_S \tag{3}$$

$$B_I + B_S \rightarrow B_I + B_S \equiv B_I B_S \tag{4}$$

$$B_I + V_2 \rightarrow V + B_S \tag{5}$$

$$V + B_S \rightarrow VB_S \tag{6}$$

$$I + VB_S \rightarrow B_S \tag{7}$$

$$I + V_2 \rightarrow V \tag{8}$$

$$V + V \rightarrow V_2 \tag{9}$$

where V ≡ single vacancy, I ≡ self-interstitial, B_S ≡ substitutional boron, B_I ≡ interstitial boron, and V_2 ≡ divacancy. We assume similar reactions in the aluminum-doped silicon where $A\ell_S$ ≡ substitutional aluminum and $A\ell_I$ ≡ interstitial aluminum replace B_S and B_I in the equations. We have calculated the damage under different irradiation conditions, one with continuous constant flux and the other with pulsed flux, as in the case of a rotating satellite. Table II lists the rate equations and Table III lists the numerical values of parameters used for the calculations.

We present no definitive results here since we are still testing and improving the program. Preliminary results show that at higher doping levels the damage component due to V and V_2 at a particular fluence decreases, while that due to defects involving the dopant increases as more secondary and tertiary defects are produced. In the boron-doped material the major defects in the more heavily doped material are the vacancy-boron substitutional pair and the boron interstitial-boron substitutional pair, whereas in the aluminum-doped material they are the vacancy-aluminum substitutional pair and the aluminum interstitial. This was expected since the aluminum interstitial is not mobile at room temperature and cannot migrate to an aluminum substitutional site. The calculations show equal amounts of damage in both types of materials however. Figures 4 and 5 show calculations for two different aluminum concentrations. The effect of each of these defects on the minority carrier lifetime in the material is not yet determined.

CONCLUSIONS

It is difficult to compare the computer calculations with experimental results at this point since neither aspect of the research is completed. In addition, our measurements have been made on material with large carbon and oxygen concentrations and indeed the carbon interstitial and the carbon-oxygen-vacancy complex have been the dominant defects observed. The aluminum defects predicted by the computer calculations have been observed in EPR studies and we are continuing to study the as yet unidentified DLTS peaks in aluminum-doped silicon. We are also studying p-type silicon with low carbon and oxygen concentrations and with dopants other than aluminum or boron. These experiments should be useful for comparison with the damage production as modeled by the computer calculations and will also provide information on defect characteristics and identity necessary for the construction of the model. This joint approach to the problem of radiation damage in silicon solar cells should give us the necessary information to produce radiation resistant devices.

REFERENCES

1. Lee, Y. H.; Cheng, L. J.; Mooney, P. M.; and Corbett, J. W. in "Solar Cell High Efficiency and Radiation Damage", NASA Conf. Pub. 2002 (NASA, Wash. DC, 1977) p. 165.

2. Mooney, P. M.; Cheng, L. J.; Süli, M.; Gerson, J. D.; and Corbett, J. W.: Phys. Rev. B 15, 3836 (1977).

3. Lee, Y. H.; Cheng, L. J.; Gerson, J. D.; Mooney, P. M.; and Corbett, J. W.: Solid State Comm. 21, 109 (1977).

4. Watkins, G. D.; and Corbett, J. W.: Phys. Rev. 138A, 543 (1965).

5. Watkins, G. D.; and Brower, K. L.: Phys. Rev. Letters 36, 1329 (1976).

6. Lee, Y. H.: Corbett, J. W.; and Brower, K. L.: Phys. Stat. Sol. (a) 41, 637 (1977).

7. Brower, K. L.: Phys. Rev. B1, 1908 (1970).

8. Watkins, G. D.: Phys. Rev. 155, 802 (1967).

9. Watkins, G. D.: in Radiation Damage in Semiconductors (Dunod, Paris, 1967) p. 97.

10. Troxell, J. R.; and Watkins, G. D.: Bull. Am. Phys. Soc. 23, 214 (1978).

11. Cheng, L. J.; Sours, P. W.; Karins, J. P., Corelli, J. C.; and Corbett, J. W. in "Solar Cell High Efficiency and Radiation Damage", NASA Conf. Publ. 2020 (NASA, Wash. DC, 1977) p. 179.

12. Watkins, G. D.: Phys. Rev. B12, 5824 (1976).

TABLE I.- DEFECTS OBSERVED BY DLTS IN BORON-DOPED AND Aℓ-DOPED ELECTRON IRRADIATED SILICON

	Peak	Energy Level	Capture Cross Section (cm^2)	Annealing Temperature	Identity
B-doped and Aℓ-doped Si	H_2	E_v + 0.23 eV	$\sigma_p = 3 \times 10^{-16}$	out 270°C	$[V_2]^+$
	H_3	E_v + 0.29 eV	$\sigma_p = 3 \times 10^{-16}$	out 30°C	$[C_I]^+$
	H_4	E_v + 0.33 eV	$\sigma_p = 2 \times 10^{-16}$	in 30°C, out 400°C	$[V+O+C]^+$
	H_5	E_v + 0.44 eV	$\sigma_p = 10^{-19}$	out 400°C	?
B-doped only		E_c - 0.27 eV	$\sigma_p = 2 \times 10^{-13}$	out 170°C	$[B_I+O_I]$ (tentative)
		E_v + 0.30 eV	$\sigma_p = 2 \times 10^{-16}$	in 170°C, out 400°C	[B+O+V] (tentative)
Aℓ-doped only	H_1	E_v + 0.17 eV	$\sigma_p = 4 \times 10^{-15}$		Aℓ associated
	H_6	E_v + 0.55 eV	$\sigma_p = 10^{-19}$		?
	H_7	E_v + 0.48 eV		in 145°C, out 250°C	?
	H_8	E_v + 0.22 eV		in at 400°C	?
	H_9	E_v + 0.20 eV		in at 445°C	?
	E_1	E_c - 0.29 eV			?

TABLE II.- RATE EQUATIONS

$$\frac{\partial[V]}{\partial t} = G - 4\pi(D_V+D_I)R_{VI}\,[V][I] - 4\pi D_V[V](2\,R_{VV}[V] + R_{VB_I}[B_I] + R_{VB_S}[B_S]) + 4\pi D_{B_I}[B_I]R_{V_2B_I}[V_2] + 4\pi D_I[I]R_{V_2I}[V_2]$$

$$\frac{\partial[I]}{\partial t} = G + 2G_{V_2} - 4\,(D_V+D_I)R_{VI}[V][I] - 4\,D_I[I]\,(R_{IB_S}[B_S] + R_{IVB_S}[VB_S] + R_{V_2I}[V_2])$$

$$\frac{\partial[V_2]}{\partial t} = G_{V_2} - 4\pi D_{B_I}R_{V_2B_I}[B_I][V_2] - 4\pi D_I R_{V_2I}[I][V_2] + 8\pi D_V R_{VV}[V]^2$$

$$\frac{\partial[B_S]}{\partial t} = -4\pi D_I R_{IB_S}[I][B_S] + 4\pi D_V R_{VB_I}[V][B_I] - 4\pi D_{B_I}R_{B_IB_S}[B_I][B_S] + 4\pi D_{B_I}R_{V_2B_I}[B_I][V_2] - 4\pi D_V R_{VB_S}[V][B_S] + 4\pi D_I R_{IVB_S}[I][VB_S]$$

$$\frac{\partial[B_I]}{\partial t} = 4\pi D_I R_{IB_S}[I][B_S] - 4\pi D_V R_{VB_I}[B_I][V] - 4\pi D_{B_I}R_{B_IB_S}[B_I][B_S] - 4\pi D_{B_I}R_{V_2B_I}[B_I][V_2]$$

$$\frac{\partial[B_IB_S]}{\partial t} = 4\pi D_{B_I}R_{B_IB_S}[B_I][B_S]$$

$$\frac{\partial[VB_S]}{\partial \tau} = 4\pi D_V R_{VB_S}[V][B_S] - 4\pi D_I R_{IVB_S}[I][VB_S]$$

[ ] indicate concentration

TABLE III.- NUMERICAL VALUES OF PARAMETERS USED FOR COMPUTER CALCULATIONS

Capture Radii

$$R_{VI} = R_{VV} = R_{VB_I} = R_{VB_S} = R_{V_2B_S} = R_{V_2I}$$
$$= R_{IB_S} = R_{IVB_S} = R_{B_IB_S} = 5\ \text{Å}$$

Generation rates

$G = 5 \times 10^{12}/\text{cm}^2/\text{sec}$ generation rate of V,I

$G_{V_2} = 5 \times 10^{9}/\text{cm}^2/\text{sec}$

Diffusion coefficients

$D_I = 3.16 \times 10^{-3}\text{cm}^2/\text{sec}$

$D_V = 4.15 \times 10^{-7}\text{cm}^2/\text{sec}$

$D_{B_I} = 1.00 \times 10^{-6}\text{cm}^2/\text{sec}$

$D_{A\ell_I} = 0$

Rotating satellite

flux on for 10^{-4}sec $(g, G_{V_2} = 0)$

flux off for 10^{-4}sec $(G, G_{V_2} = 0)$

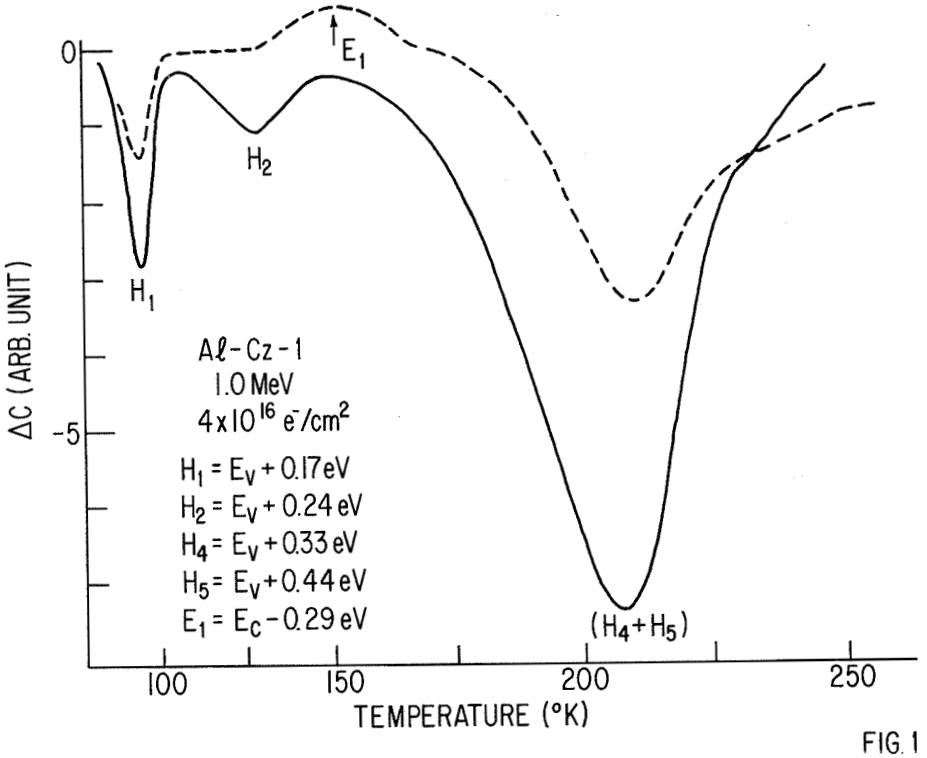
0
-5
ΔC (ARB. UNIT)
E1
H2
H1
Aℓ-Cz-1
1.0 MeV
4x10^16 e⁻/cm²
H1 = EV + 0.17eV
H2 = EV + 0.24 eV
H4 = EV + 0.33 eV
H5 = EV + 0.44 eV
E1 = EC - 0.29 eV
(H4+H5)
100
150
200
250
TEMPERATURE (°K)

FIG. 1

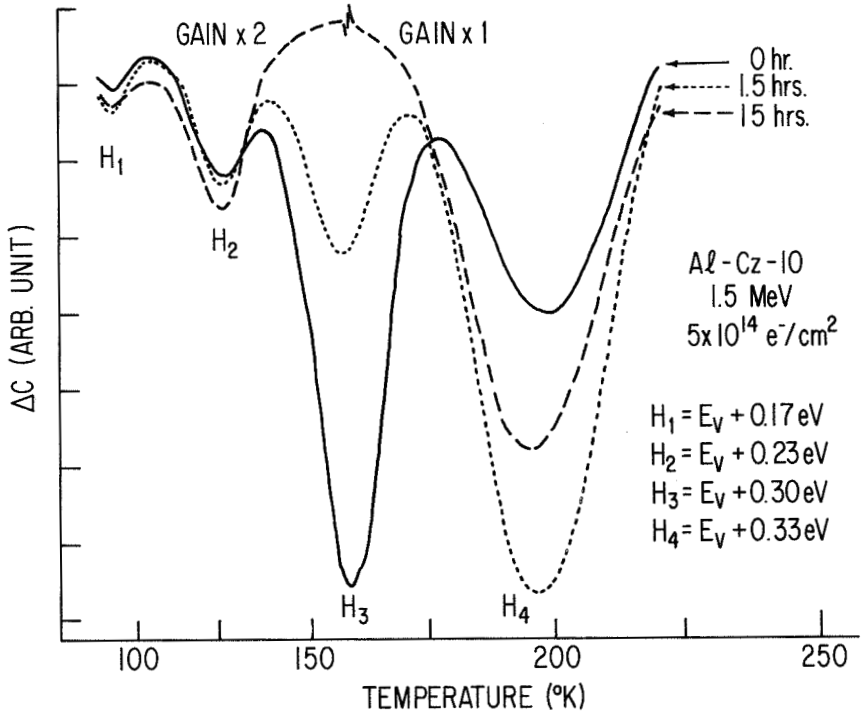
GAIN x 2
GAIN x 1
0 hr.
1.5 hrs.
15 hrs.
H1
H2
H3
H4
ΔC (ARB. UNIT)
Aℓ-Cz-10
1.5 MeV
5x10^14 e⁻/cm²
H1 = EV + 0.17eV
H2 = EV + 0.23eV
H3 = EV + 0.30eV
H4 = EV + 0.33eV
100
150
200
250
TEMPERATURE (°K)

FIG. 2

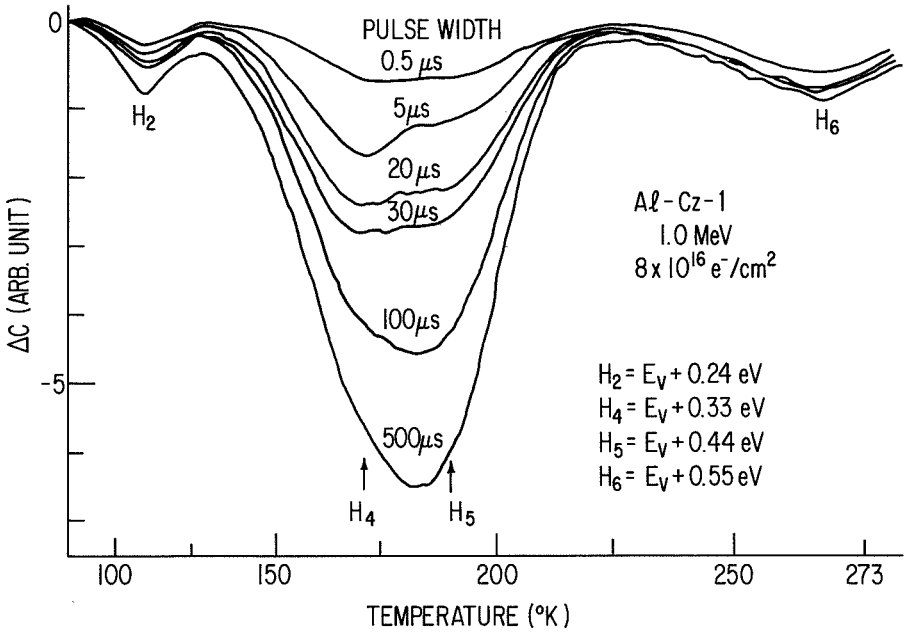
0
-5
ΔC (ARB. UNIT)
PULSE WIDTH
0.5 μs
5μs
20μs
30μs
100μs
500μs
H2
H4
H5
H6
Aℓ-Cz-1
1.0 MeV
8 x 10^16 e⁻/cm²
H2 = EV + 0.24 eV
H4 = EV + 0.33 eV
H5 = EV + 0.44 eV
H6 = EV + 0.55 eV
100
150
200
250
273
TEMPERATURE (°K)

FIG. 3

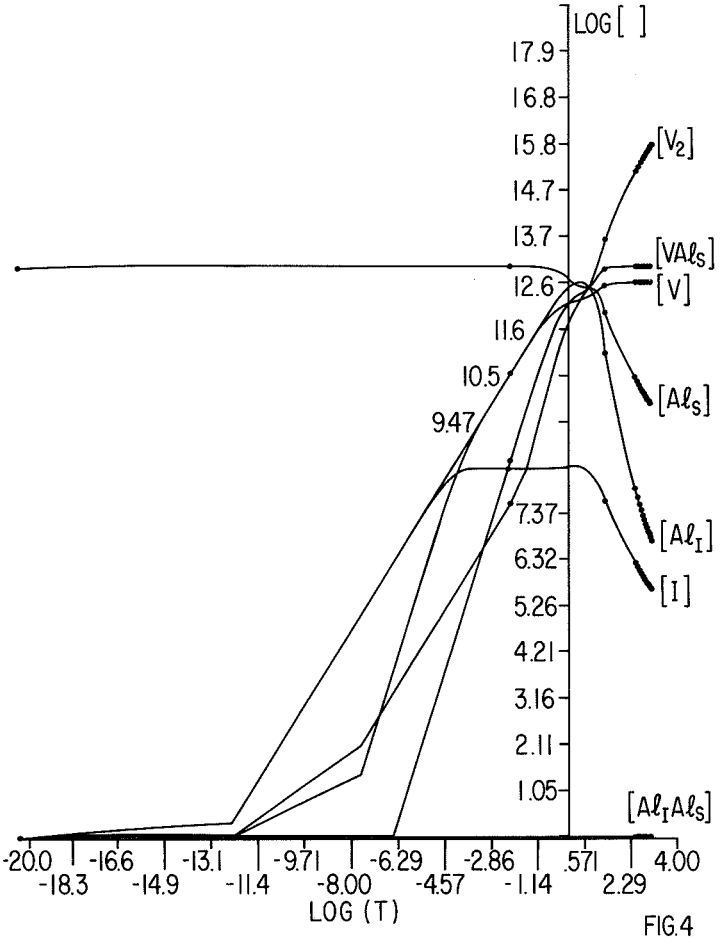
LOG[ ]
17.9
16.8
15.8
14.7
13.7
12.6
11.6
10.5
9.47
7.37
6.32
5.26
4.21
3.16
2.11
1.05
[V2]
[VAℓS]
[V]
[AℓS]
[AℓI]
[I]
[AℓIAℓS]
-20.0
-18.3
-16.6
-14.9
-13.1
-11.4
-9.71
-8.00
-6.29
-4.57
-2.86
-1.14
.571
2.29
4.00
LOG (T)

FIG.4

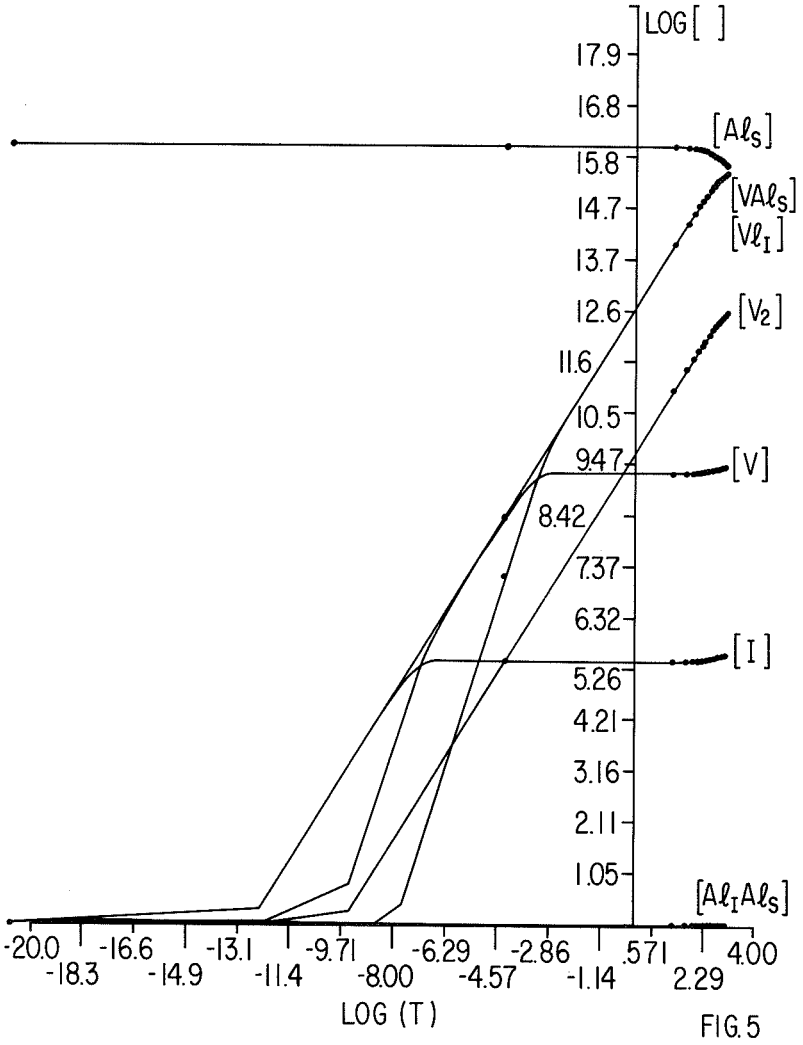
LOG[ ]
17.9
16.8
15.8
14.7
13.7
12.6
11.6
10.5
9.47
8.42
7.37
6.32
5.26
4.21
3.16
2.11
1.05
[Alₛ]
[VAlₛ]
[Vl_I]
[V₂]
[V]
[I]
[Al_IAlₛ]
-20.0
-18.3
-16.6
-14.9
-13.1
-11.4
-9.71
-8.00
-6.29
-4.57
-2.86
-1.14
.571
2.29
4.00
LOG (T)

FIG. 5

OXYGEN MICRODISTRIBUTION IN SILICON AND ITS EFFECTS ON ELECTRONIC PROPERTIES

Harry C. Gatos
Massachusetts Institute of Technology

ABSTRACT

The oxygen distribution in silicon on a microscale was investigated in Czochralski grown crystals. It was not uniform and there were maxima and minima in oxygen concentration. The effects of oxygen, for various heat treatments, on the electronic characteristics of Si were studied by spreading resistance measurements and scanning microscopy in the EBIC mode. In low carrier concentration p-type material, the striated distribution of oxygen can lead to p-n junctions located at the oxygen concentration maxima. The implications of the oxygen distribution in Si will be discussed in the context of applications.

SUMMARY OF SILICON SOLAR CELL RADIATION DAMAGE WORKSHOP

Richard L. Statler
Naval Research Laboratory

BULK MATERIAL VS. DEVICE STUDIES

Device processing stages introduce new defects in the silicon through sawing, grinding, heating, impurity diffusion, implantation damage, etc., thereby adding to the number of the intrinsic defects formed by the material preparation and single crystal growth. For this reason and in order to maintain as simple and well-controlled material as possible in which to study radiation damage, it is of great importance to continue studies in bulk materials before device processing. One thing which is presently lacking and for which there is an expressed desire is a source for well-controlled, uniformly grown bulk silicon. Closely coupled to this need is the ability for increased sensitivity of impurity detection in silicon, as for example oxygen concentration, carbon, copper, and other impurities. Efforts must continue in the direction of improving the control and characterization of the single crystal ingot to enable researchers through the use of complementary measurements to understand the role of defects.

However, radiation characterization of devices should not wait upon further elucidation of the defect structure in p-type silicon. Because the cell processing does introduce a number of defects, and because other types of radiation effects (such as trapped charge distributions in oxide or surface layers) affect cell performance significantly, careful radiation studies should accompany device development where there is a good probability for space applications.

DEVICE ANNEALING STUDIES

A number of papers at this meeting, and those already in the literature, have shown the variety of post-irradiation annealing behavior associated with cell parameters such as the type and concentration of dopant, the manner of crystal growth (i.e., float zone or Czochralski), and the energy and type of radiation. Annealing studies have two purposes. First, if various measurements (e.g., DLTS, resistivity, EPR, carrier lifetime, diode parameters) are performed, one can learn something about the formation and dissolution of defects during thermal processes. Secondly, there is a strong interest in restoring power output to satellite solar arrays which become radiation degraded during the mission. Of particular note, the Solar Power Satellite concept is practical only if solar cell degradation can be limited to a small percent over 20 or 30 years.

Experimental results presented at this meeting show the importance of both isothermal and isochronal annealing. For example, a long heat soak at temperatures of 200°C was required to show up annealing in some AlGaAs cells. We conclude that both isothermal and isochronal annealing studies will be fruitful areas of investigation.

Laser annealing of radiation damage is of interest as an application tool for the SPS. Since this involves cells with attached coverglass using a CO_2 laser whose beam is absorbed within the coverglass, the annealing mechanism is related to thermal activation of defect centers, and not to some type of optical or photon interaction in the silicon.

OTHER RESEARCH AREAS

There are additional areas of research which are deserving of further study. A brief list, without detailed comment would include: synergistic effects in covered cells exposed to ultraviolet and charged particles, radiation effects in charged oxide experimental cells ("dry" vs. "wet" oxide, effect of included impurities in the oxide layer), how to control photon degradation and its relation to heavy doping, the vertical junction cell, the n-i-p cell, n^+p cell with very high resistivity.

Other needed information are the radiation damage coefficients over a range of particle energies for gallium arsenide type cells and the newer silicon cells.

GOALS AND ACHIEVEMENTS

Perhaps the most ambitious goal for radiation hardness is the Solar Power Satellite with a 10 to 15% power loss in 30 years. We have seen substantial progress in radiation hardening since the 2nd Solar Cell High Efficiency and Radiation Damage Meeting in 1977. As an example, experimental results show that a 50 micron silicon cell will degrade 17% in P_{max} in a 20 year geosynchronous orbit, based on this power loss after 1×10^{15} 1-MeV electrons/cm^2. We feel that there are still great gains to be made in the fields of understanding radiation damage and in hardening solar cells.

RADIATION DAMAGE IN GaAs SOLAR CELLS

E. J. Conway and G. H. Walker
National Aeronautics and Space Administration
Langley Research Center

INTRODUCTION

Radiation damage of space borne equipment is an important consideration for almost all systems which fly higher than the bottom of the radiation belts. Without geomagnetic shielding, spacecraft face a radiation environment which varies in particle type, intensity, energy, and time. Electron and proton radiation provide the greatest damage hazard. This paper will report recent results of electron and proton irradiation and annealing of GaAs solar cells, and also will speculate on some implications of these results.

Langley Research Center has been actively involved in GaAs solar cell research for several years. Our space radiation effects effort began approximately two years ago. Its goal is to improve the radiation stability of the cells. Thus, in general, unshielded shallow junction, p-GaA&As/p-GaAs/n-GaAs cells and materials are studied.

In the following sections, we will report on an inhouse effort at LaRC, on contractual studies at Hughes Research Laboratory, and on grant research at University of Florida.

I. Electron Irradiation Damage and Annealing
Langley Research Center

Inhouse studies have emphasized 1 MeV electron damage (irradiations performed at LeRC) and thermal annealing of GaAs solar cells. We have studied both the damage and annealing as a function of electron fluence and of junction depth. Cell degradation was found to be less severe for shallow junction cells. Also, the degree of recovery (due to thermal annealing) was greater for shallow junction cells.

In this report we will emphasize the annealing studies. Our results are in the form of short circuit current (I_{SC}), normalized to initial short circuit current (I_{SCO}), because this is a simple measurable quantity (not the product of several) and is the more radiation and annealing sensitive simple quantity.

Figure 1 shows the effect on relative short circuit current of annealing 0.8 μm junction depth cells, at 200°C for 10, 20, and 30 hours. For damage due to fluences from 10^{14} and 10^{15} 1 MeV electrons cm^{-2}, recovery was essentially complete. The annealing recovery after a fluence of 10^{16} electrons cm^{-2} appeared to cease upon reaching 0.83. These results suggested that more complex damage occurs at high fluence and leads to more complex annealing characteristics (Ref. 1).

Figure 2 shows the results of annealing several shallow junction cells after irradiation with 10^{15} 1MeV electrons cm^{-2}. Each set of cells was

isothermally annealed and the data analyzed for annealing kinetics. Annealing was found to be first order with an activation energy of 1.25 ev. All results indicated that I_{sc}/I_{sco} annealed to only 0.98, confirming an uncompletely recovered component.

Lang, et al. (Ref. 2), had investigated 1 MeV electron irradiation and annealing of GaAs using deep level transient spectroscopy (DLTS). He found six levels, three of which annealed at an activation energy of 1.4 eV, and two more at 1.75 eV. Our values are in good agreement with those of Lang for the low activation energy annealing stage, and (based on Lang's results) we should have seen no further annealing for the times and temperatures used. Thus, we believe that two important annealing stages exist for GaAs, one associated with a 1.25 eV activation energy and another with an activation of 1.75 eV.

We are currently finishing a calculational study on simultaneous irradiation and annealing. Using the activation energies and frequency factors from our work and Lang's, we are estimating the significance of the expected degradation. We expect the results to show that when irradiation occurs at its natural rate in space, continuous thermal annealing can be very effective in reducing the resulting damage.

II. Proton Irradiation of GaAs Solar Cells
Hughes Research Laboratory

In space, solar cells are not only subject to electron irradiation, but also to bombardment from protons trapped in the radiation belts and from those originating in solar flares. The proton energy spectrum is very wide, from less than 100 KeV to more than 100 MeV. However, there are many more protons at low energy than at high energy.

For the last two years, Hughes Research Laboratory has been measuring the effect of various proton energies and fluences on GaA&As/GaAs solar cells. These cells were generally irradiated unshielded to permit unambiguous interpretation of results and to provide a firm basis for shielding studies.

Cells with junction depths less than 0.5 μm were irradiated at high energy (15 MeV and 40 MeV) and at low energy (50 KeV, 100 KeV and 290 KeV). Silicon solar cells were also irradiated to permit a direct comparison between the effects on GaAs cells and Si cells. Figure 3 summarizes the available results. At high proton energies, the performance of GaAs cells does not degrade as rapidly with increasing fluence as does the performance of Si cells. However, at low energies, GaAs cells degrade more rapidly than Si. At some intermediate energy, shown schematically by crossing of dashed lines, the two kinds of cells must be equally sensitive. With a 12 mil cover glass, GaAs cells show no degradation with energy (to 290 KeV) at a fluence of 10^{12} cm^{-2} as shown by the 100% line at low energy in Figure 3. This is expected since the range of 290 KeV protons is much less than one mil.

Analysis of spectral response measurements indicate that neither 50 KeV (range $\sim$ 0.4 μm) nor 100 KeV (range $\sim$ 0.8 μm) protons cause much damage below the junction. This is the case because both the window thickness and the junction depth (measured from the inside of the window) provide shielding to the junction. This observation suggests that a benefit might be derived from using a thick window. For example, a 2 mil window could stop protons up

to 5 MeV. Windows have been kept thin in the past to permit extended blue response for enhanced beginning-of-life (BOL) efficiency. Preliminary indications are that with a thick window and reduced BOL efficiency, a high end-of-life efficiency could be maintained with low weight and great simplicity in comparison with cover glass shielding. The major problems appear to be the effects of radiation on the optical and electrical properties of the conductive GaA&As window.

III. Electronic Property Changes of GaA&As and GaAs Solar Cell Materials due to Proton and Electron Irradiation - Univ. of Florida

This fundamental effort supports the more empirical radiation studies performed on cells. Independent measurements are made of macroscopic parameters, such as efficiency and short circuit current. Fundamental microscopic-level measurements of radiation induced defect characteristics, such as trap energy, density and capture cross section, are correlated with macroscopic measurements and important new information is developed.

The University of Florida and Hughes Research Laboratory performed some cooperative studies on low energy proton (.05, .10 and .29 MeV) irradiated diodes and cells. Deep level transient spectroscopy (DLTS) measurements were made of radiation induced trap density and carrier capture cross sections. The total capture cross section [Σ(TOT)] was computed by multiplying each trap density by its electron or hole cross section and adding. Figure 4 shows the relative short circuit current and relative efficiency plotted against Σ(TOT). The points are labeled for the proton irradiation energy and fluence.

Although Figure 4 is based on some preliminary data, it suggests that one means for comparing irradiation effects at different energies and different fluences is by means of the carrier total capture cross section. Σ(TOT) is a macroscopic parameter and should be correlatable with macroscopic parameters other than those shown in Figure 4, such as diffusion length.

The electron binding energy of radiation induced defects has been measured for some sets of radiation and material parameters. For low energy proton irradiation, these levels are shown in the first three columns of Figure 5. For 1 MeV proton irradiation of n-GaAs, two electron traps at E_c - 0.14 eV and E_c - 0.46 eV have been measured also (Fig. 5, column 4). An increasing number of levels were measured as the proton energy was increased up to 0.29 MeV. However, at a proton energy of 1 MeV only two electron traps were found (the deeper of which became deeper with increasing fluence). This result suggests that qualitatively different defects could be introduced when low energy protons are stopped in GaAs solar cells.

The last column of Figure 5 illustrates schematically the six-energy levels which Lang, et al. (Ref. 2) found to result from 1 MeV electron irradiation. Lang identified five electron traps and one hold trap. This is significantly different from the number and distribution produced by 1 MeV protons.

Although the results illustrated in Figure 5 do not strongly affect our view of radiation degradation, they do affect our approach to annealing. If different particles and different energies produce qualitatively different

damage, for example bound aggregates of defects for low energy protons and isolated simple defects for high energy electrons, then annealing kinetics may be different also. As a first approximation, many of us have assumed that all damage anneals like electron damage; however, this must be checked carefully.

University of Florida studies will be focussing on this in the coming year.

SUMMARY

We are performing a calculational study of the simultaneous 1 MeV electron irradiation and annealing effects in GaAs solar cells. Separate experiments suggest that operation of the cells near 200°C should continuously anneal the damage and significantly reduce the effect of long term electron irradiation.

Under irradiation by high energy protons, GaAs cells do not degrade as rapidly as do Si cells. For low energy protons, GaAs cells degrade more rapidly; however, if the cells are provided with sufficiently thick cover glass radiation shields, then no cell damage occurs. A thick GaA&As window might provide a light-weight, integral shield, but severely damaged windows would require effective annealing to make this concept useable.

Degradation of solar cell performance parameters appears to correlate well with increasing total cross section for carrier capture. Deep level transient spectroscopy (DLTS) has identified numerous trap energy-levels produced by protons. A comparison between the energy-levels produced by protons and by electrons which are not stopped in the material indicate that the damage produced by protons and electrons may be qualitatively different. Thus, annealing of proton damage may be very different from the annealing of electron damage.

REFERENCE

1. Walker, G. H.; Conway, E. J.; J. Electrochem. Soc. 25, 10, p. 1726, 1978.

2. Lang, D. V.; Logan, R. A.; and Kimerling, L. C.: Phys. Rev. B 15, 10, p. 4874, 1977.

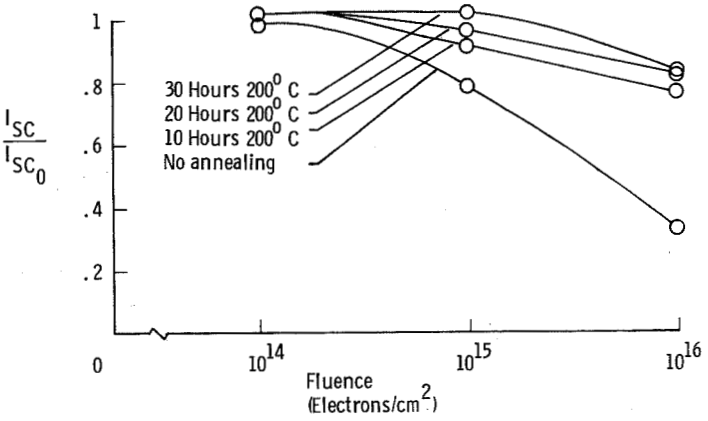

Figure 1. - Annealing recovery of short circuit current for one MeV electron irradiated cells.

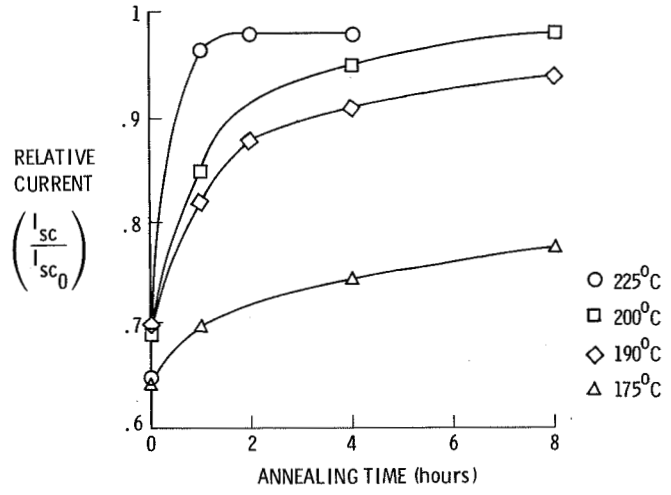

Figure 2. - Recovery of short circuit current as a function of annealing time.

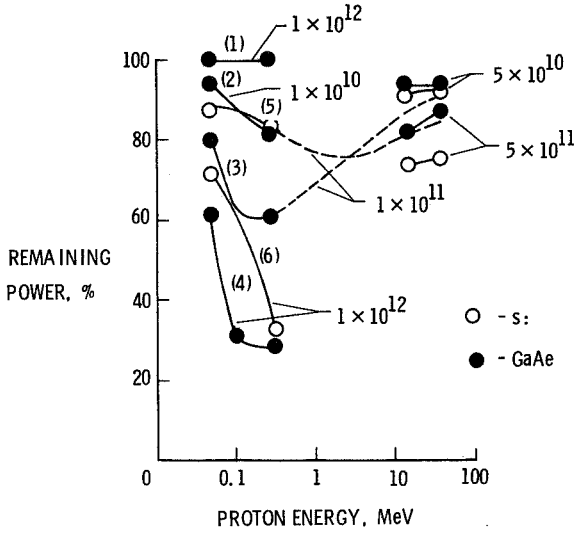

Figure 3. - Proton radiation damage: GaAs and Si solar cells.

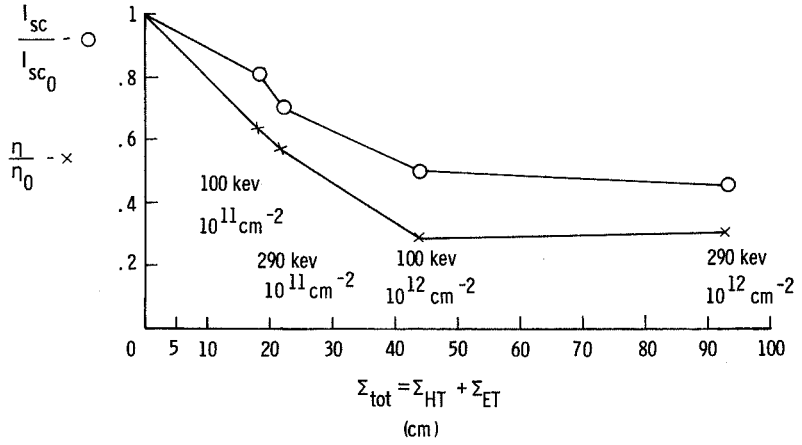

Figure 4. - Total carrier cross section effects for proton irradiated GaAs solar cells.

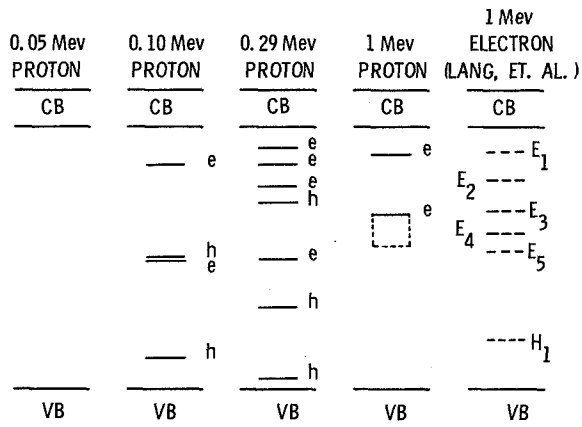

Figure 5. - Comparison of radiation induced trap levels in GaAs.

FABRICATION OF HIGH EFFICIENCY AND RADIATION RESISTANT GaAs SOLAR CELLS*

S. Kamath, R.C. Knechtli and R. Loo
Hughes Research Laboratories

B. Anspaugh
Jet Propulsion Laboratory

SUMMARY

In our development of the technology for making GaAs solar cells suitable for space applications, we are concerned with AMO efficiency, radiation hardness and reproducible fabrication. Systematic improvements in fabrication yield were obtained by appropriate control of the liquid phase epitaxial growth process, contact fabrication and surface preparation. To improve radiation hardness, we decreased the junction depth while overcoming the penalty in decreased solar cell efficiency which tends to go hand-in-hand with the reduction of junction depth in (AlGa) As-GaAs solar cells. We have succeeded in making cells with an AMO efficiency of 18% and a junction depth of 0.5 μm, as compared to junction depths on the order of 1.0 μm which had previously been reported. With respect to the damage caused by proton irradiation, we have been able to correlate the nature of the observed damage to the energy and penetration depth of the damaging protons.

FABRICATION TECHNOLOGY

In developing the technology for GaAs solar cells for space applications, we emphasized the reproducible fabrication of large area (2 cm x 2 cm) solar cells. The infinite solution liquid epitaxial growth developed at HRL is ideally suited for the growth of large area layers of GaAs and AlGaAs required for these cells. The growth system illustrated in Figure 1 has been described in past papers. The figure also shows a new modification of the graphite substrate holder that enables us to grow on multiple substrates and proceed with batch processing, leading to reduced cost per cell. Irradiation of the solar cells produced early in the program with junction depths of about 1 μm led us to conclude that shallower junctions would lead to considerable improvement in radiation hardness. The main objection to a shallow junction in the GaAs cell is that it causes the electrical junction to approach the (AlGa)As-GaAs heterophase boundary which is a region of heavy strain and dislocations; this generally leads to a lower fill factor for the cell. In our case, lowering the junction depth from 1 μm to less than 0.5 μm led to a decrease in efficiency

*Parts of this project were supported by A.F. Contract F33615-77-C-3150 and by NASA Contract NAS 1-14727

from > 17% AMO to < 15% AMO. A detailed study of epitaxial growth parameters led us to decrease the growth temperature for (AlGa)As layers to 750°C and increase the growth time to over 5 minutes per micron to achieve improved shallow junctions of <0.5 μm. The progress achieved can be judged by the statistics in Figure 2. The performance of our best 4 cm^2 cell to date with 0.5 μm junction depth is shown in Figure 3.

Since the LPE growth tends to be the slowest step in the fabrication of cells, ultimate cost reduction for large scale production would require the adaptation of the technique to batch production. We have succeeded in demonstrating the adaptability of the HRL technique for this purpose by growing layers on 4 substrates in a single growth run, using a multiple slide bar assembly of the type illustrated in Figure 1. We are presently extending this capability to even larger numbers.

RESISTANCE TO RADIATION DAMAGE

For space applications, the ability of GaAs solar cells to withstand radiation by high energy particles is of great importance in addition to superior beginning of life efficiency vis-a-vis silicon. Our first step to determining the radiation resistance of the GaAs cells was to study the damage produced by 1 MeV electrons at normal incidence. This study led us to formulate a model which showed the critical importance of decreasing junction depth to increase radiation resistance. The results on cells produced during the past year with 0.5 μm junction depth fully confirm our model. Our theoretical calculations indicate, however, that minimum radiation damage is likely to occur at about 0.2 μm. Recently we have fabricated and tested cells with a junction depth of 0.3 μm and AMO efficiency of 16%. The results are shown in Figure 4 and again confirm our model. We are continuing our systematic studies towards lowering the junction depth to 0.2 μm without adversely affecting the efficiency of the cell.

In practical space missions, we have to be concerned with irradiation by protons as well as electrons. We have investigated the behavior of GaAs cells under proton irradiation. Data in Figure 5 represent the effect of both protons and electrons on a number of our cells on a semilogarithmic plot. The cells are all similar with a junction depth of 0.5 μm. The electrons were 1 MeV and the protons were 100 and 290 KeV. Within measurement accuracy, 100 KeV and 290 KeV protons had the same effect on the solar cell power output. It is interesting to observe that in the semilog plot, the curves representing electron and proton damage are parallel. It lends credence to the concept of equivalent fluence over extended ranges of fluence for these cells.

The radiation damage caused by high energy particles is obviously a function of their energy. As far as protons are concerned, they produce most damage at the end of their track, after penetration in the solar cell. The nature of the damage which they produce is therefore largely determined by their depth of penetration into the solar cell. This led us to examine the damage caused in our cells as a function of proton penetration depth. The

results are shown in Fig. 6. While we still lack measurements in the intermediate proton energy range, the observation of the damage caused by low energy protons is especially instructive. As we start with very low energy protons (< 50 KeV), they are arrested within the surface p-layer of the GaAs, before even reaching the junction. Their major effect is therefore, to increase bulk recombination in this layer, thus decreasing the short-circuit current without affecting the junction quality. Consistently with this, we observe in Fig. 6 that the short-circuit current decreases with increasing proton energy before the open-circuit voltage is much affected. As the proton energy is increased up to about 100 KeV, most protons are arrested in the junction region. The resulting deterioration of the junction quality leads to increasing leakage current and correspondingly lower open-circuit voltage. As the proton energy is further increased above 100 KeV, most protons penetrate beyond the junction and do their damage in the n-doped base region. This leads to additional bulk recombination and further reduction of the short circuit current. As the proton energy is further increased above 300 KeV, the protons are arrested at depths past the active part of the cell. As the energy of all protons traversing the active part of the solar cell keeps increasing, the damage which they cause in this part of the cell decreases and the effect on both short-circuit current and open-circuit voltage decreases with further increases in proton energy. In summary, the measurements of Fig. 6 show that the protons arrested in the vicinity of the junction have a most deleterious effect on the open-circuit voltage, while the protons arrested within the active part of the cell, but further away from the junction affect mostly the short-circuit current. An interesting practical result is the fact that the shallow active depth of the GaAs solar cells (< 2 μm, because GaAs is a direct bandgap material) limits to a very low and narrow energy range (< 0.5 MeV) the protons which cause most damage. This leads to most effective coverglass shielding of GaAs solar cells for protection against proton damage in a real space environment. In particular, this compares favorably with Si solar cells where most damage is caused by protons with an energy on the order of 2 MeV, as compared to 200 KeV for GaAs solar cells.

To compare the radiation damage caused by protons on GaAs and on Si solar cells respectively, we have summarized in Fig. 7 the results of a number of our measurements. We show the damage caused by a given fluence to both types of cells, as a function of proton energy. While very low energy protons cause more damage to GaAs than to Si solar cells, at higher energies the reverse is true. Insofar as these solar cells are readily protected against low energy protons, but remain susceptible to the higher energy protons, Fig. 7 shows that GaAs solar cells compare favorably with Si solar cells in their ability to resist proton radiation damage in a real space environment.

EFFICIENCY

The initial motivation for developing GaAs solar cells was their potential for better AMO efficiency than Si solar cells. Our present state-of-the-art for a 4 cm^2 shallow junction GaAs solar cell has the characteristics shown in Fig. 3. The fill factor of the cell is still relatively poor, even though

its AMO efficiency is 18%. The theoretical upper limit for the fill factor of such a cell is 0.88. Some of our deeper junction cells, have a fill factor as high as 0.86. On this basis, we consider realistic an extrapolation to a fill factor of 0.85, as a result of further progress in controlling the crystal quality at the interface and in the junction region. Such an extrapolation leads to an AM- efficiency of 20.3%. Under ideal conditions, Fig. 8 shows that an AMO efficiency of 24% can be achieved with a GaAs solar cell. This idealized calculation makes however, no allowance for any losses associated with contact shadowing, reflection, or for junction imperfections leading to a lower fill factor. The ideal calculation also assumes the p-doping level to be at the limit of degeneracy ($p = 7.10^{18}$ holes/cm^3). For these reasons, we consider our estimate of an AMO efficiency of 20%, based on our experimental results, to be more realistic.

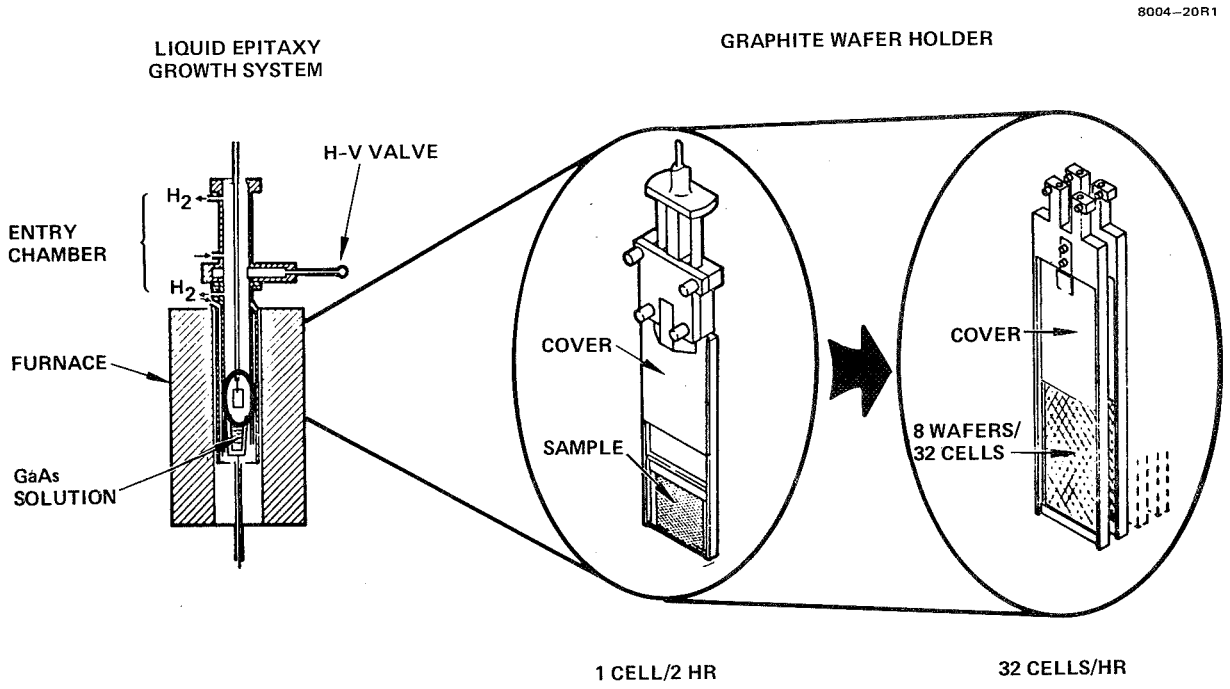

Figure 1. - Batch fabrication of GaAs solar cells.

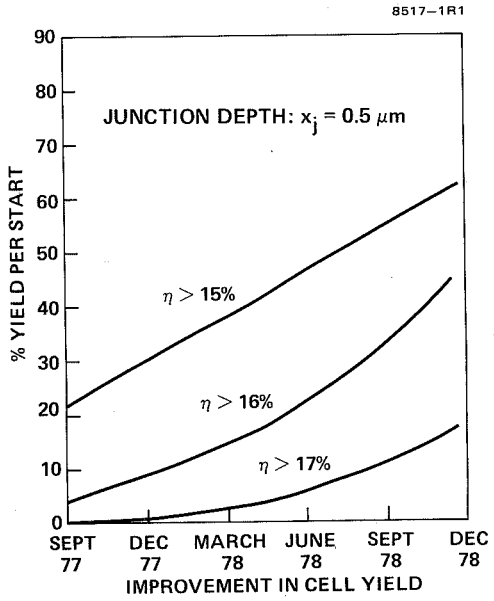

Figure 2. - Improvement of GaAs solar cell yield with time.

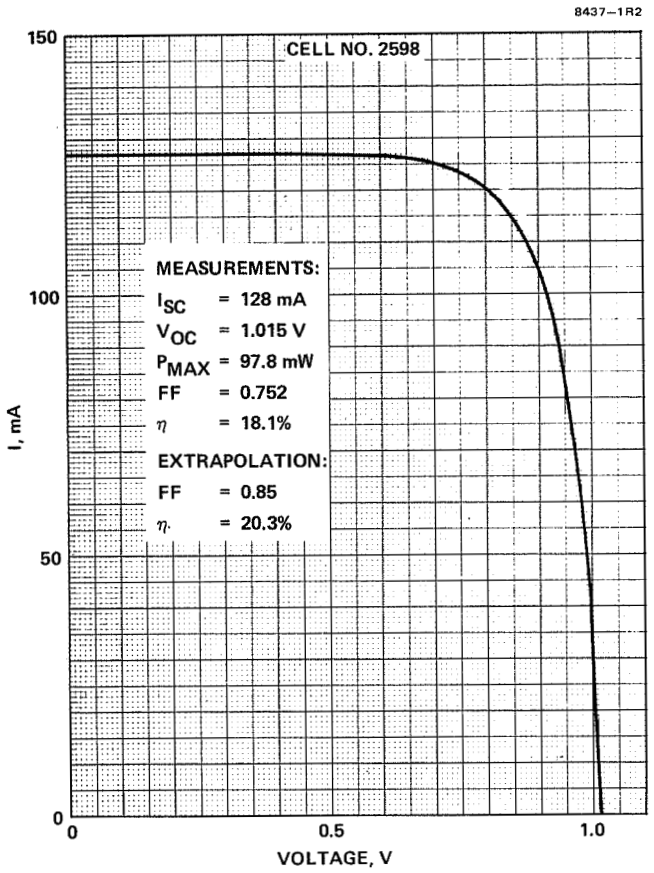

Figure 3. - High efficiency GaAs solar cell.

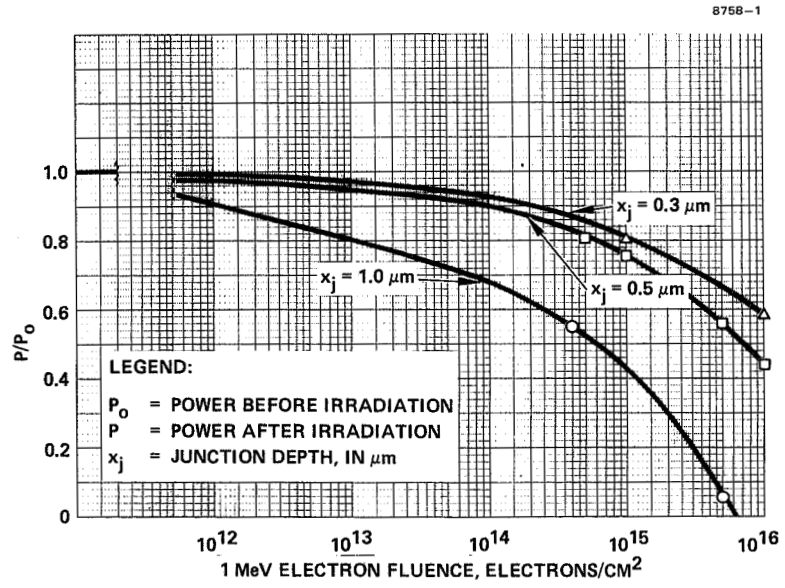

Figure 4. - Effect of junction depth on radiation damage.

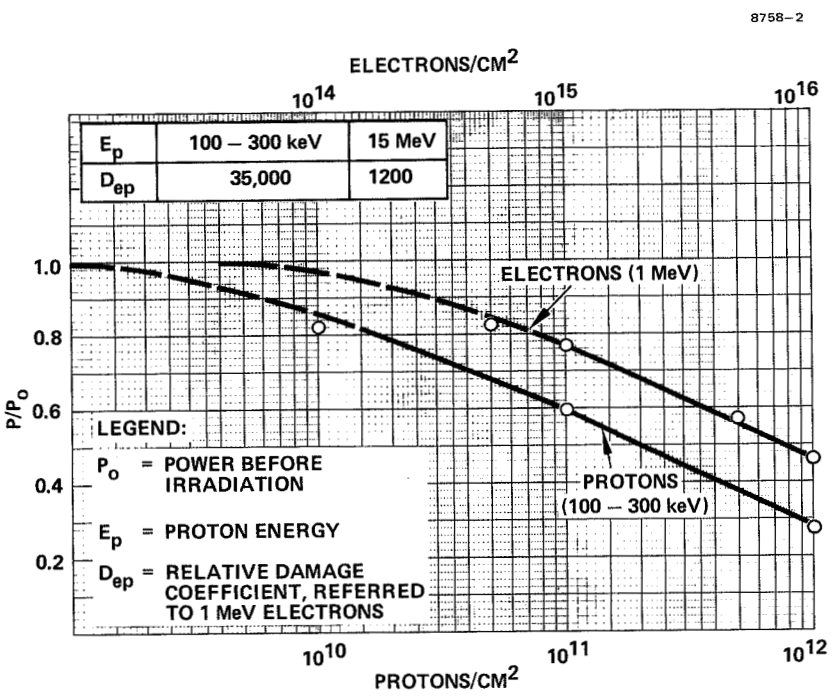

Figure 5. - Proton versus electron radiation damage.

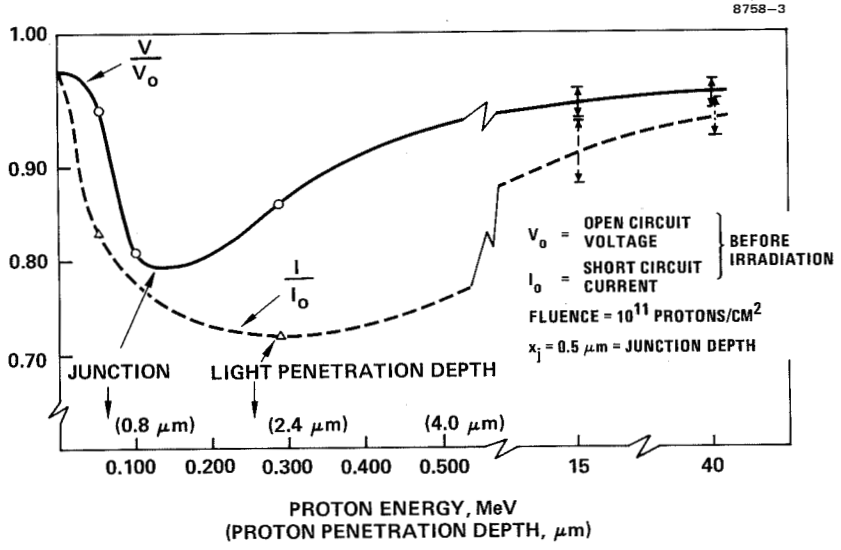

Figure 6. - Effect of proton energy on radiation damage.

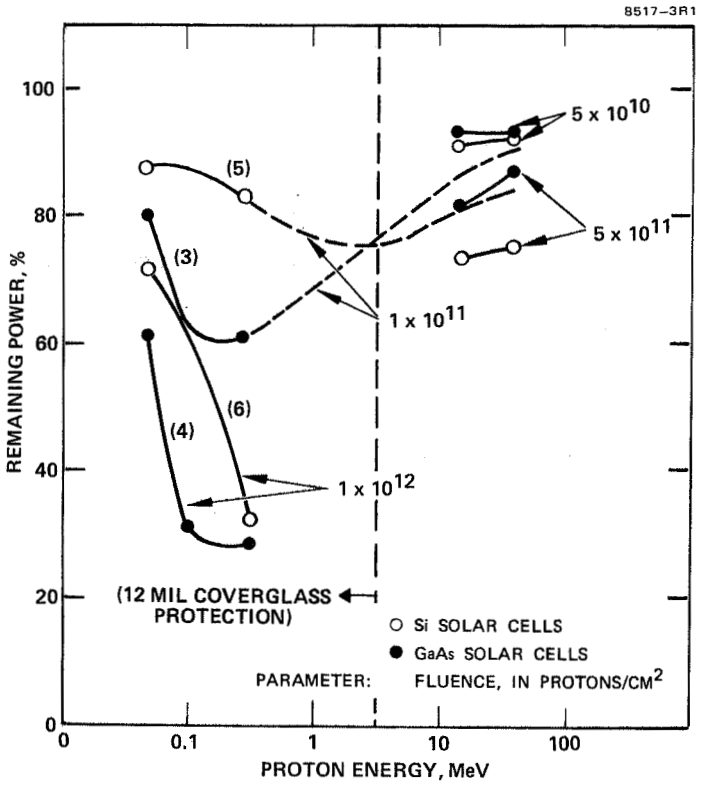

Figure 7. - Proton radiation damage on GaAs versus Si solar cells.

8758-4

PARAMETER	BEST ESTIMATE	THEORETICAL MAXIMUM
SHORT-CIRCUIT CURRENT	32 mA/CM^2	35 mA/CM^2
OPEN CIRCUIT VOLTAGE	1.01 V	1.05 V
FILL FACTOR	0.85	0.88
EFFICIENCY	20.3%	23.9%

EXPECTED EFFICIENCY $\simeq$ 20%
MAXIMUM EFFICIENCY $\simeq$ 24%

Figure 8. - Theoretical limit for GaAs solar cell efficiency.

TEMPERATURE AND INTENSITY DEPENDENCE OF THE PERFORMANCE OF AN ELECTRON-IRRADIATED (AlGa)As/GaAs SOLAR CELL

Clifford K. Swartz and Russell E. Hart, Jr.
National Aeronautics and Space Administration
Lewis Research Center

SUMMARY

The performance of a Hughes, liquid-phase epitaxial 2-centimeter-by-2-centimeter, (AlGa)As/GaAs solar cell was measured before and after irradiations with 1-MeV electrons to fluences of $1x10^{16}$ electrons/cm^2. The temperature dependence of performance was measured over the temperature range 135 to 415 K at each fluence level. In addition, temperature dependences were measured at five intensity levels from 137 to 2.57 mW/cm^2 before irradiation and after a fluence of $1x10^{16}$ electrons/cm^2. For the intermediate fluences, performance was measured as a function of intensity at 298 K only.

At a fluence of $1x10^{16}$ electrons/cm^2, the maximum power had decreased to about 40 percent of original, with most of the loss in short-circuit current. This performance is typical of cells with 0.5-micrometer-deep junctions. Variation of short-circuit current density with temperature showed the presence of three distinct slopes. The upper slope, above about 310 K, had a temperature coefficient twice that of the intermediate slope. The temperature breakpoint between these two slopes varied with fluence level. A third slope existed at temperatures below 210 K. The temperature coefficient of the open-circuit voltage did not change with temperature or with irradiation. In contrast, the temperature coefficient of maximum power at the fluence of $1x10^{16}$ electrons/cm^2 was about one-half its unirradiated value. Over the intensity range studied, the open-circuit voltage varied as the logarithm of intensity, with slopes from 3 kT/q to 1 kT/q.

INTRODUCTION

The behavior of solar cells in a radiation environment is of great importance for space applications. Studies have shown that (AlGa)As/GaAs solar cells are generally less susceptible to radiation damage than silicon cells. However, these studies have only determined performance at room temperature after irradiation. Their data are not sufficient for system analyses of the (AlGa)As/GaAs cells. Additional data on performance as a function of temperature and intensity, as well as temperature coefficients of performance, are also needed. This paper reports the electrical characteristics of a (AlGa)As/GaAs solar cell for a wide range of temperatures and illumination intensities as a function of radiation damage. These conditions are typical of those encountered in space.

PROCEDURE AND APPARATUS

The cell used in this electron irradiation test was a typical Hughes Research Laboratory, 2-centimeter-by-2-centimeter (AlGa)As/GaAs solar cell that is in laboratory production. A cross section of the cell is shown in figure 1. These cells are formed by liquid-phase epitaxial (LPE) deposition of n-type GaAs on n^+ GaAs substrates. Subsequently, an (AlGa)As layer is also formed by LPE. The junction is obtained during the growth of the p-type (AlGa)As layers by allowing the p-dopant to diffuse into the n-type GaAs substrate. Both (AlGa)As window thickness and GaAs cell junction depth are approximately 0.5 micrometer. This cell was also covered with a 300-micrometer-thick cover glass.

The Lewis Research Center Cockraft-Walton accelerator was used for the 1-MeV-electron irradiation. The cells were mounted on a metal plate, and the defocused beam was swept across them in a horizontal plane. The irradiations were conducted in air at a dose rate low enough that the cell temperature never exceeded 40°C. The dose was measured with a Faraday cup. Immediately after each irradiation level was reached, the cells were stored in a nitrogen atmosphere for about 20 hours. The performance of the cells was then measured under a X-25L xenon-arc solar simulator. The intensity of the simulator was adjusted to a simulated 137-mW/cm^2 (AMO) condition by using an airplane-flown, calibrated (AlGa)As/GaAs reference solar cell. The temperature of the cell was maintained at 25°C during the performance measurements. The spectral response of the cell was measured with a filter wheel, consisting of nine narrow-bandpass monochromatic interference filters spanning the wavelength range from 0.4 to 1.0 micrometer.

After the measurements in the standard test facilities, the cell was mounted on a temperature-controlled block located inside a box purged with dry nitrogen. Vacuum was used to hold the cell in good thermal contact with the control block. The cell was again illuminated with the X-25L xenon-arc solar simulator. The intensity of the light was adjusted to give the previously measured short-circuit current of the (AlGa)As test cell. The cell was then cycled over the temperature range 415 to 135 K; performance was measured with an automatic data acquisition system at 5-kelvin intervals. These measurements were repeated after each incremental fluence level was reached. Before irradiation and at a fluence of $1x10^{16}$ electrons/cm^2, the temperature dependence of the cell performance was also measured at intensities of 137, 60.35, 11.75, 4.19, and 2.57 mW/cm^2. At the intermediate fluences, the performance as a function of intensity was measured only at 25°C.

RESULTS

The degradation in performance of the (AlGa)As/GaAs solar cell after 1-MeV-electron irradiation is shown in figure 2 normalized to the initial starting data. The data show a loss in maximum power of about 60 percent at a fluence of $1x10^{16}$ electrons/cm^2. The decrease in performance is primarily due to a loss in the short-circuit current. This is verified by the spectral response measurements shown in figure 3. This performance is typical of (AlGa)As/GaAs solar cells with a junction depth of about 0.5 micrometer (ref. 1).

A typical plot of the temperature dependence at one particular fluence is shown in figure 4. The data show that the open-circuit voltage V_{oc} varies linearly with temperature. However, the plot of short-circuit current density J_{sc} shows three distinct slopes over the temperature range 135 to 415 K. One slope was in the higher temperature range of 300 to 415 K and is called the upper slope. A second slope was in the intermediate temperature range of 200 to 300 K. The third slope was at temperatures below 200 K. This low-temperature range is outside the normal operating temperature of the cell, and temperature coefficients were therefore not calculated.

Temperature coefficients for each cell parameter were determined for each fluence level and are presented in figure 5. The temperature coefficient of the V_{oc} remained constant with fluence at a mean value of -2.03 mV/K. However, the temperature coefficient for J_{sc} depended on both the radiation fluence and the temperature range. The temperature coefficient of the upper slope (above 300 K) for J_{sc} was 0.03 mA/cm^2 K for the unirradiated condition. The temperature coefficient dropped very rapidly after irradiation with 1-MeV electrons to a fluence of $1x10^{13}$ electrons/cm^2. After this initial irradiation, the temperature coefficient remained constant at a mean value of 0.0213 mA/cm^2 K to a fluence of $1x10^{16}$ electrons/cm^2. In the intermediate temperature range, the temperature coefficients of J_{sc} remained constant at 0.0108 mA/cm^2 K, independent of fluence. Temperature coefficient of maximum power density P_{max} started at -0.045 mW/cm^2 K in the unirradiated condition but decreased to less than half that value (0.018 mW/cm^2 K) at a fluence of $1x10^{16}$ electrons/cm^2.

In obtaining temperature coefficients for J_{sc}, we found that the intercept between the upper slope and the intermediate slope varied. The temperature at which the two slopes intercepted is shown in figure 6 as a function of fluence. The intercept occurred at 325 K for the unirradiated condition. The temperature at which the intercept occurred gradually decreased with fluence to $3x10^{15}$ electrons/cm^2. After the last fluence level of $1x10^{16}$ electrons/cm^2 was reached, the temperature at which the intercept occurred rose sharply for some unexplained reason.

The short-circuit current was linear with light intensity to 137 mW/cm^2 (AMO), as shown in figure 7. Fluences to $1x10^{16}$ electrons/cm^2 had no effect on this linearity.

The variation of V_{oc} with intensity can supply insight into the physics of the cell, provided V_{oc} is plotted as the abscissa, as shown in figure 8. This is contrary to normal practice. Because I_{sc} is linear with intensity, the ordinate is proportional to current. Thus, this plot becomes the forward-diode characteristic of the device without the effects of series resistance (ref. 2).

In the unirradiated condition, this solar cell has an A value as determined from the slope of about 2.5 at intensities below 137 mW/cm^2. As the solar cell is irradiated, the slopes approach an A value of 1.15. The dotted-line extensions of the zero-fluence and $1x10^{16}$ electron/cm^2 curves were obtained from subsequent measurements made at light intensities greater than AMO. The slopes of these data are also about 1.15.

These data show that in the forward diode characteristic the recombination generation component of the reverse saturation current I_0 was dominant at light levels below AMO in the unirradiated condition. In the irradiated condition, the diffusion component became dominant at fluences above $1x10^{14}$ electrons/cm^2.

The intensity dependence of the temperature coefficient for this GaAs solar cell is shown in figure 9. The data show the V_{oc} temperature coefficient to decrease with increasing intensity to 137 mW/cm^2. The percent change in the J_{sc} temperature coefficient remained unchanged within 2 percent over the intensity range used in these studies.

SUMMARY OF RESULTS

A typical Hughes (AlGa)As/GaAs solar cell was subjected to 1-MeV-electron-irradiation to a fluence of $1x10^{16}$ electrons/cm^2. The performance of the solar cell was measured over the temperature range 135 to 415 K and at five intensity levels from 137 to 2.57 mW/cm^2 after each fluence level was reached.

The following results were obtained from these data:

1. Three distinct slopes were observed in the variation of short-circuit current density J_{sc} with temperature.

2. Above 300 K, the J_{sc} temperature coefficient was initially 0.03 mA/cm^2 K but it decreased after a fluence of $1x10^{13}$ electrons/cm^2 to 0.0213 mA/cm^2 K.

3. At 200 to 300 K, the J_{sc} temperature coefficient was 0.0108 mA/cm^2 K and showed no change in temperature.

4. The open-circuit-voltage temperature coefficient remained constant at -2.03 mV/K with fluence.

5. The maximum-power temperature coefficient at a fluence of $1x10^{16}$ electrons/cm^2 was about one-half its unirradiated value of -0.045 mW/cm^2 K.

6. The recombination generation component of the reverse saturation current was dominant at light levels below 137 mW/cm^2 (AMO) in the unirradiated condition. The diffusion coefficient dominated at fluences above $1x10^{14}$ electrons/cm^2.

REFERENCES

1. Kamath, S.; and Wolff, G.: High Efficiency GaAs Solar Cell Development. Final Rep. Aug. 1976-July 1978, Hughes Aircraft Co., Jan. 1979. (AFAPL-TR-78-96)

2. Wolf, Martin; and Rauschenbach, Hans: Series Resistance in Solar Cell Measurements. Advan. Energy Convers., vol. 3, no. 2, Apr.-June 1963, pp. 455-479

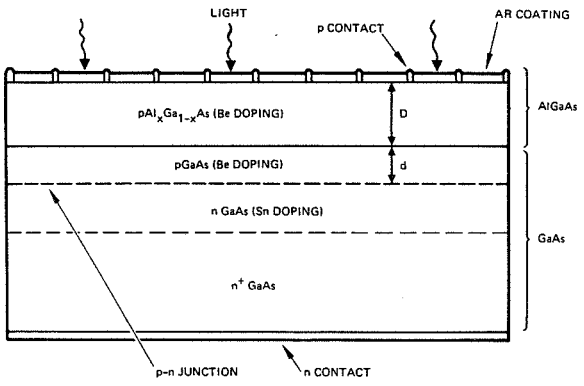

Figure 1. - GaAs solar cell structure.

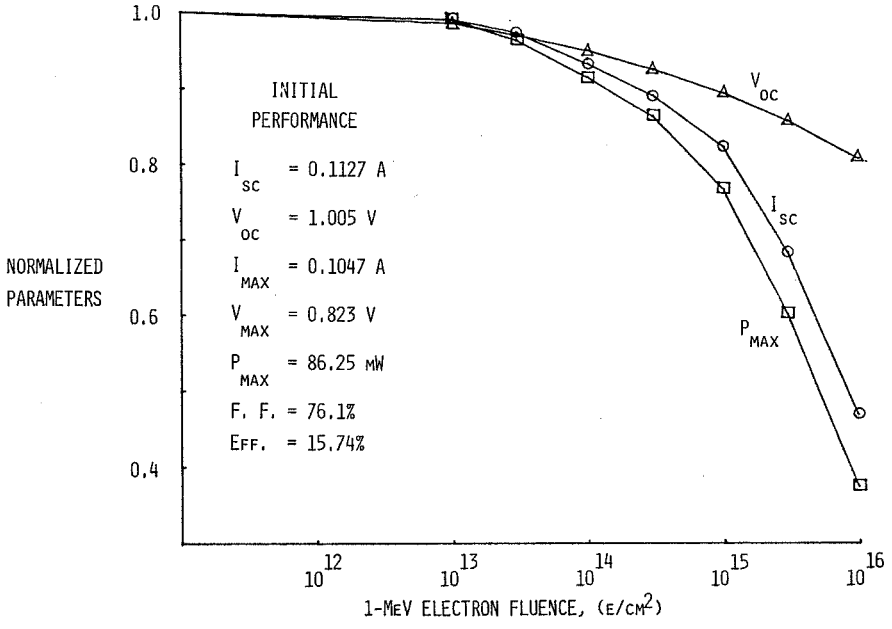

Figure 2. - Performance of (AlGa)As solar cell irradiated with 1-MeV electrons.

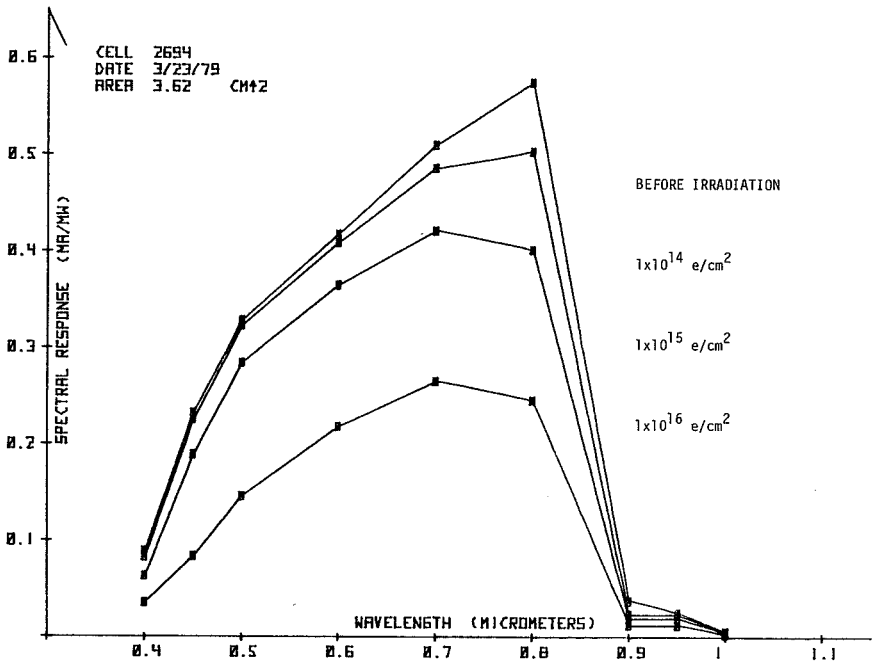

Figure 3.- Spectral response of 1-MeV-irradiated (AlGa)As solar cell.

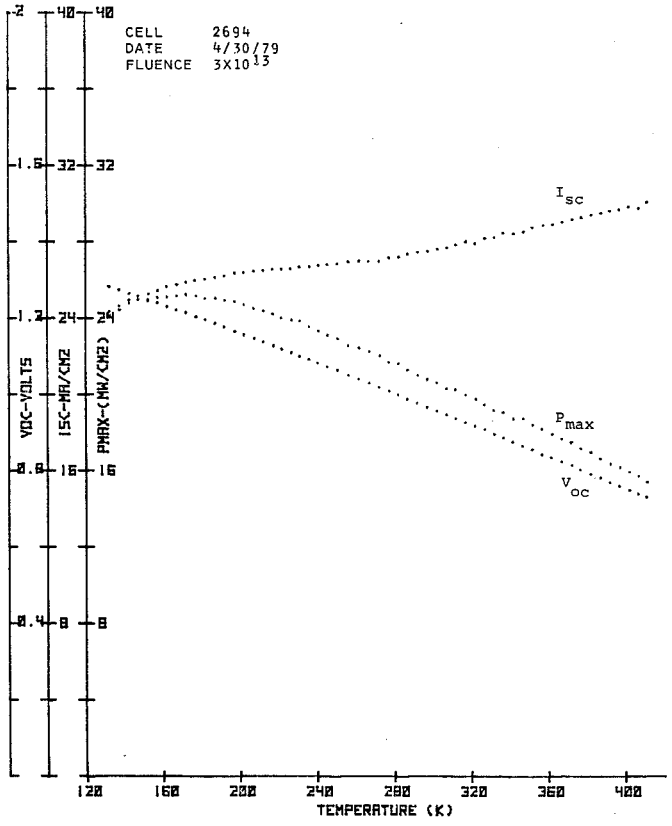

Figure 4.- Temperature dependence of (AlGa)As solar cell.

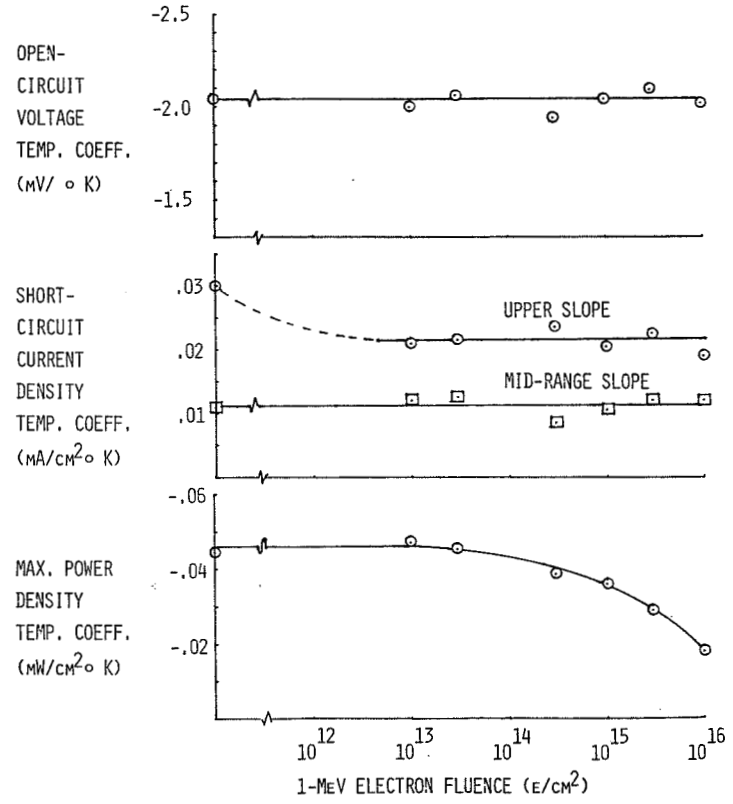

Figure 5.- Temperature coefficients of 1-MeV-irradiated (AlGa)As solar cell.

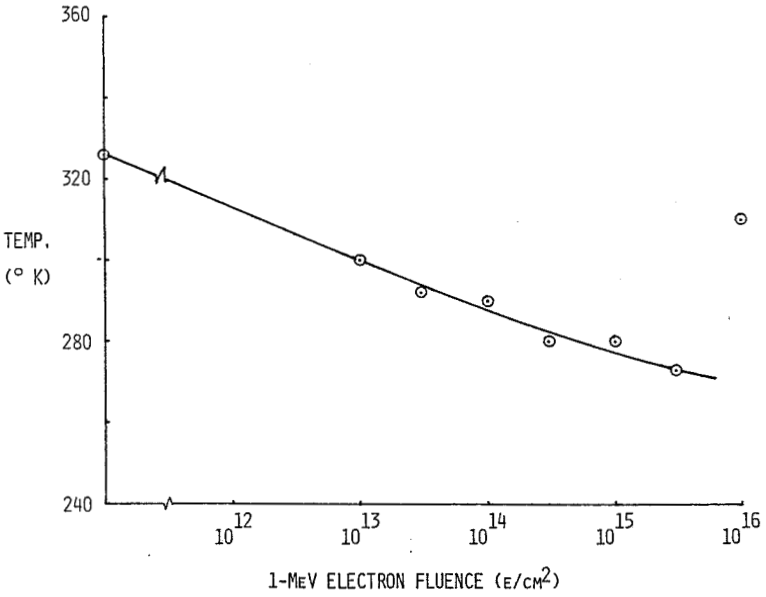

Figure 6.- Temperature for intercept point of upper and midrange current density slopes.

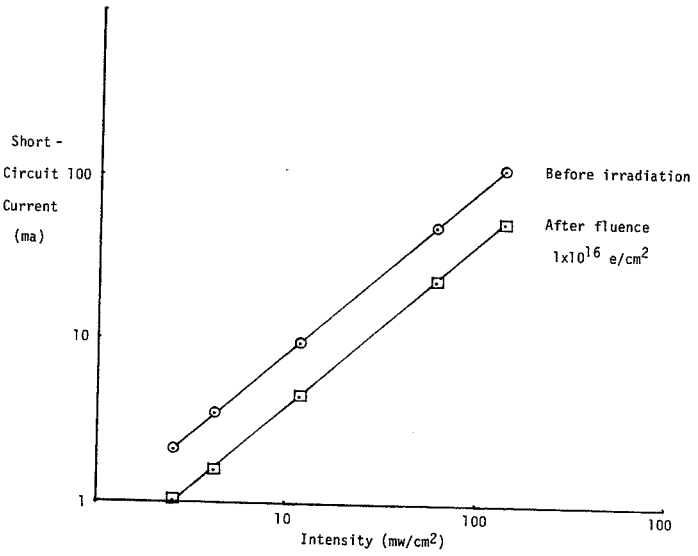

Figure 7.- Short-circuit dependence with intensity for irradiated (AlGa)As solar cell.

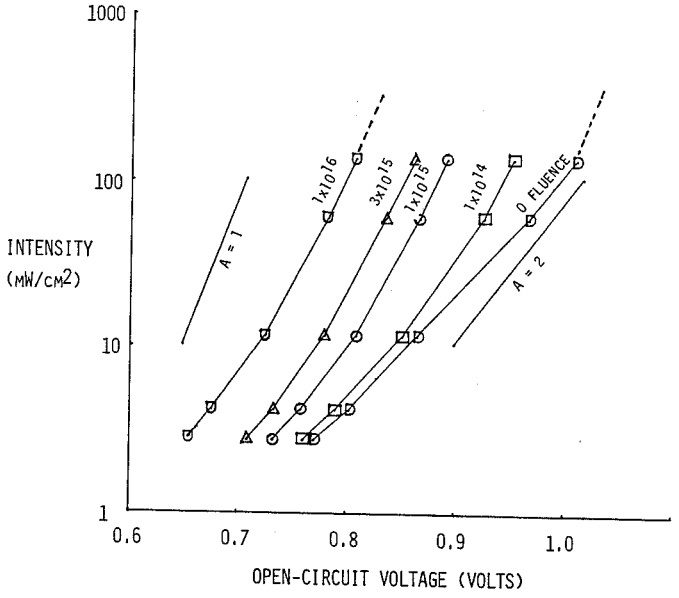

Figure 8.- Open-circuit voltage - intensity variation in irradiated (AlGa)As solar cell.

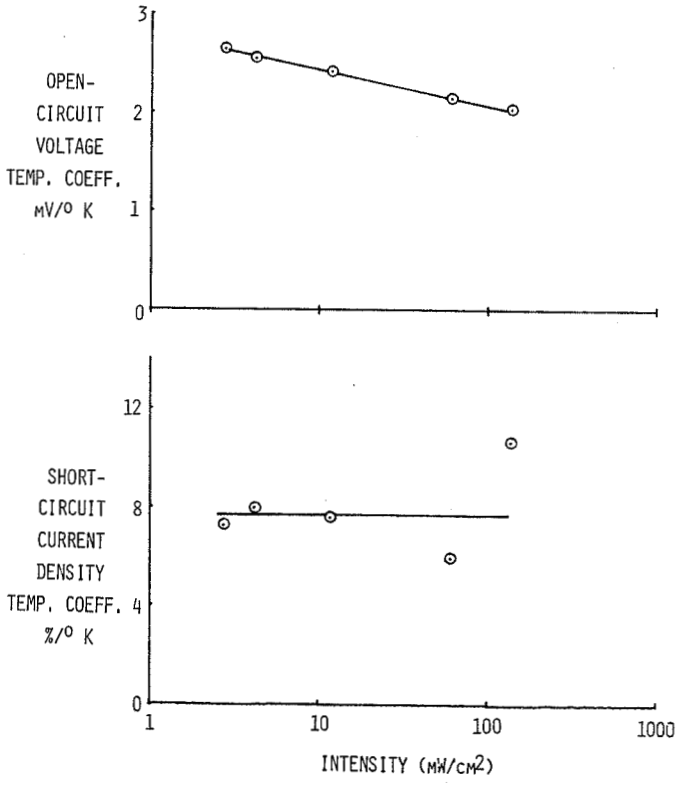

Figure 9.- Intensity dependence of (AlGa)As solar cell on temperature coefficient.

SHALLOW-HOMOJUNCTION GaAs SOLAR CELLS*

John C. C. Fan
Lincoln Laboratory, Massachusetts Institute of Technology

SUMMARY

We have developed single-crystal GaAs shallow-homojunction solar cells on GaAs or Ge substrates, without $Ga_{1-x}Al_xAs$ window layers, that have conversion efficiencies exceeding 20% at AM1 (17% at AM0). Using a simple theoretical model, we have obtained good fits between computer calculations and experimental data for external quantum efficiency and conversion efficiency of cells with different values of n^+ layer thickness. The calculations not only yield values for material properties of the GaAs layers composing the cells but will also permit the optimization of cell designs for space and terrestrial applications. Preliminary measurements indicate that the shallow-homojunction cells are resistant to electron irradiation. In the best test so far, bombardment with a 1×10^{16} cm^{-2} fluence of 1 MeV electrons reduced the short-circuit current by only about 6%.

We have recently developed (ref. 1,2) single-crystal GaAs shallow-homojunction solar cells without $Ga_{1-x}Al_xAs$ window layers, that have conversion efficiencies of about 20% at AM1 (17% at AM0). The cells employ an $n^+/p/p^+$ structure, prepared by chemical vapor deposition (CVD) on either GaAs or Ge substrates, in which surface recombination losses are reduced because the n^+ layer is so thin that most of the carriers are generated in the p layer below the junction. Figure 1 shows schematic diagrams of GaAs solar cells grown on a Ge substrate (on the left side) and on a GaAs substrate (on the right side). An oxide film formed by anodization of the n^+ layer is used as an antireflection coating. Two different metallization schemes have been developed -- electroplated Sn or electroplated Au. Figure 2 shows a schematic diagram of our CVD system showing the H_2-$AsCl_3$ and doping gas flow control, and also a cross sectional view of the reactor tube. Figure 3 shows the photocurrent as a function of applied voltage for a GaAs shallow-homojunction solar cell grown on a GaAs single-crystal substrate with 20% conversion efficiency at AM1, as measured at 20°C. Solar cells grown on single-crystal Ge have characteristics very similar to those of cells grown on GaAs, as long as the n^+ layer thickness is the same.

By using a simple analytical model (ref. 3), we have obtained good fits between computer calculations and experimental data for the external quantum efficiency and AM1 conversion efficiency of cells with different values of n^+ layer thickness. Figure 4 shows external quantum efficiency as a function of wavelength for GaAs cells with n^+ layer thickness of 450, 750, 1000, and 1550 Å. The solid curves were calculated using only three adjustable parameters, while the points were measured. From the best values of the adjustable parameters, we obtained values of L_p (hole diffusion length in n^+ layer) ~ 0.05 μm, L_n (electron diffusion length in p layer) ~ 20 μm, and effective S_p (recombination velocity on n^+ surface) $\sim 10^7$ cm/sec. Using these values, we calculated the conversion efficiency at AM1 as a function of n^+ layer thickness.

* This work was supported by the Department of the Air Force.

The calculated efficiency values compare well with the measured values as shown in (fig. 5). Having demonstrated the applicability of this simple analytical model, we can now use it in optimizing cell designs for space and terrestrial applications.

To investigate the potential of our cells for space applications, we have performed some initial experiments that show these cells to be resistant to electron irradiation. Cells with the n^+/p structure should be considerably more radiation resistant than those with p^+/n structure because the minority carrier diffusion length is much larger for electrons than for holes. The thin n^+ layer not only minimizes the effect of surface recombination velocity but also allows almost all the electron damage effects to occur in the p layer, where the electron diffusion lengths are long. The back-surface-field p/p^+ structure also restricts the effects of electron damage to the narrow active p region ($\sim 2\ \mu m$). We have confirmed this superior space resistance in a series of experiments using 1 MeV electrons with fluence up to 10^{16} e/cm^2.

Figure 6 shows the maximum power per unit area P_{max} in mW/cm^2 for one of our 1/2 cm x 1 cm GaAs shallow-homojunction cells grown on Ge substrates as a function of cumulative electron fluence. The cell initially had P_{max} of over 22 mW/cm^2 (cell efficiency η at AM0 was 16.7%), which slowly decreased with increasing fluence to about 13 mW/cm^2 at 10^{16} e/cm^2. Our results compare very favorably with reported results on three other types of space cells (ref. 4,5), as shown in (fig. 6). Both the initial and final values of P_{max} are higher for our cell than for any of the others.

The reduction in P_{max} for our cell occurs because the open-circuit voltage V_{oc} and short-circuit current I_{sc} both decrease by about 20% after 10^{16} e/cm^2 electron dosage. The decrease in V_{oc} corresponds to an increase in leakage current, as indicated by an increase in saturation current density J_o for the injected current component from 6×10^{-18} A/cm^2 to 1×10^{-14} A/cm^2. The diode factor remained the same, however, at 1.1. The decrease in I_{sc} may be attributed to the degradation of electron diffusion length in the p layer of the cell, as well as to an observed change in the anodic antireflection (AR) coating.

The decrease in I_{sc} should be greatly reduced if the doping level in the p layer of the cell is lowered from 1×10^{17} /cm^3, so that the electron diffusion length is increased, and if the anodic AR coating is not used. This prediction has been confirmed by our experiments on another cell, which has a lower p doping level ($\sim 10^{16}$/cm^3) and no AR coating. Figure 7 shows the characteristics of this cell after successive electron irradiations. After 10^{16} e/cm^2 dosage, I_{sc} decreases only slightly to about 94% of the original value. This small decrease is confirmed by the quantum efficiency measurements on the cell at various electron dosages (also shown in the figure). The cell, however, still exhibits a significant decrease in V_{oc}. As in the previous cell, the diode factor changed only slightly, from 1.1 before irradiation to 1.3 after 10^{16} e/cm^2 dosage. The value J_o, however, increased greatly from 2×10^{-18} A/cm^2 to 1×10^{-11} A/cm^2, thus reducing the V_{oc}.

Our initial experimental results indicate that the $n^+/p/p^+$ shallow-homojunction GaAs solar cells are resistant to electron irradiation. A very small change in I_{sc} was observed for a cell with low doping level in the p layer and no AR coating. The changes in V_{oc} are tentatively attributed to an increase in leakage current, partially from the exposed edges of the etched mesas in our cells. This increase in leakage current is expected to be reduced when our cell area is increased from 0.5 cm^2 to 4 cm^2, and

when the exposed mesa edges are protected with an encapsulant. A different AR coating using Si_3N_4 is also being developed. Therefore, by optimizing the design and fabrication of shallow-homojunction GaAs cells, even better cells can be obtained which would provide high power density and very long life in space.

REFERENCES

1. Fan, J. C. C.; Bozler, C. O.; and Chapman, R. L., Appl. Phys. Lett., vol. 32, 1978, p. 390.

2. Bozler, C. O.; Fan, J. C. C.; and McClelland, R. W., Inst. Phys. Conf. Ser. No. 45, Chapter 5, 1979, p. 429.

3. Hovel, H. J.: Solar Cells, vol. 11 of Semiconductors and Semimetals Academic Press, New York, 1975.

4. Meulenberg, A.; Curtin, D. J.; and Cool, R. W., Conference Record of 12th IEEE Photovoltaic Specialists Conf., Baton Rouge, Louisana, 1976, p. 238.

5. Kamath, S. and Wolff, G., Final Report: High Efficiency GaAs Solar Cells, AFAPL-TR-78-96, Jan. 1979.

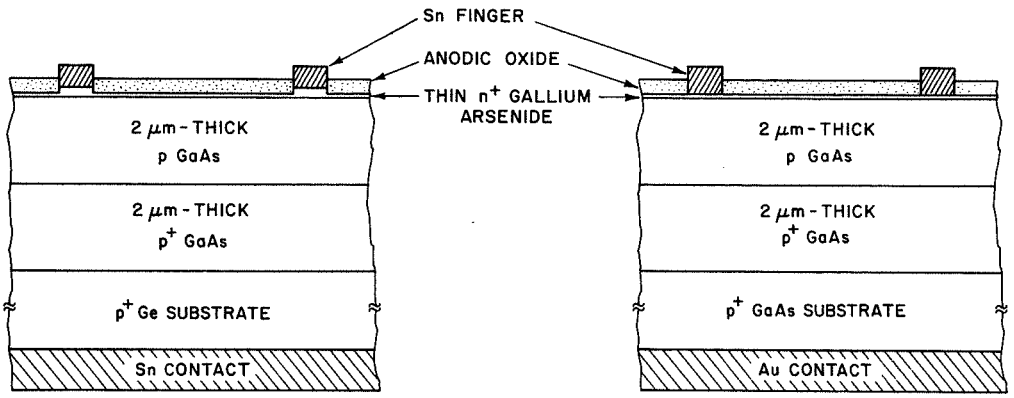

Fig. 1 Schematic diagram of GaAs solar cells grown on GaAs and Ge substrates.

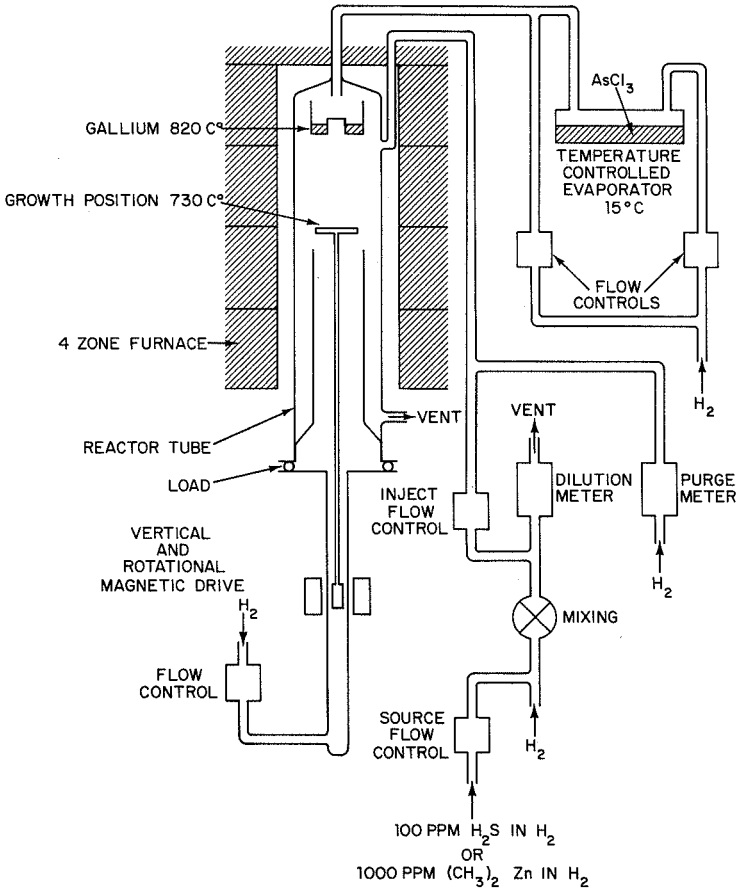

Fig. 2 Schematic diagram of GaAs vapor deposition system showing the $AsCl_3$-Ga-H_2 and doping gas flow control, and also a cross sectional view of the reactor tube.

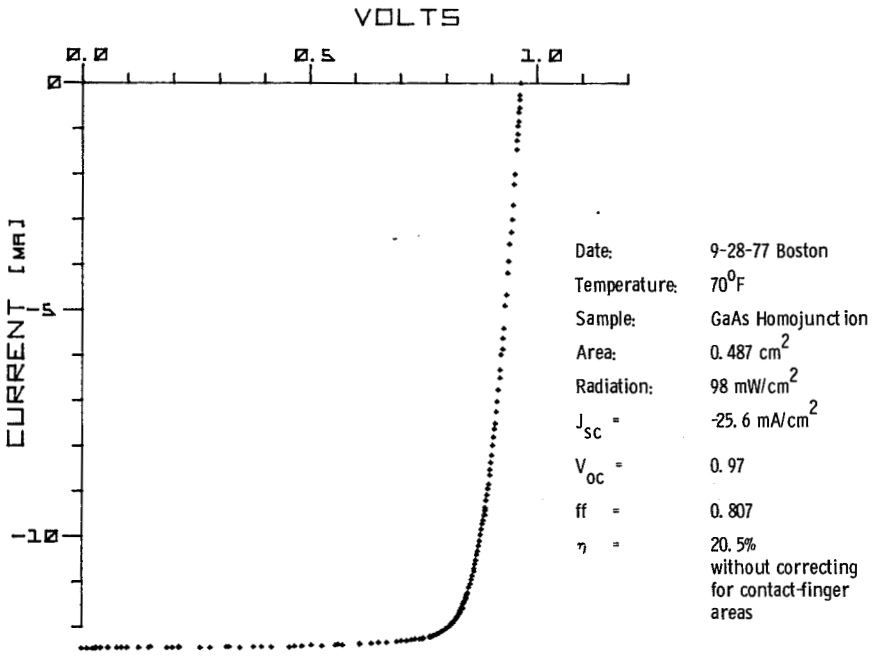

Fig. 3 Photocurrent as a function of applied voltage for a GaAs shallow-homojunction solar cell with 20% conversion efficiency at AM1, as measured at 20°C.

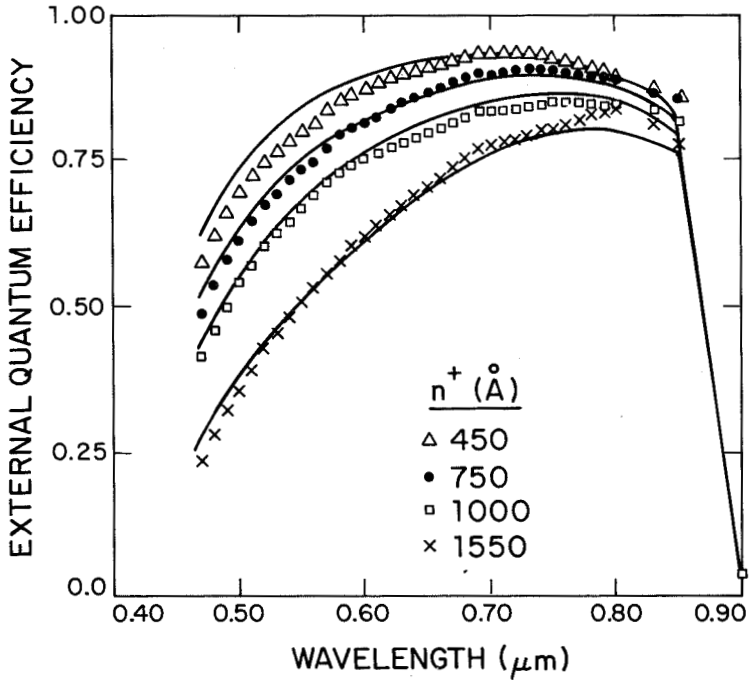

Fig. 4 External quantum efficiency as a function of wavelength for GaAs shallow-homojunction solar cells with n^+ layer thickness of 450, 750, 1000, and 1500 Å.

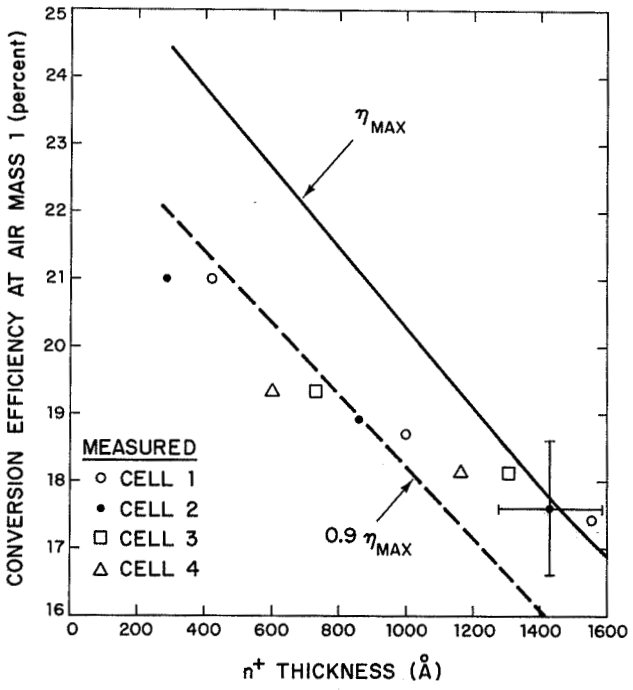

Fig. 5 Efficiency at AM1 as a function of n^+ layer thickness. Measured values are represented by points, calculated values of maximum conversion efficiency η_{max} and of 0.9 η_{max} by solid and dashed lines, respectively.

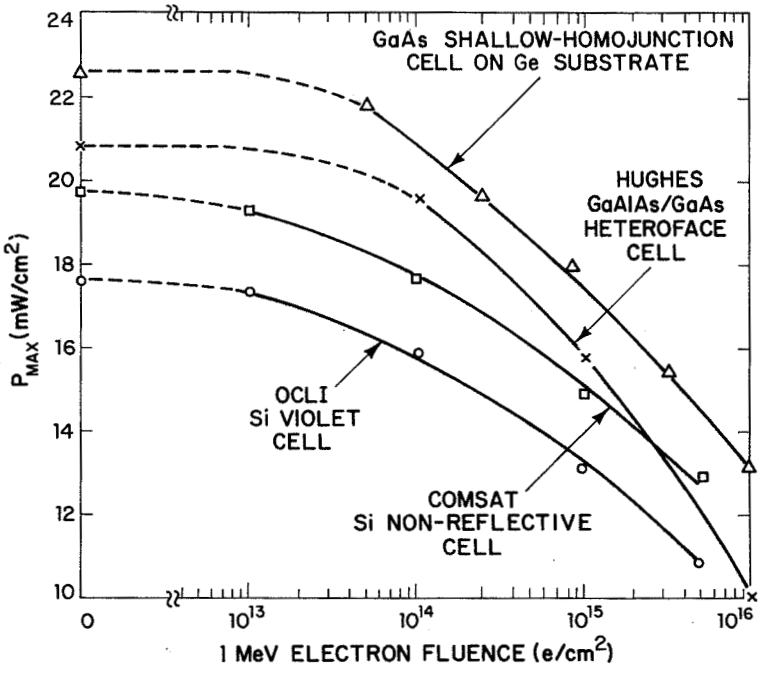

Fig. 6 The maximum output power density at AM0, P_{max}, for Cell 1 as a function of cumulative electron fluence. The results for three other types of cells were included for comparison.

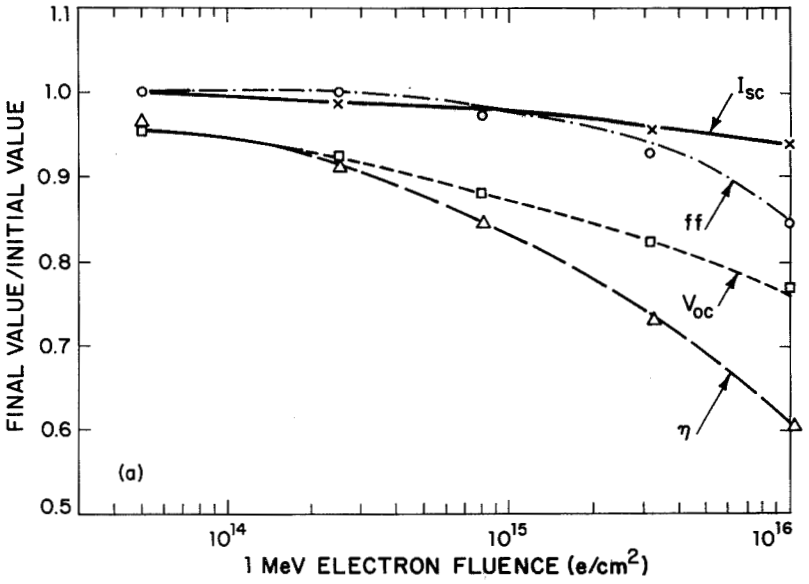

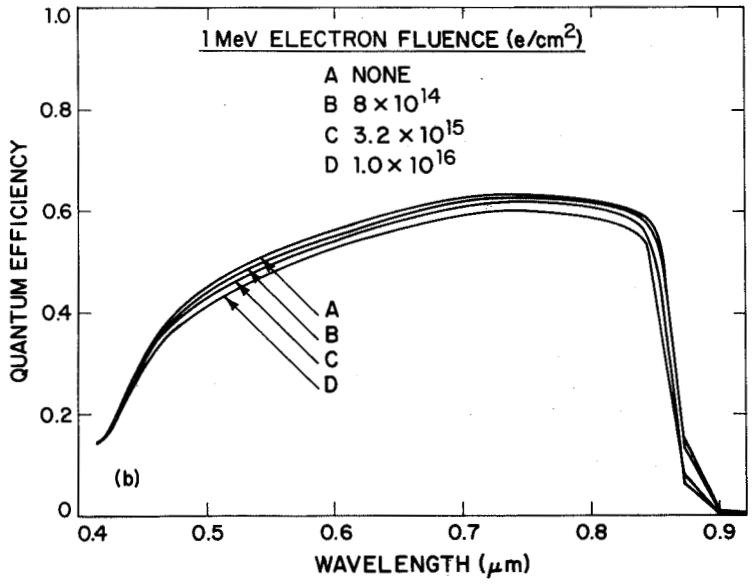

Fig. 7 a) The characteristics of Cell 2 as a function of cumulative electron fluence.
b) The quantum efficiency measurements on Cell 2 at various electron fluences.

RADIATION EFFECTS IN GaAs AMOS SOLAR CELLS*

B. K. Shin and R. J. Stirn
Jet Propulsion Laboratory

ABSTRACT

Inasmuch as GaAs solar cells show considerable potential for space applications, the behavior of these cells in a radiation environment is of great interest. This report presents the results of radiation damage produced in AMOS (Antireflecting-Metal-Oxide-Semiconductor) cells with Sb_2O_3 interfacial oxide layers by 1-MeV electrons. The degradation properties of the cells as a function of irradiation fluences were correlated with the changes in their spectral response, C-V, dark forward, and light I-V characteristics. The active n-type GaAs layers were grown by the OM-CVD technique, using sulfur doping in the range between 3×10^{15} and 7×10^{16} cm^{-3}. At a fluence of 10^{16} e/cm^2, the low-doped samples showed I_{SC} degradation of 8% and V_{OC} degradation of 8%. The high-doped samples showed I_{SC} and V_{OC} degradation of 32% and 1%, respectively, while the fill factor remained relatively unchanged for both. AMOS cells with water vapor-grown interfacial layers showed no significant change in V_{OC}.

INTRODUCTION

Results of 1-MeV electron damage in n-base heteroface Al(Ga)As/GaAs solar cells are relatively sparse (ref. 1). More importantly, the results to date are primarily for base carrier concentrations in the low 10^{17} cm^{-3} regime. Also, since the photovoltaic parameters of the solar cell are affected by the Al(Ga)As layer thickness and depth of the junction, it has not been possible to separate damage effects occurring in the p- and n-regions of the cell. On the other hand, the wider body of literature of electron damage in bulk n-GaAs (refs. 2,3) usually measured only majority carrier removal or trap properties, such as by DLTS (Deep Level Trap Spectroscopy), and not the more important (for solar cells) changes in photovoltaic parameters or minority carrier lifetimes upon irradiation.

This paper presents preliminary results of radiation damage in GaAs introduced by 1-MeV electrons using Schottky barrier structures. This approach has the distinct advantage of being able to use GaAs with carrier concentrations

*This paper presents the results of one phase of research conducted at the Jet Propulsion Laboratory, California Institute of Technology, for the Department of Energy by agreement with the National Aeronautics and Space Administration.

much less than 10^{17} cm^{-3} and observing degradation characteristics of GaAs Schottky barrier solar cells as developed at JPL. Since these are majority carrier devices, i.e., the voltage output and fill factor are not controlled by minority carrier diffusion from the bulk, reduced radiation damage should be observed as compared to junction type p/n solar cells. A disadvantage of using Schottky structures is that annealing studies of radiation damage are not possible since the devices are unstable at temperatures above 200°C.

The addition of an intentional interfacial oxide layer between the Schottky barrier metal and the GaAs has been found to dramatically increase the open circuit voltage V_{OC} from about 500 to 800 mV (ref. 4). Consequently, the irradiation studies of Schottky barrier solar cells were performed on devices incorporating two types of oxide layers to determine if electron irradiation will influence the V_{OC} by modifying the interface states controlling the Schottky barrier height.

EXPERIMENTAL DETAILS

The solar cells used in the present investigation were prepared by growing n-type GaAs epilayers by organo-metallic chemical vapor deposition (OM-CVD) techniques on Te-doped substrates and fabricating AMOS (Anti-reflecting Metal-Oxide-Semiconductor) solar cells on this material. The substrates* had doping concentrations of 2.7 x 10^{17} cm^{-3} and crystal orientation approximately 2°-off [100] toward the [110] direction. The active epilayer was sulfur-doped with the doping concentrations ranging from $3x10^{15}$ to $7x10^{16}$ cm^{-3}. The epilayers of 3 to 4μm in thickness were grown at 700°C using arsine (AsH_3) and trimethyl-gallium (TMG) flow rates of 1.9 x 10^{-4} and 4.5 x 10^{-5} moles/min, respectively. These epilayers were used to fabricate fully gridded and AR-coated 1x1-cm AMOS cells. No attempt was made to optimize the design parameters to increase radiation hardness.

Prior to cell fabrication, ohmic back contacts were made by sintering Au-Ge-Ni evaporated contacts for 3 min in hydrogen at 480°C. The interfacial oxide layers of the AMOS cells were formed using either vacuum-deposited Sb_2O_3 oxides or saturated water vapor (H_2O/O_2) native oxides. The non-native Sb_2O_3 oxides of 38 Å thickness were deposited at a rate of 0.6 Å/sec in an oil-free vacuum chamber. The H_2O/O_2-generated oxides were formed at 23°C by passing water-vapor-saturated O_2 over freshly etched GaAs placed in a quartz tube. Typical oxide formation time of 48 to 72 hours is required to obtain uniform oxide layers of 38 Å in the later case. A 60 Å-thick Ag layer of 1-cm^2 area was next evaporated at a typical rate of 5 Å/sec to form the Schottky barrier.

The 1-MeV electron irradiation was performed at JPL using the Dynamitron Particle Accelerator with fluences between 10^{14} and 10^{16} e/cm^2. The irradiation was carried out at room temperature using an electron flux of $\leq 10^{12}$ e/cm^2-sec.

---

*Epidyne (now National Semiconductor, Hawthorne, CA)

Properties of cells as a function of irradiation fluences were evaluated by the light current-voltage (I-V) characteristics, spectral response measurements, capacitance-voltage (C-V) and dark forward I-V characteristics. Light I-V measurements were obtained with samples at 28°C by using either the ELH lamps at input power density of 100 mW/cm^2 for AM1 simulation or the Aerospace Controls Model 302 xenon arc source at an input power density of 135 mW/cm^2 for AM0 simulation. Absolute spectral response measurements were made in the wavelength ranges between 0.4μm and 0.9μm using a prism monochromator. The output current of a standard Si PIN diode previously calibrated with a UDT 21A Power Meter was used to obtain absolute values of the collection efficiency.

The diodes were further evaluated using measurements of C-V and dark forward I-V characteristics in a light-tight box. The measurements of capacitance as a function of reverse voltage were obtained with a Boonton 74C-S8 Capacitance Bridge operating at 100 kHz.

RESULTS AND DISCUSSION

Light I-V characteristics for two Sb_2O_3-oxide AMOS solar cells using ELH light simulation with carrier concentrations representing the extremes of those used in this study are given in figure 1 for pre-irradiated and post-irradiated conditions. The Sb_2O_3-oxide cells used in this study did not have permanent contacts applied, and thus, could not be measured in-situ with the AM0 simulator. Solar cells with native oxides did have such contacts, but unfortunately did not include GaAs layers with concentrations below 1x10^{16} cm^{-3}.

Note that the lower-doped sample showed considerably less degradation in short-circuit current (I_{SC}). This is because the space charge region width in low-doped GaAs is a significant fraction of the light-absorption depth, and photo-generated carriers in this region which are field-aided in their collection are little affected by radiation-induced defects. A second contributing factor to the lower degradation in more lightly-doped GaAs is probably a lower degradation constant related to minority carriers collected at the barrier by diffusion from the neutral region -- just as for silicon.

There is some degradation in V_{OC} for these cells -- more for the lighter-doped GaAs. Though the amount of degradation at 10^{16} e/cm^2 fluence, for example, is much less than usually observed in p/n junction-type solar cells, it is clearly more than that found for AMOS solar cells using H_2O/O_2 native oxides, as shown in figure 2. This figure shows the V_{OC} normalized to the pre-irradiated value as a function of fluence for several samples of various doping concentrations with both the native and the deposited interlayer oxides. Two features are clearly observed from these curves: (1) The overall degradation of V_{OC} is not of major significance, since at a fluence of 10^{16} e/cm^2, the degraded values range from 2 to 8%, and (2) the degradation characteristics of the two types of oxides, the H_2O/O_2 or the Sb_2O_3 oxides, are quite distinguishable. In particular, the native oxide cells show negligible change, consistent with earlier unpublished results obtained at JPL on Te-doped GaAs layers. The small change is to be expected since the AMOS cell is a majority carrier device, as mentioned above.

To supplement the results for V_{OC}, the dark forward I-V characteristics were measured and the values of both the saturation current density J_o and the diode ideality factor n obtained using the least square fitting. The plots of J_o and n as a function of fluence are shown in figures 3 and 4, respectively. Samples with both types of oxide (H_2O/O_2 and Sb_2O_3) interlayers are shown for comparison. The differences in J_o (and n) between samples relate more to differences in surface treatment and handling immediately prior to oxidation rather than to differences in doping or even oxide type. The values of J_o and n do not change much with increasing fluence except at fluences higher than 10^{15} e/cm^2, with more change seen in the Sb_2O_3-oxide solar cells. J_o and the n-factor are intimately related to each other in Schottky barriers with interfacial oxide layers.

The effects of electron irradiation on the short-circuit current for cells with various doping concentrations are shown in figure 5. As expected, the degradation is more pronounced in I_{SC} than in V_{OC}. The results for a LPE-grown Al(Ga)As-GaAs heteroface solar cell (ref. 1) with junction depth of 0.5μm and the donor doping of 10^{17} cm^{-3} is also included for comparison. Clearly, the percentage change in I_{SC} per given fluence primarily depends on the doping concentrations and is independent of the type of oxide used. This is typical of the Schottky barrier cells, with relatively high doping, where the degradation of I_{SC} is primarily due to a decrease in diffusion length as for Si solar cells. More specifically, the change in I_{SC} is directly related to the ratio of light-generated carrier density in the depletion region to that in the bulk. Finally, the anomalous behavior of 10^{16} cm^{-3} doped cells is noteworthy for fluence between 10^{15} and 10^{16} e/cm^2. This reverse degradation reproducibly occurred for several samples tested with the same doping level. To our knowledge, such irregularity has not been reported in the literature, although GaAs solar cells with doping concentrations of 10^{16} cm^{-3} are rarely made. Further experiments on this matter are planned.

Figure 6 shows the absolute collection efficiency as a function of wavelength from 0.4μm to the bandgap region, for both unirradiated and 10^{16} e/cm^2 irradiated cells having various bulk concentrations. The spectral response is consistent with the behavior of the short-circuit current, in that the red region is more affected for the highly-doped cell. The zero-bias depletion width of the lightly doped cells is large ($\sim$0.7μm for $n_0 = 3\times10^{15}$ cm^{-3}) before the irradiation, increasing with fluence because of carrier removal. Since the absorption depths for λ = 0.7μm and 0.5μm is 0.65μm and 0.1μm, respectively, it is clear that most of the incident energy will be absorbed within the depletion width for the lower-doped cells.

The dependence of fill factor (FF) as a function of fluence for four H_2O/O_2 samples is shown in figure 7. Averaged FF values were used since the values at each fluence level were very similar for all of the samples evaluated. At the highest fluence level, the spread of FF is only ±0.2% from the average value. The unirradiated FF of 0.79 is reasonably good and gradually decreases to 0.73 at 6.25 x 10^{15} e/cm^2 -- a decrease of less than 8%. The small change of FF in Schottky barrier devices is due to the relatively small change in J_o with fluence, as compared to junction-type solar cells.

Power degradation for the H_2O/O_2 cells with doping concentrations of $1x10^{16}$ and $5x10^{16}$ cm^{-3} is shown in figure 8. A typical degradation characteristic for a heteroface cell with Al(Ga)As/GaAs structure grown by LPE is also included for comparison. In the H_2O/O_2 AMOS cells, about 24% degradation is obtained for lower-doped cell ($n_0 = 1x10^{16}$ cm^{-3}) at 10^{16} e/cm^2. Even lower power degradation (17%) was observed on the $3x10^{15}$ cm^{-3} cells having Sb_2O_3 oxide interlayer when measured with ELH simulation. However, due to absence of contacts, no in-situ AMO values are given. Note the anomalous behavior of the 10^{16} cm^{-3} sample due to the aforementioned behavior in I_{sc} (fig. 5).

When the carrier concentration is plotted against a critical fluence at which I_{sc} degrades by the same amount, e.g. 25%, (fig. 9), an apparent break in the slope occurs at the same carrier concentration at which the I_{sc} degradation was observed (10^{16} cm^{-3}). For this figure, data was taken from an earlier study, not previously reported, where the GaAs epi-layers were commercially purchased Te-doped layers. At this time, it is not clear whether an abrupt change in slope is indeed real, or if the two slopes are indicative of two very separate mechanisms. Thus, the critical fluence should tend to become independent of doping in the light-doping range, where substantially all of the carriers are generated in the space-charge region. At higher doping levels, where substantially all of the carriers must diffuse from the neutral region of the bulk GaAs, one would expect a constant dependence of the critical fluence on carrier concentration. A determination of the detailed mechanisms will require additional studies and will be reported subsequently.

REFERENCES

1. "High Efficiency GaAs Solar Cell" Final Report, January 1979, AFAPL-TR-78-96, Hughes Aircraft Company.

2. D. V. Lang, R. A. Logan, and L. C. Kimerling, Phys. Rev. B15, 4874 (1977).

3. J. W. Farmer and D. C. Look, submitted to Physical Review.

4. R. J. Stirn and Y. C. M. Yeh, IEEE Trans. Electron Dev. ED-24, 476 (1977).

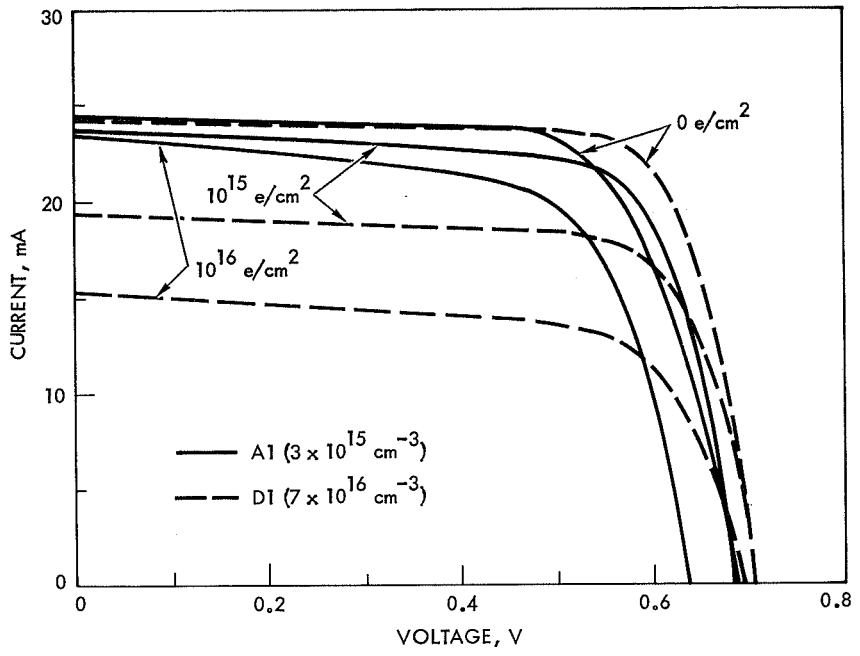

Figure 1. Light I-V Characteristics of Non-Irradiated and 1-MeV Electron-Irradiated GaAs AMOS Solar Cells With Sb_2O_3-Oxide Interlayer

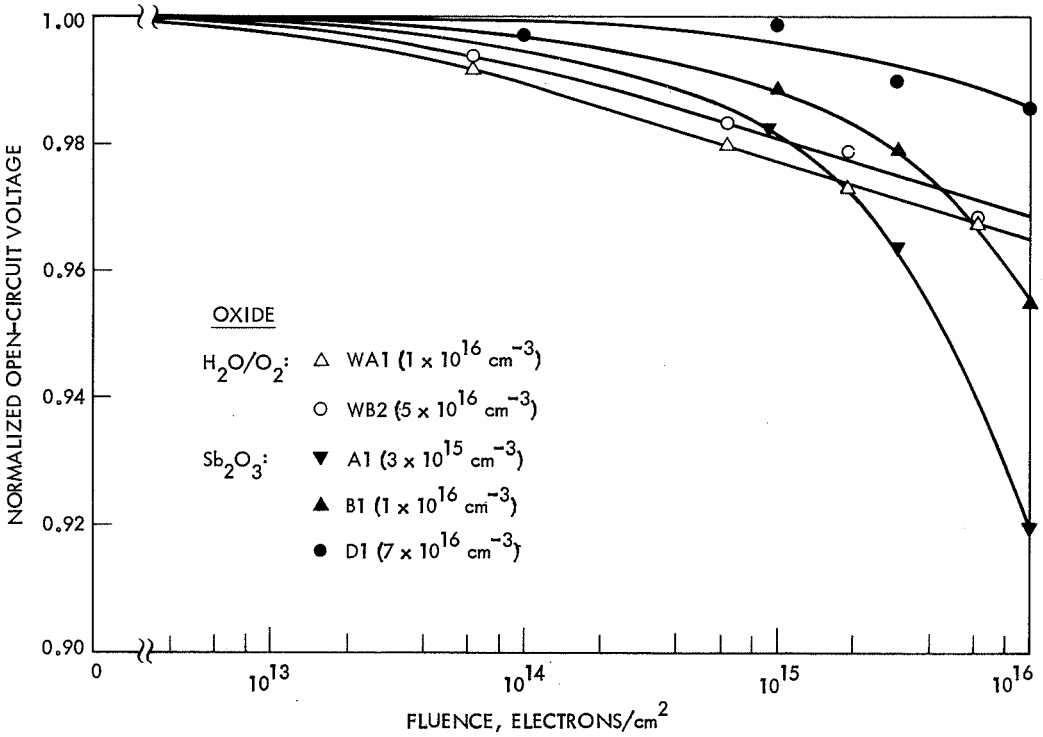

Figure 2. Normalized Open-Circuit Voltage as a Function of Fluence for GaAs AMOS Solar Cells Irradiated with 1-MeV Electrons

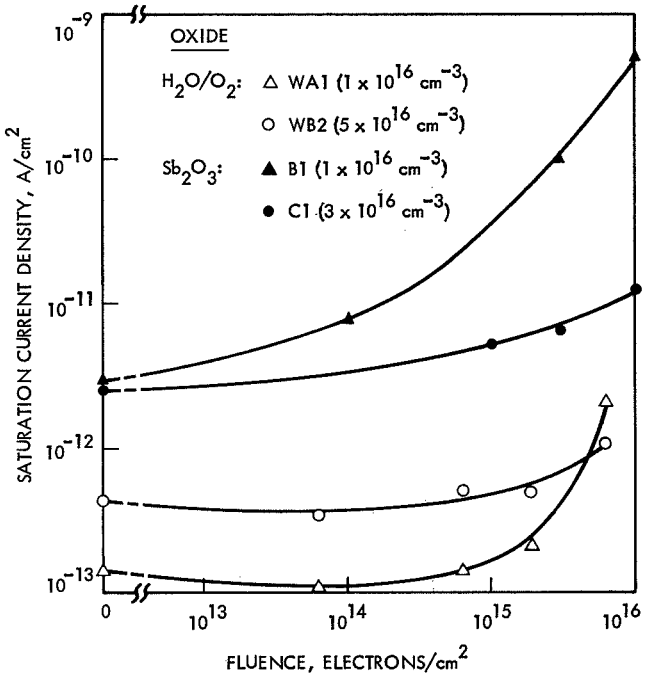

Figure 3. Saturation Current Density as a Function of Fluence for GaAs AMOS Solar Cells Irradiated with 1-MeV Electrons

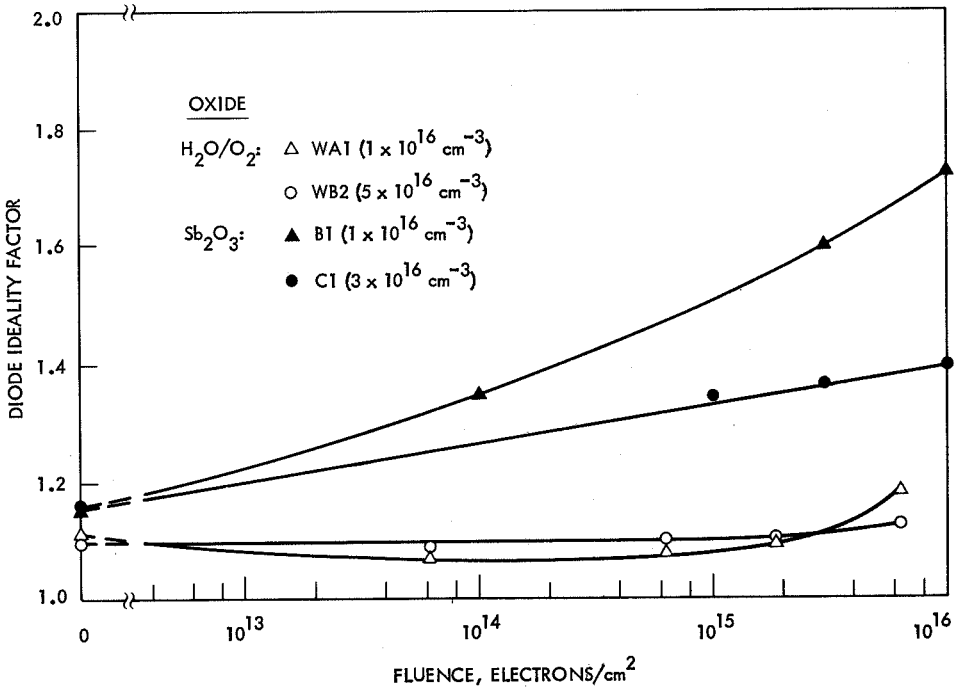

Figure 4. Diode Ideality Factor as a Function of Fluence for GaAs AMOS Solar Cells Irradiated with 1-MeV Electrons

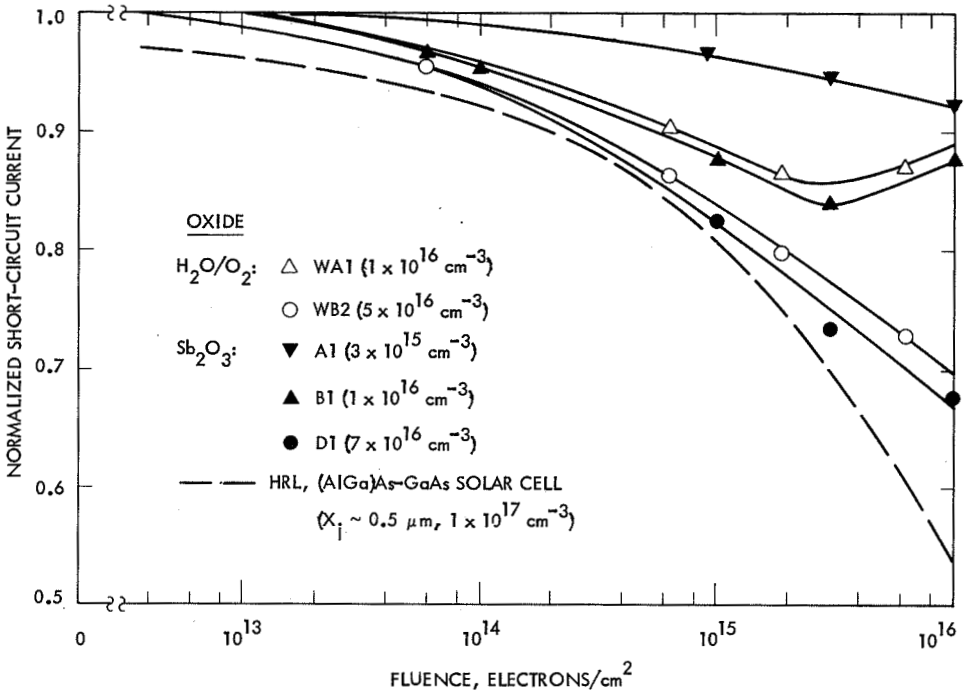

Figure 5. Normalized Short-Circuit Current as a Function of Fluence for GaAs AMOS Solar Cells Irradiated with 1-MeV Electrons

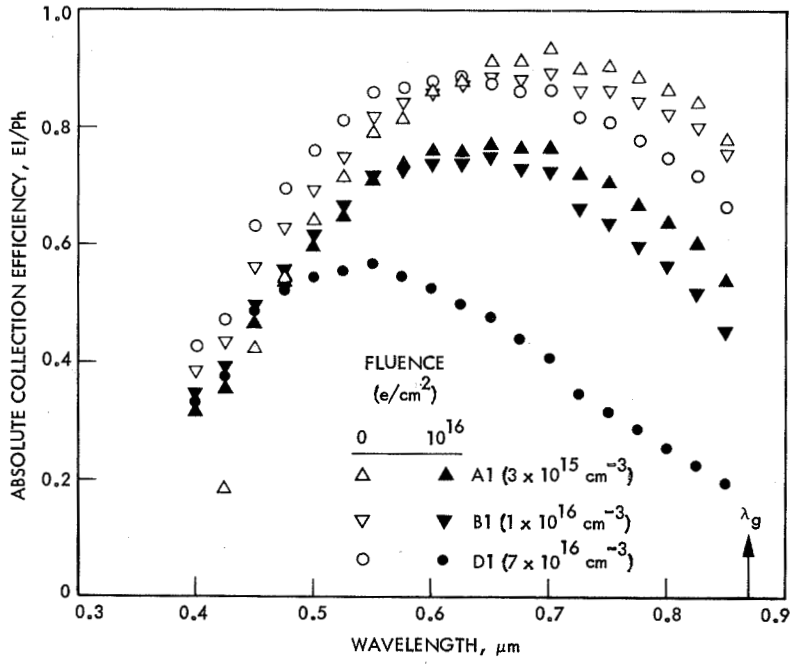

Figure 6. Absolute Spectral Response of GaAs AMOS Solar Cells Non-Irradiated and Irradiated with 1-MeV Electrons to 10^{16} e/cm^2 Fluence

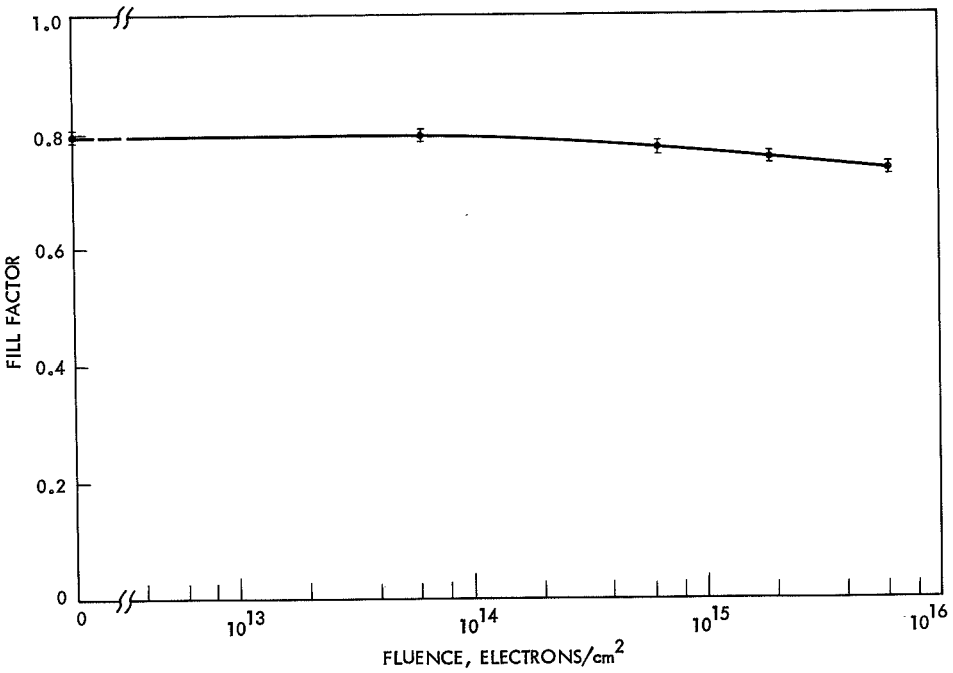

Figure 7. Fill Factor as a Function of Fluence for GaAs AMOS Solar Cells with H_2O/O_2 Oxide Interlayers Irradiated with 1-MeV Electrons (Averaged for four samples)

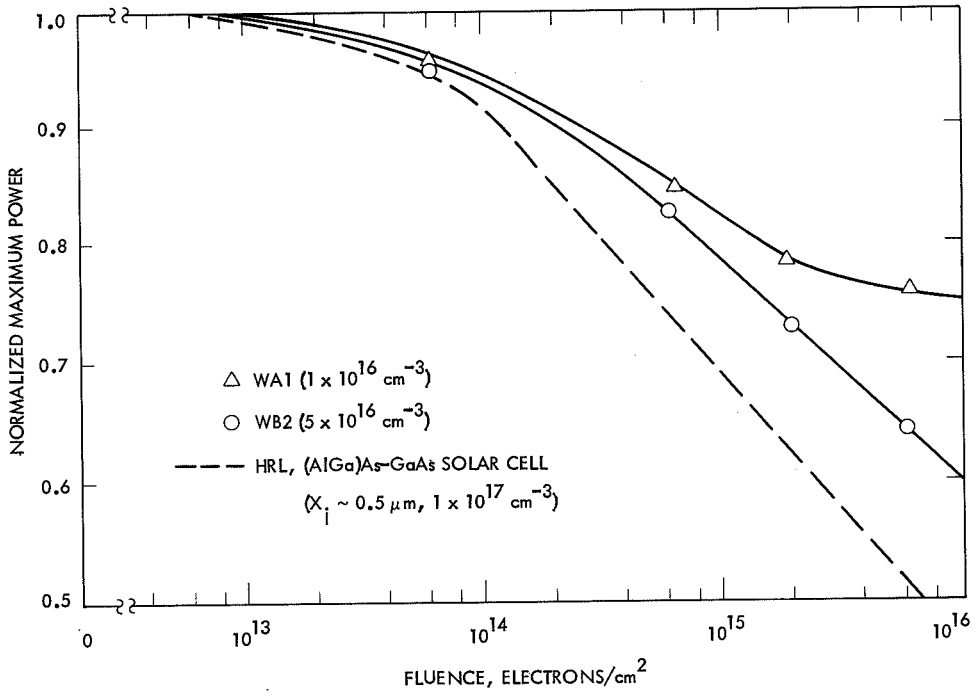

Figure 8. Normalized Maximum Power as a Function of Fluence for GaAs AMOS Solar Cells with H_2O/O_2- Oxide Interlayer Irradiated with 1-MeV Electrons

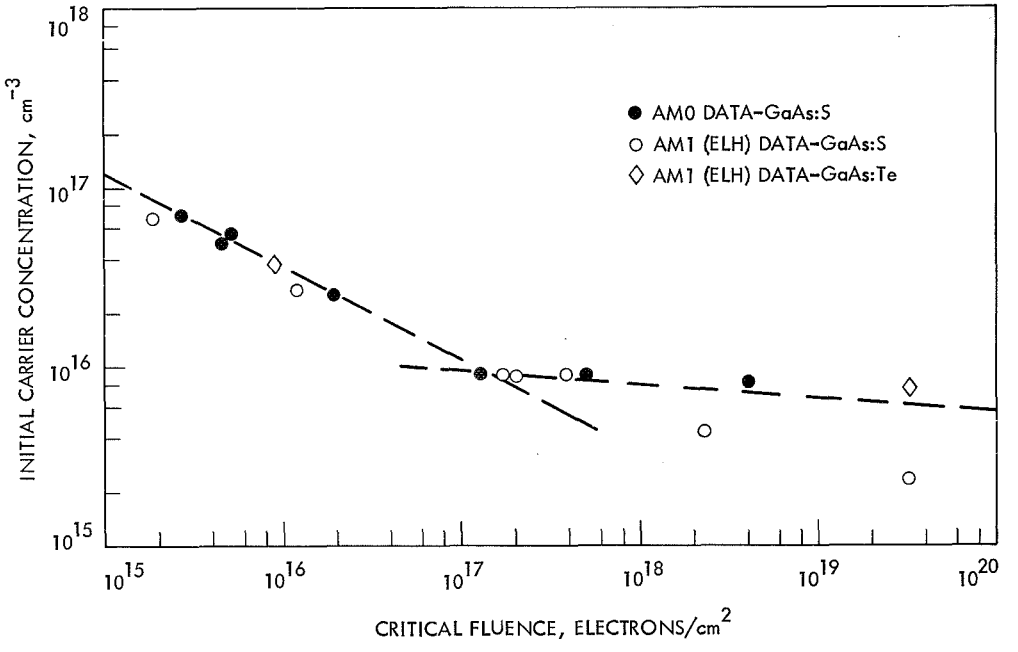

Figure 9. Initial (Non-Irradiated) Carrier Concentration of GaAs AMOS Solar Cells as a Function of Critical Fluence at which the Short-Circuit Current Degraded by 25% of the Unirradiated Value

CAPACITANCE TRANSIENTS IN p-TYPE GaAs MOS STRUCTURES AND APPLICATION TO LIFETIME MAPPING DURING SOLAR CELL FABRICATION*

G. Vitale†, J. J. Loferski, and Y. Ercil
Division of Engineering
Brown University

ABSTRACT

In recent years, analysis of capacitance transients in small-area MOS capacitors has made it possible to obtain extremely localized values of the minority carrier generation lifetime in silicon single-crystal wafers and in devices made from this semiconductor. For example, Schwuttke, et al. (ref. 1) have used this technique to produce generation lifetime maps on silicon wafers. They have shown that the values of generation lifetime can vary widely from point to point and that the values are extremely sensitive to crystal growth and wafer-handling procedures. They have shown that there is a correlation between the performance of recombination lifetime dependent parameters of semiconductor devices made at various locations on a silicon wafer and the generation lifetime at those locations. More recently, Baliga and Adler (ref. 2) obtained lifetime versus depth profiles in diffuse layers of Si. The development of low-temperature oxide preparation techniques has led to the application of this method for monitoring the lifetime at many stages in the fabrication of Si power devices (ref. 3). It could, therefore, be used to monitor τ at the various stages in the manufacture of solar cells.

It is a feature of this lifetime measurement method that the time constant of the capacitance transient is related to the generation lifetime through the ratio of doping concentration N to the intrinsic carrier concentration n_i in the semiconductor. Thus in the case of Si having N_o of $10^{16}/cm^3$, the capacitance decay constant τ_c is 10^6 times the generation lifetime τ_g so that, if $\tau_g = 1$ μsec, $\tau_c = 1$ sec. This shift of time scales is particularly advantageous when applied to measuring, mapping, and profiling minority carrier lifetimes in direct gap semiconductors with bandgaps larger than Si and therefore n_i values substantially lower than in Si. For example, a nanosecond lifetime in p-type GaAs having acceptor concentrations N_A of $10^{16}/cm^3$ would give rise to a capacitance decay constant of several seconds. Until now, however, this technique for measuring τ_g has been limited to silicon because that is the only semiconductor on whose surface it has been possible to produce the high-quality native oxide required in

*This work has been supported by Department of Energy Contract EG-77-C-03-1579 and EG-77-C-03-1712 and partially by the Brown University Material Research Laboratory, funded by the National Science Foundation.

†Permanent address: Universita di Napoli, Istituto Elettrotecnico, via Claudio 21, 80125, Napoli, Italy.

MOS capacitors intended for such studies. The oxide must allow the surface to be driven into deep inversion by a voltage pulse; the transient occurs as carriers generated in the space charge region of the semiconductor accumulate at the surface.

In this paper we report on fabrication on p-type GaAs of MOS structures in which the quality of the oxide is such that the surface can be driven into deep inversion by a voltage pulse. We have measured the capacitance transients in such MOS capacitors as a function of step amplitude and temperature and have analyzed the transients by an extension of the method developed by Zerbst (ref. 4) for silicon. The oxides were produced by plasma oxidation on an LPE-grown p-type GaAs specimen with N_A of $3x10^{17}/cm^3$. The capacitors were produced by depositing 50-μm-diameter gold dots over the native oxide and, therefore, the lifetime is localized to the area under the dot. The method permits extraction of both the bulk lifetime and the interface recombination velocity. We have measured these parameters on samples with different N_A and have found a correlation between τ_g and N_A. Lifetime values in the range of several tenths of a nanosecond to about 1 nanosecond have been observed on our particular wafers; interface recombination velocities in the range of 10^5 cm/sec were observed. However, our GaAs was from a single source and was a small sampling of the variety possible in GaAs; therefore, we do not mean to attach much significance to the "uniformity" of τ_g in our specimens. The important part of our message is that it is possible to produce high-quality native oxides on GaAs and that this important technological advance makes possible lifetime measurement, mapping, and profiling in this material. Further development of this technique should allow monitoring of the effects of various processing steps on the lifetime of GaAs and, therefore, ultimately on the performance of GaAs solar cells.

REFERENCES

1. G. H. Schwuttke, K. Yang, and H. Kappert, Phy. Stat. Sol. (a) 42, 553, (1977).

2. B. J. Baliga and M. S. Adler, IEEE Trans. Electron Devices, ED-25, 472 (1978).

3. NBS Special Publication 400-29, pp. 23-25, April 1977.

4. M. Zerbst, Z. Agnew, Phy. 22, 30 (1966).

ANNEALING IN ELECTRON IRRADIATED AlGaAs SOLAR CELLS*

Bruce E. Anspaugh and John A. Scott-Monck
Jet Propulsion Laboratory
California Institute of Technology

SUMMARY

Preliminary data is presented on the annealing characteristics of AlGaAs solar cells. Devices with varying AlAs "window" thickness and junction depth were irradiated with 1 MeV electrons, at two different temperatures, to $1x10^{15}$ e/cm^2. Additional annealing data on AlGaAs cells exposed to $1x10^{16}$ e/cm^2 is also described.

INTRODUCTION

It has been shown that properly fabricated AlGaAs solar cells display initial power output and performance under electron irradiation that is superior to even advanced laboratory silicon solar cells (ref. 1 and 2). This work was done as part of the JPL program to investigate the potential of thermal annealing as a means of extending the operating lifetime of solar cell arrays. The data reported from the NTS-2 flight experiment (ref. 3 and 4) also acted as an incentive to examine the effect of irradiating AlGaAs solar cells at elevated temperature.

EXPERIMENTAL METHOD

All the irradiations were performed with the JPL Dynamitron using 1 MeV electrons. A complete description of this facility may be found in reference 5. The initial experiment was devised to examine the effect of cell temperature during irradiation on electrical performance. All cells used in this test were obtained from Hughes Research Labs (HRL). The AlAs window layer was less than 0.5 m and the junction depth was between 0.4 and 0.5 μm.

Five cells were mounted to a temperature controlled copper block and held at 125°C under vacuum during the irradiation. In order to give the samples an opportunity to anneal during this test, the flux was reduced to $2x10^{10}$ e/cm^2-sec. The cells received a total fluence of $1x10^{15}$ e/cm^2. I-V measurements at 28°C AMO intensity were made before and after the test while the cells were in the target chamber. A second group of five cells were than irradiated at

*The research described in this paper was carried out at the Jet Propulsion Laboratory, California Institute of Technology, under NASA Contract NAS7-100.

28°C using the same flux and fluence as the previous test, and pre and post-irradiation I-V data was obtained.

Once this test was concluded, two cells from each test group were placed on a quartz boat and held within the constant temperature zone of a diffusion furnace under flowing nitrogen. I-V data at 28°C under AMO conditions was recorded after each heat treatment. The tests began at 200°C, and were continued, in 50°C increments, to a final temperature of 400°C. Time at any temperature ranged from 15 to 110 minutes.

In another test a group of four AlGaAs cells supplied by HRL were irradiated to fluence levels of $1x10^{15}$ and then $1x10^{16}$ e/cm^2 under vacuum, employing normal fluence ($1x10^{12}$ e/cm^2-sec). The window layer thickness of these devices was 1.1 μm and the junction depth 0.3 μm. I-V data was obtained after each fluence level. One cell of each type was then given post irradiation heat treatments at 200°C in order to investigate annealing behavior as a function of time at temperature.

RESULTS AND DISCUSSION

There was no difference in electrical degradation between the cell groups irradiated at different temperatures. A summary of the pre and post testing electrical data, as well as the results of an additional 125°C heat treatment of those cells irradiated 28°C is given in Table 1. This is unexpected in view of the flight experiment information of references 3 and 4. It is possible that the higher fluence used in this experiment may have masked voltage and fill factor annealing or that this annealing phenomenon occurs only when the cells are exposed to the proton spectrum of space.

The recovery of output power as a function of annealing temperature is plotted in figure 1. After 15 min. at 200°C, the samples had regained nearly 10 percent of the power lost during the irradiation. The percentage of recovery reached over 70 percent after 110 min. at 250°C. However, higher annealing temperatures did not seem to have a significant influence on maximum power recovery, in fact there was some degradation in output at temperatures of 350 to 400°C. It was also noticed that the antireflection coatings were becoming paler in color at ~400°C. After a 30 min. anneal at 400°C the samples began to display evidence of contact shunting. The shunting became extreme after an hour at this temperature and the experiment was discontinued.

Figure 2 shows the effect of annealing time at 200°C on the recovery of two AlGaAs cells which had been irradiated to $1x10^{16}$ e/cm^2. Table 2 contains the pertinent electrical data for the samples after $1x10^{15}$ and $1x10^{16}$ e/cm^2. There is a great deal of recovery in output power exhibited at 200°C, and it takes many hours to bring about maximum recovery at this temperature.

CONCLUSIONS

Preliminary results indicate that significant recovery of output in electron irradiated AlGaAs cells can be achieved by thermal annealing. The onset of recovery appears to be between 125 and 200°C. Since silicon solar cells show little, if any recovery at these temperatures, these results are extremely encouraging. With AlGaAs cells, the problem of providing sufficient heat to the solar panel would be greatly reduced compared to a silicon solar cell panel.

Our data does not match the results obtained from the NTS-2 flight experiment. We observe recovery of short circuit current and open circuit voltage at temperatures greater than 125°C, while the flight data showed recovery of open circuit voltage and fill factor at ∿80°C. Our experiments provide no direct assistance in interpreting the puzzling information yielded by the NTS-2 flight experiment.

REFERENCES

1. Stuerke, C.: Air Force High Efficiency Solar Panel-GaAs Cell Development, Thirteenth IEEE Photovoltaic Specialists Conference, p. 551, June 1978.

2. Loo, R.; Goldhammer, L.; Anspaugh, B.; Knechtli, R.; and Kamath, G.: Electron and Proton Degradation in (AlGa) As-GaAs Solar Cells: Thirteenth IEEE Photovoltaic Specialists Conference, p. 562, June 1978.

3. Walker, D. H.: Results of the Solar Cell Experiments on the NTS-2 Satellite After 223 Days in Orbit. NRL Memorandum Report 3860, September 1978.

4. Walker, D. H.,; and Statler, R. L: Results of the Solar Cell Experiments Aboard the NTS-2 Satellite After 447 Days in Orbit. NRL Memorandum Report 3935, March 9, 1979.

5. Anspaugh, B.E.; and Miyahira, T. F.: Electron Irradiation of Modern Solar Cells. Solar Cell High Efficiency and Radiation Damage Conference Proceedings, NASA Conf. Publication 2020, p. 207, May 1977.

AlGaAs ELECTRICAL PERFORMANCE AFTER $1x10^{15}$ e/cm^2

(5 SAMPLES EACH TEST)

Condition	I_{sc} (mA)	V_{oc} (mV)	P_{max} (mW)
$\phi = 0$	108.7	992	83.9
$\phi = 10^{15}$ (28°C)	94.6	899	68.5
125°C-15 hrs	94.2	901	68.5
$\phi = 0$	109.4	985	82.7
$\phi = 10^{15}$ (125°C)	94.9	899	68.3

TABLE 1

AlGaAs ELECTRICAL PERFORMANCE AFTER $1x10^{16}$ e/cm^2

(4 SAMPLES)

Fluence (e/cm^2)	I_{sc} (mA)	V_{oc} (mV)	P_{max} (mW)
$\phi = 0$	104.9	964	79.8
$\phi = 10^{15}$	92.4	887	64.9
$\phi = 10^{16}$	79.6	808	49.3

TABLE 2

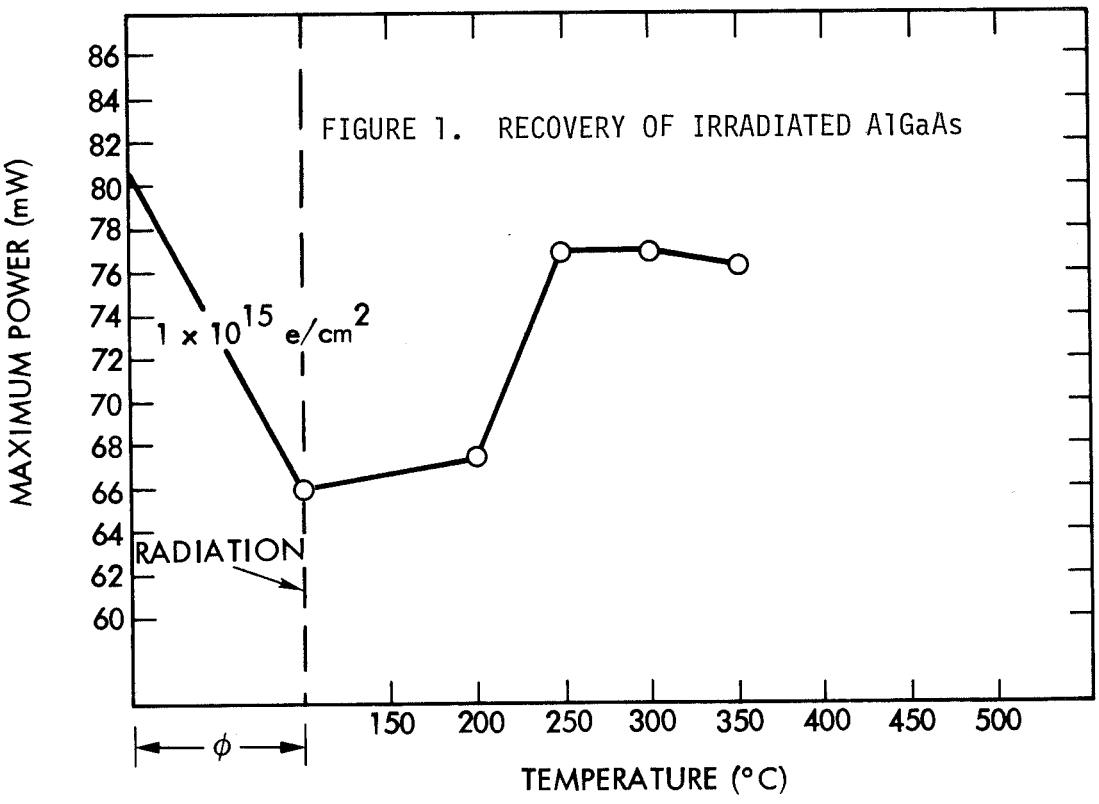

FIGURE 1. RECOVERY OF IRRADIATED AlGaAs

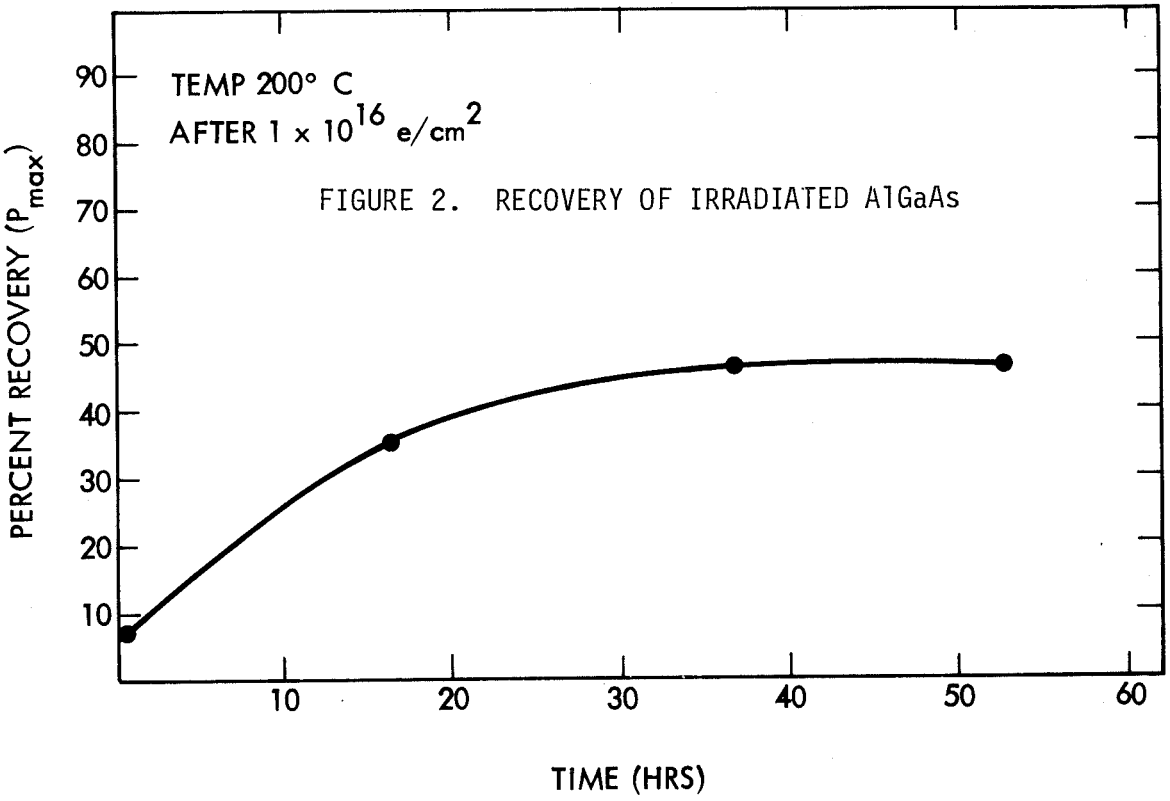

FIGURE 2. RECOVERY OF IRRADIATED AlGaAs

SUMMARY OF GaAs SOLAR CELL PERFORMANCE AND RADIATION DAMAGE WORKSHOP

G. S. Kamath
Hughes Research Laboratories

The workshop considered the GaAs solar cell capability and promise in several steps:

(1) Maximum efficiency
(2) Space application
(3) Major technology problems
    (a) AR coating optimization
    (b) Contacts
(4) Radiation resistance
(5) Cost and availability
(6) Alternatives

The workshop believes that GaAs solar cells are fast approaching the fulfillment of their potential as candidates for space cells. A maximum efficiency of 20 to 31 percent AM0 can be reasonably expected from GaAs based cells, and this may go a little higher with concentration. The use of concentration in space needs to be more carefully evaluated.

The space application of the cells seems quite justified in view of the high efficiency and the good radiation damage data obtained to date. However, more extensive testing of the cells is necessary before they can be space qualified for use in actual space missions. Some small-scale flight tests have to be conducted following a rigorous qualification scheme before the cells will be easily accepted by the space system community. The exact way to achieve this desirable result has to be developed.

The major technological problems that need to be solved are the electrical contacts to the cells (metallurgy, bonding, and interconnect problems) and the optimization of AR coating. The reliability of both the contacts and the AR coating under all possible environmental conditions likely to be encountered in actual missions (humidity, temperature, shelf life) and their acceptability for all process variables (especially bonding and panel interconnect and panel deployment during launch and life in space) are still a serious concern and need to be evaluated. Some of these are engineering problems and would need a supply of cells made under well-controlled conditions to ensure the cell's uniformity and reproducibility."Research" cells would not be adequate to meet this need.

The AR coating problem is still somewhat open. The best known candidate that has been most in use is Ta_2O_5. This material has been space qualified for Si cells and is reasonably satisfactory for the heterostructure cells with (AlGa)As as a window layer. However, an oxide, even though refractory, may have limitations in (AlGa)As and needs to be looked at more carefully. Alternatives, such as Si_3N_4 and TiO_x are still to be fully evaluated. Silicon ni-

tride may have special value and has been used on a research basis, especially with the homojunction cells developed by Lincoln Laboratory, MIT.

The homojunction cells produced by CVD have several attractive features and need to be examined carefully for their potential. They offer the n on p structure, and, since they are being produced by CVD, can be fabricated on Ge and possibly on other substrates. The CVD approach is thus an alternative and complement to the presently developed LPE capability and should be developed in parallel with the full realization of the LPE GaAs cells.

While there is a considerable amount of scattered data on GaAs cells with respect to their radiation damage characteristics, the scatter in them is considerable. This arises largely because the cells are made by a variety of methods with little control on the structural properties that play a major role in controlling the radiation damage characteristics. There are still uncertainties even about basic considerations such as the relative resistance of n on p versus p on n structures. The reliability of various models which predict cell behavior needs to be evaluated more carefully, especially in terms of defining relevant material parameters more carefully. The situation is rapidly improving, however, and in view of the short history of the heterostructure GaAs cell compared to Si, is very encouraging.

The susceptibility of the GaAs cell to damage by low-energy protons is a concern. However, this region is fortunately the one for which the coverglass offers the maximum protection. The thickness of the coverglass has to be chosen carefully for each mission to minimize weight-to-power ratio for the panel without jeopardizing the radiation resistance. The damage equivalence (protons to electrons) is not too well known and needs to be defined to permit space optimization of the cell and coverglass for various missions. It is especially important in this respect to work with cells with very similar properties and parameters so that the random structural properties of the cells do not affect the data.

The last topic discussed was the cost and availability of the cells. The availability of Ga was not considered a primary problem, at least for any foreseeable period of time if space missions are considered. The possibility of using Ge as a substrate has some short-term attraction because of the highly developed Ge technology which makes large area Ge substrates readily available. However, the sources of Ge are few and its cost has been recently rising. The cost of Ga has been, on the other hand, falling. The possibility exists of using Si as a substrate. That will certainly be extremely attractive, especially if thin film cells can be developed. A large number of problems, however, need to be solved and a new technique such as the Mo-CVD fully developed before a practical realization of this attractive alternative can be fully evaluated.

The advantages of CVD versus LPE were discussed briefly. The important point is that LPE is here, fully developed and producing space-quailty cells on a cost competitive basis with the present-day Si cells. The application of these cells to space missions, to a degree, will only strengthen the GaAs cell acceptance in the systems area and allow further development of GaAs cells for future expanded application. Without such acceptibility, GaAs cells may stay as a curiosity with promise for a long time to come.

A REVIEW OF AIR FORCE HIGH EFFICIENCY CASCADED MULTIPLE BANDGAP SOLAR CELL RESEARCH AND DEVELOPMENT

W. P. Rahilly
Air Force Aero Propulsion Laboratory
Wright-Patterson Air Force Base

SUMMARY

At the time of their conception, the cell stack systems to be discussed represent the best semiconductor materials combinations to achieve Air Force program goals. These systems will be investigated thoroughly in Phase I and most promising system, from the standpoint of high efficiency, will be taken into Phase II for further development with large area emphasized (at least 4 cm^2). The emphasis in the Air Force cascaded cell program is placed on eventual non-concentrator application. This use of the final cell design considerably relieves the low resistance requirements for the tunnel junction. In a high concentration application the voltage drop across the tunnel junction can be a very serious problem.

INTRODUCTION

Significant increases in silicon solar cell conversion efficiencies were observed in the early 1970's. These changes were due to modified N^+ diffusion techniques that resulted in much shallower P/N photovoltaic junctions which significantly increased the blue response of the cells. Further improvements brought about by increasing front surface absorption (texturing etch and better AR coats) and the effective and controlled introduction of a P^+ back surface region has raised the laboratory demonstrated silicon solar cell efficiencies up to 16% AMO at 25°C.

Within the last six years or so, improvements in the techniques for growth of III-V semiconductor materials on III-V substrates or Ge substrates has resulted in the demonstration of efficiencies greater than 18% AMO at 25°C for GaAs based solar cells with greater than 16% typically reproduced. Also, the radiation damage resistance of these structures looks very promising for space applications involving the earth's radiation belts.

However, space missions are growing in complexity with attendant growth in power needs. The silicon cell technology does not lend confidence in exceeding 18% in production and the GaAs cells most likely will not exceed 20% in a production environment. The growing power demand along with the

growing realization of successful III-V semiconductor material growth technology has ressurected an old idea for very high conversion efficiency--namely the cascaded (series connected) multi-bandgap solar cell (ref. 1). Theoretical analyses of these structures projects conversion efficiencies in the low 30% range for two cell stacks and approaching 40% for three or more serially connected cells in a monolithic structure (ref. 2). The Air Force views this possible solar cell technology with guarded optimism but does realize the impact that high efficiencies can have on broadening the flexibility of future space missions. For this reason, the Air Force has initiated cascaded multiple bandgap research and development programs that will utlimately lead to a very high conversion efficiency space power system.

This paper details the what, why, and how of the development of the multi-bandgap solar cell for Air Force space applications.

AIR FORCE CASCADED SOLAR CELL DEVELOPMENT

The objective of the cascaded solar cell development is to fabricate and demonstrate cells with greater than 25% AMO conversion efficiencies measured at 25°C. The approach, within available and planned budgeting is to fund two contractors who have the responsibility to investigate four individual cascaded structures. The research and development conducted by the contractors is separated into two phases. In Phase I each contractor will determine the best semiconductor materials system with emphasis on conversion efficiency that will be taken in Phase II for the purpose of demonstrating greater than 25% AMO for cell sizes of at least 2 cm x 2 cm. Delivery of one hundred 2 cm x 2 cm solar cell assemblies at the close of the second phase is required. The program is twenty four months for each contractor with Phase I being a fourteen month duration. The specific contractors for this dual awarded program are Research Triangle Institute at Research Triangle Park, North Carolina and Rockwell International with facilities at both Anaheim and Thousand Oaks, California participating.

The payoff for cascaded cell technology is lower total area and total power systems and the establishment of a solar cell basis for future high voltage, high power systems. This particular type of cell has considerable payoff for low orbit application in cost also. For higher orbit application (such as half synchronous) the cost factor is projected to be the same as that for silicon and lower than GaAs single junction cells but with a considerably smaller panel size (ref. 3).

The major problem areas that plague the cascaded solar cell development are associated with the understanding of and the single crystal growth of certain III-V semiconductor materials in serial fashion that are not lattice matched (depending on the specific cell design). Also, the development of proper anti-reflective coatings and contact metalization materials combinations and deposition techniques are critical to making a useful device. In what follows, these problem areas will be discussed in relation to the structures as proposed by the two contractors.

Research Triangle Institute (RTI)

The four materials systems under investigation at RTI are illustrated in Figure (1). The bandgap for each material as well as the method of growth are provided. The fifth materials system is a modification of the second system and has considerable potential.

System I - GaInP Cell on GaInAs Cell

This structure has an GaAlAsSb window of greater than 2.0 electron-volt (ev) bandgap (indirect) on a GaInP top cell and tunnel junction (both 1.6 ev) on a lower cell made of GaInAs (.95 ev) in turn on either a GaAs single crystal substrate or a Ge substrate with a GaAs layer grown on. This structure employs liquid phase epitaxial (LPE) growth for the GaInAs and GaAlAsSb, and vapor phase epitaxial growth for the GaInP portion. The cell is lattice matched to the underlying GaAs layer or substrate by using graded layers (or lattice matching layers) with increasing amounts of indium. There may be as many as five such layers. There are essentially an infinite number of upper and lower cell combinations (GaInP on GaInAs) where the semiconductor lattices of each will be matched, however the matching of the upper and lower bandgaps is not optimum for efficiency in every case. Nevertheless the matching of the lattices can be achieved with a resultant 25% efficiency. The lattice matching of the GaAlAsSb window to the top cell can be achieved with little difficulty. The P electrical dopant in the GaInAs material is magnesium. The P dopant for the GaInP material has been tentatively selected to be cadmium. There is a variety of N dopants that can be used; both selinium and germanium are being investigated for the GaInAs and GaInP materials.

System 2 - GaAlAs Cell on an GaInAs Cell

This structure has an GaAlAs window of near 2 ev bandgap (indirect) on a closely lattice matched GaAlAs top cell and tunnel junction (both 1.6 ev) on a 1.2 ev bandgap GaInAs cell on an appropriate substrate as discussed above. This particular structure is attractive since the top contact metalization is reasonably well understood (ref. 4). The lattice mismatch between GaAlAs and GaInAs is less than 0.7% but is a somewhat troublesome problem to resolve in relation to maintaining high crystalline perfection. The P dopant for the GaAlAs material is germanium. As above the N dopant can be selected from a variety of choices.

System 3 - GaAlAsSb Cell on an GaInAs Cell

The GaAlAsSb window (2 ev bandgap) top cell and tunnel junction (1.6 ev bandgap) are all lattice matched and are lattice matched to .95 ev bandgap GaInAs lower cell. This system has particular problems, however. The control of miscibility gap in the GaAlAsSb material in the bandgap range of interest for the top cell and tunnel junction can negate the entire cell design. Recent data does suggest, though, that the miscibility problem may be confined to a smaller bandgap range than first thought (ref. 5). The contact materials systems are not know for GaAlAsSb at least from solar cell

environmental considerations. It is anticipated that the P dopant for the GaAlAsSb material will be germanium.

System 4 - GaAlAsSb Cell on a GaAsSb Cell

This structure is lattice matched all the way down to the substrate where step grading of GaAsSb to the substrate lattice is required. The problems of miscibility and achieving the proper bandgap for the top cell and tunnel are the same as discussed in System 3. The GaAsSb lower cell (1.2 ev bandgap) has been fabricated with good diode shape but low open circuit voltage. The present thought is that the minority carrier lifetime in both layers is being limited by Sb vacancies. The P dopant for the GaAsSb material is germanium.

System 5 - GaAlAs Cell on a CaAs Cell

This structure is considered as a special case of System 2. The upper cell and tunnel junction must have a bandgap of 1.93 ev to achieve reasonable matching to the lower cell. The projected efficiency for this structure is over 25%. There are four significant advantages with this structure: (a) no serious match problems anwhere, (b) A Ta_2O_5 antireflective coating would be applicable since the bottom cell is GaAs, (c) The contact metalization systems for such semiconductor materials are reasonably well understood for solar cell application and (d) the entire structure can be placed on a germanium lower cell with potential efficiency under AMO of over 30%. Of course, if the System 5 structure was to be placed on a germanium lower cell, the latter, cell would have to have a GaAs layer grown on it to allow for LPE growth--or the lower tunnel and middle cell would have to be grown by vapor means. Again, the P dopant used in the GaAlAs materials system is germanium.

Rockwell International (RI)

The four systems proposed by RI are based on the GaAlAs/GaAs cell structure. Two of the four systems are two cell stacks and the other two are three cell stacks. Figure (2) provides the information pertaining to the system materials compositions. The fifth system is the GaAlAs cell on a GaAs cell; fabricated using MO-CVD.

System 1 - GaAs Cell on a Ge Cell

The window, top cell and the tunnel junction for this system are lattice matched materials with bandgaps of greater than 2 ev for the window, 1.43 ev for the top cell and a Ge heteroface tunnel junction and bottom cell. The Ge cell has two bandgaps; one direct at .8 ev and one indirect at .67 ev. For the Ge cell, the direct bandgap controls the light generated current and the indirect bandgap controls the cell voltage characteristics. Indeed, the above remark should be qualified in that the direct and indirect bandgaps contribute roughly equally to the light generated current. Since the GaAs top cell will limit the overall stacked cell, external current, the division of light generated current in the cell is a moot issue as long as the tunnel

is sufficiently thin. The conduction of majority carriers through the tunnel is accomplished primarily by defect states and the rest by band to band. The major problems are with System 1 is growth of the GaAs on the Ge cell. The best suited method to date is deposition from the vapor phase with MO-CVD the most attractive. Since this stack design strongly depends on cascade cell voltage, achievement of open circuit voltages for the Ge cell must approach .3 volts. Good quality Ge material and careful processing techniques are of paramount importance. However, for research purposes, if reasonable, cell voltage characteristics can be achieved with successful cascade action with the GaAs materials applied, then the technology for this structure will have been established--requiring mostly refined deposition techniques and quality of material and process controls. The P dopant in the Ge is boron. The P and N dopants in the GaAs material are zinc and selinium respectively.

System 2 - GaAs Cell on a GaInAs Cell

This system can be constructed in several different ways. The method selected by RI is to fabricate the GaAl window and GaAs top cell on an N^+ GaAs substrate. On the opposite side of the substrate, a P^+ InP layer can be grown followed by a GaInAs bottom cell. This approach resolves the potential lattice mismatch problem throughout the cell by restricting the mismatch to the wafer backside. There the InP P^+ layer will serve as the positive conductivety side of a combined defect states and band to band tunnel. During growth of the P^+ InP layer by LPE, the majority of lattice defects will be pinned to the growth interface resulting in a good quality single crystal surface which is lattice matched to the GaInAs bottom cell of bandgap around .8 ev. The P dopant for the GaInAs will most likely be germanium. The N dopant can be chosen from a wide selection.

System 3 - GaAlAs Cell on a GaAs Cell on a GaAsSb Cell

This structure is a three cell stack with the top cell and tunnel bandgaps near 2 ev placed on a GaAs cell inturn placed on a GaAs substrate. On the reverse side of the substrate a 1 ev cell is grown. The lattice matching of GaAs to the GaAsSb is resolved with a P^+ GaAlAsSb layer between. The bottom cell can also be a Ge cell wherein the Ge P^+ layer is put down by decomposition of $GeCl_4$. A four cell stack is possible using the GaAsSb 1 ev cell followed by a Ge cell on the substrate backside. However, the complexity is considerable. The problems associated with the third system are primarily restricted to demonstration of the high bandgap cell and tunnel and achievement of a quality GaAsSb cell. Included in the problem is the selection of the appropriate dopants so as to maintain their distributions during cell stack processing.

System 4 - GaAlAs Cell GaAs Cell on a GaInAsP Cell

This stack is essentially the same as system 3 except for the GaInAsP bottom cell. This design still permits the growth of a fourth cell that serves as the bottom cell. The connection of the GaAs substrate to the GaInAsP cell can be accomplished via the P^+ InP layer as in the second system.

System 5 - AlGaAs Cell on a GaAs Cell

The remarks to be made here are essentially those of system 5 of RTI. However, the difference is that RI is investigating the structure using MO-CVD. This structure does have potential for a three cell stack using a Ge cell as the bottom generator. The P and N dopants used in this system are zinc and selinium respectively.

CONCLUDING REMARKS

The most difficult problems in both contractual programs are (1) growth of quality semiconducting layers under lattice mismatching conditions and (2) proper control of the P and N dopants in the tunnel junctions during layer growths. All of the cascade cell designs by RTI can possibly use only the anti-reflective coating. The two three-cell stack concepts of RI can potentially use one anti-reflection coating; the other two systems most likely will require at least a three layer anti-reflective coating to ensure sufficient absorption beyond one micron wavelength. The metallization schemes for these cell designs have not yet been defined except for the case of the GaAlAs/GaAs combinations.

All of the systems except the GaAs/Ge combination discussed have potential for exceeding the 25% AMO @ 25°C goal. The GaAs/Ge system most likely will show slightly over 20% in the best case. It is interesting to note that both contractors view the high bandgap GaAlAs cell on a GaAs cell as a viable candidate - an attractive realization of this view is that the material combination is being quite successfully investigated using totally the LPE technology in one case and MO-CVD in the other.

REFERENCES

1. Jackson, E.D., "Transactions on the Conference on the Use of Solar Energy, Tuscon, Arizona, 31 October to 1 November, 1955, page 122. See also U.S. Patent Nr. 2,949,498, 16 August 1960

2. Lamorte, M.F., Hauser, J.R., Littlejohn, M.A.,Simons, M., "Solar Cell Design Study", Research Triangle Institute, Final Report, Contract F33615-76-C-1283, February 1977.

3. These findings are based on an analysis completed by the author. The results of this study will be forthcoming in the Journal of Energy.

4. Kamath, S., Wolff, G., "High Efficiency GaAsSolar Cells", Final Report, AFAPL-TR-78-96, January 1979.

5. Private communication between author and S. Bedair of Research Triangle Institute.

	BOTTOM CELL	TUNNEL JUNCTION	TOP CELL	WINDOW	BASIC PROCESS	COMMENTS -
SYSTEM 1	GaInAs (.95EV)	GaInP (1.6EV)	GaInP (1.6EV)	AlGaAsSb (>2EV)	LPE & VPE	GaInP DIFFICULT TO GROW
SYSTEM 2	GaInAs (1.2EV)	GaAlAs (1.8EV)	GaAlAs (1.8EV)	GaAlAs (>2EV)	LPE	GaAlAs NOT LATTICE MATCHED TO GaInAs
SYSTEM 3	GaInAs (.95EV)	AlGaAsSb (1.6EV)	AlGaAsSb (1.6EV)	AlGaAsSb (~2EV)	LPE	AlGaAsSb DIFFICULT TO GROW AND DOPE
SYSTEM 4	GaAsSb (1.2EV)	AlGaAsSb (1.8EV)	AlGaAsSb (1.8EV)	AlGaAsSb (>2EV)	LPE	CHOICE OF BANDGAP LIMITED FOR BOTTOM CELL
SYSTEM 5	GaAs (1.43EV)	GaAlAs (1.93EV)	GaAlAs (1.93EV)	GaAlAs (>2EV)	LPE	BANDGAP AND TUNNEL GROWTH DIFFICULT

FIGURE 1 - RESEARCH TRIANGLE INSTITUTE'S CELL SYSTEMS

	BOTTOM CELL	TUNNEL JUNCTION	TOP CELL	WINDOW	BASIC PROCESS	COMMENTS
SYSTEM 1	Ge (.67 INDIR) (.8 EV DIR)	P+ Ge/ N+ GaAs HETERO	GaAs (1.43EV)	GaAlAs (>2EV)	MO-CVD	QUALITY GaAs GROWTH ON Ge DIFFICULT
SYSTEM 2	GaInAs (.7EV)	P+ InP/ N+ GaAs HETERO	↓	↓	LPE	QUALITY InP LAYER GROWTH DIFFICULT
SYSTEM 5	GaAs (1.43EV)	GaAlAs (1.93EV)	GaAlAs (1.93EV)	↓	MO-CVD	HIGH BANDGAP GaAlAs DIFFICULT TO GROW

	BOTTOM CELL	LOWER TUNNEL	MIDDLE CELL	UPPER TUNNEL	TOP CELL	WINDOW	BASIC PROCESS	COMMENTS
SYSTEM 3	GaAsSb (1EV)	P+ AlGaAsSb N+ GaAs HETERO	GaAs (1.43EV)	AlGaAs (~2EV)	AlGaAs (~2EV)	AlGaAs (>2EV)	MO-CVD	Sb VACANCIES APPEAR TO REDUCE LIFETIME
SYSTEM 4	InGaAsP (1EV)	P+ InP/ N+ GaAs HETERO	↓	↓	↓	↓	LPE	InP LAYER A PROBLEM AS ABOVE

FIGURE 2 - ROCKWELL INTERNATIONAL'S CELL SYSTEMS

EFFICIENCY OF TANDEM SOLAR CELL SYSTEMS AS FUNCTION OF TEMPERATURE AND SOLAR ENERGY CONCENTRATION RATIO

N. A. Gokcen
Bureau of Mines
U.S. Department of the Interior

and

J. J. Loferski
Division of Engineering
Brown University

ABSTRACT

This paper presents the results of a comprehensive theoretical analysis of tandem photovoltaic solar cells as a function of temperature and solar concentration ratio. The I-V characteristics of the solar cells were assumed to be governed by the relation

$$I = I_o(e^{qV/AkT} - 1)$$

with $I_o = Ke^{-E_G/BkT}$ and $A = B$. The overall efficiencies of tandem cell stacks consisting of as many as 24 cells having gaps in the 0.7- to 3.6-eV range were calculated for temperatures of 200, 300, 400, and 500 K and for illumination by an AM0 solar spectrum having concentration ratios C of 1, 100, 500, and 1000 suns. For ideal diodes ($A = B = 1$), the calculations show that the optimized overall efficiency has a limiting value η_{opt} of approximately 70 percent for $T = 200$ K and $C = 1000$. As shown in the accompanying figure, for $T = 300$ K and $C = 1000$, this limiting efficiency approaches 60 percent. The table shows the optimum combination of E_G values for various numbers of solar cells, $T = 300$ K, and various concentration ratios. Most of the gain in efficiency occurs with between 6 and 10 semiconductors in the tandem system (e. g., for $T = 300$ K and $C = 1000$ an optimized, six-cell system has a theoretical limit efficiency of about 53 percent). Calculations were also conducted for the $A = B = 2$ case (nonideal diode behavior); in this case the limiting value of η for a 24-cell system is about 65 percent at 200 K and 55 percent at 300 K.

Variation of optimum efficiency with number of cells

Bandgap Range: 0.7 to 3.0; A=B=1; 300K

100 Suns:

No. of Cells:	1	2	3	6	12	24
E_G values (eV):	1.4	1.8 & 1.0	2.3, 1.5 & 0.9	2.6, 2.1, 1.7 1.3, 1.0, 0.7	0.7 to 2.9 in intervals of 0.2	0.7 to 3.0 in intervals of 0.1
Efficiency:	26.43	37.05	42.52	40.13	54.10	55.96

500 Suns:

No. of Cells:	1	2	3	6	12	24
E_G values (eV):	1.3	1.8 & 1.0	2.2, 1.4 & 0.8	2.6, 2.2, 1.8 1.4, 1.0, 0.7	0.7 to 2.9 in in intervals of 0.2	0.7 to 3.0 in intervals of 0.2
Efficiency:	27.62	38.80	44.46	52.26	56.38	58.21

1000 Suns:

No. of Cells:	1	2	3	6	12	24
E_G values (eV):	1.3	1.8 & 1.0	2.2, 1.4 & 0.8	2.5, 2.1, 1.7 1.0 & 0.7	0.7 to 2.3 in intervals of 0.2	0.7 to 3.0 in intervals 0.2
Efficiency:	28.18	39.56	45.37	53.21	57.37	59.22

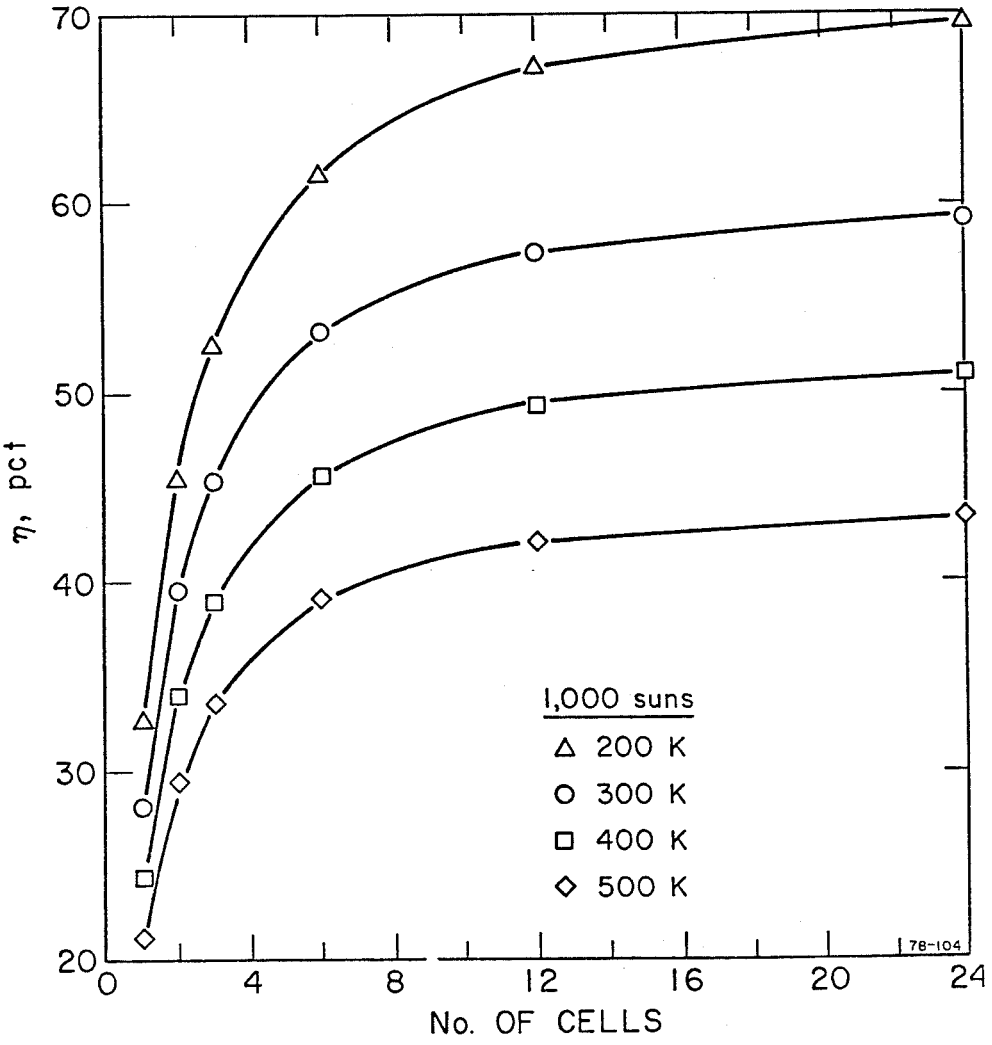

Variation of efficiency with number of cells at various temperatures. C = 1000; AMO spectrum.

COMPUTER MODELING OF A TWO-JUNCTION, MONOLITHIC CASCADE SOLAR CELL*

M. F. Lamorte and D. Abbott
Research Triangle Institute

ABSTRACT

The theory and design criteria for monolithic, two-junction cascade solar cells are described. The departure from the conventional solar cell analytical method and the reasons for using the integral form of the continuity equations are briefly discussed. The results of design optimization are presented. The energy conversion efficiency that is predicted for the optimized structure is greater than 30% at 300 K, AM0 and one sun.

The analytical method predicts device performance characteristics as a function of temperature. In this paper, the range is restricted to 300 to 600 K. While the analysis is capable of determining most of the physical processes occurring in each of the individual layers, only the more significant device performance characteristics are presented.

SYMBOLS

η	conversion efficiency, %
D_{ni}, D_{pi}	electron and hole diffusion coefficient, respectively, in region i, $cm^2\ sec^{-1}$
ΔE_{ci}, ΔE_{vi}	conduction and valence bandedge discontinuity, respectively, at x_i interface, eV
$E_G(x_i)$	bandgap at x_i interface, eV
E_{ci}, E_{vi}	conduction and valence bandedge, respectively, at x_i interface, eV
E_{FO}	equilibrium Fermi level, eV
F	V-I solar cell curve fill-factor

*This work was supported by the Avionics Laboratory, Wright-Patterson Air Force Base. Rewriting the computer program to include Fermi-Dirac statistics was supported by the U.S. Department of Energy and Sandia Laboratories, Albuquerque, NM.

J_{scT}, J_{scB} short-circuit current density of top and bottom cells, respectively, mA cm^{-2}

J_{nOT}, J_{pOT} electron and hole saturation current components, respectively, of top cell, mA cm^{-2}

J_{nOB}, J_{pOB} electron and hole saturation current components, respectively, of bottom cell, mA cm^{-2}

L_{ni}, L_{pi} electron and hole diffusion length, respectively, in region i, cm

n_{pOi}, n_{pi} equilibrium and non-equilibrium electron concentration, respectively, in region i, cm^{-3}

N_{Ai}, N_{Di} acceptor and donor concentration, respectively, in region i, cm^{-3}

p_{nOi}, p_{ni} equilibrium and non-equilibrium hole concentration, respectively, in region i, cm^{-3}

q electronic charge

R_{ni}, R_{pi} electron and hole interaction parameter, respectively, in region i, describing carrier confinement

s surface recombination velocity, cm sec^{-1}

T temperature, K

V_{mp} photovoltage at maximum power points, volts

V_{Oc} open-circuit photovoltage, volts

x distance into cascade structure, cm

INTRODUCTION

The characteristics and limitations of silicon solar cells are well known. Maximum theoretical efficiencies for silicon cells range as high as 21% under AM0 spectral conditions [1,2], although experimental values have remained below 18% at irradiation levels of one sun [3,4]. Studies have been conducted to increase efficiency through the reduction of surface reflection loss, the use of n^+-p and p^+-n structures [5], the establishment of a built-in field in the "dead" surface layer to improve spectral response and to reduce dark current [6], and the provision of a reflective surface [7] and a retarding field at the back contact interface to reduce dark current [8-12]. Each of these improvements has increased silicon cell efficiency, but the gains have not been sufficient to discourage investigations of alternative solar cell materials. Moreover, at high illumination levels and elevated temperatures, the applicability of silicon

cells is limited by a rapid decrease in efficiency with increasing temperature [3,4,13].

An ideal solar cell material will have a different bandgap energy than silicon and will absorb photons by direct optical transitions. Materials with reasonable diffusion length and direct optical transitions have high efficiency because losses due to incomplete absorption, spectral response, and dark current are improved. If, in addition, the material is metallurgically compatible with other semiconductor materials, monolithic devices may be fabricated with window layers [14] and minority carrier confinement structures. Silicon is difficient with respect to these criteria.

Most prominent among the material alternatives to silicon are the III-V compound semiconductors. Major advantages of these materials are higher theoretical efficiencies and improved temperature performance [1,2,13].

Efficiency calculations for the binary compounds (InP, GaAs, AlSb) with ideal homojunctions and structural characteristics have indicated maximum values of 25% or more [1,2,13]. Although heterojunction cells with GaAs as one of the materials appear to have most promise for actually approaching theoretically predicted efficiency values, it is unlikely that single-junction cells fabricated from III-V compounds will ever achieve efficiency levels above 22% at 300 K and a concentration of one sun.

CASCADE (MULTIJUNCTION, MULTIBANDGAP) SOLAR CELL

Few approaches are available for increasing the conversion efficiency of the single-junction solar cell [15-20]. This arises because the single-junction cell absorbs photons from only a portion of the solar spectrum and it incompletely utilizes the energy of those photons that it absorbs. Three approaches -- the cascade cell, a multiple-cell beam splitting system, and the thermophotovoltaic cell -- have been proposed to increase efficiency above that of the single-junction cell. In this paper, attention is directed to the monolithic cascade cell.

The monolithic cascade structure consists of multiple layers of different bandgap materials [21-25]. The properties of III-V compound semiconductors are such that these materials are well suited to the synthesis of monolithic, multiple-junction cells having theoretical efficiency values approximately 50% higher than single-junction GaAs solar cells. The cascade cell may be fabricated to operate as a two-terminal device, or the cells may be operated separately as a three-terminal device [21]. In this paper, the two-terminal device is discussed.

The monolithic cascade solar cell discussed is a two-junction device, but unlike a mechanically stacked configuration, it avoids the large losses associated with multiple optical interfaces [21-24]. As depicted in Figure 1, the cell consists of wide (top) and narrow (bottom) bandgap junctions joined electrically through a tunnel junction formed as an integral part of the monolithic structure. This multilayer device incorporates the desirable features of heterojunction and graded bandgap designs in a single integrated unit. The

active layers consist of III-V ternary compounds selected so as to achieve the desired bandgap in each junction as well as to ideally minimize lattice mismatch between the various layers. The cascade structure may be fabricated on a substrate, such as GaAs, using liquid phase epitaxy (LPE) or vapor phase epitaxy (VPE) technology. Compositional grading may be employed between the substrate and the active layers to avoid problems associated with lattice mismatch. Design optimization studies of this structure have resulted in very promising characteristics as described in this paper [21-24]. The optimum bandgap combination, materials and/or alloys used in the active layers, and other design parameters are functions of the operating conditions. The bandgap energies, for example, increase for cells optimized for high temperature operations.

COMPUTER MODELING RESULTS

In this section we present and discuss some of the results of the computer modeling. The materials selected and the structure design are optimized for operation at 300 K under AM0 spectral conditions and for one sun. While the computer program provides much information relating to terminal characteristics and internal phenomena, only the more significant results are presented in the interest of brevity.

Optimized Band Structure

The band structure shown in Figure 2 and the corresponding listing of the design parameters presented in Table 1 provide the optimized structure obtained from the computer modeling--i.e., the design parameters giving the maximum efficiency for operation at 300 K, AM0, and one sun [21-24]. Region 1 serves as the window layer, regions 2 and 3 form the top cell homojunction, regions 4 and 5 the tunnel junction, regions 6 and 7 the bottom cell homojunction, and region 8 the substrate. In the following discussion, the AlGaAs-GaInAs materials combination is selected. While the structure contains seven active layers, the loss due to incomplete absorption in the top cell is negligible so that the tunnel junction is optically inactive. However, if the tunnel junction bandgap is made smaller than the top cell bandgap, it will become optically active and produce a photovoltage that is in opposition to the photovoltage produced by the top and bottom cells. The effect of the photovoltage generated in the tunnel junction in such a design may be minimized by making the n^+ and p^+ tunnel junctions less than 0.5 μm. When the n^+ and p^+ regions exceed 1.0 μm and the bandgap value is less than 0.3 eV less than the top cell, the cascade cell efficiency is reduced to a value lower than the top cell operating as a single-junction cell. Therefore, to insure maximum efficiency, the tunnel junction bandgap should be equal to or greater than the top cell bandgap.

The window layer shown has a built-in field intensity of 3000 Vcm^{-1}, but the influence of the field on efficiency is small because it is thin (i.e., 0.1 μm), its bandgap is significantly larger than the top cell bandgap, and the conduction bandedge discontinuity, ΔE_{c1}, confines minority electrons to region 2. The confinement markedly reduces the dark current while the field intensity in the window layer plays a minor role in reducing dark current. Photon absorption

in the window layer is minimized for maximum efficiency through the selection of its thickness and bandgap value at the surface.

Similarly, the valance band discontinuity, ΔE_{v3}, at x_3 confines minority holes to region 3, thereby increasing spectral response and reducing the hole contribution to dark current. While ΔE_{v3} is influenced by the choice of the tunnel junction bandgap, the tunnel junction bandgap is made as small as possible because of the difficulty in obtaining a tunnel junction in wider bandgap materials. Our results show, however, that for effective carrier confinement, the minority carrier bandedge discontinuities surrounding a homojunction solar cell should be 6 kT to 7 kT. Beyond 7 kT, the dark current approaches an asymtotic value. Similar statements may be made for ΔE_{c5} and ΔE_{v7} with respect to the lower bandgap cell [21-24].

In order for the minority carrier bandedge discontinuities to be effective in reducing dark current, the minority carrier diffusion lengths must be greater than their respective layer thicknesses. Typically in the materials considered here, the diffusion lengths are several times greater than the layer thicknesses. The computer program determines the optimum thickness to obtain maximum efficiency.

The two-terminal cascade cell requires that the terminal current must pass through each of the three junctions. This requirement strongly affects the choice of materials, predominantly through the bandgap combination. The terminal operating current is obtained by maximizing conversion efficiency.

The band structure that results from the modeling makes the top and bottom cells "potential wells" for minority carriers produced by photon absorption as well as for the dark current injected carriers [21]. This condition is obtained from the integral form of the continuity equation used in the analysis which results in the V-I solar cell equation and because in the analytical treatment, the band structure details described above are incorporated. Thus, in one relationship most of the significant parameters which strongly affect conversion efficiency are included.

Voltage-Current Relationship

The analytical method employed here gives the V-I solar cell equation for the cascade cell, including the voltage drop across the tunnel junction which is required to conduct the terminal current. Should the tunnel junction produce a photovoltage, the sum of the photovoltage and the voltage drop required to conduct the terminal current, in the absence of a photovoltage, must be subtracted from the sum of the top and bottom cell photovoltages. The V-I relationship of the cascade cell is used to calculate the power at the maximum power point from which the conversion efficiency is obtained. This is the focal point of the analytical method and the corresponding computer program. In an optimally designed cell, the current at the maximum power point of the cascade cell is nearly identical to the current at the maximum power points of the V-I curves of the individual cells. This manifests itself through nearly equal short-circuit currents and relatively small differences in dark currents of top and bottom cells over a wide range of temperature.

The temperature dependencies of the material parameters (mobility, bandgap, carrier concentration, relative occupation of electrons in direct and indirect conduction band minima, etc.) are included in the computer program. Temperature effects on the solar cell V-I curve are manifest through changes in V_{mp}, V_{Oc}, F, and to a lesser degree, J_{sc}. While calculations were performed at surface recombination velocities of 0, 10^6, and 10^7 cm sec^{-1}, all calculations are represented for 10^6 cm sec^{-1}.

The family of V-I curves for the optimized cascade cell is shown in Figure 3, with temperature a parameter, and for a 10^6 cm sec^{-1} surface recombination velocity. It is seen that the photovoltage at the maximum power point and the open-circuit voltage are strong functions of temperature, while the short-circuit current is nearly independent of temperature. The shape and the temperature dependence of the cascade solar cell V-I curves exhibit behavior similar to that of a single solar cell with a short-circuit current density of approximately 30 mA cm^2, an open-circuit voltage of 1.75 volts, and an apparent bandgap value of approximately 2.57 eV (i.e., the sum of the bandgaps of top and bottom cells). Each point on the V-I curve represents the sum of the photovoltaic voltages of top and bottom cells minus the tunnel junction voltage drop, all for a given terminal current. These curves show that the open-circuit voltage is approximately 1.75 times that of a single-junction GaAs solar cell and more than three times that of Si cells.

Lower surface recombination values increase the short-circuit current, and higher values of recombination reduce the current while photovoltage changes are considerably smaller because of their logarithmic dependence on current. This behavior is also observed on a single-junction solar cell.

Bandgap Combination

To illustrate the influence of bandgap values on efficiency, allow either the top or bottom bandgaps to change while maintaining the other constant. Figure 4 shows the efficiency vs. the top cell bandgap while the bottom bandgap is held constant at 0.954 eV; Figure 5 allows the bottom bandgap to change while the top cell bandgap is held constant at 1.62 eV.

In Figure 4, maximum efficiency occurs at a bandgap value of 1.62 eV for the top cell. For a surface recombination velocity lower than 10^6 cm sec^{-1}, the optimum bandgap value shifts to higher values, and for higher recombination velocity the shift is to lower bandgap values. On either side of 1.62 eV, the efficiency drops rapidly. In the low bandgap region, the slope is relatively constant and its value is approximately 46%/eV, while beyond 1.7 eV, the slope is approximately 30%/eV. The slope in the low bandgap region is more than 50% greater than it is in the high bandgap region.

Maximum efficiency in Figure 5 occurs at 0.954 eV, representing the optimum bottom cell bandgap value. This optimum value is insensitive to surface recombination velocity and to air mass from AM0 to AM5 [26]. On either side of this maximum, the efficiency decreases with nearly constant slopes. The slope below 0.954 eV is 17.5%/eV, which is considerably smaller than the value above 0.954 eV

which is 49%/eV. The former is lower while the latter is higher than either slope given in Figure 4.

The curves in Figures 4 and 5 show that decreasing the bottom cell bandgap from its optimum value, while maintaining all other design parameters at their optimum values, results in a small decrease in cascade efficiency. However, increasing the top cell bandgap from its optimum value produces a larger decrease in efficiency. If either the bottom cell bandgap is increased or the top cell bandgap is decreased, while holding all other design parameters at their optimum values, an equally sharp drop in efficiency results. This is substantiated by comparing the slope in Figure 4 below 1.62 eV with the slope in Figure 5 above 0.954 eV. The slopes are nearly equal, being 46%/eV for the former and 49%/eV for the latter.

Reducing the bottom cell bandgap serves to increase the photon flux absorbed, to increase the short-circuit current, and to reduce the photovoltage. This does not change the top cell terminal operating current significantly. Therefore, the reduction in efficiency arises through a smaller contribution to the cascade efficiency from the bottom cell. Increasing the top cell bandgap reduces the photon absorption in the top cell, reducing its short-circuit but increasing its photovoltage. There is a reduction in efficiency in the bottom cell, because of a mismatch in maximum power point operating current between top and bottom cells, but a smaller decrease in the top cell.

Layer Thickness

The behaviors of the top and bottom cells with respect to the thickness of the n- and p-type regions are similar. While in this presentation the bottom cell behavior is discussed, the results apply equally as well to the top cell behavior. Figure 6 shows the effect on efficiency when varying the ratio of the p-type layer to the total thickness of the p- plus n-layers of the bottom cell. The efficiency exhibits a peak at a ratio of 0.35 for the bottom cell. In the top cell the peak efficiency occurs for a ratio of 0.445. For low values of the ratio, the rate of increase of efficiency is greater in magnitude than the magnitude of the rate of decrease for high ratios. This results because for low ratios, the incomplete absorption loss predominates and serves to significantly reduce efficiency.

The form of dark current components is given by

$$J_{n0i} = q \frac{D_{ni}}{L_{ni}} n_{p0i} R_{ni} \qquad (1)$$

for the electron contribution and

$$J_{p0i} = q \frac{D_{pi}}{L_{ni}} p_{n0i} R_{pi} \qquad (2)$$

for holes, where the subscript i is assigned the value T or B to denote the top

and bottom cells, respectively. The interaction parameter R_{ni}, relating to electron confinement in the p-type region, increases with increasing p-type ratio, resulting in increased contribution from photoexcited electrons to short-circuit current (i.e., spectral response) and an increased contribution to dark current from injected electrons. Moreover, as the p-type ratio increases, the corresponding n-type ratio, $(x_7-x_6)/(x_7-x_5)$, decreases, resulting in R_{pB} decreasing. Therefore, the hole contribution to normalized spectral response and dark current in the n-region also decrease as shown in Figures 6(b) and 6(c). Figure 6(c) shows the electron normalized spectral response in the p-type region to be lower than the hole normalized spectral response for thin p-regions. For thick p-regions, the reverse is true.

It should be noted that maximum efficiency occurs in the neighborhood where the electron and hole contributions to dark current are equal. This is typical of single- or multijunction behavior where the cell structures are optimized.

The second set of calculations allows the total thickness of the n- plus the p-region to increase. Figure 7 relates to the bottom cell. The ratio of the p-layer to the total thickness of the homojunction is maintained at the optimum ratio obtained and shown in Figure 6(a). For maximum efficiency, the optimum total thickness of the top homojunction obtained is 3.4 μm, as shown in Figure 7(a); and for the top cell it is shown to be 1.8 μm. It is observed that the efficiency decreases sharply for values lower than the optimum thickness in Figure 7(a). This occurs because the incomplete absorption loss predominates in both n- and p-type regions for smaller thickness values, but becomes negligible for large thickness values. The dark current components increase sharply for increasing values, and beyond the optimum thickness the rate of increase becomes smaller, as shown in Figure 7(b). Also, while incomplete absorption is the major loss for small thickness values, both the electron and hole normalized spectral responses are very high due to the thin n- and p-regions, as shown in Figure 7(c). The absolute spectral response, of course, increases as the homojunction regions become thicker.

SUMMARY AND CONCLUSIONS

The solution to the integral form of the continuity equation results in the V-I solar cell expression for each of the component cells as well as for the cascade cell as a unit. The computer program determines the design parameters for maximum efficiency. The analysis predicts a cascade cell conversion efficiency in excess of 31% at 300 K, AM0, and one sun.

The cascade V-I solar cell curve behaves as if the device is fabricated from a single p-n junction. The voltage at the maximum power point and the open-circuit voltage exhibit values that suggest a bandgap value equal to the sum of the bandgaps of the top and bottom cells. In contrast, the current at the maximum power point and the short-circuit current values are more characteristic of the top cell bandgap.

The computer modeling predicts that maximum efficiency does not occur for maximum short-circuit current or for minimum dark current, but occurs for a set of design parameters between these extremes. Maximum efficiency occurs for thin

window layers <0.1 μm. The conduction bandedge discontinuity at the window layer heterointerface has a marked effect on efficiency and results in the window layer built-in field having a small influence.

Efficiency, photovoltage, dark current, fill-factor, and spectral response are shown to exhibit temperature dependencies similar to those of single-junction solar cells.

REFERENCES

1. J. J. Loferski, J. Appl. Phys., 27, 96 (1956).

2. J. J. Wysocki and P. Rappaport, J. Appl. Phys. 31, 571 (1960).

3. E. L. Burgess and J. G. Fossum, IEEE Trans. Electron Devices, ED-24, 433 (1977).

4. J. G. Fossum, ERDA Photovoltaic Concentrator Systems Workshop, Scottsdale, AZ, May 24, 1977, U. S. Dept. of Energy, Washington, D.C.

5. H. J. Hovel, Solar Cells, Vol. II, Semiconductors and Semimetals, Ed.: A. C. Beer and R. K. Willardson, Academic Press, Inc., New York, N.Y., (1976).

6. J. Lindmayer and J. F. Allison, Comsat Tech. Rev. 3, 1 (1973).

7. D. Redfield, Appl. Phys. Lett. 25, 647 (1974).

8. J. Mandelkorn and J. H. Lamneck, Jr., J. Appl. Phys. 44, 4785 (1973).

9. M. P. Godewski, C. R. Baraona, and H. W. Brandhorts, Jr., 10th Photovoltaic Specialists Conf., IEEE, Palo Alto, CA, November 13-15, 1973.

10. H. W. Brandhorst, Jr., C. R. Baraona, and C. K. Swartz, 10th Photovoltaic Specialists Conf., IEEE, Palo Alto, CA, November 13-15, 1973.

11. J. Mandelkorn, J. H. Lamneck and L. R. Scudder, 10th Photovoltaic Specialists Conf., IEEE, Palo Alto, CA, November 13-15, 1973.

12. J. G. Fossum, IEEE Int. Electron Devices Meeting, Washington, D.C. (1975).

13. H. J. Hovel, IBM J. Res. Dev. 22, 112 (1978).

14. J. M. Woodall and H. J. Hovel, Appl. Phys. Lett. 21, 379 (1972).

15. N. S. Alvi, C. E. Backus, and G. S. Masden, 12th Photovoltaic Specialists Conf., IEEE, Baton Rouge, LA, November 15-18, 1976.

16. R. L. Moon, L. W. James, H. A. VanderPlas, Y. G. Chai and G. A. Antypas, 13th Photovoltaic Specialists Conf., IEEE, Washington, D.C., June 5-8, 1978.

17. G. W. Masden and C. E. Backus, 13th Photovoltaic Specialists Conf., Washington, D.C., June 5-8, 1978.

18. W. Blocker, Proc. IEEE 66, 104 (1978).

19. E. D. Jackson, Trans. Conf. on the Use of Solar Energy (Tucson, 1955, University of Arizona Press, AZ) 5, 122 (1958).

20. L. W. James, IEEE Int. Electron Devices Meeting, Washington, D.C., December 1-3, 1975.

21. Solar Cell Design Study: Final Report, Contract No. F33615-76-C-1283, Research Triangle Institute, February 1977.

22. M. F. Lamorte and D. Abbott, 12th Photovoltaic Specialists Conf., IEEE, Baton Rouge, LA, November 15-18, 1976 ("Analysis of a Two-Junction Monolithic Solar Cell in a Structure Using $Al_uGa_{1-u}As$ and $Ga_vIn_{1-v}As$").

23. M. F. Lamorte and D. Abbott, DOE Photovoltaic Concentrator Systems Workshop, Scottsdale, AZ, May 24-26, 1977.

24. M. F. Lamorte and D. Abbott, 13th Photovoltaic Specialists Conf., IEEE, Washington, D.C., June 5-8, 1978.

25. L. M. Fraas and R. C. Knechtli, 13th Photovoltaic Specialists Conf., IEEE, Washington, D.C., June 5-8, 1978.

26. M. F. Lamorte and D. Abbott, to be published in Solid State Electronics.

TABLE I. - DESIGN PARAMETERS OF OPTIMIZED BANDSTRUCTURE

DESIGN PARAMETER	300 K	DESIGN PARAMETER	300 K
$E_G(0)$	1.83 eV	X_1	0.1 μm
$E_G(X_1)$	1.80	$X_2 - X_1$	0.8
$E_G(X_2)$, $E_G(X_3)$	1.62	$X_3 - X_2$	1.0
$E_G(X_4)$, $E_G(X_5)$	1.62	$X_4 - X_3$	0.1
$E_G(X_6)$, $E_G(X_7)$	0.954	$X_5 - X_4$	0.1
$E_G(X_8)$	1.439	$X_6 - X_5$	1.2
$E_{Fo} - E_{v1}$	0.07	$X_7 - X_6$	2.2
$E_{Fo} - E_{v2}$	0.129	N_{A1}	10^{18} cm^{-3}
$E_{c3} - E_{Fo}$	0.037	N_{A2}, N_{D3}	10^{17}
$E_{c4} - E_{Fo}$	-0.242	N_{D4}, N_{A5}	10^{20}
$E_{Fo} - E_{v5}$	0.004	N_{A6}, N_{D7}	10^{17}
$E_{Fo} - E_{v6}$	0.119	N_{D8}	10^{17}
$E_{c7} - E_{Fo}$	0.037		
$E_{c8} - E_{Fo}$	0.061		
ΔE_{c1}	0.239		
ΔE_{v1}	0.059		
ΔE_{c3}	0.279		
ΔE_{v3}	0.279		
ΔE_{c5}	0.781		
ΔE_{v5}	0.115		
ΔE_{c7}	0.024		
ΔE_{v7}	0.461		

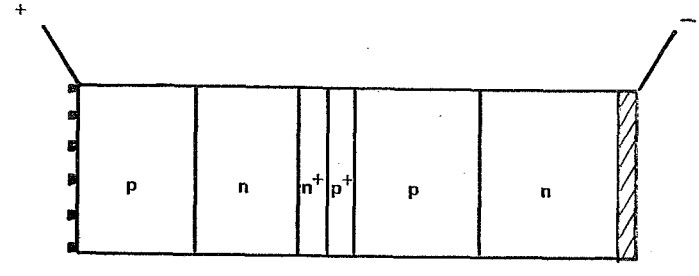

(a) PHYSICAL STRUCTURE

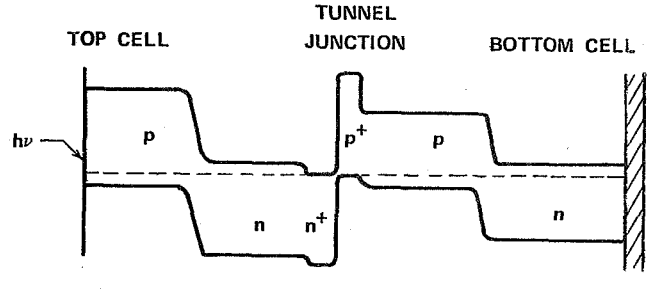

(b) ENERGY BAND STRUCTURE

Figure 1. - Monolithic two-junction solar cell.

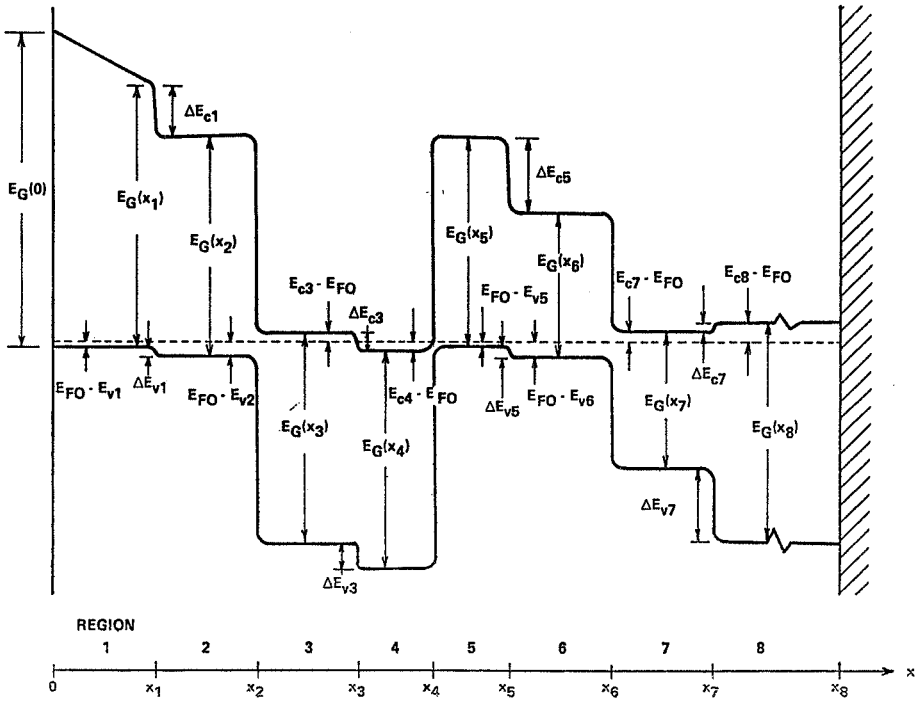

Figure 2. - Band structure of two-junction, voltage-aiding, two-terminal cascade solar cell.

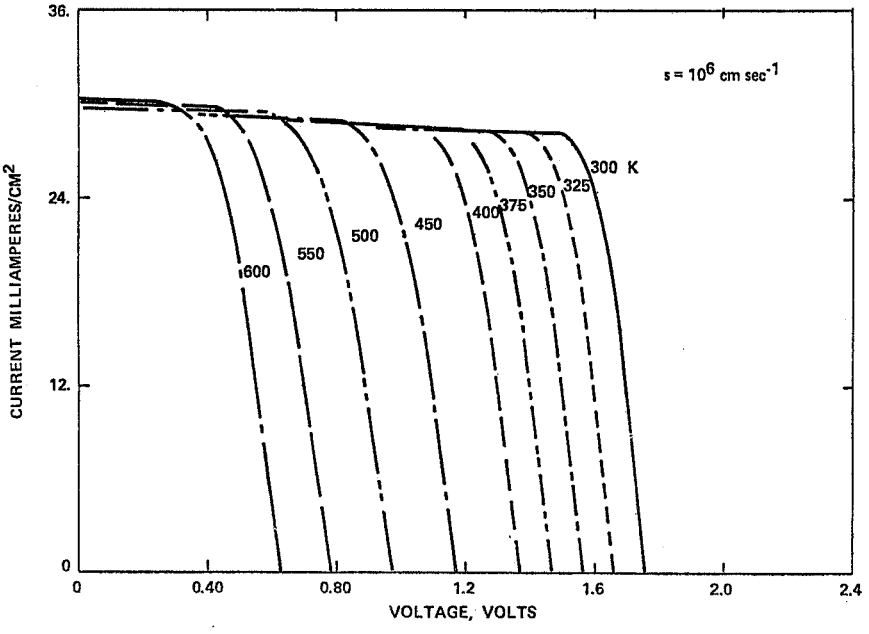

Figure 3. - Cascade solar cell V-I curve with temperature a parameter and for $s = 10^6$ cm sec^{-1} AM0 on a structure optimized for 300 K operation and AM0.

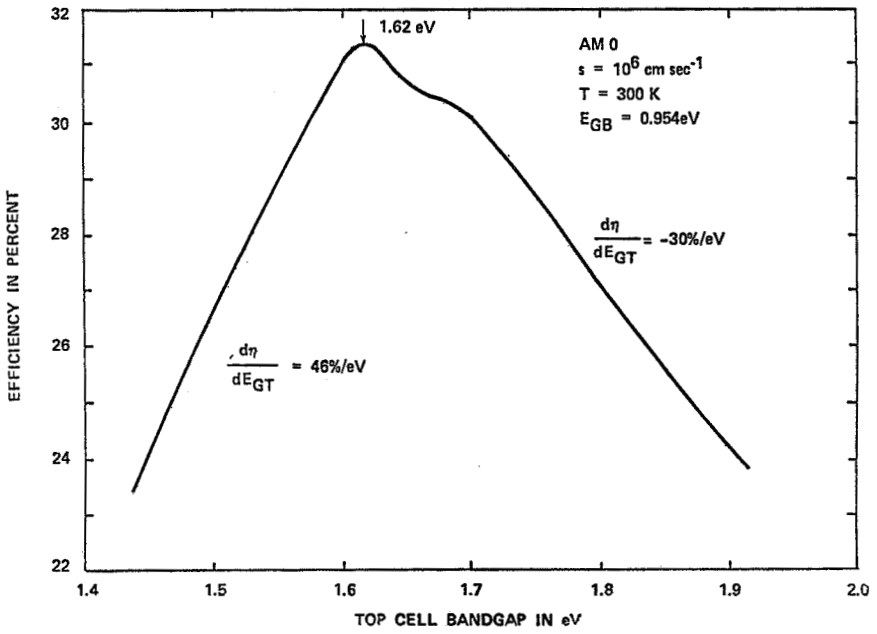

Figure 4. - Conversion efficiency as function of bandgap of top cell for optimized structure.

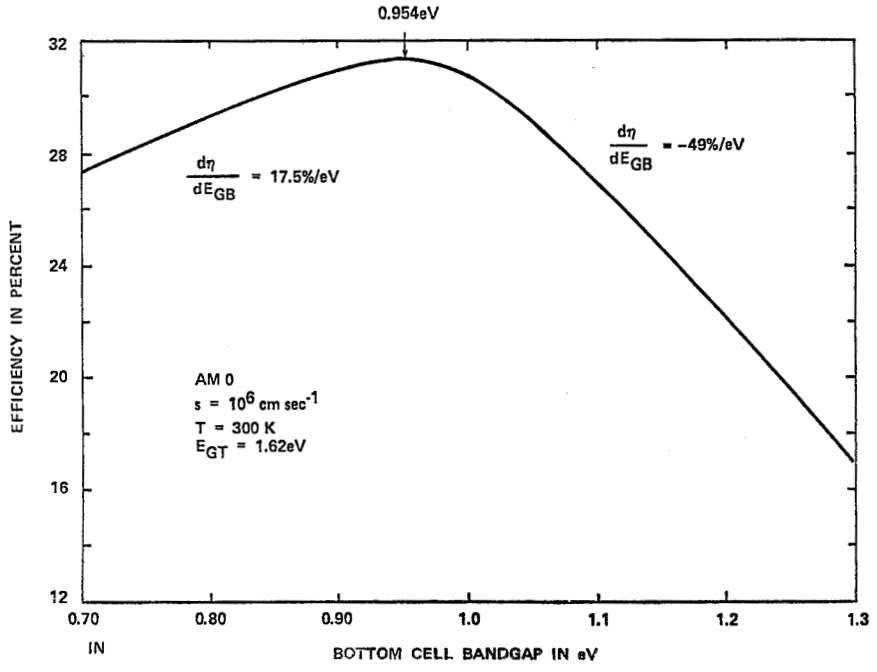

Figure 5. - Conversion efficiency as function of bandgap of bottom cell for optimized structure.

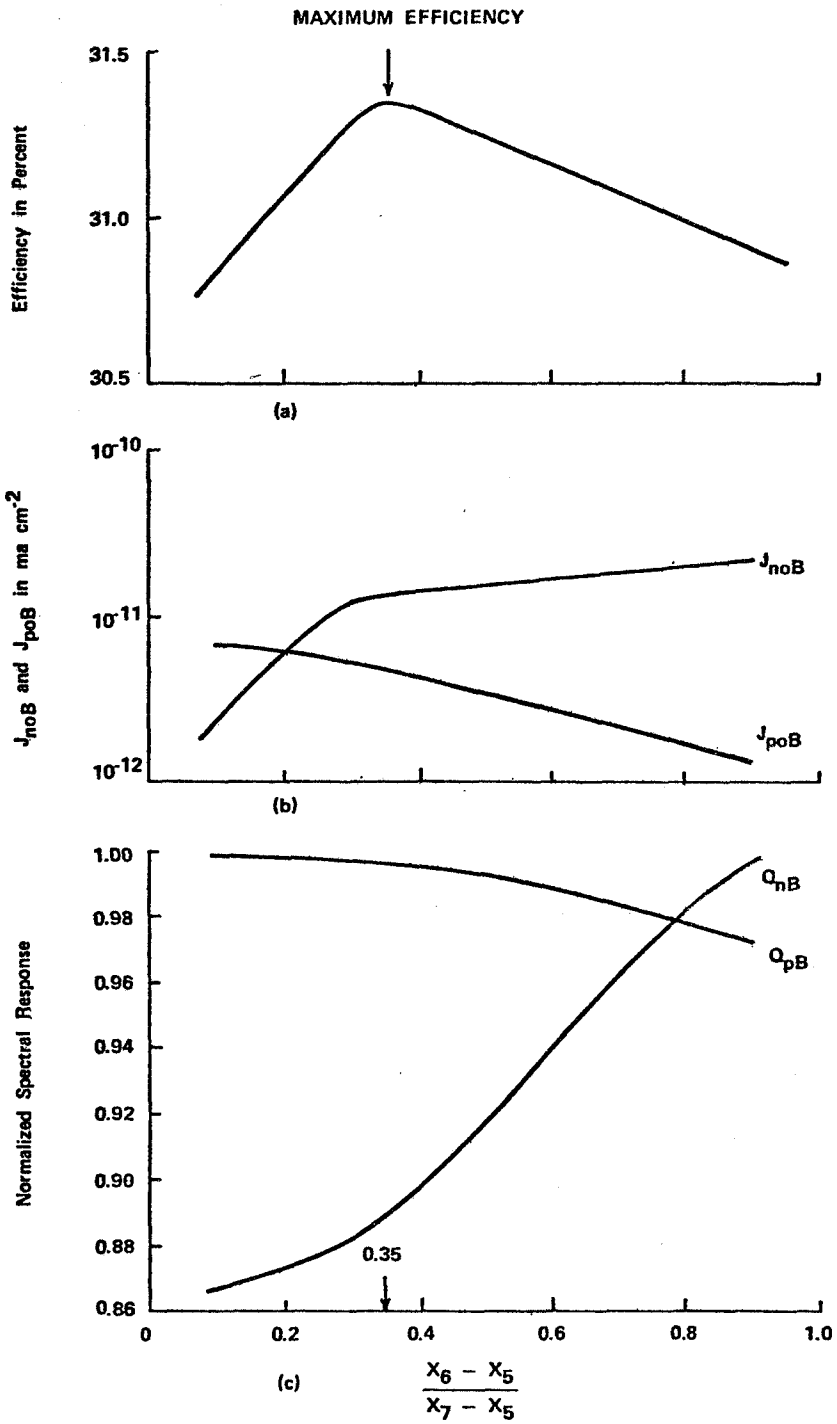

Figure 6. (a) Cascade cell efficiency, (b) electron and hole saturation current values of the bottom cell, and (c) electron and hole normalized spectral response of the bottom cell vs. the ratio of the p-layer thickness to the total thickness of the bottom cell homojunction.

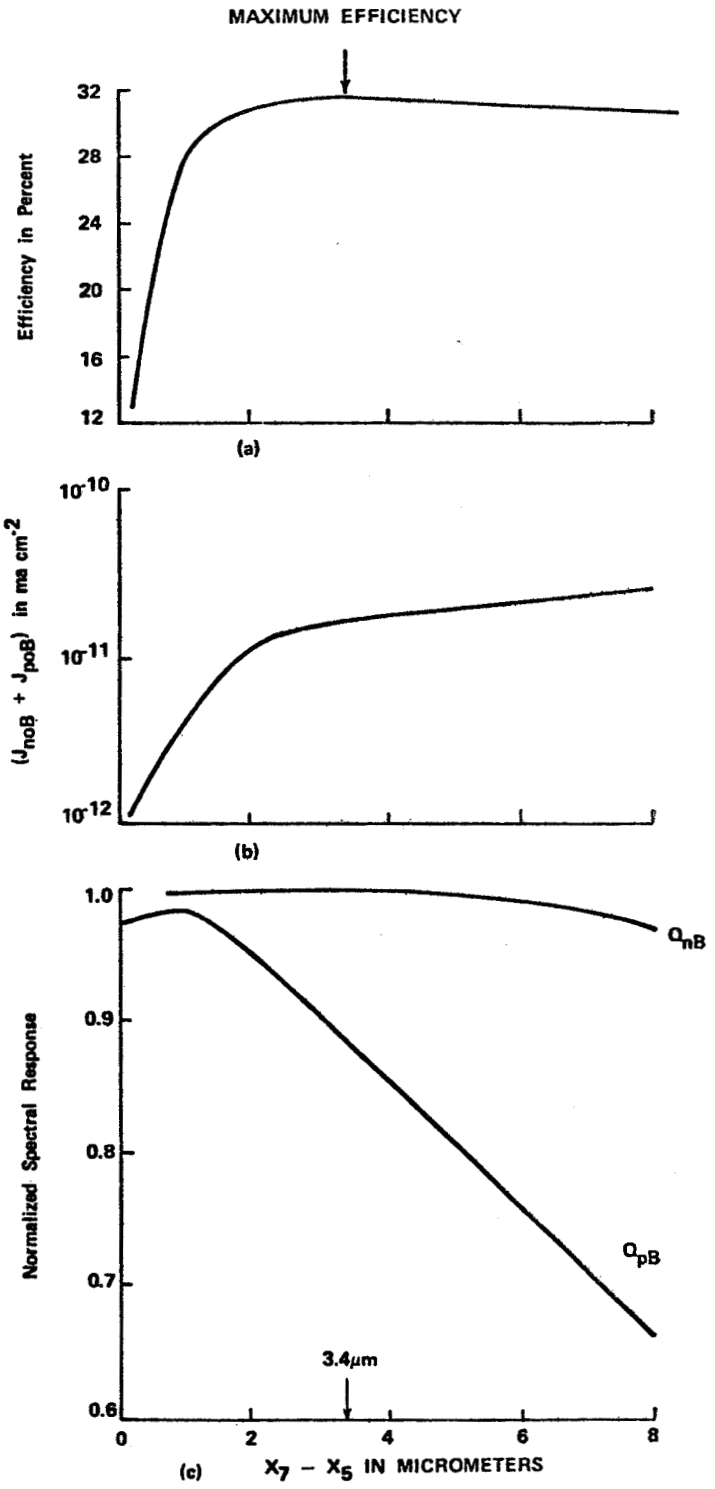

Figure 7. (a) Cascade cell efficiency, (b) total saturation current of the bottom cell, and (c) electron and hole normalized spectral response of the bottom cell vs. the total thickness of the bottom cell homojunction.

INTERCELL OHMIC CONTACTS FOR HIGH EFFICIENCY MULTIJUNCTION SOLAR CONVERTERS*

Stanley W. Zehr, D. L. Miller, J. S. Harris, Jr.
Rockwell International Electronics Research Center

SUMMARY

The monolithic multijunction converter is an attractive approach to achieving solar/electric conversion with greater than 30% efficiency. A major technical challenge in the development of such devices is the requirement for low resistance, optically transparent intercell contacts between adjacent junctions. These contacts should transmit, without significant loss, the spectral fraction of the incident sunlight which is not absorbed and converted in the overlying junction materials. Their contact resistances must be low enough to prevent significant I^2R loss at the designed current density levels. They should also exhibit adequate thermal conductivity to prevent device overheating when subjected to the designed illumination level.

Recent encouraging results for the development of such contacts are presented.

INTRODUCTION

The realization of high efficiency, monolithic multijunction solar converters is critically dependent on minimizing performance losses caused by their intercell ohmic contacts (IOC). This involves reducing the major sources of thermal and electrical resistance while maximizing optical transparency for the solar spectral fraction transmitted to the underlying, power-producing junctions.

In this paper we consider the types of losses expected from a tunnel junction IOC formed in GaAs. In our example, the IOC serves to transmit the optical, electrical and thermal flux passing from a well-optimized GaAs solar cell to an underlying cell having a bandgap of 0.7eV. The overall structure is shown schematically in Fig. 1.

The calculated performance parameters of such a converter excluding any IOC losses are summarized in Fig. 2 for operation at 300°K under 1 and 1000 SUNs AMO. For these calculations a conventional lumped circuit element model[1] is used for each cell, and it is assumed that the GaAs cell has an ideal diode factor n=1 and a dark saturation current density, $J_o=10^{-18}$amp/cm^2. The 0.7eV device is assumed to have n=1.7 and $J_o=10^{-4}$amp/cm^2 for operation at 1 SUN, and n=1, $J_o=10^{-7}$amp/cm^2 for 1000 SUNs operation. The values for the 0.7eV cell are representative of those measured in our laboratory for experimental GaSb

* This work has been partially supported by the U. S. Air Force under contract No. F33615-78-C-2036.

devices[2]. Other performance losses due to reflection, front surface contact shadowing and less than perfect carrier collection have been ignored in these calculations, although a modest level (.005 Ω) of series resistance is included.

We proceed by considering the questions: 1) what are the specific types of losses to be expected for a tunnel homojunction IOC? 2) which of these are likely to be of major concern in a practical device? 3) what are the allowable magnitudes of critical IOC design parameters which can maintain each type of loss below an arbitrary limit of 1% of the initially calculated peak output power?

We later list some of the potential advantages of fabricating tunnel junction IOC's by molecular beam epitaxy (MBE), and report the electrical behavior of some experimental MBE tunnel junction structures fabricated in our laboratory.

SOURCES OF LOSS IN TUNNEL JUNCTION IOCs

The major electrical losses are controlled by the effective contact resistance of the IOC. The optical losses are determined by the degree of absorption and reflection of photons having energies in the bandwidth 1.42 to 0.7eV. The thermal loss contributions, if any, arise from possible temperature increases in the upper cell due to I^2R losses in the IOC and to any increase in thermal resistance due to its presence.

Electrical Losses

For a cm^2 of IOC area, the ohmic power loss is given by $J_m^2 R_c$ where J_m is the current density (amp/cm^2) at peak output power and R_c is the effective contact resistance (Ωcm^2) of the IOC. Thus at 1 SUN for $J_m^2 R_c \leq .01 P_m$ (the 1% loss criterion):

$$R_c \leq \frac{1}{(29 \times 10^{-3})^2} \cdot (.01)(30.96 \times 10^{-3}) = .368\,\Omega cm^2 .$$

The equivalent value for 1000 SUN operation is $4.8 \times 10^{-4}\ \Omega cm$. The resulting heat loads are $3.1 \times 10^{-4}\ W/cm^2$ and $.46\ W/cm^2$ respectively for 1 SUN and 1000 SUNs and the corresponding voltage drops across the IOC are 10.7 mV and 14.6 mV.

The I^2R heating thus developed in the IOC adds to the heat load which must be effectively dissipated to maintain a low converter operating temperature. For typical semiconductors with thermal conductance in the range of several tenths of a watt/°K cm, and thicknesses of the order of several hundredths of a cm, even a 10% ohmic IOC loss at 1000 SUN operation contributes less than 1°C to the temperature difference between the upper and lower cells. This upper bound can be estimated using the relation:

$$\Delta T = \frac{J_m^2 R\, l}{kA}$$

where ΔT = temperature difference of the boundaries of a layer of thickness l, area A, and thermal conductivity k due to a source of steady heat flux of strength J^2R located at the higher temperature surface of the layer.

Optical Losses

Interface Reflection

If the IOC is designed such that there is an interface between materials having different refractive indices, there will be reflection losses. The magnitude of these losses will, in general, vary slightly with wavelength since refractive indices are usually weak functions of wavelength. A review of refractive index values measured for III-V compounds with bandgaps of interest for multijunction solar cell applications shows that they all lie in the range of ~ 3.4 to ~ 4.1 . Over this limited range, even without the use of anti-reflection design principles, involving optimally dimensional thin layers, these differences lead to losses of $\leqslant 0.7\%$, according to the reflectivity relation:

$$R = \frac{(n_1 - n_2)^2}{(n_1 + n_2)^2} .$$

Even for a heterojunction involving GaAs (n = 4.025) and Ge (n = 5.6), the reflection losses would be no more than $\sim 3\%$.

Below Bandgap Absorption

Because of the high doping used in the formation of tunnel junctions, free carrier absorption of below bandgap photons can be an important potential loss mechanism. The magnitudes of these losses for n++and p++ GaAs doped to $10^{20}\,cm^{-3}$ are indicated by the curves of Fig. 3a. These show the transmitted photon fraction as a function of layer thickness for 1.35eV and 0.7eV photons. As noted, to maintain at least 99% transmission of 0.7eV photons, the p++ layer must be no more than 160Å thick. The equivalent transmission thickness for a similarly doped n++ layer is shown to be $\sim$1250Å. The thicknesses for 99% transmission of higher energy photons up to nearly bandgap energy can be significantly greater as indicated by the transmission vs. thickness curves for 1.35eV photons. The actual absorption vs. photon energy curve for p = $10^{20}\,cm^{-3}$ GaAs is shown in Fig. 3b[4] along with an estimated curve for n = $10^{20}\,cm^{-3}$ GaAs developed by extrapolating available literature data[5] for lower doped material.

As summarized in Fig. 4, the above considerations suggest that the most critical source of performance loss in GaAs tunnel IOC's operating at high solar concentrations is expected to be that due to excessive contact resistance. Also indicated is a need for careful thickness control of the heavily doped layers to maintain an acceptably low level of absorption loss for below band-gap photons.

There is evidence in the literature than tunnel IOC's having acceptable contact resistance for even 1000 SUN operation can be realized. Holonyak & Lesk[6] report alloyed GaAs tunnel diodes with peak current densities of 2000 - 10,000 amp/cm^2 coupled with peak voltages of 0.1 to 0.25 Volts. While it is not clear from their paper which peak voltage goes with which peak

current density, even the most conservative combination implies an effective contact resistance of no more than $1.25 \times 10^{-4}\ \Omega cm^2$ for these devices. This compares well with the $4.8 \times 10^{-4}\ \Omega cm^2$ calculated as an upper limit for 1% I^2R loss under 1000 SUN AMO operation. Because of the non-transparency of these alloyed diodes, there is a need to demonstrate acceptably low contact resistance in tunneling structures formed by other methods.

PRELIMINARY RESULTS FOR GaAs TUNNEL JUNCTIONS FORMED BY MBE

A number of potential advantages of molecular beam epitaxy as a means of fabricating tunneling structures are listed in Fig. 5.

To begin to explore the behavior of such junctions, the structures shown schematically in Fig. 6 were fabricated. Be was used as the p++ dopant because of its relatively low diffusivity compared to Zn or Cd and because neither Zn or Cd are useable with MBE because of their high vapor pressure. The electrical characteristics of the structures were measured in the as-grown condition and after a subsequent heat treatment in which they were subjected to the same thermal history that they would experience if a high performance GaAs cell were later grown on them by LPE. The point of this additional heat treatment experiment was to note any changes in I-V characteristics which might result. The concern was that diffusion of dopants might degrade the performance of the original structures and make them unsuitable for use as IOCs.

The I-V curves obtained for the two structures before and after the indicated heat treatment are shown in Fig. 7. Their qualitative appearance indicates a tendency toward more ohmic behavior following heat treatment.

Semi-quantitative estimates of their upper bound specific contact resistance are presented in Fig. 8. These values were obtained using the multiple area contact method of Cox & Strack[7]. This technique is ordinarily used to measure the specific resistance of surface contact metallization, by separating it from all other sources of resistance in the test structure and measurement system. In the present case, the tunnel contact resistance is lumped with the surface contact resistance so that the measured result is at best an upper bound. Other experiments on just the surface contacts, without the tunnel structures, indicate that their contributions to the measured upper bound value for the complete structure is $<10\%$. The measured values are sufficiently low for use in 1 SUN devices. For concentrated illumination beyond $\sim$20 SUNs, however, their I^2R losses would exceed the 1% loss criterion.

Based on tunnel junction theory[8], it is expected that with thinner layers and higher doping levels these structures can approach sufficiently close to the low contact resistances reported for alloyed devices to be useful for high concentration operation.

SUMMARY

Potential sources and levels of performance losses have been assessed for GaAs tunnel junction IOC's. Our conclusion is that only electrical losses due to excessive contact resistance and optical losses due to excessive free carrier absorption in the highly doped layers are of practical significance. There is reason to believe that both these types of loss can be maintained at acceptably low levels for good overall device performance.

Evaluation of preliminary GaAs tunnel junction structures formed by MBE indicate acceptable contact resistance values for 1 SUN operation but not for concentrator applications above ~20 SUNs. It is expected that with thinner layers and higher doping, sufficiently low resistances can be achieved to allow operation at high solar concentration (~1000 SUNs). It was found that the structures tested had sufficient thermal stability to allow subsequent LPE growth of a high performance GaAs window solar cell structure.

REFERENCES

1. Hovel, H. J., Semiconductors and Semimetals 11, Solar Cells, ed. R. K. Willardson and A. C. Beer, Academic Press, New York (1975), chapter 3.

2. Huai-Tung Yang - Private communication.

3. Neuberger, M., Handbook of Electronic Materials 2, III-V Semiconducting Compounds, IFI/Plenum, New York (1971).

4. Kudman, I and Seidel, T., Absorption Edge in Degenerate p-Type GaAs, J. Appl. Phys. 33, 771, (1972).

5. Spitzer, W. G. and Whelan, J. M., Infrared Absorption and Electron Effective Mass in n-Gallium Arsenide, Phys Rev. 114, 59, (1959).

6. Holonyak, N, Jr. and Lesk, I. A., Gallium Arsenide Tunnel Diodes, Proc. IRE 48, 1405 (1960).

7. Cox, R. H. and Strack, H., Ohmic Contacts for GaAs DEvices, SSE 10, 1213, (1967).

8. Kane, E. O., Theory of Tunneling, J. Appl. Phys. 32, 83, (1961).

A TWO BANDGAP SOLAR CELL

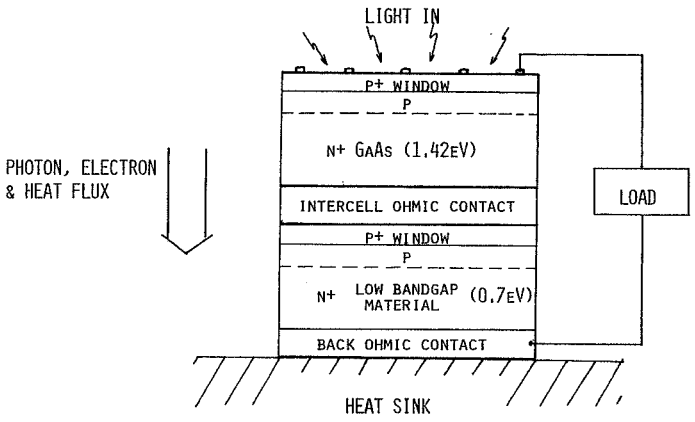

Figure 1

PERFORMANCE PARAMETERS FOR A TWO-BANDGAP SOLAR CELL*

INSOLATION	1 SUN, AMO (.135w/cm^2)	1000 SUN, AMO (135w/cm^2)
TOP CELL (1.42eV)		
J_{SC} (amp/cm^2)	32×10^{-3}	32
V_{OC} (volt)	.943	1.12
P_M	26.4×10^{-3}	32.01
BOTTOM CELL (0.7eV)		
J_{SC} (amp/cm^2)	34×10^{-3}	34
V_{OC} (volt)	0.26	0.56
P_M	5.06×10^{-3}	14.06
TOTAL DEVICE		
J_M (amp/cm^2)	29×10^{-3}	31.1
V_M (volt)	1.067	1.48
P_M	30.96×10^{-3}	46.1
FF	.793	.84
η (%)	22.9	34.1
I^2R_S LOSS (%)	.013	10.5

*Total Series Resistance, $R_S = .005\Omega/cm^2$ 300°K Operating Temperature.

Figure 2

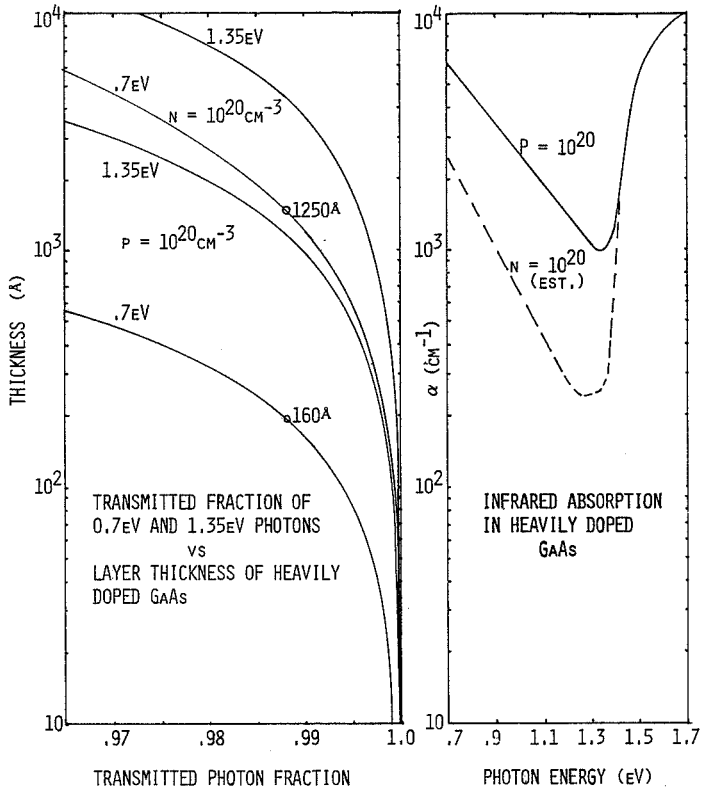

Figure 3

PARAMETERS FOR 1% LOSSES AT INTERCELL OHMIC CONTACT

	1 SUN, AMO	1000 SUN, AMO
ELECTRICAL		
CONTACT RESISTANCE, R_C:	$<.37$ ohm-cm^2	$<4.8 \times 10^{-4}\ \Omega$-cm^2
OPTICAL		
ABSORPTION IN HEAVILY DOPED (10^{20}) LAYERS, THICKNESS:	P^{++} GaAs, $T \lesssim 160$Å N^{++} GaAs, $T \lesssim 1250$Å	
REFLECTION AT INTERFACE:	LOSS IS <1% FOR MOST III-V HETEROJUNCTIONS*	
THERMAL		
LOSS OF OUTPUT DUE TO UPPER CELL HEATING:	NO PROBLEM	NO PROBLEM

* FOR GaAs/Ge, INTERFACIAL REFLECTION LOSS IS 2.7%

Figure 4

POTENTIAL ADVANTAGES OF MBE FOR INTERCELL OHMIC JUNCTIONS

- LOW GROWTH TEMPERATURES (~400-550°C FOR GaAs)
- EXCELLENT THICKNESS CONTROL IN THE 100Å-1000Å RANGE
- EXPANDED CHOICE OF DOPING SPECIES, CONCENTRATIONS AND PROFILES
- REALIZATION OF VERY ABRUPT JUNCTION TRANSITIONS

Figure 5

MBE OHMIC JUNCTIONS IN GaAs

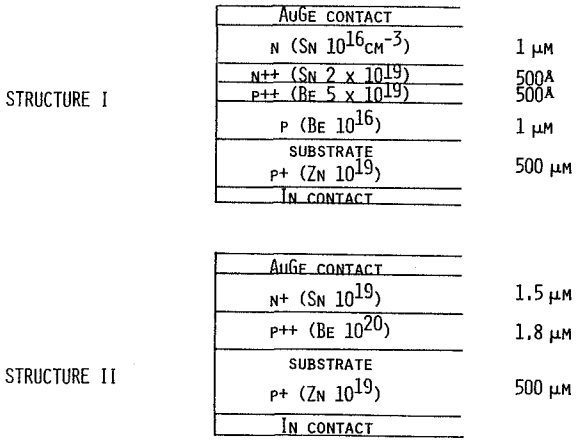

Figure 6

TYPICAL I-V CURVES FOR MBE INTERCELL OHMIC CONTACTS

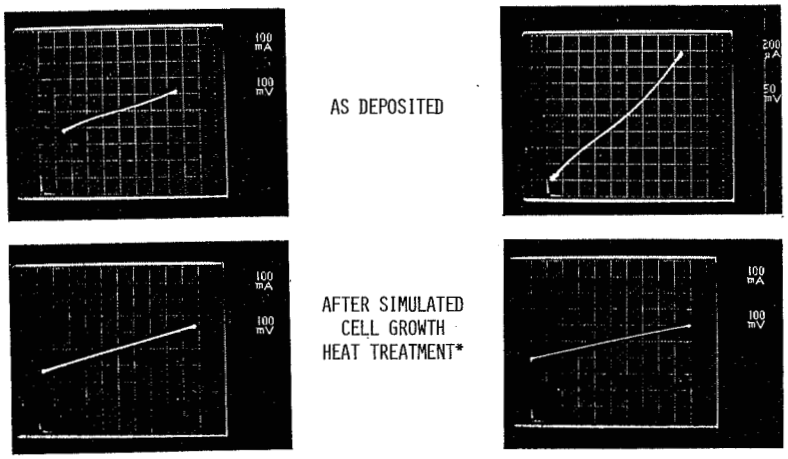

STRUCTURE I

STRUCTURE II

* HEAT R.T. TO 745°C
HOLD 1/2 HR @ 745°C
COOL 10°C @ 1°C/MIN
FURNACE COOL TO R.T.

Figure 7

ESTIMATED CONTACT RESISTANCE FOR MBE OHMIC CONTACTS

	AS GROWN	AFTER HEAT TREATMENT
STRUCTURE I (500Å LAYERS)	$<.03\,\Omega cm^2$	$<.025\,\Omega cm^2$
STRUCTURE II (1-2μM LAYERS)	$<.04\,\Omega cm^2$	$<.07\,\Omega cm^2$

1% LOSS AT ~10-15 SUNS, AMO

NEED $\sim 5 \times 10^{-4}\,\Omega cm^2$ FOR 1% LOSS AT 1000 SUNS, AMO

Figure 8

SUMMARY OF WORKSHOP ON 30 PERCENT DEVICES

J. J. Loferski
Division of Engineering
Brown University

The conclusions of the workshop are summarized as responses to the Workshop Questions presented to the participants.

Q.1. Is 30% AMO a reasonable target?

A.1. Yes! Tandem cell systems utilizing only two solar cells and no concentration have theoretical limiting AMO efficiencies in excess of 30% for cells operating at 300K. For large numbers of cells, the efficiency approaches 50% at 300K. If the cells can be cooled below 300K as is possible in space, these limiting efficiencies increase. For example, the efficiency of a two cell tandem stack becomes 40% at 200K; the efficiency of a 24 cell stack, 62% at 200K.

Q.2. Does 30% AMO efficiency require concentration?

A.2. Concentration makes it easier to achieve high efficiencies, but as indicated in the response to Q.1., it is not absolutely necessary. Theoretical analysis of tandem systems shows that the highest limiting efficiency for a two cell system is about 40% for 1000 fold concentration compared to 32% for no concentration. The limiting efficiency for a 24 cell system is about 60% for 1000 fold concentration compared to 50% for no concentration. It was conjectured that the concentration level appropriate for space applications is more likely to be in the 10X to 20X range because of orientation problems. If the problem associated with higher concentration levels are solvable in space, then higher concentration may be the preferred path to follow. Concentration should reduce radiation damage effects because the cells can be placed inside the satellite rather than on its "skin." Furthermore, if concentration is combined with the possibility of adjusting the radiation balance of the cell and therefore its temperature, it should be possible to anneal radiation damage by raising the cell temperature. As noted in the response to Q.1., operation of the cells at a reduced temperature increases the limiting efficiencies. For example, the limiting efficiency of a 24 cell tandem stack for 1000 fold concentration and T=200K is 70%.

Q.3. Is a higher efficiency target reasonable?

A.3. As indicated in the responses to Q.1. and Q.2., a higher efficiency target does not violate fundamental laws of physics. If high concentration and temperatures below 300K are options available on future space missions, then efficiencies as high as 50% would not be unreasonable targets. In the near term (say by 1981), AMO efficiencies in the 22 to 25% range will be achieved

with no concentration. The cells will probably be of the monolithic design. Achievement of the higher efficiencies which are theoretically possible will require a larger research and development effort than that currently devoted to the problem.

Q.4. What concepts and materials are most promising? What are their strengths? What are their critical problems? What approaches are needed to overcome the problems?

A.4. Tandem cell systems with or without concentration are the most promising for achievement of high efficiencies. Theoretical analyses of such systems have demonstrated that high efficiencies are indeed possible as indicated above. The problem is constructing the cells needed to demonstrate what is achievable in actual systems and then to produce such systems on a commerical scale. Semiconductor alloy systems which provide a wide range of band gaps, lattice constants, electron affinities, and other parameters of relevance to high efficiency cells are the first requirement. A number of such alloy systems exist and have been receiving attention. The best developed of these is based on III-V semiconductors. To reduce lattice mismatch, it is necessary to exercise separate control over lattice constant and energy gap as in quaternary alloys of the type $Al_xGa_{(1-x)}As_ySb_{(1-y)}$. Thus far good solar cells in Sb containing alloys have eluded researchers; this inferior performance has been attributed to low minority carrier lifetime in Sb containing alloys. (The antimony is needed to reduce the energy gap of the alloy below the value of Ga As; energy gaps around 1.0 eV are needed to obtain efficiencies in excess of 30% in two cell tandem stacks.)

Another less developed but promising system is that based on chalcopyrite semiconductors of the type $CuInSe_2$, $AgInS_2$, $CuAlTe_2$, etc. Alloys of these semiconductors have been synthesized, and it has been shown that their band gaps and lattice constants can be separately adjusted. Yet another possible system is based on the second chalcopyrite semiconductor family whose members are of the type $ZnSiP_2$, $CdSiAs_2$, etc.

The critical problems associated with achievement of high efficiency in the tandem cell systems begin with preparation of the required materials as homogeneous single crystals either free standing or epitaxially grown on appropriate substrates. In the case of monolithic cells, it was conjectured that the number of different energy gap materials which could be built into a monolithic structure would be smallest for the LPE process; larger for the VPE process; yet larger for the Metal Organic CVD process and largest for Molecular Beam Epitaxy. The most promising way to produce a multisemiconductor solar cell would be to employ MBE; however, MBE may be too expensive for producing cells in quantities needed for satellite power supplies.

Another critical problem is materials characterization. The materials from which tandem cells will be fabricated are direct gap semiconductors in which the lifetime is in the nanosecond range, and the diffision length is several microns. Convenient, reliable methods for measuring these parameters on wafers before, during, and after processing are needed. One immediate problem related to III-V cells is the already cited observation that Sb reduces lifetime; this subject requires further investigation.

Lifetime mapping in three dimensions will ultimately be required to get the most out of cells intended for solar cell applications, and therefore, encouragement of techniques which make this possible is important.

Cells intended for space applications have some special problems. Radiation damage must be assessed in the complex cells needed for high efficiency systems. Attention to operating temperature is important because the optimum combination of band gaps depends on T. As already noted, low T helps increase efficiency, and therefore, power supply designs which result in low T are preferred.

A basic question for realization of high efficiencies is the efficiency ultimately achievable from heterojunction structures. Heterojunctions provide one way to fabricate cells from semiconductors which have various band gaps, and in theory, if everything goes well, their efficiency should be the same as that attainable from heterojunction cells. This will be true only if I_o of the heterojunction is comparable to the I_o value for a good homojunction from the same semiconductor.

Elimination of interface states is required if these low values of I_o are to be reached. More investigation of the nature and role of these interface states is needed if the full potential of heterojunction cells is to be realized.

Q.5. What concepts, materials, and physical processes should get more attention?

A.5. This question has been partially answered above. More materials research is essential. A better understanding of lifetime in these alloys is required. Evaluation of Metal Organic--CVD as a high thruput process is needed. Work to produce monolithic cells by MBE should be supported. A more immediate problem: development of manufacturing processes for the high-quality substrates needed for the various epitaxial processes.

Other concepts for conversion of solar radiation should be monitored and explored. These include electromagnetic wave conversion; parametric converters based on light sensitive capacitance as in lanthanum fluoride; thermophotovoltaic systems utilizing Ge p-i-n cells combined with a 1500K black body radiator with the radiator heated by concentrated sunlight. Thermoelectric and thermionic conversion were discussed briefly, but no one in the group knew of any developments which warrant re-examination of those methods. There was a brief discussion of cell size and complex monolithic cells. Is it better to use small area cells and therefore, small area concentrators? If cell size is in the range of mm^2, good cells can be cut out of large wafers as is done in the manufacture of integrated circuits, and the overall efficiency of the solar cell system would be increased.

Finally, since DoE is currently the major source of funding on photovoltaic cells, NASA should maintain close coordination with DoE. NASA should support activities of special importance to its missions which are missing from the DoE program, e.g. high efficiency cells for AMO systems with no concentration. Such cells may be too expensive for terrestrial application but make sense in space. Another example, cells intended for intermediate concentration systems and cells intended for operation around 200K or whatever reduced temperature is appropriate to space power supplies.

APPENDIX - ATTENDEES

Evelyn Anagnostou, MS 302-1
NASA Lewis Research Center
21000 Brookpark Rd.
Cleveland, OH 44135

Lynn M. Anderson, MS 302-1
NASA Lewis Research Center
21000 Brookpark Rd.
Cleveland, OH 44135

Bruce Anspaugh
Jet Propulsion Laboratory
4800 Oak Grove Dr.
Pasadena, CA 91103

G. Mervin Ault, MS 3-5
NASA Lewis Research Center
21000 Brookpark Rd.
Cleveland, OH 44135

Cosmo Baraona, MS 302-1
NASA Lewis Research Center
21000 Brookpark Rd.
Cleveland, OH 44135

Daniel T. Bernatowicz, MS 302-1
NASA Lewis Research Center
21000 Brookpark Rd.
Cleveland, OH 44135

Henry W. Brandhorst, Jr., MS 302-1
NASA Lewis Research Center
21000 Brookpark Rd.
Cleveland, OH 44135

Jacob D. Broder, MS 302-1
NASA Lewis Research Center
21000 Brookpark Rd.
Cleveland, OH 44135

An-Ti Chai, MS 302-1
NASA Lewis Research Center
21000 Brookpark Rd.
Cleveland, OH 44135

Edmund Conway
NASA Langley Research Center
Hampton, VA 23365

Henry B. Curtis, MS 302-1
NASA Lewis Research Center
21000 Brookpark Rd.
Cleveland, OH 44135

Randy Davis
Westinghouse Electric Corp.
1310 Beulah Rd.
Pittsburgh, PA 15235

Henry M. DeAngelis
RADC/ESB (Mail Stop 30)
Hanscom Air Force Base, MA 01731

Peter Drevinsky
RAD/ESR, Mail Stop 30
Hanscom Air Force Base, MA 01731

John Fan
Massachusetts Institute of Technology
Lincoln Laboratory
Lexington, MA 02173

Dennis Flood, MS 302-1
NASA Lewis Research Center
21000 Brookpark Rd.
Cleveland, OH 44135

Americo F. Forestieri, MS 302-1
NASA Lewis Research Center
21000 Brookpark Rd.
Cleveland, OH 44135

Harry C. Gatos
Materials Science & Engineering
Massachusetts Institute of Technology
Cambridge, MA 02139

Michael P. Godlewski, MS 302-1
NASA Lewis Research Center
21000 Brookpark Rd.
Cleveland, OH 44135

Chandra Goradia
Cleveland State University
331 Stillwell Hall
Cleveland, OH 44115

Robert Hall
General Electric R&D Center
P.O. Box 8
Schenectady, NY 12301

Russell E. Hart, Jr., MS 302-1
NASA Lewis Research Center
21000 Brookpark Rd.
Cleveland, OH 44135

Allen Herman
Dept. of Physics
Tulane University
New Orleans, LA 70118

Frank Ho
Optical Coating Laboratories, Inc.
15251 E. Don Julian Rd.
City of Industry, CA 91736

Peter Iles
Optical Coating Laboratories, Inc.
15251 E. Don Julian Rd.
City of Industry, CA 91736

Kent Jefferies, MS 501-7
NASA Lewis Research Center
21000 Brookpark Rd.
Cleveland, OH 44135

Jay Jellison
Oak Ridge National Laboratory
P.O. Box X
Oak Ridge, TN 37830

G. S. Kamath
Hughes Aircraft Corp.
3011 Malibu Canyon Rd.
Malibu, CA 90265

Allen R. Kirkpatrick
Spire Corp.
Patriots Park
Bedford, MA 01730

Thomas M. Klucher, MS 302-1
NASA Lewis Research Center
21000 Brookpark Rd.
Cleveland, OH 44135

K. C. Knechtli
Hughes Aircraft Corp.
3011 Malibu Canyon Rd.
Malibu, CA 90265

Michael F. Lamorte
Research Triangle Institute
P.O. Box 12194
Research Triangle Park, NC 27709

John Lear
Martin Marietta Co.
P.O. Box 179
Denver, CO 80201

Joseph J. Loferski
Dept. of Engineering
Brown University
Providence, RI 02912

Walter T. Matzen
Texas Instruments
P.O. Box 225012 (MS 82)
Dallas, TX 75265

George Mazaris, MS 302-1
NASA Lewis Research Center
21000 Brookpark Rd.
Cleveland, OH 44135

Stanley S. Marsik, MS 49-5
NASA Lewis Research Center
21000 Brookpark Rd.
Cleveland, OH 44135

Andrew Meulenberg, Jr.
Comsat Laboratories
22300 Comsat Dr.
Clarksburg, MD 20734

John Minnuci
Spire Corp.
Patriots Park
Bedford, MA 01730

Kim Mitchell
Solar Energy Research Institute
1536 Cole Blvd.
Golden, CO 80401

Patricia Mooney
Physics Department
State University of New York
Albany, NY 12222

Arnost Neugroshel
University of Florida
College of Engineering
Dept. of Electrical Engineering
Gainesville, FL 32611

R. W. Opjorden
Spectrolab Inc.
12500 Gladstone Ave.
Sylmar, CA 91342

Siegfried Othmer
Northrop Research Laboratories
1 Research Park
Palos Verdes, CA 90274

Patrick Rahilly
AFAPL/POE-2
Wright-Patterson AFB, OH 45433

Lynwood Randolph
RTS-3/NASA Headquarters
Washington, DC 20546

Peter Randtke
Hughes, Industrial Products Division
6855 El Camino Real
Carlsbad, CA 92008

Ben Rose (Code ELP)
Air Force Weapons Laboratory
Kirkland AFB, NM 87117

Louis Rosenblum, MS 49-5
NASA Lewis Research Center
21000 Brookpark Rd.
Cleveland, OH 44135

Bernd Ross
AF-JPL Consultant
2154 Blackmore Ct.
San Diego, CA 92109

Richard J. Schwartz
Purdue University
Dept. of Electrical Engineering
Lafayette, IN 47901

John Scott-Monck
Jet Propulsion Laboratory, MS 125-231
4800 Oak Grove Dr.
Pasadena, CA 91103

Hans-Joachim Schurig
TRW Systems
1 Space Park
Redondo Beach, CA 90278

Bok Shin, MS 125-231
Jet Propulsion Laboratory
4800 Oak Grove Dr.
Pasadena, CA 91103

Richard L. Statler (6623)
Naval Research Laboratory
Washington, DC 20375

Richard Stirn
Jet Propulsion Laboratory
4800 Oak Grove Dr.
Pasadena, CA 91103

George Storti
Solarex Corp.
1335 Piccard Dr.
Rockville, MD 20850

Clifford K. Swartz, MS 302-1
NASA Lewis Research Center
21000 Brookpark Rd.
Cleveland, OH 44135

George Vendura
Hughes Aircraft Corp.
P.O. Box 92919
A/P Station 366/V330
Los Angeles, CA 90009

Frank Walker
Boeing Research Division
M/S 8C-62
P.O. Box 3999
Seattle, WA 98124

Irving Weinberg, MS 302-1
NASA Lewis Research Center
21000 Brookpark Rd.
Cleveland, OH 44135

Victor G. Weizer, MS 302-1
NASA Lewis Research Center
21000 Brookpark Rd.
Cleveland, OH 44135

John Woollam, MS 302-1
NASA Lewis Research Center
21000 Brookpark Rd.
Cleveland, OH 44135

Joseph Wise
AFAPL/POE-2
Wright-Patterson AFB, OH 45433

Martin Wolf
University of Pennsylvania
308 Moore Dr.
Philadelphia, PA 19103

Y. H. Wu
University of Pennsylvania
308 Moore Dr.
Philadelphia, PA 19103

Rosa T. Young
Oak Ridge National Laboratory
P.O. Box X
Oak Ridge, TN 37830

Stanley W. Zehr
Rockwell Science Center
Thousand Oaks, CA 91360

1. Report No.	2. Government Accession No.	3. Recipient's Catalog No.
NASA CP-2097		

4. Title and Subtitle	5. Report Date
SOLAR CELL HIGH EFFICIENCY AND RADIATION DAMAGE - 1979	August 1979
	6. Performing Organization Code
7. Author(s)	8. Performing Organization Report No. E-133
	10. Work Unit No.
9. Performing Organization Name and Address National Aeronautics and Space Administration Lewis Research Center Cleveland, Ohio 44135	11. Contract or Grant No.
	13. Type of Report and Period Covered Conference Publication
12. Sponsoring Agency Name and Address National Aeronautics and Space Administration Washington, D.C. 20546	14. Sponsoring Agency Code

15. Supplementary Notes

16. Abstract

The third in a series of conferences on solar cell high efficiency and radiation damage was held at the Lewis Research Center on June 13 and 14, 1979. Experts on solar cell technology assembled to express their judgments on attainable goals for space solar cells and on the most viable approaches past the remaining barriers to these goals. The emphasis was on the exchange and discussion of ideas and opinions rather than data. Papers were presented and workshops held on the following topics: silicon high efficiency solar cells, silicon solar cell radiation damage, GaAs solar cell performance and radiation damage, and 30 percent devices.

17. Key Words (Suggested by Author(s))	18. Distribution Statement
Solar cells; Radiation damage; Photovoltaic; Silicon; Gallium arsenide	Unclassified - unlimited STAR Category 44

19. Security Classif. (of this report)	20. Security Classif. (of this page)	21. No. of Pages	22. Price*
Unclassified	Unclassified	307	A14

* For sale by the National Technical Information Service, Springfield, Virginia 22161

☆ U.S. GOVERNMENT PRINTING OFFICE: 1979 -657-059/5203

National Aeronautics and
Space Administration

Washington, D.C.
20546

Official Business
Penalty for Private Use, $300

SPECIAL FOURTH CLASS MAIL
BOOK

Postage and Fees Paid
National Aeronautics and
Space Administration
NASA-451

NASA

POSTMASTER: If Undeliverable (Section 158
Postal Manual) Do Not Return